PhD thesis - Corrections

- Pag. 7, Section 2.2.1, paragraph 1, last line: the reference (Gibson & Ashby, 2001) has been removed, as it is not necessary

- Pag. 8, paragraph 2, line 9: the typographical error has been corrected (‘mechanism’ replaced by ‘mechanisms’)

- Pag. 12, Section 2.3.1, last paragraph, line 2: the typographical error has been corrected (‘suggests’ replaced by ‘suggest’)

- Pag. 30: in the graphs, the vertical axis label has been improved

- Pag. 40, Section 3.5.1, paragraph 1, line 1: the typographical error has been corrected (‘tool’ replaced by ‘tools’)

Queen Mary
University of London

THEORETICAL AND NUMERICAL MODELLING OF BIOLOGICALLY INSPIRED COMPOSITE MATERIALS

Federica Ongaro

A thesis submitted for the degree of Doctor of Philosophy

2017

To my loving family,
Annarosa, Giuseppe and Marco

Declaration

I, Federica Ongaro, confirm that the research included within this thesis is my own work or that where it has been carried out in collaboration with, or supported by others, this is duly acknowledged and my contribution indicated. Previously published material is also acknowledged.

I attest that I have exercised reasonable care to ensure that the work is original, and does not to the best of my knowledge break any UK law, infringe any third party's copyright or other Intellectual Property Right, or contain any confidential material.

I accept that the College has the right to use plagiarism detection software to check the electronic version of the thesis.

I confirm that this thesis has not been previously submitted for the award of a degree by this or any other university.

September 2017

Acknowledgements

First and foremost, I would like to gratefully acknowledge the Queen Mary University of London for the financial support that made this PhD project possible.

For their supervision throughout my PhD journey, I am thankful to my supervisors, Dr. Ettore Barbieri and Prof. Nicola M. Pugno.

Lastly, the most difficult people to thank: my parents, Annarosa and Giuseppe, and my brother, Marco. I will never be enough thankful to you for the support and the love you always gave me.

Abstract

The cellular nature of many biological materials, providing them with low density, high strength and high toughness, have fascinated many researchers in the field of botany and structural biology since at least one century. Bamboo, sponges, trabecular bone, tooth and honeybee combs are only few examples of natural materials with cellular architecture.

It has been widely recognised that the geometric and mechanical characteristics of the microscopic building blocks play a fundamental role on the behavior observed at the macroscale.

Up to date, many efforts have been devoted to the analysis of cellular materials with empty cells to predict the structure-property relations that link the macroscopic properties to the mechanics of their underlying microstructure.

Surprisingly, notwithstanding the great advantages of the composite solutions in nature, in the literature a limited number of investigations concern cellular structures having the internal volumes of the cells filled with fluids, fibers or other bulk materials as commonly happens in biology. In particular, a continuum model has not been derived and explicit formulas for the effective elastic constants and constitutive relations are currently not available.

To provide a contribution in this limitedly explored research area, this thesis describes the mathematical formulation and modelling technique leading to explicit expressions for the macroscopic elastic constants and stress-strain relations of biologically inspired composite cellular materials.

Two examples are included. The first deals with a regular hexagonal architecture inspired by the biological parenchyma tissue. The second concerns a mutable cellular structure, composed by mutable elongated hexagonal cells, inspired by the hygroscopic keel tissue of the ice plant *Delosperma nakurense*. In both cases, the predicted results are found to be in very good agreement with the available data in the literature.

Then, by taking into account the benefits offered by the complex hierarchical organisation of many natural systems, the attention is focused on the potential value of

adding structural hierarchy into two-dimensional composite cellular materials having a self-similar hierarchical architecture, in the first case, and different levels with different cell topologies, in the second. In contrast to the traditional cellular materials with empty cells, the analysis reveals that, in the cell-filled configuration, introducing levels of hierarchy leads to an improvement in the specific stiffness.

Finally, to offer concrete and relevant tools to engineers for developing future generations of materials with enhanced performance and unusual functionalities, a novel strategy to obtain a honeycomb with mutable cells is proposed. The technique, based on the ancient Japanese art of *kirigami*, consists in creating a pattern of cuts into a flat sheet of starting material, which is then stretched to give a honeycomb architecture. It emerges a vast range of effective constants that the so-called *kirigami honeycomb* structures can be designed with, just by changing the value of the applied stretch.

Table of contents

List of figures

List of tables

1 | Introduction

1.1 Background

It is well known that nature has developed a large number of ingenious solutions that served as a source of inspiration for scientists and engineers (Fratzl & Weinkamer, 2007; Gibson *et al.*, 2010).

In the literature, many works discuss this aspect. Among others, the pioneering textbook by Thompson (Thompson, 1992) or, more recently, by Mattheck and Kubler (Mattheck & Kubler, 1995), where the authors extracted engineering principles from the structure of trees.

Nowadays, terms like *biomimetics* or *bioinspiration* (Sanchez *et al.*, 2005; Vincent *et al.*, 2006; Fratzl, 2007) are commonly used to describe the new approach in chemistry, material science and engineering. That is, researchers study biological systems to find some useful principles to create and/or improve new materials and simplify many of our day-to-day functions. See, for example, Table 1.1. Indeed, lessons learned from nature solved a variety of technical challenges in material science (Jeronimidis & Atkins, 1995), architecture (Kemp, 2004), aerodynamics and mechanical engineering (Milwich *et al.*, 2006). For instance, most are familiar with the Velcro, inspired by the way plant burrs stuck to animal fur (Cohen, 2005; Jenkins, 2012), with the high performance swimsuits, modelled on the structure of shark skin to reduce drag in water (Bixler & Bhushan, 2012), or with the super adhesive fabrics that mimic the configuration of the gecko foot (Shah & Sitti, 2004).

Differently from the engineer, nature has a relatively limited number of structural elements to choose: polymers, composites of polymers and ceramic particles (Fratzl & Weinkamer, 2007). However, even with these restrictions, nature created a wide range of systems with distinctive functions and remarkable mechanical properties that often surpass those of their components by orders of magnitude (Gibson, 2012), as trees, skeletons and shells.

In their most sophisticated form, natural systems are even able to adapt their configuration to the changing mechanical environments (Fratzl & Weinkamer, 2011; 2007). For example, the leaves of monocotyledon plants, irises and maize (Gibson, 2012), and some tubular structures, plants stems and animal quills among others, display a peculiar composite architecture where a foam-like core behaves like an elastic foundation supporting the dense outer faces (Dawson & Gibson, 2007; Gibson, 2005). Similar composite solutions can also be found in many vegetative tissues, as the parenchyma tissue and the hygroscopic keel tissue of the ice plant, characterised by a honeycomb structure having the internal volumes of the cells filled with fluids, fibers or other bulk materials to better resist external stimuli. In other cases, wood, bone or glass sponges (Aizenberg *et al.*, 2005), natural systems have a complex hierarchical architecture allowing the functional adaptation of the structure at all levels of hierarchy (Fratzl & Weinkamer, 2007). That is to say, a specific property can be tuned at different levels, independently of other parameters, and adapted to the local needs (Pan, 2014; Gao, 2010). According to Fratzl & Weinkamer (2007) and Lakes (1993), structural hierarchy plays a key role in the exceptional mechanical properties of natural materials and properties like superplasticity and increased toughness are due to hierarchy.

Up to date, the most investigated biological systems are cellular materials. The latter, due to their peculiar characteristic of having remarkable mechanical properties at low weight, inspired the man-made honeycombs and foams (Gibson *et al.*, 2010; Meyers *et al.*, 2008; Altenbach & Oechsner, 2010; Gibson & Ashby, 2001; Gibson, 2012), very promising for engineering applications in a variety of industries including aerospace, automotive, marine and constructions (Wilson, 1990; Thompson, 1992; Bitzer, 1994). As an example, cellular solids are widely used as lightweight fillers in sandwich panels, crash energy absorbers, thermal and acoustic insulators, negative Poisson's ratio materials.

1.2 Scope and outline

In the literature, many efforts have been devoted to the characterisation of cellular materials with empty cells. Surprisingly, notwithstanding the great advantages of the composite solutions in nature, few investigations concern cellular materials with filled cells.

To help filling this research gap, the present thesis aims to provide theoretical models to predict the effective properties of biologically inspired filled cellular materials and to suggest some possible ways to create/improve low-weight cellular structures. In

Table 1.1 Biological inspiration: examples of natural systems and their selected functions

bacteria	biological motor
plants	chemical energy conversion, superhydrophobicity, self-cleaning, drag reduction, adhesion, motion, hydrophilicity
insects, spiders, lizards and frogs	superhydrophobicity, reversible adhesion in dry and wet environments
aquatic animals	low hydrodynamic drag, energy production
birds	aerodynamic lift, light coloration, camouflage, insulation
seashells, bones, teeth	high mechanical strength
spider web	biological self-assembly
moth-eye effect and structural coloration	antireflective surfaces, structural coloration
fur and skin of polar bear	thermal insulation
biological systems	self-healing, sensory-aid devices

addition, the theoretical results are verified by comparison with the available data, by numerical simulations and by some practical applications to the biological systems.

The thesis is organised in seven chapters, including this introduction.

Initially, Chapter 2 introduces the basic concepts to describe the topological, geometrical and mechanical properties of two-dimensional cellular materials, with reference to the pioneering work of Gibson and Ashby (Gibson & Ashby, 2001).

Then, Chapters 3 and 4 focus on composite cellular materials and, in particular, describe the mathematical formulation and modelling technique that lead to the closed-form expressions of the effective elastic constants and constitutive equations. Two cases are considered: the regular hexagonal architecture inspired by the parenchyma tissue (Gibson, 2012), in Chapter 3, and the mutable microstructure having elongated cells inspired by the ice plant *Delosperma nakurense* (Harrington *et al.*, 2011), in Chapter 4.

The extension of the theory to the hierarchical configuration is presented in Chapter 5. The study investigates how hierarchy affects the macroscopic elastic moduli of a two-dimensional composite cellular material, as well as the role of material heterogeneity and cell topologies at different levels in obtaining improved stiffness.

Chapter 6, in addition, provides the example of the kirigami-inspired honeycomb (Neville *et al.*, 2014). That is to say, a honeycomb obtained by applying the ancient Japanese art of paper sculptures (from the Japanese *kiru*=to cut and *kami*=paper) consisting in cutting a sheet of paper to create a particular pattern and then stretching it.

Finally, Chapter 7 summarises the main findings and highlights possible scenarios for future work.

1.3 Novelties of the thesis

With respect to the published works, this thesis introduces the following novelties.

The first consists in adopting the Euler-Bernoulli beam on Winkler foundation model to explore the mechanical behavior of composite cellular materials. According to the proposed strategy, employed here for the first time, a series of linear elastic springs, the Winkler foundation, simulates the elastic material filling the cells.

The aforementioned technique, in conjunction with an energetic approach, leads to explicit expressions for the constitutive equations and elastic moduli in the macroscopic

description. The obtained results, verified by means of numerical simulations and by comparison with the data available in the literature, offer a useful tool to predict the mechanical properties of both biological and man-made composite cellular materials.

In addition, the extension of the theory to the case of structural hierarchy provides a novel idea to avert the detrimental effect on the specific stiffness that characterises the traditional cellular materials with empty cells.

Finally, the last part of the thesis deals with the emerging field of kirigami applications in engineering. Specifically, the kirigami technique is adopted to create the so-called *kirigami honeycomb* and, for the first time, explicit relations between the pattern of cuts and the overall mechanical response are reported.

2 | Cellular materials: overview and basic theoretical tools

A lesson which is relevant to all studies
of the properties of cellular solids is this:
first characterize your cells
M. F. Ashby, L. J. Gibson

2.1 Overview

At mesoscopic scale, cellular materials, honeycombs and foams, are discrete materials characterised by a more or less clearly distinguishable architecture. They are generated by tessellating a unit cell, a concave space bounded by edges or solids faces, throughout the space.

The use of cellular structures, allowing a material to have good mechanical properties at low weight, is very common in nature. Biological systems such as wood, bone, tooth, mollusk shells, crustaceans and many siliceous skeleton species like radiolarians, sea sponges and diatoms (Gordon *et al.*, 2008) are some examples.

People have used natural cellular materials for millennia; wooden artefacts have been found in the Egyptian pyramids and cork has been used for the soles of shoes since Roman times (Gibson & Ashby, 2001). Today, the structure of natural cellular materials is mimicked in engineering honeycombs, where the cells are obtained by extrusion of planar faces, and foams, where the cells are polyhedra packed in the three-dimensional space.

Because of their unique properties arising from the cellular architecture, honeycombs and foams are widely used in a variety of applications. For example, the low density makes them ideal core materials in lightweight and high-performance sandwich panels used in aerospace components and sporting equipment. The low compressive strength and the high deformation capacity provide excellent shock mitigation and energy

absorption characteristics in impulsive phenomena. Finally, small cells and low volume fraction lead to closed-cell foams that are excellent thermal insulators.

In addition to the relative density, defined as the ratio of the density of the cellular solid to the density of the cell walls, two sets of parameters affect the mechanical behavior of honeycombs and foams. The first characterises the constituent material while the second is related to the geometric and topological properties of the microstructure.

The basic theoretical tools to understand the mechanics of two-dimensional cellular materials, topic of the present thesis, are provided in the following section.

2.2 Two-dimensional cellular materials: basic theoretical tools

2.2.1 Cell shape

Honeycombs (or planar lattices) are generated by tessellating a polygon to fill the plane without gaps or overlaps, and such that neighbouring polygons share full edges and have coincident vertices. In addition, angles meeting at one vertex sum up to 2π.

Classically, honeycombs are classified as regular, semi-regular or irregular (Fleck *et al.*, 2010). In the first case, the tessellation is composed by a single type of regular polygon, the square, the triangle or the hexagon, while the second is based on two or more kinds of them. In particular, only eight semi-regular tessellations exist (Cundy & Rolett, 1961; Lockwood & Macmillan, 1978). An example, sketched in Figure 2.1c, is the triangular-hexagonal lattice, known as the Kagome. Finally, the irregular tessellations are constructed from two or more irregular polygons of different size, like the random Voronoi lattice (Gibson & Ashby, 2001) or the Penrose tiling (de Bruijn, 1981). In what follows, only regular honeycombs are considered.

2.2.2 Stretch and bending-dominated lattices: the role of nodal connectivity

From a geometric point of view, a two-dimensional cellular material can be described as a number of vertices, V, joined by edges, E, surrounding cells, C, related by the Euler's law (Gibson & Ashby, 2001)

$$C - E + V = 1. \tag{2.1}$$

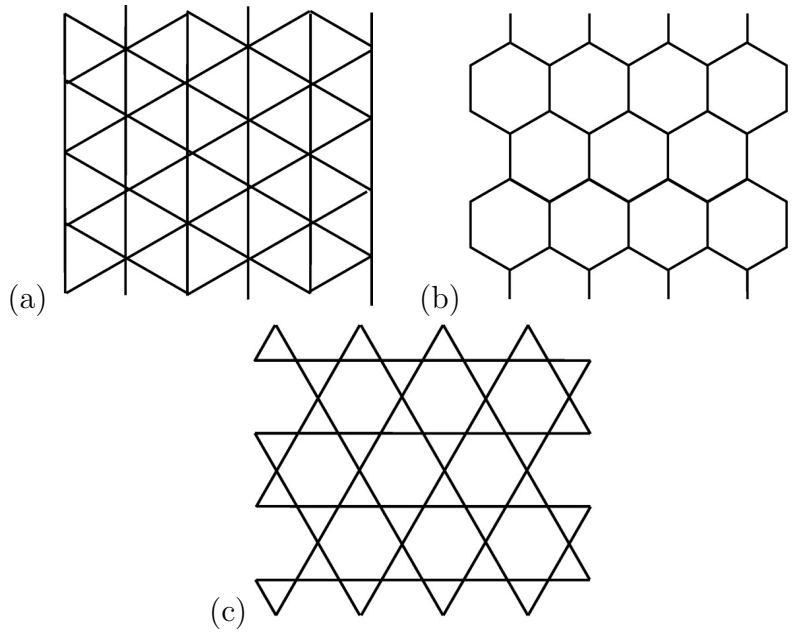

Figure 2.1: The regular (a) triangular and (b) hexagonal lattices, (c) the semi-regular Kagome tessellation

The number of edges that meet at a vertex, defined *nodal connectivity* Z_e, can be expressed by

$$Z_e = \frac{2E}{V} \tag{2.2}$$

since each edge connects two vertices (Gibson & Ashby, 2001). The hexagonal, square and triangular lattices have, respectively, $Z_e = 3$, $Z_e = 4$ and $Z_e = 6$.

The macroscopic properties of a honeycomb are strongly affected by its nodal connectivity rather than by the regularity of its microstructure. The reason is related to how the honeycomb responds to macroscopic loads, that is to say with a bending or stretch-dominated behavior. The distinction of a bending and a stretch-dominated lattice, exhaustively described in Fleck *et al.* (2010), is connected to the collapse response of a pin-jointed frame of the same morphology. If the parent pin-jointed frame has either no collapse mechanism or only a periodic collapse mechanism that do not produce macroscopic strain, the welded-joint version (the lattice itself) is stretch-dominated. Conversely, when the parent frame exhibits collapse mechanisms that generate macroscopic strain, the welded-joint structure is bending-dominated.

By applying the Maxwell's necessary condition for a planar pin-jointed frame made up of b struts and j frictionless joints to be rigid (Deshpande *et al.*, 2001),

$$b - 2\,j + 3 = 0, \tag{2.3}$$

Fleck et al. (Fleck *et al.*, 2010) suggested two classes of planar lattices according to their connectivity Z_e. The first, with $Z_e > 4$, are the rigid lattices that possess no collapse mechanisms. If loaded, their members carry tension or compression, leading to a stretch-dominated structure. In the second case, with $Z_e < 4$, the lattices are not rigid and external loads cause their members to bend. The boundary case $Z_e = 4$ includes both types of behavior depending on the collapse mechanism arising in the lattice. For example, the Kagome microstructure collapses by no-strain producing mechanism and is classified as stretch-dominated. Differently, the square microstructure has a bending-dominated behavior (collapse mechanism leading to macroscopic strain) if loaded in the diagonal direction and a stretch-dominated behavior when the load is aligned with the walls. A detailed description, that is beyond the scope of the present thesis, can be found in Hutchinson & Fleck (2005), where the authors proposed a methodology based on the Bloch-wave analysis to explore the collapse mechanism of different structures.

Finally, in terms of mechanical efficiency, one key findings of Ashby (2006) is that the specific stiffness and the specific strength of the stretch-dominated structures are higher than those in which the dominant mode of deformation is by bending.

2.2.3 Honeycomb mechanics

Figure 2.2 illustrates the compressive stress-strain curves of a honeycomb subjected to in-plane loads: Figure 2.2a in the case of a bending-dominated structure and Figure 2.2b in the case of a stretch-dominated one.

As it can be seen, there are generally three zones. Firstly, a linear elastic regime corresponding to the bending, Figure 2.2a, or stretching, Figure 2.2b, of the cell walls. Then, a stress plateau where the cells progressively collapse at a nearly constant stress by elastic buckling, plastic yielding or brittle crushing. Finally, at high strains, a regime of densification in which a great number of cells are collapsed, their opposite walls impinge and further deformations compress the constituent material itself. In terms of deformations, in the linear-elastic regime they are homogeneous throughout the specimen and, as in ordinary solids, the Hooke's law can be applied. Conversely, in the plateau regime the deformations are strongly localised, with the formation of bands perpendicular to the loading direction.

In the present thesis, only the linear-elastic behavior is considered.

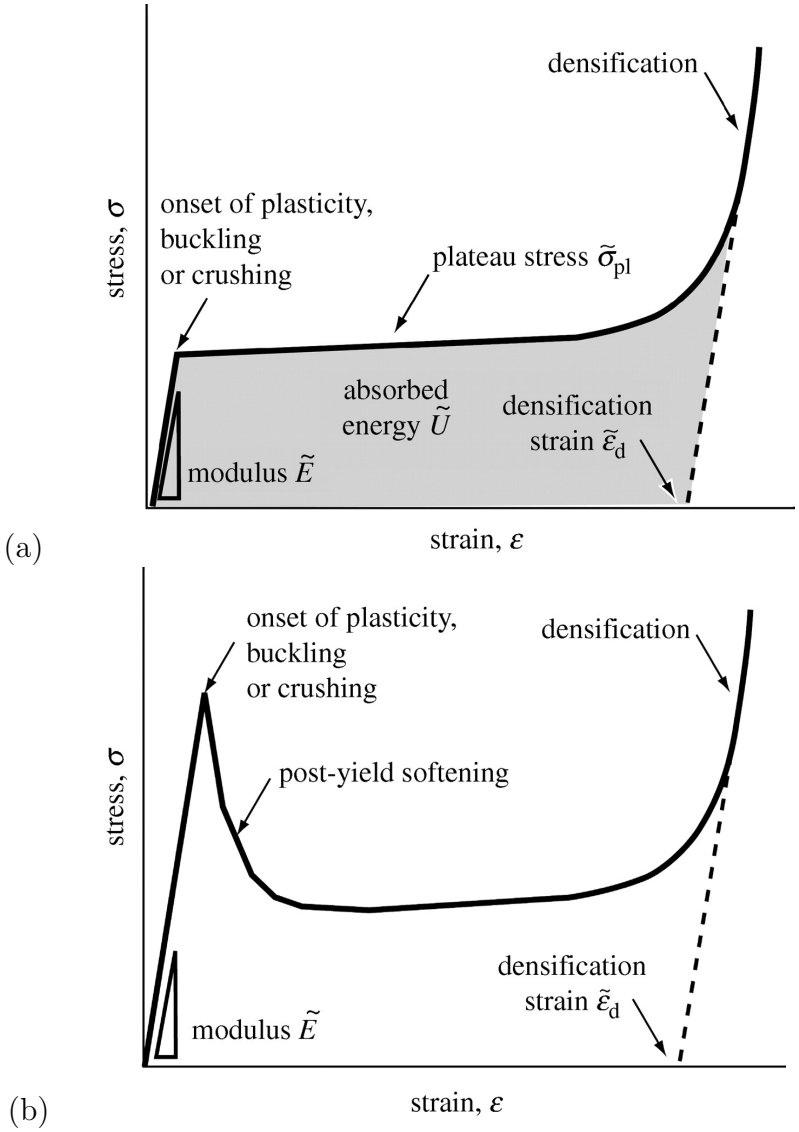

Figure 2.2: A schematic compressive stress-strain curve for (a) bending-dominated and (b) stretch-dominated structures, taken from Gibson & Ashby (2001)

2.3 Estimation of the effective properties by micro-mechanical modelling: prior works and alternative techniques

As stated in Section 2.1, cellular materials have a great variety of engineering applications. In most cases, their use serves macroscopic purposes so that a continuum description in terms of effective mechanical properties is of importance.

However, the formulation of a continuum model is hindered by two types of difficulties: the spatial variability of size and morphology of the microscopic architecture, on one side, and the crucial passage from the microscopic discrete description to the coarse continuous one, on the other.

Regarding the first aspect, the typical approach to the continuum modelling of cellular materials includes the assumption of periodicity and the selection of a *Representative Volume Element* (RVE), or *unit cell*. The latter is an important concept in the field of microstructured materials and we will come back to it later in the thesis (cf. Sections 3.2.2 and 3.6.1) as much debate has taken place on what constitutes its appropriate definition.

To overcome the second problem, energy equivalence concepts and micro-macro relations in terms of forces and displacements are usually applied. Also, linear elasticity and material isotropy, in conjunction with the underlying microstructure assumed to be governed by the classical beam theory (Altenbach & Oechsner, 2010), are three commonly used simplifications that provide explicit stress-strain relations and help clarifying the basic mechanical aspects (Davini & Ongaro, 2011).

Many authors extensively studied the mechanical modelling of cellular materials and it would be difficult to quote without omissions the vast literature flourished in the last years. Noteworthy contributions, suggesting different assumptions and techniques, are presented in the following sections. For the interested reader, the suggested references can be supplemented with the reviews proposed in Christensen (2000), Kraynik *et al.* (1998) and Warren & Kraynik (1997), concerning the mechanical behavior of honeycombs and of both liquid and solid foams.

The technical aspects regarding the analysis of structural lattices and the derivation of their equivalent constitutive equations are throughly reviewed in Noor (1988) and in Ostoya-Starzewski (2002), where an extended list of references is also provided.

2.3.1 The pioneering contribution of Gibson and Ashby

The most known and widely used micromechanical model is the *Gibson and Ashby's model* (Gibson, 1989; Gibson & Ashby, 2001; Gibson *et al.*, 1982) that focuses on the deformation mechanism of a single cell subjected to different types of external loads (Figure 2.3).

By assuming infinitesimal strains and applying the standard beam theory, the authors obtained simple power-law relations between the microstructure's parameters and the macroscopic properties of a wide range of cellular materials.

For example, in the case of a hexagonal honeycomb, the in-plane elastic constants are expressed by

$$\begin{aligned}
\frac{E_1}{E_s} &= \frac{(t/\ell)^3 \cos\theta}{(h/\ell + \sin\theta)\,\sin^2\theta}, \\
\frac{E_2}{E_s} &= \frac{(t/\ell)^3 (h/\ell + \sin\theta)}{\cos^3\theta}, \\
\nu_{12} &= \frac{\cos^2\theta}{(h/\ell + \sin\theta)\sin\theta}, \\
\nu_{21} &= \frac{\sin\theta\,(h/\ell + \sin\theta)}{\cos^2\theta}, \\
\frac{G}{E_s} &= \frac{(t/\ell)^3 (h/\ell + \sin\theta)}{(h/\ell)^2\,(1 + 2\,h/\ell)\,\cos\theta},
\end{aligned} \tag{2.4}$$

with E_1, ν_{12} and E_2, ν_{21}, respectively, the effective Young's modulus and corresponding Poisson's ratio in the $\boldsymbol{e}_1$ and $\boldsymbol{e}_2$ direction, G the effective shear modulus, E_s the Young's modulus of the constituent material. h, ℓ, t and θ geometrically characterise the microstructure, being, in turn, the length of the vertical and inclined cell walls, their thickness and inclination (Figure 2.3).

In terms of the effective Young's modulus, for the equilateral triangular microstructure (Figure 2.4a) Gibson & Ashby (2001) suggest

$$\frac{E_1}{E_s} = \frac{E_2}{E_s} = 1.15 \left(\frac{t}{\ell}\right) \tag{2.5}$$

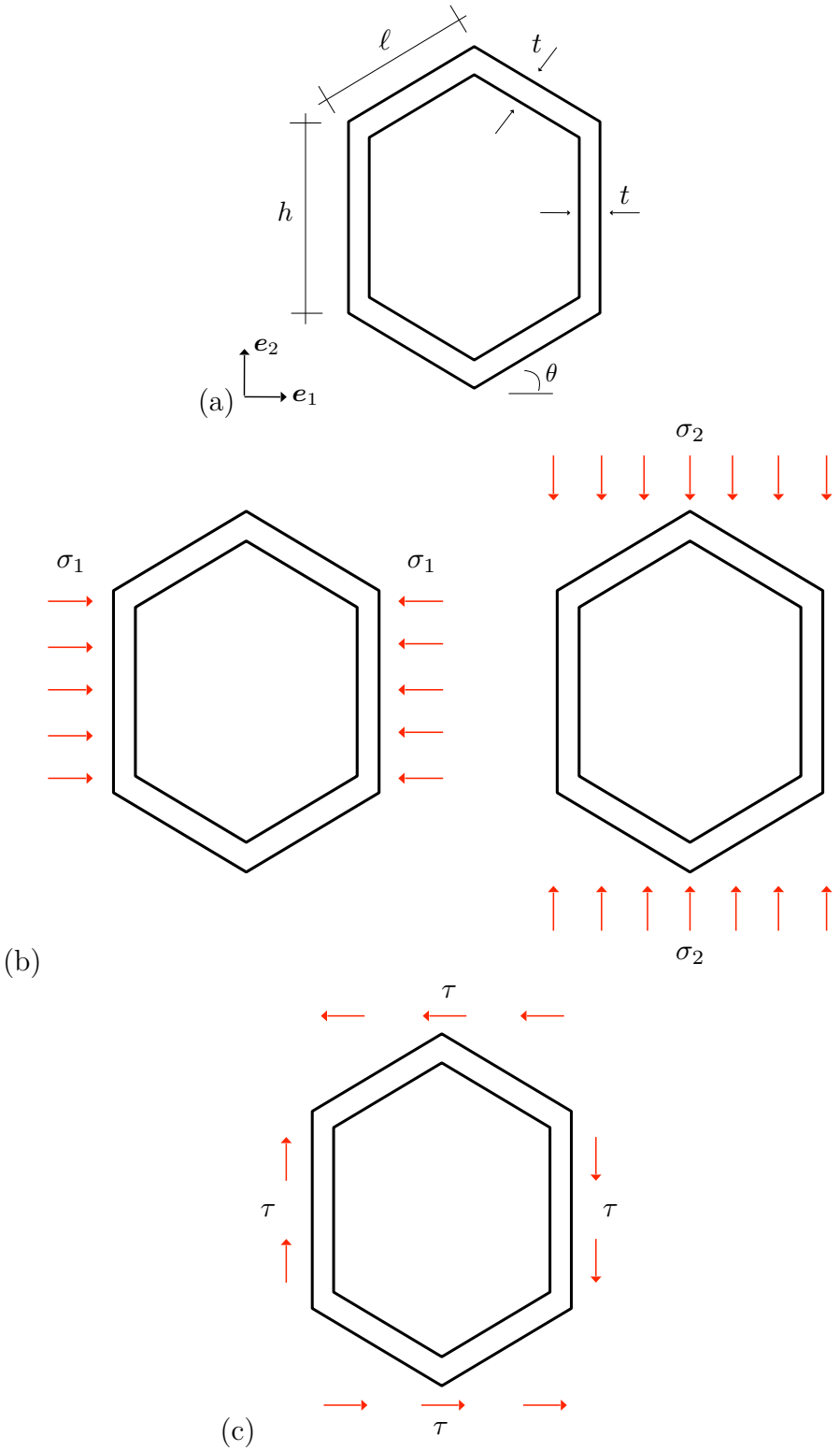

Figure 2.3: The Gibson and Ashby model: (a) the unit cell, (b) compression, (c) shear

while, for the square lattice (Figure 2.4b),

$$\frac{E_1}{E_s} = \frac{E_2}{E_s} = \frac{t}{\ell} \tag{2.6}$$

and, if loaded in the diagonal direction,

$$\frac{E_{45}}{E_s} = 2\left(\frac{t}{\ell}\right)^3. \tag{2.7}$$

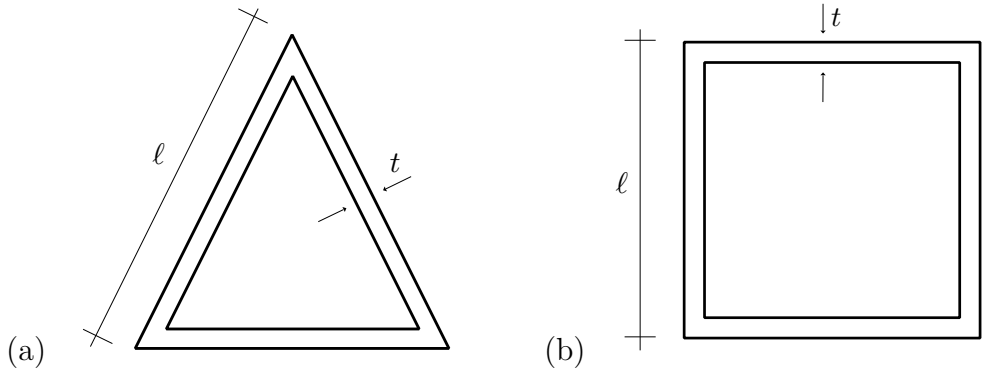

Figure 2.4: The Gibson and Ashby model: (a) the triangular and (b) the square microstructures

As it can be seen from Equations (2.4) and (2.5), the macroscopic stiffness of the triangular and hexagonal honeycomb scales with different powers of t/ℓ: the former with the first power, the latter with its cube. This difference is related to how the microstructure responds to macroscopic loads, that is to say with a stretch or bending-dominated behavior (cf. Section 2.2.2). In particular, the proportionality to the first power of t/ℓ, rather than to its cube, makes the stretch-dominated structures, typified by the triangular lattice, intrinsically stiffer and stronger than the bending-dominated ones, typified by the hexagonal microstructure. The same considerations apply in the case of the square honeycomb: stretch-dominated behavior when the load is aligned to the cell walls, Equation (2.6), bending-dominated one when loaded in the diagonal direction, Equation (2.7). However, because of the deformation mechanism involving "hard" modes (i.e., tension and compression), the stretch-dominated structures are characterised by post-yielding softening (Figure 2.2b) as the initial yield is followed by plastic buckling or brittle collapse of the struts (Ashby, 2006). Consequently, they are not the ideal candidate for energy absorbing applications that require, ideally, a stress-strain curve with a long plateau as in the case of the bending-dominated lattices (Figure 2.2a).

2.3.2 Equilibrium considerations and structural analysis-based technique

By applying the principles of structural analysis similar to that described in Gibson & Ashby (2001), Wang and Stronge (Wang & Stronge, 1999) obtained the equivalent constitutive equations for a two-dimensional hexagonal honeycomb composed of extensional and flexural elements. In Wang & Stronge (1999) the problem is performed in the context of micropolar elasticity, theory developed by Eringen (Eringen, 1967) in 1967.

A distinguishing feature of micropolar continua is the introduction of an additional deformation variable, the microrotation field, that is independent of the translational displacements assumed in classical elasticity. This model obviously encounters severe philosophical difficulties if considered as representative of a continuum. For example, the interactions between two neighbouring material elements involve the couple stresses, related to the microrotation gradients, and the Cauchy stresses, as in classical mechanics. Also, contrary to classical elasticity, the Cauchy tensor is not symmetric, as well as the strain tensor.

Regarding the hexagonal microstructure analysed in Wang & Stronge (1999), the authors described the deformation states of the representative volume element in terms of displacements and rotations of the nodes where the cell walls, represented as elastic beams, intersect. By taking into account the connectivity of the structure and enforcing the equilibrium conditions at the joints, it emerges that the relations for the normal stresses and strains obtained in Wang & Stronge (1999) are in accordance with those proposed by Gibson and Ashby (Gibson & Ashby, 2001). Conversely, assuming micropolarity and the possibility of wall stretching lead to different results in terms of the shear stresses and strains. In Wang & Stronge (1999) it is also confirmed the proportionality of the effective stiffness to the third power of t/ℓ, ratio between the thickness and the length of the cell walls (cf. Equations (2.4)).

An analysis of the micropolar behavior of two-dimensional lattice geometries, the square, the triangular and the hexagonal, was also provided by Warren and Byskov (Warren & Byskov, 2002) and by Dos Reis and Ganghoffer (Dos Reis & Ganghoffer, 2012a). In both cases, the authors represented the lattice as a sequence of elastic beams undergoing extensional and flexural deformations and derived the continuum model by means of discrete homogenization (Dos Reis & Ganghoffer, 2012b; Caillerie *et al.*, 2006). This method, whose basic idea is the periodic repetition of an elementary cell to define an infinite lattice, may be explained as follows.

Firstly, the periodic structure is parametrised by a small parameter, ϵ, defined as the ratio between a characteristic length of the unit cell and a characteristic length of the entire structure. Then, Taylor's series expansions of the displacements and rotations are inserted into the equilibrium equations of the lattice, expressed in terms of ϵ. Finally, considering the limit situation of a continuous density of cells, corresponding to $\epsilon \to 0$, gives the homogenized model. The effective properties naturally follow from the homogenization technique.

In terms of Warren & Byskov (2002) and Dos Reis & Ganghoffer (2012a), it emerges that the predicted elastic moduli agree with those in Gibson & Ashby (2001) only in the case of slender beams. For a slenderness of 10, the discrepancy is about 5%. In accordance with Christensen (2000), the study in Warren & Byskov (2002) also reveals that it is necessary to retain the second-order terms in the Taylor's expansions to induce micropolar effects. If these terms are neglected, the effective material is a classical continuum whose elastic constants coincide with those presented in Gibson & Ashby (2001).

2.3.3 Energy equivalence-based technique

An alternative approach to solve the crucial passage from micro to macro and to derive the constitutive model for two-dimensional microstructures subjected to in-plane deformations was adopted by Chen et al. (Chen *et al.*, 1998), Kumar and McDowell (Kumar & McDowell, 2004), Bazant (Bazant, 1971), Bazant and Christensen (Bazant & Christensen, 1972) and Perano (Perano, 1983). As in Wang & Stronge (1999) and Warren & Byskov (2002), in the aforementioned works the discrete lattice is idealised as a sequence of Euler-Bernoulli beams while, in the macroscopic description, the discrete structure is assumed to be represented by a micropolar continuum. Few main steps summarise the suggested technique.

Initially, an appropriate representative unit cell is defined. Secondly, summing the strain energies of its individual members, expressed as a function of the displacements and rotations of the extreme nodes, gives the strain energy of the discrete structure. Then, the discrete variables representing the joints' displacements and rotations are approximated by Taylor's series expansions of the corresponding continuous fields at the centroid of the unit cell (Bazant & Christensen, 1972; Warren & Byskov, 2002). Substituting the Taylor's expansions into the previously obtained discrete strain energy provides its continuum approximation. Finally, equating the latter to the strain energy of the hypothesised equivalent micropolar continuum and applying the standard theory of micropolar elasticity, give the effective constitutive equations and elastic moduli.

Differently from Chen *et al.* (1998) and Perano (1983), where only the first order derivatives in the Taylor's expansions are considered, in Kumar & McDowell (2004), Bazant (1971) and Bazant & Christensen (1972) also the second order terms that can be integrated by parts and converted into first order ones are retained. As pointed out in Bazant (1971) and Bazant & Christensen (1972), this strategy is necessary to ensure the equilibrium of the nodes and the connectivity of the structure. Neglecting these important aspects led Chen et al. (Chen *et al.*, 1998) to the erroneous conclusion that the strain energy density of the equilateral triangular honeycomb in the continuum approximation was three times that of the hexagonal one. Indeed, the first lattice contains three times as many beams per unit volume as the second. The authors, however, went on and calculated the effective elastic constants and constitutive equations. Again, they found incorrect results in terms of couple stress-curvature relations. Specifically, the values of the couple stresses obtained in Chen *et al.* (1998) are four times those provided by the vast majority of authors (Warren & Byskov, 2002).

Starting from the calculation of the strain energy of the unit cell, Davini and Ongaro (Davini & Ongaro, 2011) adopted the viewpoint of the homogenization theory (Braides, 2002; Dal Maso, 1993) to deduce a continuum model for a hexagonal honeycomb. As in the previous works, the analysis is restricted to linear elasticity and the microstructure is described in terms of Euler-Bernoulli beams. In Davini & Ongaro (2011), the homogenized continuum, seen as the variational limit of a sequence of discrete systems of hexagonal cells with increasingly smaller size, emerges from general theorems of Γ-convergence. At variance with Chen *et al.* (1998), Perano (1983), Bazant (1971), Bazant & Christensen (1972) and Warren & Byskov (2002), the limit model is a pseudo-polar continuum, that is a material that can undergo applied distributed couples without developing couple stresses. Regarding the effective elastic moduli and constitutive equations, the predicted expressions coincide with those proposed in Dos Reis & Ganghoffer (2012a) and agree with the findings of Gibson and Ashby (Gibson & Ashby, 2001) in the limit of slender beams.

3 | Continuum modelling of composite cellular materials

3.1 Motivation and prior works

As seen in Chapter 2, many efforts have been devoted to the prediction of the effective properties of regular cellular materials with empty cells.

In reality, if examined at the microscale, many biological systems reveal a honeycomb architecture having the internal volumes of the cells filled with fluids, fibers or other bulk materials.

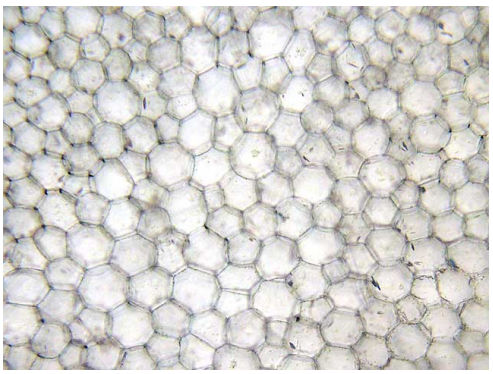

Figure 3.1: The biological parenchyma tissue. Figure taken from Razzaq (2016)

One example, that will be extensively analysed in Section 3.8, is the vegetative parenchyma tissue (Gibson, 2012; Gibson *et al.*, 2010; Bruce, 2003; Warner *et al.*, 2000; Georget *et al.*, 2003), composed by thin-walled polyhedral cells filled with a fluid (Figure 3.1). The latter, due to the hydrostatic pressure exerted against the cell walls, significantly improves the resistance of the cells and, consequently, of the whole tissue. The parenchyma, because of its low relative density, is found in many natural systems, as the leaves of monocotyledon plants. In this case, the parenchyma constitutes the lightweight inner core of the leaf and, similarly to an elastic substrate, supports the

dense and strong fiber-composite outer faces. Recent studies (Gibson, 2005; Dawson & Gibson, 2007; Gibson, 2012) reveal that this composite solution, notwithstanding the low mechanical properties of the parenchyma, makes the leaf more performant in terms of bending and buckling resistance.

In spite of the proven benefits distinguishing the biological composite configurations, the scientific literature is lacking in the context of cellular materials with filled cells.

The few available investigations (Niklas, 1992; Georget *et al.*, 2003), in most cases, deal with the mechanical behavior of pressurised plant tissues and analytically describe the influence of the turgor pressure on the effective stiffness.

In particular, Georget et al. (Georget *et al.*, 2003) evaluated the Young's modulus of the carrot tissue, modelled as a fluid-filled foam, and it emerged that the provided results were in good agreement with the experimental values.

Warner et al. (Warner *et al.*, 2000), who went in this direction, focused on the deformation mechanisms of different types of fluid-filled cellular solids to characterise the elastic behavior and initial failure of food materials. According to the authors, above a critical strain, the fluid inside the cells forces the walls to stretch rather than to bend, as it happens in the case of hollow cellular solids. By taking into account the considerations in Section 2.3.1, this leads to an improvement in the mechanical resistance of the system, since the stretch-dominated structures are stiffer and stronger than the bending-dominated ones.

In the context of sandwich panels, Burlayenko and Sadowski (Burlayenko & Sadowski, 2010) numerically evaluated the structural performance of aluminium honeycombs filled with a polyvinyl-chloride (PVC) foam. The study suggests that the effective stiffness of the honeycomb, subjected to various loading states, significantly increases due to the presence of the PVC filler.

Finally, from the analysis of the in-plane crush response of a honeycomb with circular cells, D'Mello and Waas (D'Mello & Waas, 2013) found that filling the cells with a polydimethylsiloxane (PDMS) elastomer provided an enhancement of the energy absorption capability.

Though some of the abovementioned authors numerically and theoretically analysed the morphology, composition and mechanical behavior of filled cellular materials, up to date closed-form expressions for the effective elastic moduli and constitutive equations have not been derived.

To make a contribution to this incomplete research area and to provide some useful tools for practical applications, the following sections present a continuum model for two-dimensional cellular materials with a hexagonal microstructure and the cells filled

with a generic elastic medium. The analysis is then extended to the cases of equilateral triangular cells, in Appendix A, and to the square microstructure, in Appendix B.

3.2 Problem statement

3.2.1 Geometric description

In terms of christallography, the configuration of the considered composite material can be described as the union of two simple Bravais lattices,

$$L_1(\ell) := \left\{ \mathbf{X} \in \mathbb{R}^2 : \mathbf{X} = n^1 \mathbf{l}_1 + n^2 \mathbf{l}_2 \,, \text{with}\, (n^1, n^2) \in \mathbb{Z}^2 \right\} \tag{3.1}$$

and

$$L_2(\ell) := \mathbf{s} + L_1(\ell), \tag{3.2}$$

simply shifted with respect to each other.

In a global reference system, defined by the unit orthonormal vectors $\boldsymbol{e}_1$, $\boldsymbol{e}_2$ and by the coordinate system $(X, Y)^T$, the components of the lattice vectors, $\mathbf{l}_1$ and $\mathbf{l}_2$, and of the shift vector, $\mathbf{s}$, are

$$\mathbf{l}_1 = \left[\begin{array}{cc} \sqrt{3}\,\ell & 0 \end{array} \right]^T, \quad \mathbf{l}_2 = \left[\begin{array}{cc} \dfrac{\sqrt{3}\,\ell}{2} & \dfrac{3\,\ell}{2} \end{array} \right]^T, \quad \mathbf{s} = \left[\begin{array}{cc} \dfrac{\sqrt{3}\,\ell}{2} & \dfrac{\ell}{2} \end{array} \right]^T, \tag{3.3}$$

with ℓ the length (the lattice size) of the cell walls (Figure 3.2a).

3.2.2 The unit cell

In understanding how a homogenized medium can "substitute" a heterogeneous material, it is implicitly assumed that the problem contains two well-separated scales. Namely, the microscopic scale (or local scale), small enough to clearly identify the heterogeneities, and the macroscopic scale (or overall scale), where the heterogeneities can be sweared-out (Michel *et al.*, 1999).

At the macroscopic scale, the effective properties of the composite can be derived from the geometric and mechanical parameters of the microstructure. However, analysing large size volumes on a microstructural level to gain an accurate estimation of the local fields is unsuitable and, in some cases, may involve considerable efforts. Thus, the notion of *Representative Volume Element* (RVE) is of paramount importance.

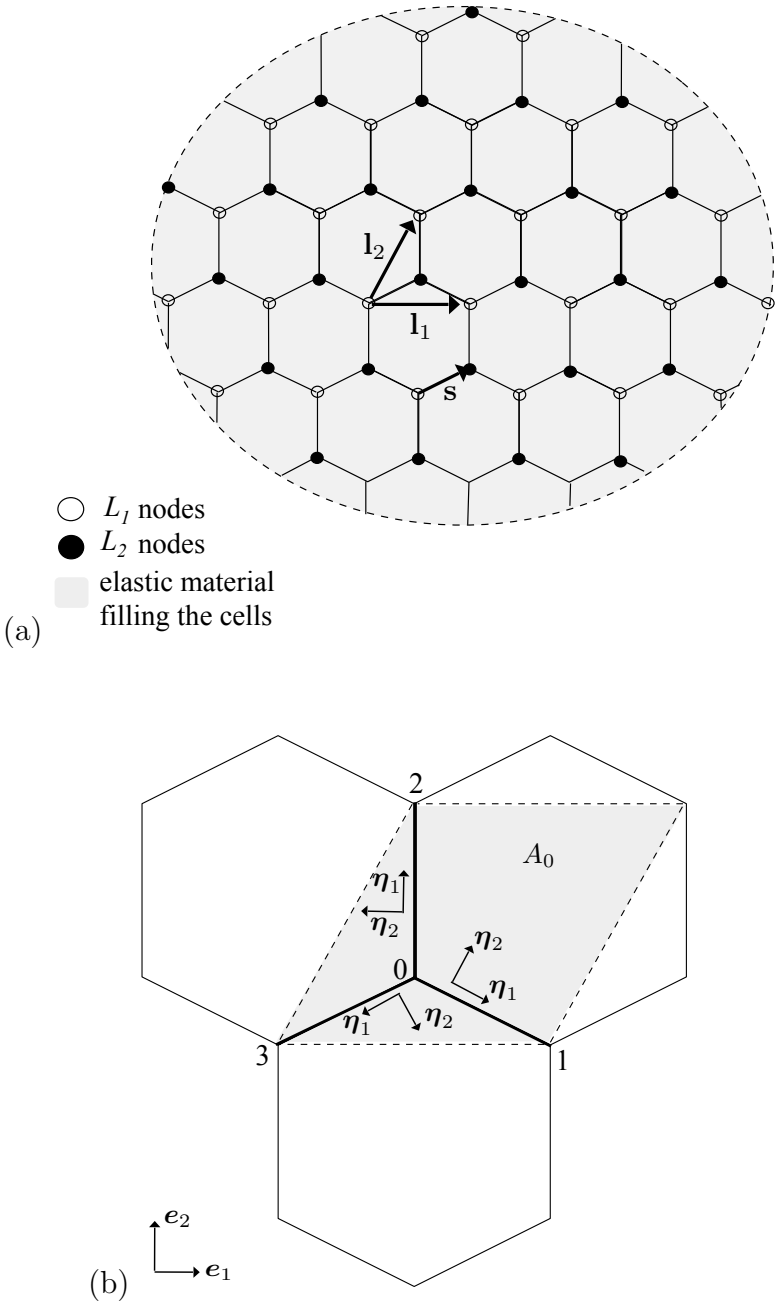

Figure 3.2: The composite cellular material: (a) the hexagonal microstructure and (b) the unit cell

The RVE is usually regarded as a volume V that is sufficiently large to include a sampling of all microstructural heterogeneities and sufficiently small to be considered as a volume element of continuum mechanics (Kanit *et al.*, 2003; Drugan & Willis, 1996). Through the RVE-based analysis, the necessary microstructure's parameters are extracted and, according to the homogenization procedure, both the RVE of the real system and the corresponding volume element of the equivalent homogeneous continuum, if deformed, are assumed to be subjected to the same stress, strain or energy fields (Burlayenko & Sadowski, 2010). From a conventional analysis at the macroscopic level, the information are then transferred between the micro (RVE) and the macro (equivalent continuum) scales and the constitutive model for the approximated homogenized material can be obtained. Although the precise definition of the RVE is still a matter of debate, in investigating materials with a periodic microstructure, as in the present thesis, the repetitive unit cell of the tessellation is generally assumed as RVE (Nemat-Nasser & Hori, 1993; Pellegrino *et al.*, 1999).

In the examined case, the unit cell (Figure 3.2b) is composed by the three external nodes, 1, 2 and 3, linked to the central one, 0, by the line elements 0-1, 0-2, 0-3, respectively represented by the vectors

$$\mathbf{b}_1 = \mathbf{l}_1 - \mathbf{s}, \qquad \mathbf{b}_2 = \mathbf{l}_2 - \mathbf{s}, \qquad \mathbf{b}_3 = -\mathbf{s}. \tag{3.4}$$

From a mechanical point of view, the connecting elements are treated as Euler-Bernoulli beams on Winkler foundation. Specifically, a series of identical and closely spaced linear elastic springs, the Winkler foundation, simulates the elastic material filling the cells (Figure 3.3). This assumption, along with a energy-based approach, provide, in the following sections, closed-form expressions for the effective elastic moduli and constitutive equations.

3.3 The Euler-Bernoulli beam on Winkler foundation: equivalence between the biphasic continuum and the continuum-springs system

The proposed modelling technique takes advantage of the simplifications associated with the Winkler model, the most famous foundation model frequently used in many engineering areas. According to this idealisation, the springs are mutually independent and, if loaded, the provided resistance is directly proportional to the deflection of the

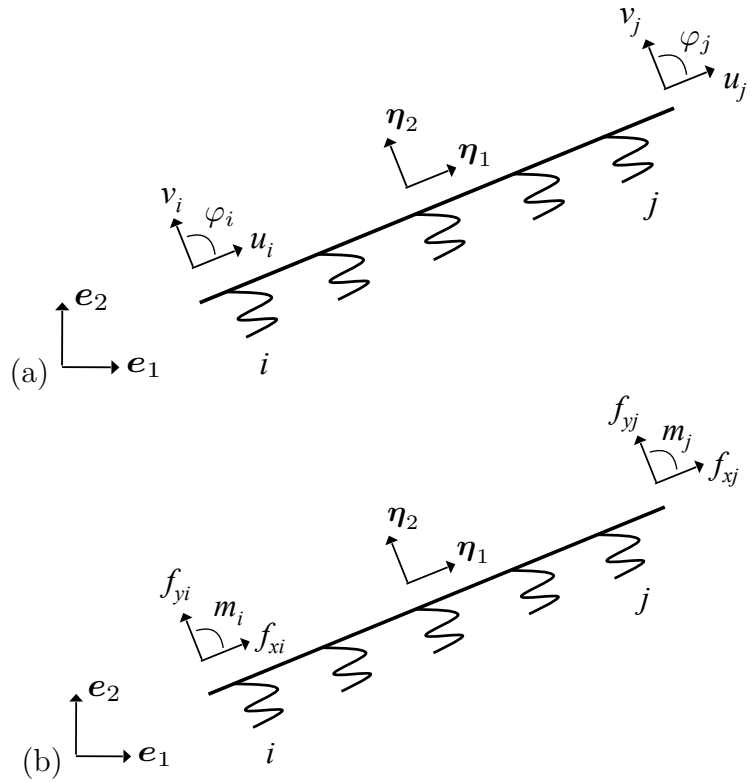

Figure 3.3: The beam on Winkler elastic foundation in the local reference system: (a) degrees of freedom, (b) forces and couples

beam via the Winkler constant K_w, representing the stiffness of the springs (Hetenyi, 1946).

The most important weakness of the Winkler model is to neglect the interactions between adjacent springs and to assume that the displacements appear only in the loaded area. Just outside of it, the deflections are zero. This leads to a discontinuity in the displacement field that, in reality, does not exist because of the continuity of the material supporting the beam (Dinev, 2012).

In the past, a number of attempts have been made to overcome this shortcoming (Avramidis & Morfidis, 2006; Vallabhan & Das, 1991; Kerr, 1964) but, in many cases, the suggested theory involves intricate mathematical techniques that are difficult to apply in practice. Consequently, aiming to obtain a more analytically tractable problem, in the present thesis the Winkler foundation is adopted to approximate the elastic material filling the cells. Since this assumption could affect the prediction ability of the resulting model, the following finite element simulations testify the validity of the proposed strategy.

3.3.1 Relation between the Winkler foundation constant and the filler's elastic moduli

As Figure 3.4 shows, the simulations consider a single composite cell and, in particular, two different configurations are examined.

In the first one (Figure 3.4a) the filling material is seen as a classical isotropic continuum having Young's modulus E_f, Poisson's ratio ν_f and shear modulus G_f, while in the second (Figure 3.4b) as a Winkler foundation. Regarding the latter, for ease of reading, in Figure 3.4b the three series of closely spaced springs in the $\mathbf{n}_1, \mathbf{n}_2, \mathbf{n}_3$ directions are schematically represented by a single spring in the corresponding direction. Specifically, with reference to Figure 3.4,

$$\mathbf{n}_1 = \begin{bmatrix} -\frac{1}{2} & -\frac{\sqrt{3}}{2} \end{bmatrix}^T, \quad \mathbf{n}_2 = \begin{bmatrix} 1 & 0 \end{bmatrix}^T, \quad \mathbf{n}_3 = \begin{bmatrix} \frac{1}{2} & -\frac{\sqrt{3}}{2} \end{bmatrix}^T. \tag{3.5}$$

Focusing on the elastic energy of the cell,

$$W_c = W_w + W_f, \tag{3.6}$$

obtained by summing the contribution of the walls, W_w, and of the filling material, W_f, provides a suitable relation between E_f, ν_f, G_f and the Winkler constant K_w.

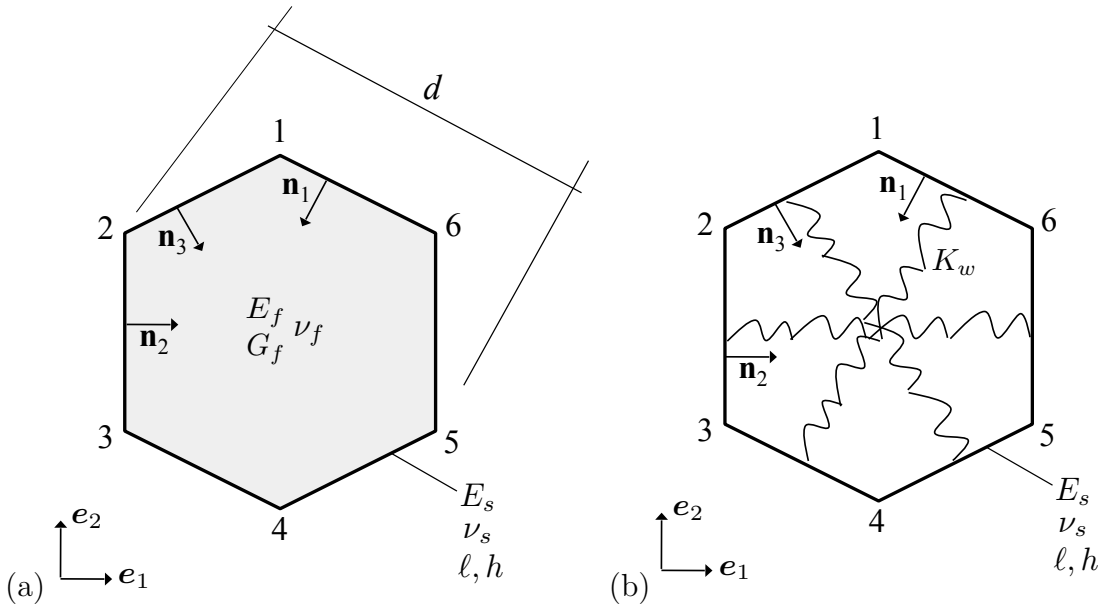

Figure 3.4: Equivalence between the biphasic continuum and the continuum-springs system: (a) filling material as a classical continuum, (b) filling material as a Winkler foundation

Specifically,

$$W_c := \begin{cases} W_{c,\,Winkler} = W_{w,\,beams} + W_{f,\,Winkler} & \text{Winkler model} \\ W_{c,\,continuum} = W_{w,\,walls} + W_{f,\,continuum} & \text{biphasic continuum,} \end{cases} \tag{3.7}$$

with $W_{w,\,beams}, W_{f,\,Winkler}$ and $W_{w,\,walls}, W_{continuum}$, in turn, the elastic energies of the cell walls and of the filling material in the cases of Winkler foundation model and biphasic continuum.

By assuming

$$W_{w,\,beams} \equiv W_{w,\,walls}, \tag{3.8}$$

the energetic equivalence

$$W_{c,\,Winkler} \equiv W_{c,\,continuum} \tag{3.9}$$

takes the form

$$W_{f,\,Winkler} \equiv W_{f,\,continuum}. \tag{3.10}$$

The first term, $W_{f,\,Winkler}$, is the sum of the elastic energies of the three series of springs:

$$W_{f,\,Winkler} = \left(\sum_{i=1}^{3} \frac{1}{2} \Delta U_i \left(\mathbf{n}_i^T \mathbf{K}_w \mathbf{n}_i \right) \Delta U_i \right) b, \tag{3.11}$$

being ΔU_i the elongation of the springs in the $\mathbf{n}_i$ direction, b the width,

$$\mathbf{K}_w := \begin{bmatrix} K_w & 0 \\ 0 & K_w \end{bmatrix} \tag{3.12}$$

the stiffness matrix of the elastic foundation, K_w the Winkler constant.

When the filling material is seen as a continuum,

$$W_{f,\,continuum} := \frac{1}{2}\int_V \boldsymbol{\sigma}_f^T\,\boldsymbol{\epsilon}_f\;dV = \left(\frac{1}{2}\int_A \boldsymbol{\epsilon}_f^T\,\mathbf{C}_f\,\boldsymbol{\epsilon}_f\,dA\right)\,b, \tag{3.13}$$

with $A = 3\sqrt{3}\ell^2/2$ the area of the cell, ℓ the length of the walls,

$$\boldsymbol{\epsilon}_f := \begin{bmatrix} \varepsilon_{11} \\ \varepsilon_{22} \\ 2\varepsilon_{12} \end{bmatrix} \leftarrow \begin{bmatrix} \varepsilon_{11} & \varepsilon_{12} \\ \varepsilon_{12} & \varepsilon_{22} \end{bmatrix} =: \mathbf{E}_f \tag{3.14}$$

and

$$\boldsymbol{\sigma}_f := \begin{bmatrix} \sigma_{11} \\ \sigma_{22} \\ \sigma_{12} \end{bmatrix} \leftarrow \begin{bmatrix} \sigma_{11} & \sigma_{12} \\ \sigma_{12} & \sigma_{22} \end{bmatrix} =: \mathbf{T}_f, \tag{3.15}$$

respectively, the infinitesimal strain tensor, $\mathbf{E}_f$, and stress tensor, $\mathbf{T}_f$, expressed in Voigt notation, $\mathbf{C}_f$ the stiffness tensor of the material within the cell, satisfying the generalised Hooke's law

$$\boldsymbol{\sigma}_f = \mathbf{C}_f\,\boldsymbol{\epsilon}_f. \tag{3.16}$$

In particular, for two-dimensional isotropic materials in plane stress tensional state, $\mathbf{C}_f$ is defined by

$$\mathbf{C}_f := \frac{E_f}{1-\nu_f^2}\begin{bmatrix} 1 & \nu_f & 0 \\ \nu_f & 1 & 0 \\ 0 & 0 & (1-\nu_f)/2 \end{bmatrix}. \tag{3.17}$$

In addition, from classical continuum mechanics, the strains ε_{ij} are expressed by

$$\mathbf{n}_i^T\mathbf{E}_f\mathbf{n}_i = \frac{\Delta\, d_i}{d}, \qquad i = 1,2,3, \tag{3.18}$$

where $\Delta\, d_i$ is the elongation in the $\mathbf{n}_i$ direction and $d = \sqrt{3}\ell$ (Figure 3.4a).

The hypothesis

$$\Delta U_i \equiv \Delta\, d_i, \qquad i = 1,2,3 \tag{3.19}$$

provides

$$\mathbf{n}_i^T \mathbf{E}_f \mathbf{n}_i = \frac{\Delta U_i}{d}, \qquad i = 1, 2, 3, \tag{3.20}$$

leading to

$$\Delta U_i = \left(\mathbf{n}_i^T \mathbf{E}_f \mathbf{n}_i\right) d, \qquad i = 1, 2, 3. \tag{3.21}$$

Finally, substituting Equation (3.21) into Equation (3.11) gives, in view of the equivalence in Equation (3.10),

$$\sum_{i=1}^{3} \frac{1}{2} d \left(\mathbf{n}_i^T \mathbf{E}_f \mathbf{n}_i\right) \mathbf{n}_i^T \mathbf{K}_w \mathbf{n}_i \left(\mathbf{n}_i^T \mathbf{E}_f \mathbf{n}_i\right) d = \frac{1}{2} \left(\boldsymbol{\epsilon}_f^T \mathbf{C}_f \boldsymbol{\epsilon}_f\right) A. \tag{3.22}$$

Considering, in turn, the deformation states defined by

$$\boldsymbol{\epsilon}_f^{(1)} := \begin{bmatrix} 1 \\ 0 \\ 0 \end{bmatrix}, \qquad \boldsymbol{\epsilon}_f^{(2)} := \begin{bmatrix} 0 \\ 1 \\ 0 \end{bmatrix}, \qquad \boldsymbol{\epsilon}_f^{(3)} := \begin{bmatrix} 0 \\ 0 \\ 1 \end{bmatrix}, \tag{3.23}$$

yields

$$\begin{cases} \dfrac{3\sqrt{3}\, K_w}{8} = \dfrac{E_f(\nu_f - 1)}{2(2\nu_f - 1)(\nu_f + 1)} \\ \dfrac{\sqrt{3}\, K_w}{2} = \dfrac{E_f}{(\nu_f + 1)} \end{cases} \rightarrow \quad \nu_f = 0.25, \quad E_f = \frac{5\sqrt{3}\, K_w}{8} \tag{3.24}$$

and, by assuming the isotropy of the filling material,

$$G_f = \frac{E_f}{2(\nu_f + 1)} = \frac{\sqrt{3}\, K_w}{4} \tag{3.25}$$

gives the shear modulus.

It should be noted that the proposed method, resulting in a fixed value of the Poisson's ratio, is in accordance with the Spring Network Theory (Alzebdeh & Ostoja-Starzewski, 1999; Ostoja-Starzewski, 2002). This condition is not excessively limiting, since in the present thesis we are interested in discussing general concepts and highlighting qualitative effects, rather than focusing on specific materials.

3.3.2 Finite element implementation: results

Regarding the cell analysed in the numerical simulations, the walls, isotropic linear elastic by assumption, have Young's modulus $E_s = 79$ GPa, Poisson's ratio $\nu_s = 0.35$, thickness $h = 1$ mm, length $\ell = 10$ mm and unitary width. By adopting the same notation of Gibson & Ashby (2001), it should be noted that, here and in the following, the subscript "s" indicates a property of the solid cell walls material.

The load conditions considered, illustrated in Figure 3.5, are uniaxial compression in the $\boldsymbol{e}_1$ and $\boldsymbol{e}_2$ direction, Figure 3.5a the first and Figure 3.5b the second, and shear, Figure 3.5c, simulated by applying forces of the same intensity at the boundary nodes of the cell. Specifically, compression forces of 10^{-3} N and shear forces of 10^{-5} N.

Constrained nodes are also introduced to avoid rigid body motions that could lead to an erroneous comparison between the deformed configurations of the two examined models.

The results of the analysis, summarised in Figure 3.6, reveal that the predictions of the Winkler model compare reasonably well with those obtained in the case of filling material as a classical continuum. As it can be seen, the difference between the two estimates of the horizontal and vertical displacements of the nodes, ΔU_X and ΔU_Y respectively, is generally $1 - 3\,\%$.

However, higher values of ΔU_X emerge at node 1 in the case of horizontal compression (Figure 3.6a). This is due to the limitations of the Winkler model, where the elastic springs only connect two opposite beams: 1-2 and 4-5, 6-1 and 3-4 (Figure 3.4b). The beams 1-2 and 3-4, 6-1 and 4-5 that, in reality, are coupled by the presence of the filling material, in the Winkler model are not connected.

Similarly, in the case of vertical compression, the high values of ΔU_X and ΔU_Y at nodes 1 and 4 are related to the limitations induced by the Winkler model (Figure 3.6b). Analogous considerations also apply with reference to Figure 3.6c. That is to say, the missing connection between the beams 1-6 and 4-5 provides high values of ΔU_X at nodes 5 and 6.

In spite of this, it can be said that Figure 3.6 reveals the validity of the Winkler model in approximating the mechanical deformations of the composite cell and that the simplifications introduced slightly affect the prediction ability of the proposed technique.

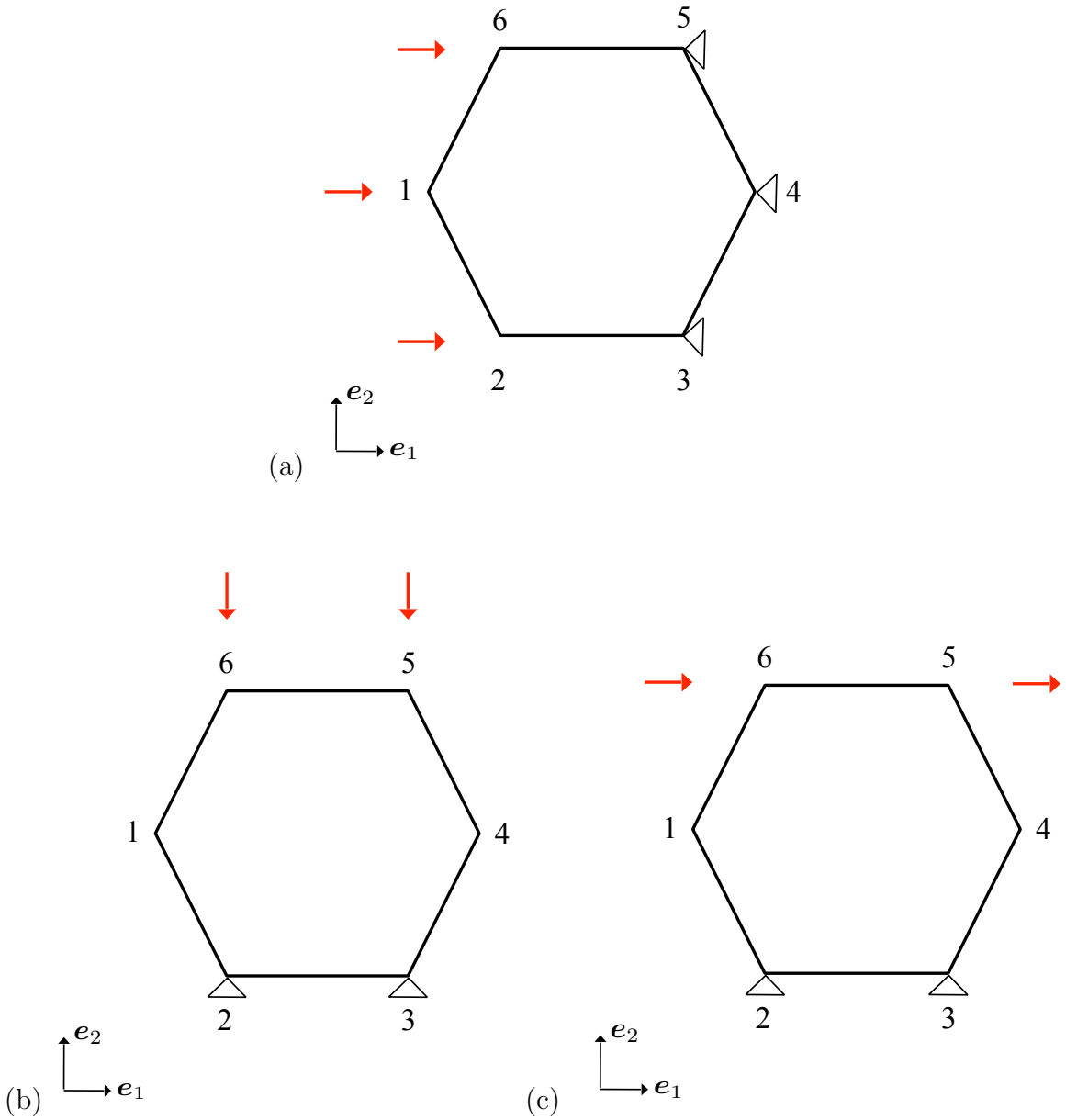

Figure 3.5: Finite element implementation of the composite cell, the load conditions: (a) uniaxial compression in the $\mathbf{e}_1$ direction, (b) uniaxial compression in the $\mathbf{e}_2$ direction, (c) shear forces

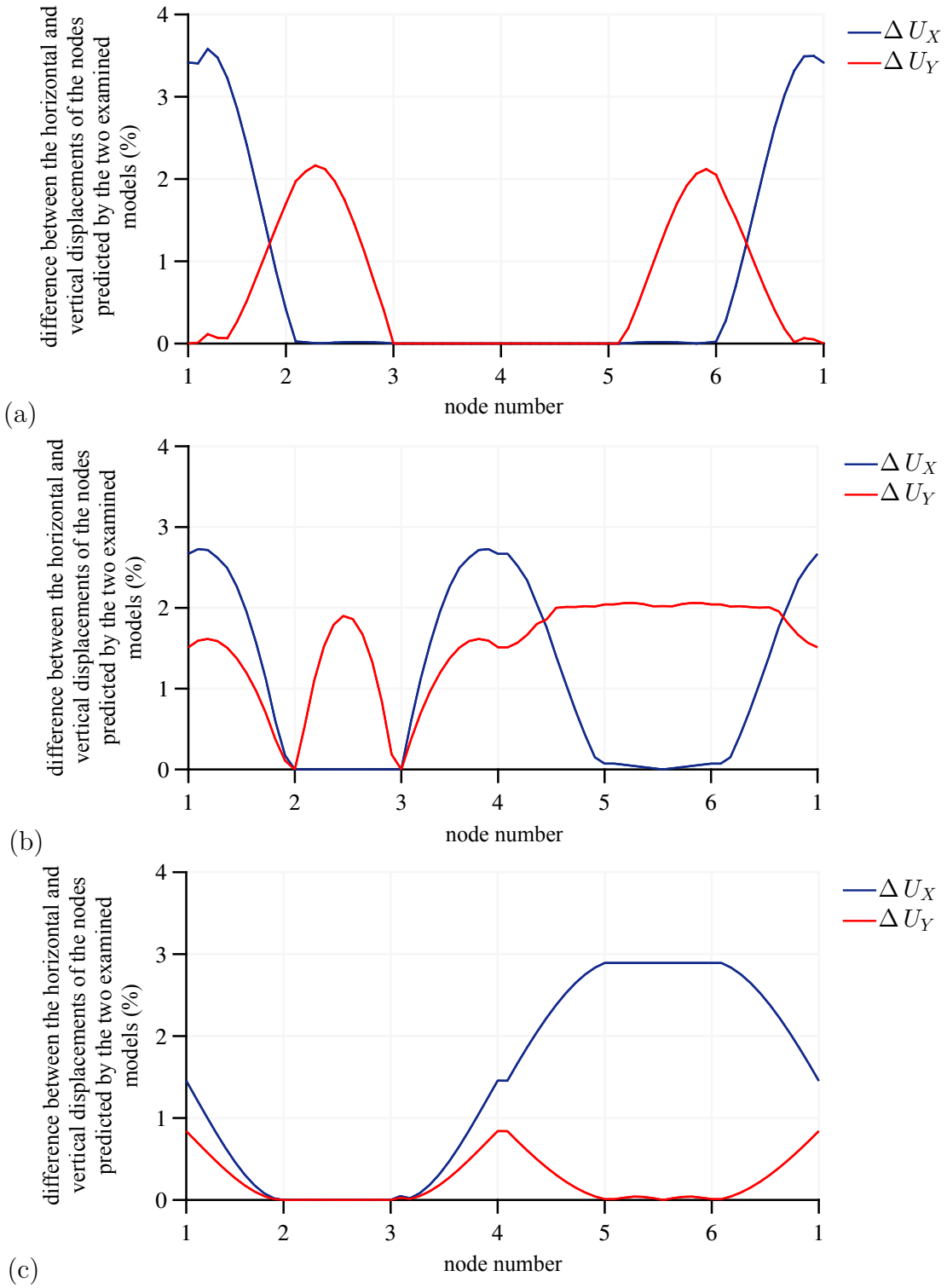

Figure 3.6: Filling material as a Winkler foundation vs filling material as a classical continuum, comparison between the nodal displacements in the case of (a) uniaxial compression in the $\boldsymbol{e}_1$ direction, (b) uniaxial compression in the $\boldsymbol{e}_2$ direction, (c) shear forces

3.4 The discrete system continuum-springs: theoretical description

3.4.1 The Euler-Bernoulli beam on Winkler foundation element

In the global reference system ($\boldsymbol{e}_1$, $\boldsymbol{e}_2$), the configuration of the e-th beam element is known by specifying the coordinates of its end nodes, I and J.

However, to analyse the generic component, it is more convenient using a local reference system, specific to the considered beam and closely dependent to its geometry (Figure 3.3). Such reference is defined by two orthonormal unit vectors, $\boldsymbol{\eta}_1^e$ and $\boldsymbol{\eta}_2^e$, and by the coordinate system (x, y). In the local notation, that will be adopted hereinafter, the extreme nodes of the beam are denoted by the indices i and j. According to the kinematics of the two-dimensional Euler-Bernoulli beam, each node has three degrees of freedom: two translations, u and v, and one rotation, φ (Figure 3.3).Thus, the following 6x1 vector completely describes the element nodal displacements

$$\mathbf{d}^e := \begin{bmatrix} \mathbf{d}_i \\ \mathbf{d}_j \end{bmatrix}^T = \begin{bmatrix} u_i & v_i & \varphi_i & u_j & v_j & \varphi_j \end{bmatrix}^T. \tag{3.26}$$

With reference to the beams 0-1, 0-2 and 0-3, the vector in Equation (3.26) takes the form

$$\mathbf{d}^1 = \begin{bmatrix} \mathbf{d}_0 \\ \mathbf{d}_1 \end{bmatrix} = \begin{bmatrix} u_0 & v_0 & \varphi_0 & u_1 & v_1 & \varphi_1 \end{bmatrix}^T, \tag{3.27}$$

$$\mathbf{d}^2 = \begin{bmatrix} \mathbf{d}_0 \\ \mathbf{d}_2 \end{bmatrix} = \begin{bmatrix} u_0 & v_0 & \varphi_0 & u_2 & v_2 & \varphi_2 \end{bmatrix}^T, \tag{3.28}$$

$$\mathbf{d}^3 = \begin{bmatrix} \mathbf{d}_0 \\ \mathbf{d}_3 \end{bmatrix} = \begin{bmatrix} u_0 & v_0 & \varphi_0 & u_3 & v_3 & \varphi_3 \end{bmatrix}^T. \tag{3.29}$$

The knowledge of the quantities in Equation (3.26) allows the approximation of the axial and transverse displacements at every point along the beam, denoted respectively by $u^e(\xi)$ and $v^e(\xi)$:

$$\mathbf{u}^e(\xi) := \begin{bmatrix} u^e(\xi) & v^e(\xi) \end{bmatrix}^T = \mathbf{N}^e(\xi)\mathbf{d}^e. \tag{3.30}$$

In Equation (3.30), $\xi := 2x/\ell - 1$ stands for the dimensionless coordinate varying from $\xi = -1$ at node i ($x = 0$) to $\xi = 1$ at node j ($x = \ell$), with ℓ the element's length. If

expressed as a function of ξ, the components of the shape function matrix

$$\mathbf{N}^e(\xi) := \begin{bmatrix} N_1 & 0 & 0 & N_2 & 0 & 0 \\ 0 & N_3 & N_4 & 0 & N_5 & N_6 \end{bmatrix} \tag{3.31}$$

are (Zienkiewicz, 1977)

$$\begin{gathered} N_1 = \frac{1-\xi}{2}, \qquad N_2 = \frac{1+\xi}{2}, \qquad N_3 = \frac{1-\xi(3-\xi^2)/2}{2}, \\ N_4 = \frac{\ell(1-\xi^2)(1-\xi)}{8}, \quad N_5 = \frac{1+\xi(3-\xi^2)/2}{2}, \quad N_6 = -\frac{\ell(1-\xi^2)(1+\xi)}{8}. \end{gathered} \tag{3.32}$$

In terms of energetics, the elastic strain energy of the Euler-Bernoulli beam on Winkler foundation element can be evaluated as the sum of three terms (Dinev, 2012):

$$w^e = w_b^e + \frac{1}{2}\, w_{wf}^{e,a} + \frac{1}{2}\, w_{wf}^{e,b}. \tag{3.33}$$

The first,

$$w_b^e := \frac{1}{2}\, (\mathbf{d}^e)^T \cdot \mathbf{k}_b^e \mathbf{d}^e, \tag{3.34}$$

is the classical elastic energy due to the axial and bending deformations of the beam, the second and the third,

$$w_{wf}^{e,a} := \frac{1}{2}\, (\mathbf{\Delta d}^{e,a})^T \cdot \mathbf{k}_{wf}^e \mathbf{\Delta d}^{e,a} \tag{3.35}$$

and

$$w_{wf}^{e,b} := \frac{1}{2}\, \left(\mathbf{\Delta d}^{e,b}\right)^T \cdot \mathbf{k}_{wf}^e \mathbf{\Delta d}^{e,b}, \tag{3.36}$$

are related to the elongation of the springs a,

$$\mathbf{\Delta d}^{e,a} := \begin{bmatrix} \mathbf{\Delta d}_i^a \\ \mathbf{\Delta d}_j^a \end{bmatrix} = \begin{bmatrix} \Delta\, u_i^a & \Delta\, v_i^a & \Delta\, \varphi_i^a & \Delta\, u_j^a & \Delta\, v_j^a & \Delta\, \varphi_j^a \end{bmatrix}^T, \tag{3.37}$$

and of the springs b,

$$\mathbf{\Delta d}^{e,b} := \begin{bmatrix} \mathbf{\Delta d}_i^b \\ \mathbf{\Delta d}_j^b \end{bmatrix} = \begin{bmatrix} \Delta\, u_i^b & \Delta\, v_i^b & \Delta\, \varphi_i^b & \Delta\, u_j^b & \Delta\, v_j^b & \Delta\, \varphi_j^b \end{bmatrix}^T. \tag{3.38}$$

As illustrated in Figures 3.7 and 3.8, the springs a and the springs b connect each beam with the opposite one in the $-\boldsymbol{\eta}_2^e$ and $+\boldsymbol{\eta}_2^e$ direction, in turn.

In particular, for the beams 0-1, 0-2 and 0-3, the quantities in Equations (3.37) and (3.38) are, respectively,

$$\boldsymbol{\Delta}\,\mathbf{d}^{1,a} = \begin{bmatrix} \boldsymbol{\Delta}\mathbf{d}_0^a \\ \boldsymbol{\Delta}\mathbf{d}_1^a \end{bmatrix} = \begin{bmatrix} \mathbf{u}_0 - \mathbf{u}_{10} \\ \varphi_0 - \varphi_{10} \\ \mathbf{u}_1 - \mathbf{u}_{11} \\ \varphi_1 - \varphi_{11} \end{bmatrix}, \quad \boldsymbol{\Delta}\,\mathbf{u}^{1,b} = \begin{bmatrix} \boldsymbol{\Delta}\mathbf{d}_0^b \\ \boldsymbol{\Delta}\mathbf{d}_1^b \end{bmatrix} = \begin{bmatrix} \mathbf{u}_0 - \mathbf{u}_6 \\ \varphi_0 - \varphi_6 \\ \mathbf{u}_1 - \mathbf{u}_5 \\ \varphi_1 - \varphi_5 \end{bmatrix}, \tag{3.39}$$

$$\boldsymbol{\Delta}\,\mathbf{u}^{2,a} = \begin{bmatrix} \boldsymbol{\Delta}\mathbf{d}_0^a \\ \boldsymbol{\Delta}\mathbf{d}_2^a \end{bmatrix} = \begin{bmatrix} \mathbf{u}_0 - \mathbf{u}_4 \\ \varphi_0 - \varphi_4 \\ \mathbf{u}_2 - \mathbf{u}_5 \\ \varphi_2 - \varphi_5 \end{bmatrix}, \quad \boldsymbol{\Delta}\,\mathbf{u}^{2,b} = \begin{bmatrix} \boldsymbol{\Delta}\mathbf{d}_0^b \\ \boldsymbol{\Delta}\mathbf{d}_2^b \end{bmatrix} = \begin{bmatrix} \mathbf{u}_0 - \mathbf{u}_9 \\ \varphi_0 - \varphi_9 \\ \mathbf{u}_2 - \mathbf{u}_8 \\ \varphi_2 - \varphi_8 \end{bmatrix}, \tag{3.40}$$

$$\boldsymbol{\Delta}\,\mathbf{u}^{3,a} = \begin{bmatrix} \boldsymbol{\Delta}\mathbf{d}_0^a \\ \boldsymbol{\Delta}\mathbf{d}_3^a \end{bmatrix} = \begin{bmatrix} \mathbf{u}_0 - \mathbf{u}_7 \\ \varphi_0 - \varphi_7 \\ \mathbf{u}_3 - \mathbf{u}_8 \\ \varphi_3 - \varphi_8 \end{bmatrix}, \quad \boldsymbol{\Delta}\,\mathbf{u}^{3,b} = \begin{bmatrix} \boldsymbol{\Delta}\mathbf{d}_0^b \\ \boldsymbol{\Delta}\mathbf{d}_3^b \end{bmatrix} = \begin{bmatrix} \mathbf{u}_0 - \mathbf{u}_{12} \\ \varphi_0 - \varphi_{12} \\ \mathbf{u}_3 - \mathbf{u}_{11} \\ \varphi_3 - \varphi_{11} \end{bmatrix}, \tag{3.41}$$

where, for brevity,

$$\mathbf{u}_i := \begin{bmatrix} u_i & v_i \end{bmatrix}^T. \tag{3.42}$$

Regarding the factor 1/2 in the second and third term of Equation (3.33), it is introduced to take into account that each spring is shared between two opposite beams and contributes only half of its strain energy to the unit cell.

Additionally, $\mathbf{k}_b^e$ and $\mathbf{k}_{wf}^e$ are, on order, the stiffness matrix of the classical Euler-Bernoulli beam and of the Winkler foundation (Janco, 2010), denoted by lowercase letters since they are expressed in the local reference. Their components, obtained by applying the minimum energy principle (Tsiatas, 2014), are given by

$$[\mathbf{k}_b^e]_{ij} := \begin{cases} \displaystyle\int_{-1}^{1} C_\ell N_i^{'}(\xi) N_j^{'}(\xi)\, d\xi, & i,j = 1,4, \\ \displaystyle\int_{-1}^{1} D_\ell N_i^{''}(\xi) N_j^{''}(\xi)\, d\xi, & i,j = 2,3,5,6, \\ 0, & \text{otherwise} \end{cases} \tag{3.43}$$

and

$$\left[\mathbf{k}_{wf}^{e}\right]_{ij} := \begin{cases} \displaystyle\int_{-1}^{1} K_w N_i(\xi) N_j(\xi)\, d\xi, & i,j = 2,3,5,6, \\ \\ 0, & \text{otherwise}, \end{cases} \tag{3.44}$$

with

$$C_\ell := \frac{E_s\, h}{1-\nu_s^2} \quad \text{and} \quad D_\ell := \frac{E_s\, h^3}{12(1-\nu_s^2)} \tag{3.45}$$

respectively, the tensile and bending stiffness (per unit width) of the beams, E_s, ν_s and h their Young's modulus, Poisson's ratio and thickness, K_w the Winkler foundation constant and

$$(\cdot)^{'} := \frac{\partial(\cdot)}{\partial\xi}, \qquad (\cdot)^{''} := \frac{\partial^2(\cdot)}{\partial\xi^2}. \tag{3.46}$$

Substituting the relations in Equation (3.32) into Equations (3.43) and (3.44) and integrating over the element, lead to

$$\mathbf{k}_b^e = \begin{bmatrix} C_\ell/\ell & 0 & 0 & -C_\ell/\ell & 0 & 0 \\ 0 & 12D_\ell/\ell^3 & 6D_\ell/\ell^2 & 0 & -12D_\ell/\ell^3 & 6D_\ell/\ell^2 \\ 0 & 6D_\ell/\ell^2 & 4D_\ell/\ell & 0 & -6D_\ell/\ell^2 & 2D_\ell/\ell \\ -C_\ell/\ell & 0 & 0 & C_\ell/\ell & 0 & 0 \\ 0 & -12D_\ell/\ell^3 & -6D_\ell/\ell^2 & 0 & 12D_\ell/\ell^3 & -6D_\ell/\ell^2 \\ 0 & 6D_\ell/\ell^2 & 2D_\ell/\ell & 0 & -6D_\ell/\ell^2 & 4D_\ell/\ell \end{bmatrix} \tag{3.47}$$

and

$$\mathbf{k}_{wf}^e = \begin{bmatrix} 0 & 0 & 0 & 0 & 0 & 0 \\ 0 & 13\,K_w/35 & 11\,K_w\ell/210 & 0 & 9\,K_w/70 & -13\,K_w\ell/420 \\ 0 & 11\,K_w\ell/210 & K_w\ell^2/105 & 0 & 13\,K_w\ell/420 & -K_w\ell^2/140 \\ 0 & 0 & 0 & 0 & 0 & 0 \\ 0 & 9\,K_w/70 & 13\,K_w\ell/420 & 0 & 13\,K_w/35 & -11\,K_w\ell/210 \\ 0 & -13\,K_w\ell/420 & -K_w\ell^2/140 & 0 & -11\,K_w\ell/210 & K_w\ell^2/105 \end{bmatrix}. \tag{3.48}$$

It should be noted that there are different approaches in evaluating the stiffness matrix of the beam element on elastic foundations (Tsiatas, 2014). The two main techniques are based on either the use of approximated shape functions (Janco, 2010; Kuo & Lee, 1994; Hosur & Bhavikatti, 1996; Chen, 1998) or the development of exact ones (Eisenberger & Yankelevsky, 1985; Sen *et al.*, 1990; Razaqpur & Shah, 1991). In the first case, both $\mathbf{k}_b^e$ and $\mathbf{k}_{wf}^e$ are evaluated by adopting the Hermitian cubic shape

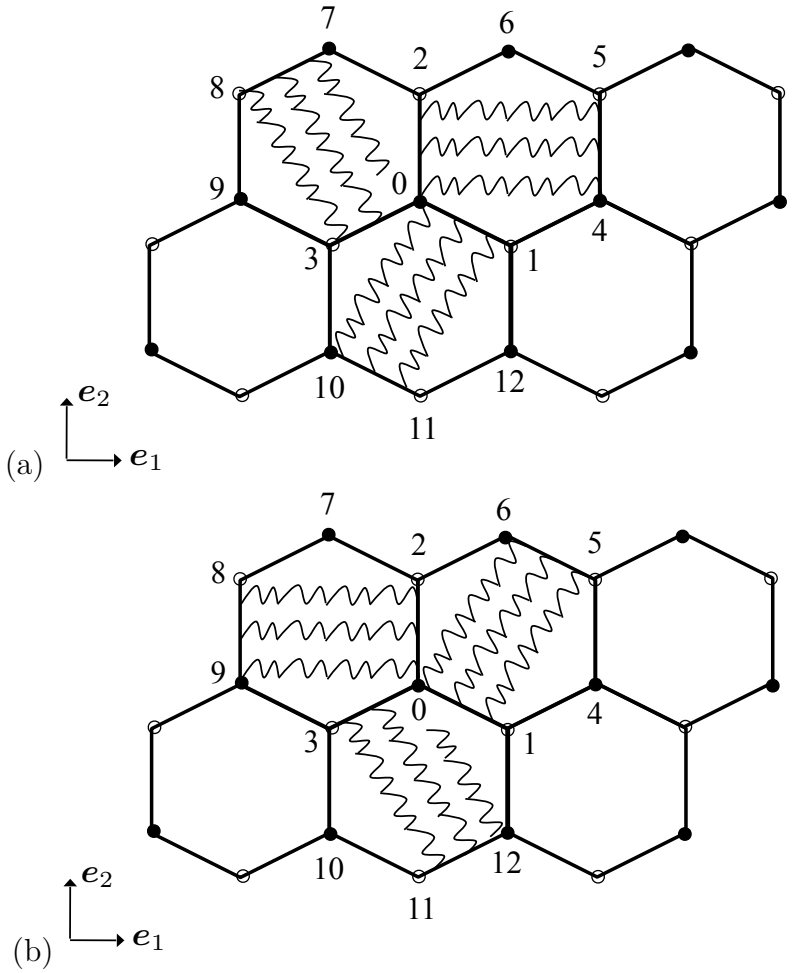

Figure 3.7: The two sets of elastic springs: (a) springs a, (b) springs b

functions typical of the Euler-Bernoulli beam, listed in the set of Equations (3.32). In the second, the shape functions are derived by solving the governing differential equation of the Euler-Bernoulli beam resting on Winkler foundation (Eisenberger & Yankelevsky, 1985). Despite the simplifications introduced, several existing studies, dealing with a broad range of engineering problems (Janco, 2010; Tsiatas, 2014; Karkon & Karkon, 2016), conclude that the results of the numerical implementations based on the approximated solution compare favourably to those obtained by the exact ones. Considering this and aiming to obtain a theoretical model that is able to address all the relevant issues, yet easy to recall in practice, in the present thesis the approximated approach is adopted (cf. Equation (3.44)).

Finally, similarly to Equation (3.33), the forces and couples acting at the extreme nodes of the beam,

$$\mathbf{f}^e := \begin{bmatrix} \mathbf{f}_i \\ \mathbf{f}_j \end{bmatrix} = \begin{bmatrix} f_{xi} & f_{yi} & m_i & f_{xj} & f_{yj} & m_j \end{bmatrix}^T, \tag{3.49}$$

are obtained by adding the contribution of the Winkler foundation,

$$\mathbf{f}_{wf}^{e,a} := \mathbf{k}_{wf}^e \, \boldsymbol{\Delta}\mathbf{d}^{e,a} \tag{3.50}$$

and

$$\mathbf{f}_{wf}^{e,b} := \mathbf{k}_{wf}^e \, \boldsymbol{\Delta}\mathbf{d}^{e,b}, \tag{3.51}$$

to that of the classical Euler-Bernoulli beam,

$$\mathbf{f}_b^e := \mathbf{k}_b^e \, \mathbf{d}^e : \tag{3.52}$$

$$\mathbf{f}^e = \mathbf{f}_b^e + \frac{1}{2}\,\mathbf{f}_{wf}^{e,a} + \frac{1}{2}\,\mathbf{f}_{wf}^{e,b}. \tag{3.53}$$

Again, as the springs are shared between opposite beams, the factor 1/2 is introduced in the last two terms of Equation (3.53).

3.4.2 Elastic energy of the discrete problem

For any given deformation, the elastic energy representative of the whole discrete structure, W, can be evaluated from that of the three beams composing the unit cell of the periodic array (Figure 3.2b), 0-1, 0-2 and 0-3.

As it can be seen in Figure 3.2b, the first node of each beam coincides with the central point 0. Accordingly, if $\mathbf{d}_0$ and $\boldsymbol{\Delta}\mathbf{d}_0^a$, $\boldsymbol{\Delta}\mathbf{d}_0^b$ denote, respectively, the displacements of

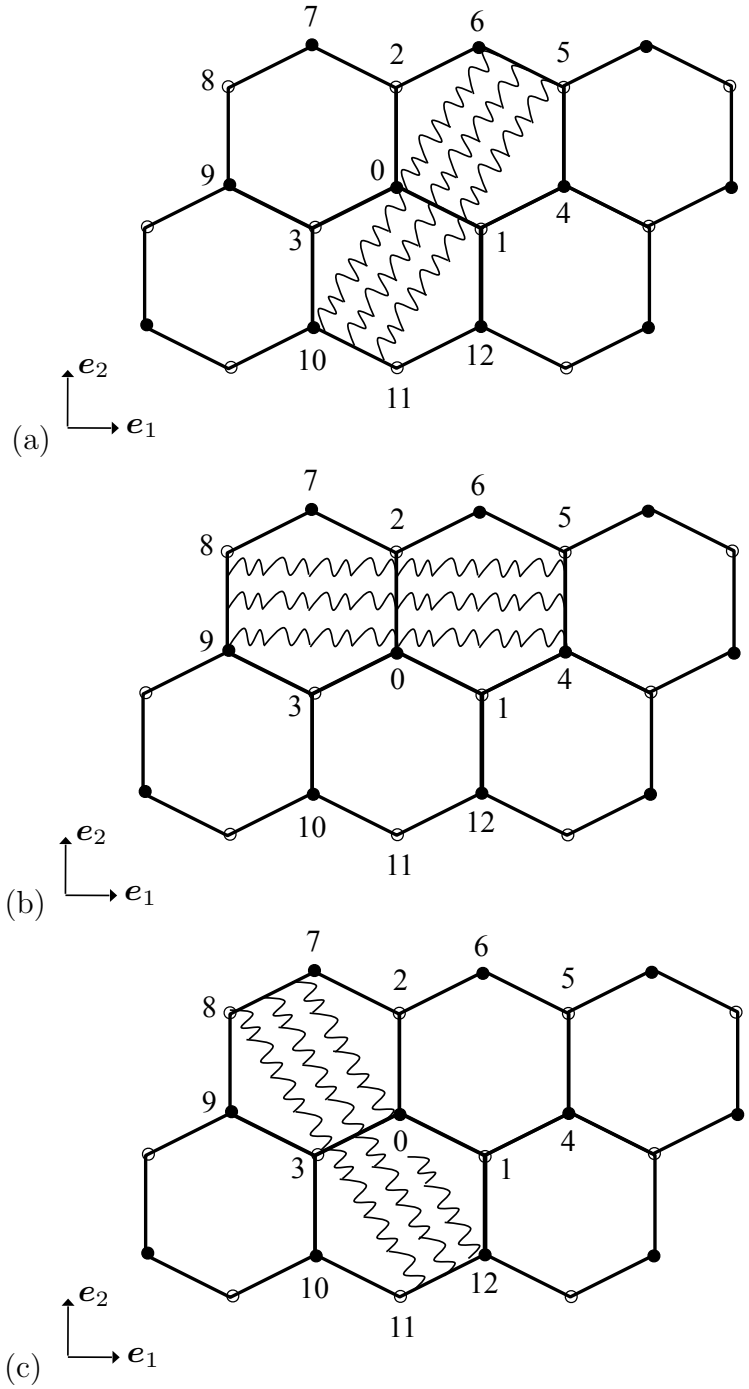

Figure 3.8: The triplet of elastic beams with focus on springs: (a) beam 0-1, (b) beam 0-2, (c) beam 0-3

the beam and the elongation of the springs a and of the springs b at joint 0, Equation (3.53) takes the form

$$\mathbf{f}^e = \begin{bmatrix} \mathbf{f}_0 \\ \mathbf{f}_j \end{bmatrix} = \begin{bmatrix} \mathbf{k}_{b,01}\,\mathbf{d}_j + \mathbf{k}_{b,00}\,\mathbf{d}_0 \\ \mathbf{k}_{b,11}\,\mathbf{d}_j + \mathbf{k}_{b,10}\,\mathbf{d}_0 \end{bmatrix} + \frac{1}{2}\begin{bmatrix} \mathbf{k}_{wf,01}\,\boldsymbol{\Delta}\mathbf{d}_j^a + \mathbf{k}_{wf,00}\,\boldsymbol{\Delta}\mathbf{d}_0^a \\ \mathbf{k}_{wf,11}\,\boldsymbol{\Delta}\mathbf{d}_j^a + \mathbf{k}_{wf,10}\,\boldsymbol{\Delta}\mathbf{d}_0^a \end{bmatrix} + \frac{1}{2}\begin{bmatrix} \mathbf{k}_{wf,01}\,\boldsymbol{\Delta}\mathbf{d}_j^b + \mathbf{k}_{wf,00}\,\boldsymbol{\Delta}\mathbf{d}_0^b \\ \mathbf{k}_{wf,11}\,\boldsymbol{\Delta}\mathbf{d}_j^b + \mathbf{k}_{wf,10}\,\boldsymbol{\Delta}\mathbf{d}_0^b \end{bmatrix}, \quad (3.54)$$

where $\mathbf{f}_0$ and $\mathbf{f}_j$ are, in turn, the forces and couples at the nodes 0 and $j = 1, 2, 3$,

$$\mathbf{k}_{b,11} := \begin{bmatrix} \frac{C_\ell}{\ell} & 0 & 0 \\ 0 & \frac{12D_\ell}{\ell^3} & -\frac{6D_\ell}{\ell^2} \\ 0 & -\frac{6D_\ell}{\ell^2} & \frac{4D_\ell}{\ell} \end{bmatrix}, \quad \mathbf{k}_{wf,11} := \begin{bmatrix} 0 & 0 & 0 \\ 0 & \frac{13K_w}{35} & -\frac{11K_w\ell}{210} \\ 0 & -\frac{11K_w\ell}{210} & \frac{K_w\ell^2}{105} \end{bmatrix},$$

$$\mathbf{k}_{b,10} := \begin{bmatrix} -\frac{C_\ell}{\ell} & 0 & 0 \\ 0 & -\frac{12D_\ell}{\ell^3} & -\frac{6D_\ell}{\ell^2} \\ 0 & \frac{6D_\ell}{\ell^2} & \frac{2D_\ell}{\ell} \end{bmatrix}, \quad \mathbf{k}_{wf,10} := \begin{bmatrix} 0 & 0 & 0 \\ 0 & \frac{9K_w}{70} & \frac{13K_w\ell}{420} \\ 0 & -\frac{13K_w\ell}{420} & -\frac{K_w\ell^2}{140} \end{bmatrix},$$

$$\mathbf{k}_{b,01} := \begin{bmatrix} -\frac{C_\ell}{\ell} & 0 & 0 \\ 0 & -\frac{12D_\ell}{\ell^3} & \frac{6D_\ell}{\ell^2} \\ 0 & -\frac{6D_\ell}{\ell^2} & \frac{2D_\ell}{\ell} \end{bmatrix}, \quad \mathbf{k}_{wf,01} := \begin{bmatrix} 0 & 0 & 0 \\ 0 & \frac{9K_w}{70} & -\frac{13K_w\ell}{420} \\ 0 & \frac{13K_w\ell}{420} & -\frac{K_w\ell^2}{140} \end{bmatrix},$$

$$\mathbf{k}_{b,00} := \begin{bmatrix} \frac{C_\ell}{\ell} & 0 & 0 \\ 0 & \frac{2D_\ell}{\ell^3} & \frac{6D_\ell}{\ell^2} \\ 0 & \frac{6D_\ell}{\ell^2} & \frac{4D_\ell}{\ell} \end{bmatrix}, \quad \mathbf{k}_{wf,00} := \begin{bmatrix} 0 & 0 & 0 \\ 0 & \frac{13K_w}{35} & \frac{11K_w\ell}{210} \\ 0 & \frac{11K_w\ell}{210} & \frac{K_w\ell^2}{105} \end{bmatrix} \quad (3.55)$$

the sub-matrices obtained by partitioning $\mathbf{k}_b^e$ and $\mathbf{k}_{wf}^e$.

Also, after writing Equation (3.54) in the global reference system (see Appendix C), imposing the equilibrium conditions at point 0 and condensing the corresponding degrees of freedom, lead to

$$W = W_b + \frac{1}{2}W^a_{wf} + \frac{1}{2}W^b_{wf} \equiv W\left(\tilde{\mathbf{D}}, \boldsymbol{\Delta}\tilde{\mathbf{D}}^a, \boldsymbol{\Delta}\tilde{\mathbf{D}}^b\right), \tag{3.56}$$

with

$$W_b := \frac{1}{2}\tilde{\mathbf{D}}^T \cdot \tilde{\mathbf{K}}_b\tilde{\mathbf{D}}, \tag{3.57}$$

$$W^a_{wf} := \frac{1}{2}\left(\boldsymbol{\Delta}\tilde{\mathbf{D}}^a\right)^T \cdot \tilde{\mathbf{K}}_{wf}\boldsymbol{\Delta}\tilde{\mathbf{D}}^a, \tag{3.58}$$

$$W^b_{wf} := \frac{1}{2}\left(\boldsymbol{\Delta}\tilde{\mathbf{D}}^b\right)^T \cdot \tilde{\mathbf{K}}_{wf}\boldsymbol{\Delta}\tilde{\mathbf{D}}^b, \tag{3.59}$$

$\tilde{\mathbf{K}}_b$ and $\tilde{\mathbf{K}}_{wf}$ the global stiffness matrices suitably re-arranged,

$$\tilde{\mathbf{D}} := \begin{bmatrix} \mathbf{D}_1 \\ \mathbf{D}_2 \\ \mathbf{D}_3 \end{bmatrix} = \begin{bmatrix} U_1 & V_1 & \varphi_1 & U_2 & V_2 & \varphi_2 & U_3 & V_3 & \varphi_3 \end{bmatrix}^T \tag{3.60}$$

and

$$\boldsymbol{\Delta}\tilde{\mathbf{D}}^a := \begin{bmatrix} \boldsymbol{\Delta}\mathbf{D}^a_1 \\ \boldsymbol{\Delta}\mathbf{D}^a_2 \\ \boldsymbol{\Delta}\mathbf{D}^a_3 \end{bmatrix} = \begin{bmatrix} \Delta U^a_1 & \Delta V^a_1 & \Delta\varphi^a_1 & \Delta U^a_2 & \Delta V^a_2 & \Delta\varphi^a_2 & \Delta U^a_3 & \Delta V^a_3 & \Delta\varphi^a_3 \end{bmatrix}^T, \tag{3.61}$$

$$\boldsymbol{\Delta}\tilde{\mathbf{D}}^b := \begin{bmatrix} \boldsymbol{\Delta}\mathbf{D}^b_1 \\ \boldsymbol{\Delta}\mathbf{D}^b_2 \\ \boldsymbol{\Delta}\mathbf{D}^b_3 \end{bmatrix} = \begin{bmatrix} \Delta U^b_1 & \Delta V^b_1 & \Delta\varphi^b_1 & \Delta U^b_2 & \Delta V^b_2 & \Delta\varphi^b_2 & \Delta U^b_3 & \Delta V^b_3 & \Delta\varphi^b_3 \end{bmatrix}^T, \tag{3.62}$$

the vectors of nodal displacements and elongation of the two sets of springs expressed in the global reference system.

In particular,

$$\boldsymbol{\Delta}\,\mathbf{D}^a_1 = \begin{bmatrix} \mathbf{D}_1 - \mathbf{D}_{11} \end{bmatrix} = \begin{bmatrix} \mathbf{U}_1 - \mathbf{U}_{11} \\ \varphi_1 - \varphi_{11} \end{bmatrix}, \tag{3.63}$$

$$\boldsymbol{\Delta}\,\mathbf{D}^a_2 = \begin{bmatrix} \mathbf{D}_2 - \mathbf{D}_5 \end{bmatrix} = \begin{bmatrix} \mathbf{U}_2 - \mathbf{U}_5 \\ \varphi_2 - \varphi_5 \end{bmatrix}, \tag{3.64}$$

$$\boldsymbol{\Delta}\,\mathbf{D}_3^a = \left[\ \mathbf{D}_3 - \mathbf{D}_8\ \right] = \begin{bmatrix} \mathbf{U}_3 - \mathbf{U}_8 \\ \varphi_3 - \varphi_8 \end{bmatrix} \tag{3.65}$$

and

$$\boldsymbol{\Delta}\,\mathbf{D}_1^b = \left[\ \mathbf{D}_1 - \mathbf{D}_5\ \right] = \begin{bmatrix} \mathbf{U}_1 - \mathbf{U}_5 \\ \varphi_1 - \varphi_5 \end{bmatrix}, \tag{3.66}$$

$$\boldsymbol{\Delta}\,\mathbf{D}_2^b = \left[\ \mathbf{D}_2 - \mathbf{D}_8\ \right] = \begin{bmatrix} \mathbf{U}_2 - \mathbf{U}_8 \\ \varphi_2 - \varphi_8 \end{bmatrix}, \tag{3.67}$$

$$\boldsymbol{\Delta}\,\mathbf{D}_3^b = \left[\ \mathbf{D}_3 - \mathbf{D}_{11}\ \right] = \begin{bmatrix} \mathbf{U}_3 - \mathbf{U}_{11} \\ \varphi_3 - \varphi_{11} \end{bmatrix}, \tag{3.68}$$

with

$$\mathbf{U}_i := \left[\ U_i \quad V_i\ \right]^T \tag{3.69}$$

for conciseness.

It is worth noting that, here and in the following, uppercase letters are used to differentiate the global variables from the local ones.

3.5 The continuum model

3.5.1 Elastic energy

One of the most powerful tools to predict the effective properties of microstructured composite materials is the homogenization method. Its main idea consists in finding a globally homogeneous continuum, equivalent to the original discrete structure, such that the energies stored in the two systems are assumed to be approximately the same.

In the examined case, it is possible to derive the continuum form of W by introducing the equivalent, continuous fields of displacement and microrotation

$$\hat{\mathbf{U}}(\cdot) := \begin{bmatrix} \hat{U}(\cdot) \\ \hat{V}(\cdot) \end{bmatrix} \qquad \text{and} \qquad \hat{\varphi}(\cdot), \tag{3.70}$$

and by assuming that in the limit $\ell \to 0$ the discrete variables U_j, V_j, φ_j in Equations (3.60) and (3.63)-(3.68) can be expressed by

$$\mathbf{U}_j := \begin{bmatrix} U_j \\ V_j \end{bmatrix} = \hat{\mathbf{U}}_0 + \nabla\hat{\mathbf{U}}\,\mathbf{b}_j, \qquad \varphi_j = \hat{\varphi}_0 + \nabla\hat{\varphi}\,\mathbf{b}_j, \qquad j = 1,2,3,5,8,11, \tag{3.71}$$

with $\hat{\mathbf{U}}_0$ and $\hat{\varphi}_0$ the values of $\hat{\mathbf{U}}(\cdot)$ and $\hat{\varphi}(\cdot)$ at the central node of the cell in the continuum description,

$$\nabla\hat{\mathbf{U}}(\cdot) := \begin{bmatrix} \dfrac{\partial\hat{U}(\cdot)}{\partial X} & \dfrac{\partial\hat{U}(\cdot)}{\partial Y} \\ \dfrac{\partial\hat{V}(\cdot)}{\partial X} & \dfrac{\partial\hat{V}(\cdot)}{\partial Y} \end{bmatrix} = \begin{bmatrix} \hat{U}_{1,1} & \hat{U}_{1,2} \\ \hat{U}_{2,1} & \hat{U}_{2,2} \end{bmatrix} \tag{3.72}$$

and

$$\nabla\hat{\varphi}(\cdot) := \begin{bmatrix} \dfrac{\partial\hat{\varphi}(\cdot)}{\partial X} \\ \dfrac{\partial\hat{\varphi}(\cdot)}{\partial Y} \end{bmatrix} = \begin{bmatrix} \hat{\varphi}_{,1} \\ \hat{\varphi}_{,2} \end{bmatrix} \tag{3.73}$$

the gradient of the displacement and rotation fields, $\mathbf{b}_j$ the vectors defined in Figure 3.9.

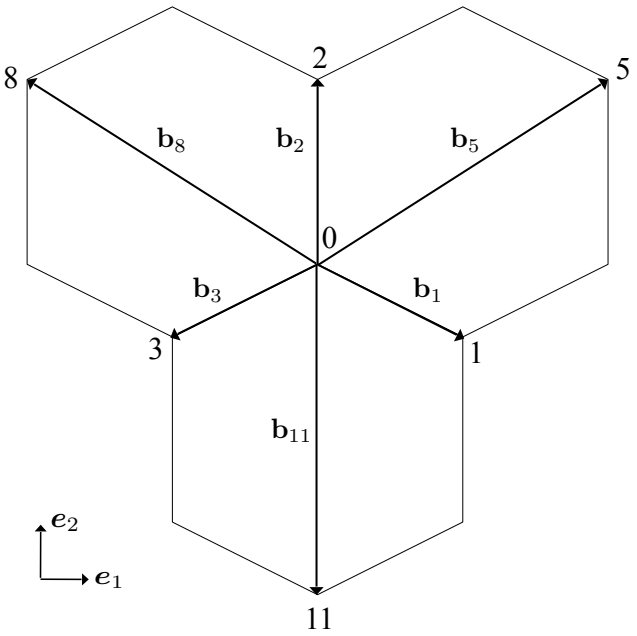

Figure 3.9: The composite cellular material: $\mathbf{b}_i$ *vectors*

Then, substituting the relations (3.71) into Equation (3.56) and dividing the expression that turns out from the calculation by the area of the unit cell, $A_0 = 3\sqrt{3}\ell^2/2$, give the strain energy density in the continuum approximation, w:

$$\frac{W(\mathbf{U},\varphi)}{A_0} \cong \frac{W(\hat{\mathbf{U}},\hat{\varphi})}{A_0} \equiv w. \tag{3.74}$$

It emerges that w is a quadratic form of the infinitesimal strains,

$$\varepsilon_{\alpha\beta} := \frac{1}{2}\left(\hat{U}_{\alpha,\beta} + \hat{U}_{\beta,\alpha}\right), \quad \alpha,\beta = 1,2, \tag{3.75}$$

and infinitesimal rotation,

$$\omega := \frac{1}{2}\left(\hat{U}_{1,2} - \hat{U}_{2,1}\right), \tag{3.76}$$

typical of classical continuum mechanics, and of the microrotation gradients, $\hat{\varphi}_{,\alpha}$:

$$\begin{aligned} w = {} & \frac{(\varepsilon_{11}^2+\varepsilon_{22}^2)\,(C_\ell^2\ell^4 + 36D_\ell C_\ell \ell^2) + 2\varepsilon_{11}\varepsilon_{22}(C_\ell^2\ell^4 - 12D_\ell C_\ell\ell^2) + 96D_\ell C_\ell \ell^2 \varepsilon_{12}^2}{4\sqrt{3}\ell^3(12D_\ell + C_\ell\ell^2)} \\ & + \frac{12D_\ell C_\ell \ell^3\,\varepsilon_{12}\hat{\varphi}_{,2} + 6D_\ell C_\ell\ell^3\,(\varepsilon_{22}-\varepsilon_{11})\,\hat{\varphi}_{,1} + 2D_\ell\ell^2(3D_\ell + C_\ell\ell^2)\left(\hat{\varphi}_{,1}^2 + \hat{\varphi}_{,2}^2\right)}{\sqrt{3}\ell^3(12D_\ell + C_\ell\ell^2)} \\ & + \frac{12D_\ell(3D_\ell + C_\ell\ell^2)\,(\omega-\hat{\varphi})^2}{\sqrt{3}\ell^3(12D_\ell + C_\ell\ell^2)} + \frac{K_w\,(271\,(\varepsilon_{11}^2+\varepsilon_{22}^2) + 408\varepsilon_{12}^2 + 134\varepsilon_{11}\varepsilon_{22})}{832\sqrt{3}} \\ & + \frac{K_w\ell\left(\ell(\hat{\varphi}_{,1}^2+\hat{\varphi}_{,2}^2) + 6\hat{\varphi}_{,1}(\varepsilon_{11}-\varepsilon_{22}) - 12\varepsilon_{12}\hat{\varphi}_{,2}\right)}{96\sqrt{3}}. \end{aligned} \tag{3.77}$$

It is not difficult to note the different physical dimensions of the coefficients in Equation (3.77): all of them are independent of ℓ, with the exception of the microrotation gradients that scale with first order in ℓ. Accordingly, in the limit $\ell \to 0$ the contribution of $\hat{\varphi}_{,\alpha}$ is missing and Equation (3.77) can be written as

$$w \equiv w\,(\varepsilon_{\alpha\beta}, (\omega - \hat{\varphi}), \hat{\varphi}_{,\alpha} = 0)\,, \tag{3.78}$$

leading to a resulting not-polar equivalent continuum.

3.5.2 Constitutive equations

As in classical mechanics, the constitutive equations of the homogenized continuum are given by

$$\sigma_{\gamma\delta} := \frac{\partial w}{\partial \hat{U}_{\gamma,\delta}}, \quad \gamma, \delta = 1, 2, \tag{3.79}$$

where w is the strain energy density defined in Equation (3.78) and $\sigma_{\gamma\delta}$ denote the components of the Cauchy-type stress tensor.

Also, from the chain rule,

$$\sigma_{\gamma\delta} = \frac{\partial w}{\partial \varepsilon_{\alpha\beta}} \frac{\partial \varepsilon_{\alpha\beta}}{\partial \hat{U}_{\gamma,\delta}} + \frac{\partial w}{\partial \omega} \frac{\partial \omega}{\partial \hat{U}_{\gamma,\delta}}, \quad \alpha, \beta, \gamma, \delta = 1, 2. \tag{3.80}$$

By observing that

$$\frac{\partial w}{\partial \varepsilon_{\alpha\beta}} \frac{\partial \varepsilon_{\alpha\beta}}{\partial \hat{U}_{\gamma,\delta}} = \frac{1}{2} \left(\frac{\partial w}{\partial \varepsilon_{\gamma\delta}} + \frac{\partial w}{\partial \varepsilon_{\delta\gamma}} \right) = \frac{\partial w}{\partial \varepsilon_{\gamma\delta}} \tag{3.81}$$

and

$$\frac{\partial w}{\partial \omega} \frac{\partial \omega}{\partial \hat{U}_{\gamma,\delta}} = \frac{1}{2} \frac{\partial w}{\partial \omega} \left(\delta_{1\gamma}\, \delta_{2\delta} - \delta_{2\gamma}\, \delta_{1\delta} \right) = \frac{1}{2} \frac{\partial w}{\partial \omega}\, e_{\gamma\delta}, \tag{3.82}$$

with $e_{\gamma\delta}$ the alternating symbol ($e_{11} = e_{22} = 0, e_{12} = -e_{21} = 1$) and δ_{ij} the Kronecker delta ($\delta_{ij} = 1$ if $i = j$, $\delta_{ij} = 0$ if $i \neq j$), it emerges that, in general, the stress tensor is not-symmetric:

$$\sigma_{\gamma\delta} = \frac{\partial w}{\partial \varepsilon_{\gamma\delta}} + \frac{1}{2} \frac{\partial w}{\partial \omega}\, e_{\gamma\delta}, \tag{3.83}$$

being

$$\sigma^{sym}_{\gamma\delta} := \frac{\partial w}{\partial \varepsilon_{\gamma\delta}} \tag{3.84}$$

and

$$\sigma^{skw}_{\gamma\delta} := \frac{1}{2} \frac{\partial w}{\partial \omega}\, e_{\gamma\delta}, \tag{3.85}$$

respectively, its symmetric and skew-symmetric parts.

The latter, in particular, depends on the difference $(\omega - \hat{\varphi})$, result that fits with the general format of the theory of continua with microstructure (Nemat-Nasser &

Hori, 1993):

$$\sigma_{11} = \frac{(C_\ell^2\ell^2 + 36D_\ell C_\ell)\varepsilon_{11} + (C_\ell^2\ell^2 - 12D_\ell C_\ell)\varepsilon_{22}}{2\sqrt{3}\,\ell(12D_\ell + C_\ell\ell^2)} + \frac{K_w(271\varepsilon_{11} + 67\varepsilon_{22})}{416\sqrt{3}},$$

$$\sigma_{22} = \frac{(C_\ell^2\ell^2 + 36D_\ell C_\ell)\varepsilon_{22} + (C_\ell^2\ell^2 - 12D_\ell C_\ell)\varepsilon_{11}}{2\sqrt{3}\,\ell(12D_\ell + C_\ell\ell^2)} + \frac{K_w(271\varepsilon_{22} + 67\varepsilon_{11})}{416\sqrt{3}},$$

$$\sigma_{12}^{sym} = \sigma_{21}^{sym} = \frac{24D_\ell C_\ell \varepsilon_{12}}{\sqrt{3}\,\ell(12D_\ell + C_\ell\ell^2)} + \frac{51K_w\,\varepsilon_{12}}{52\sqrt{3}}, \tag{3.86}$$

$$\sigma_{12}^{skw} = -\sigma_{21}^{skw} = \frac{\sqrt{3}\,D_\ell\,(\omega - \hat{\varphi})}{\ell^3},$$

$$\sigma_{12} = \sigma_{12}^{sym} + \sigma_{12}^{skw}, \quad \sigma_{21} = \sigma_{21}^{sym} + \sigma_{21}^{skw}.$$

3.5.3 Effective elastic constants

Let us consider the stress state $\sigma_{11} \neq 0$, $\sigma_{22} = \sigma_{12} = \sigma_{21} = 0$. By recalling the relations in Equation (3.86) and the Hooke's law $\sigma_{11} = E_1\,\varepsilon_{11}$, straightforward calculations give the effective Young's modulus in the $\boldsymbol{e}_1$ direction,

$$E_1 := \frac{\sigma_{11}}{\varepsilon_{11}} = \frac{(13\,K_w\,(1-\nu_s^2) + 16\lambda E_s)\,(51\,(1+\lambda^2)\,K_w\,(1-\nu_s^2) + 208\lambda^3 E_s)}{4\sqrt{3}\,(1-\nu_s^2)\,(271\,(1+\lambda^2)\,K_w\,(1-\nu_s^2) + 208\,(\lambda + 3\lambda^3)\,E_s)}, \tag{3.87}$$

and the related Poisson's ratio,

$$\nu_{12} := -\frac{\varepsilon_{22}}{\varepsilon_{11}} = \frac{67\,(1+\lambda^2)\,K_w\,(1-\nu_s^2) - 208\lambda\,(\lambda^2-1)\,E_s}{271\,(1+\lambda^2)\,K_w\,(1-\nu_s^2) + 208\lambda\,(1+3\lambda^2)\,E_s}, \tag{3.88}$$

where, for brevity, $\lambda := h/\ell$ stands for the ratio between the thickness and the length of the cell arms.

Similarly, the stress state in the $\boldsymbol{e}_2$ direction, $\sigma_{22} \neq 0$, $\sigma_{11} = \sigma_{12} = \sigma_{21} = 0$, yields

$$E_2 = E_1 \equiv E \qquad \text{and} \qquad \nu_{21} = \nu_{12} \equiv \nu. \tag{3.89}$$

Finally, the stress condition $\sigma_{12}^{sym} \neq 0$, $\sigma_{11} = \sigma_{22} = 0$ leads to the effective tangential elastic modulus

$$G := \frac{\sigma_{12}^{sym}}{2\varepsilon_{12}} = \frac{51\,(1+\lambda^2)\,K_w\,(1-\nu_s^2) + 208\lambda^3 E_s}{208\sqrt{3}\,(1+\lambda^2)\,(1-\nu_s^2)}. \tag{3.90}$$

In accordance with the conclusions of Gibson and Ashby (Gibson & Ashby, 2001), the derived elastic moduli of the limit continuum, E, ν and G, satisfy the classical relation

$$G = \frac{E}{2\,(1+\nu)}, \tag{3.91}$$

revealing the material isotropy.

It should be noted that the composite microstructure analysed in the present thesis is represented by a sequence of elastic beams of unitary width, $b = 1$. This assumption, in conjunction with the Winkler foundation to model the filler, leads to the above closed-form expressions for the effective elastic constants. Nevertheless, as a first approximation, the proposed results can be extrapolated to three-dimensional cellular materials with closed-cells by assuming a not unitary width of the beams. Accordingly, in the matrices $\mathbf{k}_b^e$ and $\mathbf{k}_{wf}^e$ defined in Section 3.4, the quantities

$$D_\ell := \frac{E_s\, h^3}{12(1-\nu_s^2)}, \qquad C_\ell := \frac{E_s\, h}{1-\nu_s^2}, \qquad K_w \tag{3.92}$$

are replaced by

$$D_\ell^* := D_\ell\, b, \qquad C_\ell^* := C_\ell\, b, \qquad K_w^* := K_w\, b, \tag{3.93}$$

with D_ℓ and C_ℓ, respectively, the bending and the axial stiffness of the beam, K_w the Winkler foundation constant, b the width.

Alternatively, to correctly capture the three-dimensional mechanical behavior and to obtain more accurate results, the beams should be replaced by plates. However, from a mathematical point of view, this leads to a less tractable problem and, probably, a closed-form expression for the effective elastic constants and constitutive equations could not be derived.

3.6 Validation of the theoretical results

As seen in the previous sections, the effective mechanical properties of composite cellular materials can be predicted by knowing the constitutive laws and spacial distribution of their components. In particular, it emerges that the macroscopic constants and stress-strain relations are strongly affected by the geometric and mechanical properties of the microstructure, such as the ratio $\lambda := h/\ell$ or the infill's stiffness, K_w. Before addressing a parametric analysis to investigate further this influence (Section 3.7),

the proposed analytical results are verified by comparison with the numerical ones, in Section 3.6.1, and with those of the other authors, in Section 3.6.2.

3.6.1 Comparison between the analytical and numerical homogenization

A different way to solve homogenization problems of heterogeneous materials, having a more or less periodic microstructure, is to use numerical techniques.

Numerical simulations, based on the finite element method (FEM), have been developed for periodic microstructures at the end of 1960 (Adams & Doner, 1967; Needleman & Void, 1972) and rapidly drawn considerable attention in the field of materials science. More recently, efforts have been made to consider more complex microstructures (Brockenborough *et al.*, 1991; Moulinec & Suquet, 1995; Moulinec & Suquet, 1997) and various mathematical techniques have been introduced. Authors, initially, focused on linear constituents (Sanchez-Palencia, 1974; Bensoussan *et al.*, 1978) but, since these pioneering studies, the method has been extended to plastic materials (Bouchitte & Suquet, 1991).

Referring the interested reader to Gusev (1997), Sab (1992) and Drugan & Willis (1996) for a more detailed discussion, in the following the main concepts to numerically evaluate the effective properties of microscopically heterogeneous media are outlined. Emphasis is on the FEM-based technique but the same ideas are also applicable to other types of discretization, as the finite difference method (FDM) or the finite volume method (FVM).

3.6.1.1 Numerical homogenization: overview

It is a well-understood fact that the overall response of heterogeneous materials is highly influenced by the material behavior and geometric arrangement of the distinct phases. Such research venture inevitably involves analyses on different length scales and makes a detailed description of the whole structure practically intractable, even on modern powerful computers.

Another complication comes from the fact that, generally, the microstructural configuration is not periodic and does not comply with the idealised geometries frequently encountered in the literature. Formally, this difficult can be resolved by assuming the periodicity of the microstructure that, for real materials, may appear to be rather artificial and inappropriate. However, the numerical studies in Terada & Kikuchi (2001) and Terada *et al.* (2000) reveal that the periodicity conditions are surprisingly well suited for the analysis of materials with disordered microstructure.

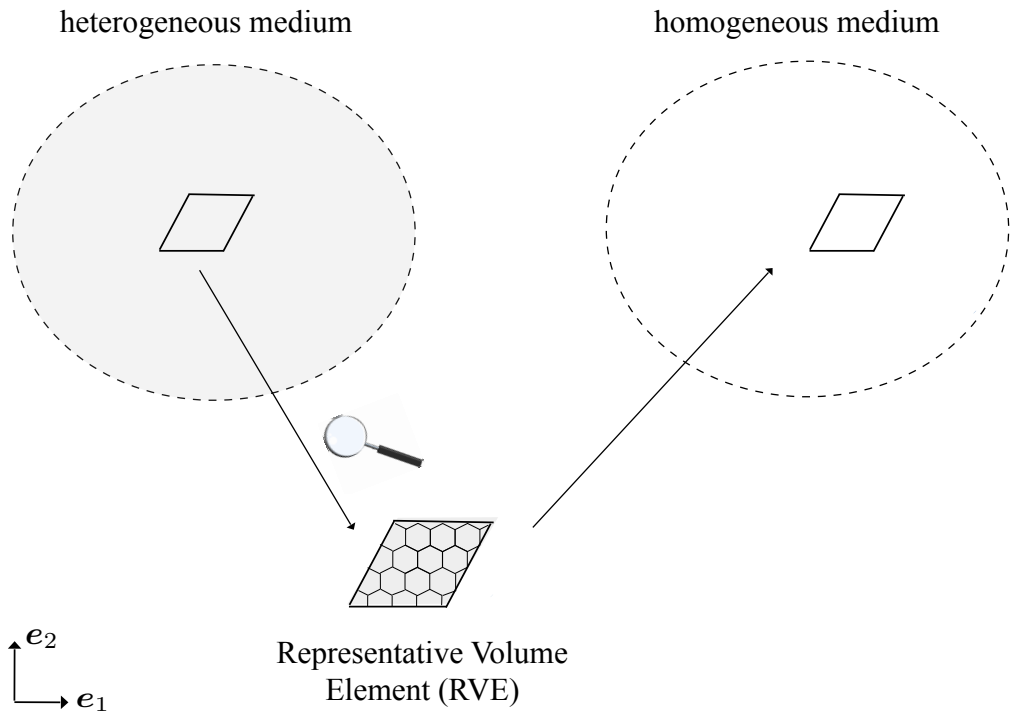

Figure 3.10: The equivalent homogenous material

In addition, due to the requirement of computational feasibility, numerical methods of homogenization usually consider a smaller sample of the heterogeneous material (Sun & Vaidya, 1996), the so-called *Representative Volume Element* (RVE), that is used to determine the corresponding effective properties of the homogenized macroscopic model. According to the commonly adopted homogenization approach (i.e., statistical homogenization), the RVE must contain a sufficient number of microheterogeneities, like grains, inclusions, voids or fibers (Kanit *et al.*, 2003), to statistically represent the whole composite and to provide the same macroscopic response as the real system.

Once a suitable RVE has been identified, appropriate boundary conditions are imposed to model different loading situations and to induce a microscopic stress, $\boldsymbol{\sigma}$, and a microscopic strain, $\boldsymbol{\epsilon}$. Through homogenization assumptions, the RVE is then regarded as a classical material element of an equivalent homogeneous medium whose effective properties are obtained by an average process (Sun & Vaidya, 1996) (Figure 3.10). That is to say, the macroscopic stress, $\overline{\boldsymbol{\sigma}}$, and the macroscopic strain, $\overline{\boldsymbol{\epsilon}}$, treated as the effective stress and the effective strain fields, are calculated by averaging their local counterparts over the considered heterogeneous domain of volume V:

$$\overline{\boldsymbol{\sigma}} :=< \boldsymbol{\sigma} >= \frac{1}{V}\int_V \boldsymbol{\sigma}\, dV, \qquad \overline{\boldsymbol{\epsilon}} :=< \boldsymbol{\epsilon} >= \frac{1}{V}\int_V \boldsymbol{\epsilon}\, dV. \tag{3.94}$$

Under the assumption of linearly elastic material behavior, the relation between $\overline{\boldsymbol{\sigma}}$ and $\overline{\boldsymbol{\epsilon}}$ is expressed by the classical Hooke's law,

$$\overline{\boldsymbol{\sigma}} = \mathbf{C}\,\overline{\boldsymbol{\epsilon}}, \tag{3.95}$$

or, by using the Voigt notation,

$$\begin{bmatrix} \overline{\sigma}_{11} \\ \overline{\sigma}_{22} \\ \overline{\sigma}_{12} \end{bmatrix} = \begin{bmatrix} C_{11} & C_{12} & C_{13} \\ C_{21} & C_{22} & C_{23} \\ C_{31} & C_{32} & C_{33} \end{bmatrix} \begin{bmatrix} \overline{\varepsilon}_{11} \\ \overline{\varepsilon}_{22} \\ 2\,\overline{\varepsilon}_{12} \end{bmatrix}, \tag{3.96}$$

with C_{ij} the components of the effective stiffness tensor, $\mathbf{C}$.

To highlight the effective engineering constants, Young's moduli, E_1 and E_2, Poisson's ratios, ν_{12} and ν_{21}, and shear modulus, G, the constitutive law in Equation (3.96) can be rewritten in terms of the homogenized compliance tensor, $\mathbf{S} = \mathbf{C}^{-1}$:

$$\begin{bmatrix} \overline{\varepsilon}_{11} \\ \overline{\varepsilon}_{22} \\ 2\,\overline{\varepsilon}_{12} \end{bmatrix} = \begin{bmatrix} S_{11} & S_{12} & S_{13} \\ S_{21} & S_{22} & S_{23} \\ S_{31} & S_{32} & S_{33} \end{bmatrix} \begin{bmatrix} \overline{\sigma}_{11} \\ \overline{\sigma}_{22} \\ \overline{\sigma}_{12} \end{bmatrix}, \tag{3.97}$$

being

$$\begin{aligned}
S_{11} &= \frac{C_{22}\,C_{33} - C_{23}\,C_{32}}{\det \mathbf{C}} \equiv \frac{1}{E_1}, & S_{12} &= -\frac{C_{13}\,C_{32} - C_{12}\,C_{33}}{\det \mathbf{C}} \equiv -\frac{\nu_{21}}{E_2}, \\
S_{22} &= \frac{C_{11}\,C_{33} - C_{13}\,C_{31}}{\det \mathbf{C}} \equiv \frac{1}{E_2}, & S_{21} &= -\frac{C_{23}\,C_{31} - C_{21}\,C_{33}}{\det \mathbf{C}} \equiv -\frac{\nu_{12}}{E_1}, \\
S_{33} &= \frac{C_{11}\,C_{22} - C_{12}\,C_{21}}{\det \mathbf{C}} \equiv \frac{1}{G}, & & \\
S_{13} &= \frac{C_{12}\,C_{23} - C_{13}\,C_{22}}{\det \mathbf{C}}, & S_{23} &= \frac{C_{13}\,C_{21} - C_{11}\,C_{23}}{\det \mathbf{C}}, \\
S_{31} &= \frac{C_{21}\,C_{32} - C_{22}\,C_{31}}{\det \mathbf{C}}, & S_{32} &= \frac{C_{12}\,C_{31} - C_{11}\,C_{32}}{\det \mathbf{C}}.
\end{aligned} \tag{3.98}$$

3.6.1.2 Boundary conditions

In the literature, three types of boundary conditions are usually prescribed on the RVE (Kanit *et al.*, 2003), kinematic uniform boundary conditions (KUBC), static uniform boundary conditions (SUBC), periodic boundary conditions (PERIODIC), so as to

produce a macroscopic strain, $\overline{\boldsymbol{\epsilon}}$, or a macroscopic stress, $\overline{\boldsymbol{\sigma}}$, within a homogeneous material having the same size of the RVE.

In particular, in the KUBC case, the boundary points of the RVE, $\boldsymbol{x} \in \partial V$, are subjected to a homogeneous displacement, $\boldsymbol{u}$, such that

$$\boldsymbol{u} := \overline{\boldsymbol{\epsilon}} \cdot \boldsymbol{x}, \quad \forall \boldsymbol{x} \in \partial V, \tag{3.99}$$

while, in the SUBC case, to a homogeneous traction, $\boldsymbol{t}$, given by

$$\boldsymbol{t} := \overline{\boldsymbol{\sigma}} \cdot \boldsymbol{n}, \quad \forall \boldsymbol{x} \in \partial V, \tag{3.100}$$

with $\boldsymbol{n}$ the unit normal to ∂V.

By taking into account that composite materials can be represented as a periodical array of RVEs, PERIODIC conditions enforce periodic displacements, $\boldsymbol{u}$, and anti-periodic tractions, $\boldsymbol{t}$, on the RVE's boundary (Figure 3.11):

$$\begin{cases} \boldsymbol{u} := \overline{\boldsymbol{\epsilon}} \cdot \boldsymbol{x} + \boldsymbol{u}^* \ : \boldsymbol{u}^+ = \boldsymbol{u}^-, & \forall \boldsymbol{x} \in \partial V, \\ \boldsymbol{t} := \overline{\boldsymbol{\sigma}} \cdot \boldsymbol{n} \ : \boldsymbol{t}^+ = -\boldsymbol{t}^-, & \forall \boldsymbol{x} \in \partial V, \end{cases} \tag{3.101}$$

where $\boldsymbol{u}^*$ is a periodic fluctuation, generally unknown, dependent on the applied global loads (Dinev, 2012; Pellegrino *et al.*, 1999). The conditions in Equation (3.101) imply that, in the composite, each RVE has the same deformation mode and that there is no separation or overlap between the neighbouring RVEs.

As pointed out in Michel *et al.* (1999), when both the loading and the RVE's geometry exhibit sufficient symmetry, Equations (3.101) can be reduced to the usual boundary conditions in Equations (3.99) or (3.100). However, in the case of multi-axial stress states, the abovementioned symmetry considerations can not be invoked and the periodicity conditions in Equation (3.101) can not be done away with.

In addition, KUBC, SUBC and PERIODIC, along with the stress and strain quantities defined in Equations (3.94), satisfy the Hill-Mandel theorem (Pellegrino *et al.*, 1999; Ptaszny & Fedelinski, 2011), ensuring the micro-macro equivalence

$$< \boldsymbol{\sigma} \cdot \boldsymbol{\epsilon} >= \overline{\boldsymbol{\sigma}} \cdot \overline{\boldsymbol{\epsilon}}, \tag{3.102}$$

with

$$< \boldsymbol{\sigma} \cdot \boldsymbol{\epsilon} >:= \frac{1}{V} \int_V \boldsymbol{\sigma} \cdot \boldsymbol{\epsilon} \, dV \tag{3.103}$$

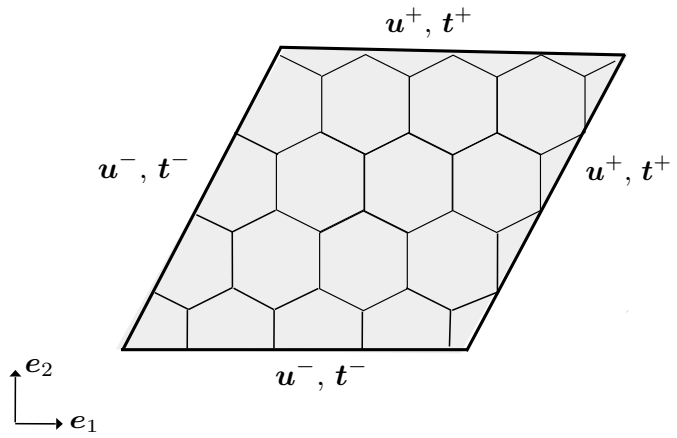

Figure 3.11: Periodic boundary conditions on the RVE

half of the averaged energy density of the heterogeneous RVE. Note that, if the boundary conditions are homogeneous as in Equations (3.99), (3.100) and (3.101), Equation (3.102) is valid for any material, homogeneous, heterogeneous or piecewise homogeneous. If the requirement of homogeneity is not fulfilled, the Hill-Mandel theorem does not apply, since the mean value of a product is generally not equal to the product of mean values.

3.6.1.3 Numerical implementation and results

Regarding the numerical simulations performed to validate the analytical predictions of Section 3.5.3, Figure 3.12 and Table 3.1 illustrate, respectively, the considered domain and the boundary conditions.

As in can be seen in Figure 3.12, the calculations involve a 75x50 mm rectangular domain discretized in an increasing number of hexagonal cells having gradually smaller length, ℓ. The cell walls, treated as Euler-Bernoulli beams on Winkler foundation elements, have Young's modulus $E_s = 79$ GPa, Poisson's ratio $\nu_s = 0.35$ and thickness $h = 0.1\ell$. Also, two values of the Winkler foundation constant are assumed: $K_w = 10^{-2}E_s$ and $K_w = 10^{-3}E_s$.

To obtain the effective elastic constants, three load conditions are considered: the first, uniaxial compression in the $\boldsymbol{e}_1$ direction (Figure 3.13a), and the second, uniaxial compression in the $\boldsymbol{e}_2$ direction (Figure 3.13b), to get the Young's moduli E_1, E_2 and Poisson's ratios ν_{12}, ν_{21}, the third, pure shear (Figure 3.13c), to gain the shear modulus G. The loading states are simulated by forces acting at the unconstrained boundary nodes of the domain, as summarised in Table 3.1.

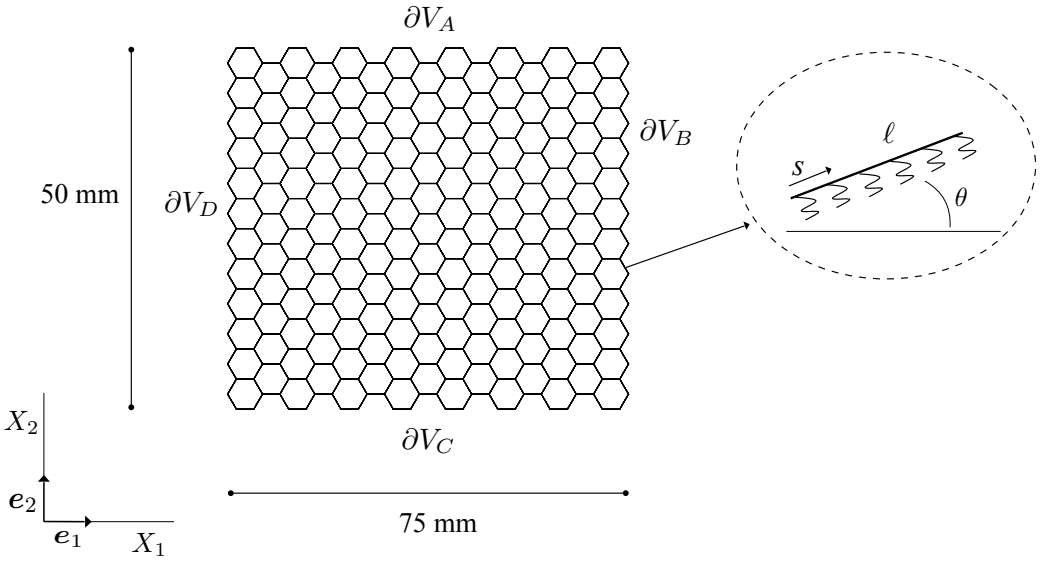

Figure 3.12: Analysed domain in the numerical simulations

Table 3.1 Boundary conditions used in the numerical simulations

Properties	Surface ∂V_A	Surface ∂V_B	Surface ∂V_C	Surface ∂V_D
S_{11}, S_{21}, S_{31} E_1, ν_{12}	Free	$-t_1 = -\overline{\sigma}_{11}$	Free	$t_1 = \overline{\sigma}_{11}$
S_{12}, S_{22}, S_{32} E_2, ν_{21}	$-t_2 = -\overline{\sigma}_{22}$	Free	$t_2 = \overline{\sigma}_{22}$	Free
S_{13}, S_{23}, S_{33} G	$t_{21} = \overline{\sigma}_{12}$	$t_{12} = \overline{\sigma}_{12}$	$-t_{21} = -\overline{\sigma}_{12}$	$-t_{12} = -\overline{\sigma}_{12}$

Operationally, the problem reduces to the solution of the boundary value problems corresponding to the three loading situations described and to the computation of the displacements at the extreme points of the beams. The displacements and derived quantities (i.e., stress, $\sigma_{ij}^{(\cdot)}$, and strain, $\varepsilon_{ij}^{(\cdot)}$) at every point along the beams are calculated by interpolation (cf. Section 3.4.1). Finally, the homogenized moduli are a consequence of Equations (3.94), (3.97) and (3.98).

When the forces act horizontally, Equation (3.97) leads to

$$\begin{bmatrix} \overline{\varepsilon}_{11}^{(1)} \\ \overline{\varepsilon}_{22}^{(1)} \\ 2\,\overline{\varepsilon}_{12}^{(1)} \end{bmatrix} = \begin{bmatrix} S_{11} & S_{12} & S_{13} \\ S_{21} & S_{22} & S_{23} \\ S_{31} & S_{32} & S_{33} \end{bmatrix} \begin{bmatrix} \overline{\sigma}_{11} \\ 0 \\ 0 \end{bmatrix} = \begin{bmatrix} S_{11}\,\overline{\sigma}_{11} \\ S_{21}\,\overline{\sigma}_{11} \\ S_{31}\,\overline{\sigma}_{11} \end{bmatrix}, \tag{3.104}$$

where $\overline{\sigma}_{11}$ is the applied stress (Table 3.1) and $\overline{\varepsilon}_{ij}^{(1)}$ the corresponding strain given by

$$\overline{\varepsilon}_{ij}^{(1)} := \frac{1}{V}\int_V \varepsilon_{ij}^{(1)}\,dV, \qquad i,j=1,2, \tag{3.105}$$

with V the volume of the examined domain. The latter, as shown in Figure 3.12, is composed by a number of beams, n_b, having the same length, ℓ, the same thickness, h, and width b. Accordingly,

$$\overline{\varepsilon}_{ij}^{(1)} = \frac{b\displaystyle\int_\Omega \varepsilon_{ij}^{(1)}\,d\Omega}{\displaystyle\sum_{m=1}^{n_b} b\,\ell_m\,h_m} = \frac{bh\displaystyle\sum_{m=1}^{n_b}\left(\int_s \varepsilon_{ij}^{(1)}(s)\,ds\right)_m}{n_b\,b\,\ell\,h} = \frac{\displaystyle\sum_{m=1}^{n_b}\left(\int_s \varepsilon_{ij}^{(1)}(s)\,ds\right)_m}{n_b\,\ell}, \qquad i,j=1,2, \tag{3.106}$$

where Ω is the area of the domain, $s=(\cos\vartheta_m,\sin\vartheta_m)$ a parametric coordinate such that $0\le s\le \ell$ (Figure 3.12), ℓ_m, h_m, ϑ_m, respectively, the length, the thickness and the inclination of the m-th beam.
Also, if

$$\varepsilon_{ij}(s) := \frac{1}{2}\left(\frac{\partial u_i^{(1)}(s)}{\partial X_j} + \frac{\partial u_j^{(1)}(s)}{\partial X_i}\right) \tag{3.107}$$

and

$$\frac{\partial u_i^{(1)}(s)}{\partial X_j} = \frac{\partial u_i^{(1)}(s)}{\partial s}\,\frac{\partial s}{\partial X_j}, \qquad \frac{\partial u_j^{(1)}(s)}{\partial X_i} = \frac{\partial u_j^{(1)}(s)}{\partial s}\,\frac{\partial s}{\partial X_i}, \qquad i,j=1,2 \tag{3.108}$$

are substituted into Equation (3.106), it follows

$$\overline{\varepsilon}_{ij}^{(1)} = \frac{\displaystyle\sum_{m=1}^{n_b} \frac{1}{2} \left(\left(u_i^{(1)}(\ell) - u_i^{(1)}(0) \right) \frac{\partial s}{\partial X_j} + \left(u_j^{(1)}(\ell) - u_j^{(1)}(0) \right) \frac{\partial s}{\partial X_i} \right)_m}{n_b \, \ell}, \tag{3.109}$$

with

$$\frac{\partial s}{\partial X_j} = \cos\vartheta_m \, \delta_{1j} + \sin\vartheta_m \, \delta_{2j}, \qquad \frac{\partial s}{\partial X_i} = \cos\vartheta_m \, \delta_{1i} + \sin\vartheta_m \, \delta_{2i}, \qquad i,j = 1,2, \tag{3.110}$$

δ_{ij} the Kroneker delta, $u_i^{(1)}(s)$ and $u_j^{(1)}(s)$ the displacements of the points along the beams due to the application of $\overline{\sigma}_{11}$. Finally, Equations (3.98) and (3.104) lead to

$$S_{11} = \frac{\overline{\varepsilon}_{11}^{(1)}}{\overline{\sigma}_{11}} \equiv \frac{1}{E_1}, \qquad S_{21} = \frac{\overline{\varepsilon}_{22}^{(1)}}{\overline{\sigma}_{11}} \equiv -\frac{\nu_{12}}{E_1}, \qquad S_{31} = \frac{2\,\overline{\varepsilon}_{12}^{(1)}}{\overline{\sigma}_{11}}. \tag{3.111}$$

With analogous calculations, forces acting vertically provide

$$\begin{bmatrix} \overline{\varepsilon}_{11}^{(2)} \\ \overline{\varepsilon}_{22}^{(2)} \\ 2\,\overline{\varepsilon}_{12}^{(2)} \end{bmatrix} = \begin{bmatrix} S_{11} & S_{12} & S_{13} \\ S_{21} & S_{22} & S_{23} \\ S_{31} & S_{32} & S_{33} \end{bmatrix} \begin{bmatrix} 0 \\ \overline{\sigma}_{22} \\ 0 \end{bmatrix} = \begin{bmatrix} S_{12}\,\overline{\sigma}_{22} \\ S_{22}\,\overline{\sigma}_{22} \\ S_{32}\,\overline{\sigma}_{22} \end{bmatrix} \tag{3.112}$$

and

$$S_{12} = \frac{\overline{\varepsilon}_{11}^{(2)}}{\overline{\sigma}_{22}} \equiv -\frac{\nu_{21}}{E_2}, \qquad S_{22} = \frac{\overline{\varepsilon}_{22}^{(2)}}{\overline{\sigma}_{22}} \equiv \frac{1}{E_2}, \qquad S_{32} = \frac{2\,\overline{\varepsilon}_{12}^{(2)}}{\overline{\sigma}_{22}} \tag{3.113}$$

while, in the case of pure shear,

$$\begin{bmatrix} \overline{\varepsilon}_{11}^{(3)} \\ \overline{\varepsilon}_{22}^{(3)} \\ 2\,\overline{\varepsilon}_{12}^{(3)} \end{bmatrix} = \begin{bmatrix} S_{11} & S_{12} & S_{13} \\ S_{21} & S_{22} & S_{23} \\ S_{31} & S_{32} & S_{33} \end{bmatrix} \begin{bmatrix} 0 \\ 0 \\ \overline{\sigma}_{12} \end{bmatrix} = \begin{bmatrix} S_{13}\,\overline{\sigma}_{12} \\ S_{23}\,\overline{\sigma}_{12} \\ S_{33}\,\overline{\sigma}_{12} \end{bmatrix} \tag{3.114}$$

and

$$S_{13} = \frac{\overline{\varepsilon}_{11}^{(3)}}{\overline{\sigma}_{12}}, \qquad S_{23} = \frac{\overline{\varepsilon}_{22}^{(3)}}{\overline{\sigma}_{12}}, \qquad S_{33} = \frac{2\,\overline{\varepsilon}_{12}^{(3)}}{\overline{\sigma}_{12}} \equiv \frac{1}{G}. \tag{3.115}$$

Again, $\overline{\sigma}_{22}$ and $\overline{\sigma}_{12}$ are the applied stress, $\overline{\varepsilon}_{ij}^{(2)}$ and $\overline{\varepsilon}_{ij}^{(3)}$ the corresponding strain calculated as in Equation (3.109).

The outcome of the analysis is presented in Tables 3.2-3.5.

Firstly, a convergence study is conducted to determine the number of elements required to produce converged material properties. This is achieved by starting with

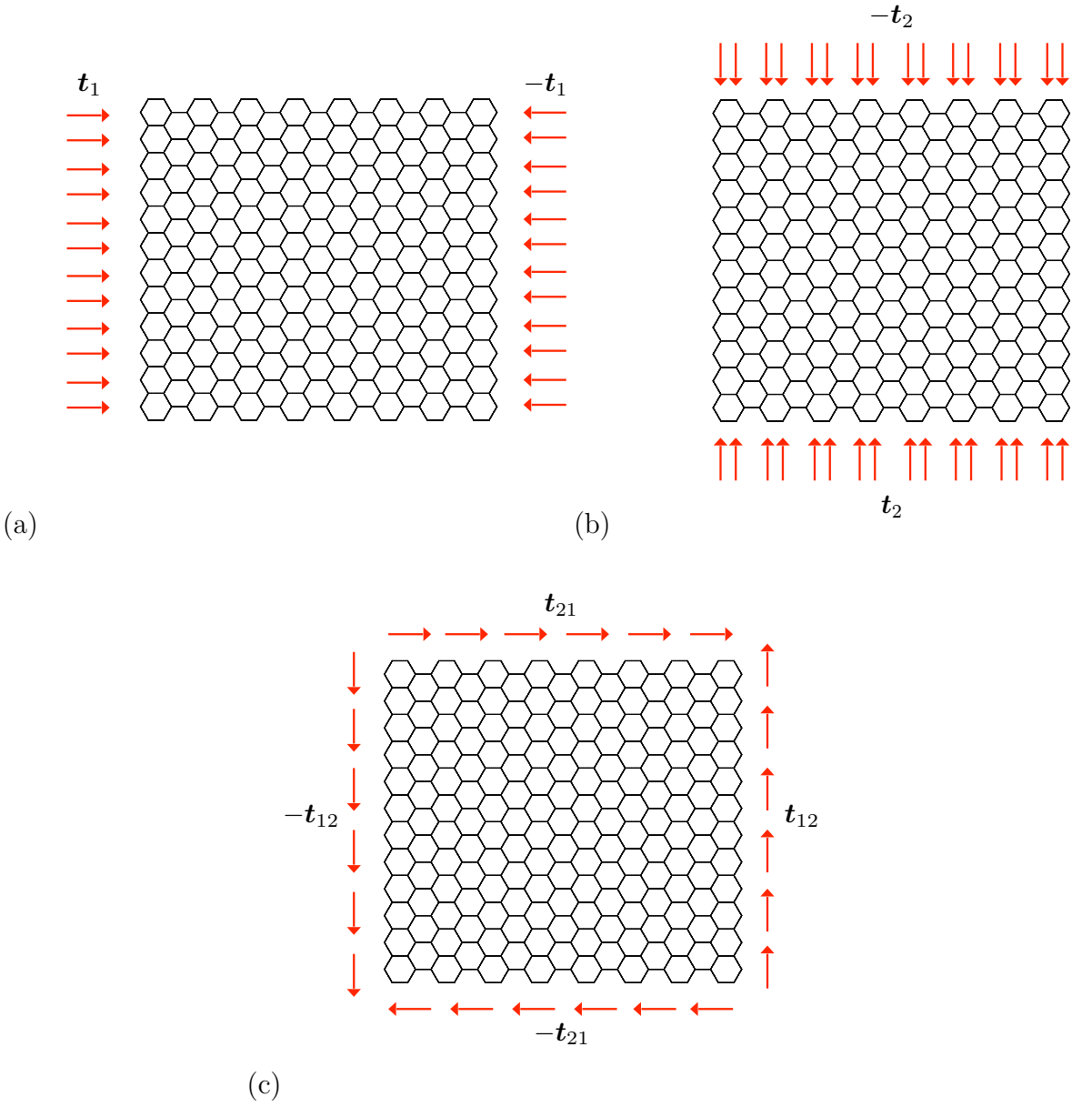

Figure 3.13: Finite element implementation, the load conditions: (a) uniaxial compression in the $\boldsymbol{e}_1$ direction, (b) uniaxial compression in the $\boldsymbol{e}_2$ direction, (c) pure shear

a small number of elements (10x7 cells) and continuously refining the mesh, i.e., the number of cells, until no variation in the results is observed. It is found that a 500x350 cells discretization is enough to get converged numerical results and to correctly capture the essential properties of the composite.

Tables 3.2-3.5 also illustrate the comparison between the theoretical and numerical solutions in terms of elastic moduli, Tables 3.3 and 3.5, and S_{ij} constants, Tables 3.2 and 3.4. Note that the analytical value of the latter quantities is obtained by substituting

$$\begin{aligned} C_{11} = C_{22} &= \frac{C_\ell^2 \ell^2 + 36 D_\ell C_\ell}{2\sqrt{3}\,\ell(12D_\ell + C_\ell \ell^2)} + \frac{271\,K_w}{416\sqrt{3}}, \\ C_{12} = C_{21} &= \frac{C_\ell^2 \ell^2 - 12 D_\ell C_\ell}{2\sqrt{3}\,\ell(12D_\ell + C_\ell \ell^2)} + \frac{67\,K_w}{416\sqrt{3}}, \\ C_{33} &= \frac{24 D_\ell C_\ell}{\sqrt{3}\,\ell(12D_\ell + C_\ell \ell^2)} + \frac{51\,K_w}{52\sqrt{3}}, \\ C_{13} = C_{23} &= C_{31} = C_{32} = 0, \end{aligned} \tag{3.116}$$

derived in Section 3.5.2, into Equations (3.98).

Generally, it emerges a good agreement between the analytical and numerical predictions, especially for $K_w = 10^{-2} E_s$. For example, let us focus on the elastic moduli. As it can be seen, for $K_w = 10^{-3} E_s$, the analytical results are averagely 2.1% smaller than the numerical ones (Table 3.3), but the data reduces to averagely 1% when $K_w = 10^{-2} E_s$ (Table 3.5). Apparently, the difference could be related to the simplifying assumptions of the theoretical model, such as the use of linear interpolants of nodal displacements and rotations instead of asymptotic expansions (Chen *et al.*, 1998; Dos Reis & Ganghoffer, 2012a; Gonella & Ruzzene, 2008). Another source of difference could be the Saint-Venant border effect, captured by the finite element simulations and neglected by the analytical approach.

However, considering the very close comparison, it can be said that the results of the numerical homogenization validate the theoretical ones.

3.6.2 Comparison with the existing literature

To further establish the validity of the presented modelling strategy, the theoretical findings of Section 3.5.3 are compared with the existing literature focusing on the same

Table 3.2 Comparison between the analytical and numerical predictions, with $K_w = 10^{-3}E_s$: S_{ij} constants (GPa^{-1})

No. cells	ℓ (mm)	S_{11}	S_{22}	S_{33}	S_{12}	S_{21}	$S_{13}, S_{23}, S_{31}, S_{32}$
10x7	5	1.03	1.04	16.38	-1.01	-1.00	0
50x35	1	1.05	1.05	16.39	-1.02	-1.01	0
100x70	0.5	1.06	1.06	16.40	-1.03	-1.02	0
200x140	0.25	1.07	1.08	16.41	-1.04	-1.03	0
250x175	0.2	1.08	1.09	16.42	-1.04	-1.04	0
400x280	0.125	1.09	1.09	16.42	-1.04	-1.04	0
500x350	0.1	1.09	1.09	16.42	-1.04	-1.04	0
Analytical results		1.12	1.12	16.67	-1.06	-1.06	0

Table 3.3 Comparison between the analytical and numerical predictions, with $K_w = 10^{-3}E_s$: elastic moduli

No. cells	ℓ (mm)	E_1 (GPa)	E_2 (GPa)	G (GPa)	ν_{12}	ν_{21}
10x7	5	0.97	0.96	0.08	0.97	0.97
50x35	1	0.95	0.95	0.06	0.96	0.97
100x70	0.5	0.94	0.94	0.06	0.96	0.97
200x140	0.25	0.93	0.92	0.06	0.96	0.96
250x175	0.2	0.92	0.91	0.06	0.95	0.95
400x280	0.125	0.91	0.91	0.06	0.95	0.95
500x350	0.1	0.91	0.91	0.06	0.95	0.95
Analytical results		0.89	0.89	0.06	0.95	0.95

Table 3.4 Comparison between the analytical and numerical predictions, with $K_w = 10^{-2}E_s$: S_{ij} constants (GPa^{-1})

No. cells	ℓ (mm)	S_{11}	S_{22}	S_{33}	S_{12}	S_{21}	$S_{13}, S_{23}, S_{31}, S_{32}$
10x7	5	0.39	0.39	6.13	-0.35	-0.35	0
50x35	1	0.39	0.39	6.15	-0.35	-0.35	0
100x70	0.5	0.39	0.39	6.16	-0.35	-0.35	0
200x140	0.25	0.40	0.39	6.18	-0.35	-0.35	0
250x175	0.2	0.40	0.40	6.19	-0.35	-0.36	0
400x280	0.125	0.40	0.40	6.20	-0.36	-0.36	0
500x350	0.1	0.40	0.40	6.20	-0.36	-0.36	0
Analytical results		0.40	0.40	6.25	-0.36	-0.35	0

Table 3.5 Comparison between the analytical and numerical predictions, with $K_w = 10^{-2}E_s$: elastic moduli

No. cells	ℓ (mm)	E_1 (GPa)	E_2 (GPa)	G (GPa)	ν_{12}	ν_{21}
10x7	5	2.55	2.56	0.16	0.90	0.91
50x35	1	2.54	2.55	0.16	0.90	0.90
100x70	0.5	2.52	2.53	0.16	0.89	0.89
200x140	0.25	2.51	2.52	0.16	0.89	0.89
250x175	0.2	2.50	2.51	0.16	0.89	0.89
400x280	0.125	2.50	2.50	0.16	0.89	0.89
500x350	0.1	2.50	2.50	0.16	0.89	0.89
Analytical results		2.48	2.48	0.16	0.89	0.89

issue. This often-adopted Popperian approach (Popper, 1965) uses the comparison with the available results as a conceptual mirror to gauge the robustness of a newly suggested theory.

However, as already pointed out (cf. Section 3.1), there is only a limited body of literature concerning the mechanical characterisation of cellular materials with filled cells. Consequently, in order to include a more comprehensive discussion, the results proposed in Section 3.5.3 are also compared with those reported in several recent works dealing with the analytical modelling of unfilled cellular materials. In the selected works, in particular, the authors obtained the equivalent properties of the lattice by means of different assumptions and techniques.

3.6.2.1 Traditional cellular materials with not-filled cells

Starting with the case of not-filled cellular materials and considering an aluminium honeycomb with E_s=79 GPa and ν_s=0.35 as in Section 3.6.1, the outcome of the aforementioned comparison is illustrated in Figure 3.14 and Table 3.6.

It emerges that the elastic constants in Equations (3.87)-(3.90), now expressed by

$$E_1 = E_2 \equiv E = \frac{4\lambda^3 E_s}{\sqrt{3}\,(1-\nu_s^2)(1+3\lambda^2)}, \tag{3.117}$$

$$\nu_{12} = \nu_{21} \equiv \nu = \frac{1-\lambda^2}{1+3\lambda^2}, \tag{3.118}$$

$$G = \frac{\lambda^3 E_s}{\sqrt{3}\,(1-\nu_s^2)(1+\lambda^2)}, \tag{3.119}$$

as the presence of the filler is neglected by assuming $K_w = 0$, are generally in accordance with those predicted in Davini & Ongaro (2011), Gibson & Ashby (2001), Dos Reis & Ganghoffer (2012a) and Gonella & Ruzzene (2008).

Specifically, in the framework of homogenization theory, Davini and Ongaro (Davini & Ongaro, 2011) obtained the constitutive model for a honeycomb subjected to in-plane deformations through an energy-based approach. In Davini & Ongaro (2011) the microstructure is represented as a sequence of elastic beams and, similarly to the present thesis, the introduction of the linear interpolants of nodal displacements and rotations into the discrete energy of the system provides its continuum approximation. General theorems of Γ-convergence give the elastic constants of the homogenized model that, as shown in Figure 3.14 and Table 3.6, coincide with Equations (3.117)-(3.119).

Regarding Gibson & Ashby (2001), the equivalent elastic moduli, obtained by applying the principles of structural analysis to the representative volume element of the lattice, agree with those expressed in Equations (3.117)-(3.119) in the limit of slender beams. For instance, after writing Equation (3.117) in terms of the Young's modulus in Gibson & Ashby (2001), E_{GA}, it emerges that the two estimates differ by a quantity related to the ratio $\lambda := h/\ell$, decreasing as $\lambda \to 0$:

$$E = \frac{E_{GA}}{(1 + 3\lambda^2)\ (1 - \nu_s^2)}. \tag{3.120}$$

Differently from Davini & Ongaro (2011), the homogenization technique in Gonella & Ruzzene (2008) interprets the discrete lattice according to the finite difference formalism. The equivalent continuum, slightly less stiff than that of the present work (Figures 3.14a and 3.14b), derives from the application of Taylor's series expansions of the nodal displacements and rotations, motivated by the multi-scale nature of the considered problem.

An alternative approach, suggested in Dos Reis & Ganghoffer (2012a), exploits a method in the context of micropolar elasticity, where the interactions between two neighbouring points involve both the the Cauchy stress, as in classical mechanics, and the couple stresses (Eremeyev, 2013). By describing the hexagonal lattice as a sequence of extensional and flexural elements, the authors obtained the homogenized stress-strain relations and elastic constants. As Figure 3.14 shows, the latter are in good agreement with Equations (3.117)-(3.119) in the limit $\lambda \to 0$.

An analysis of the micropolar behavior of the honeycomb microstructure is also provided in Chen *et al.* (1998), where the periodic medium is represented as an assembly of Euler-Bernoulli beams. An energy-based approach, in conjunction with Taylor's

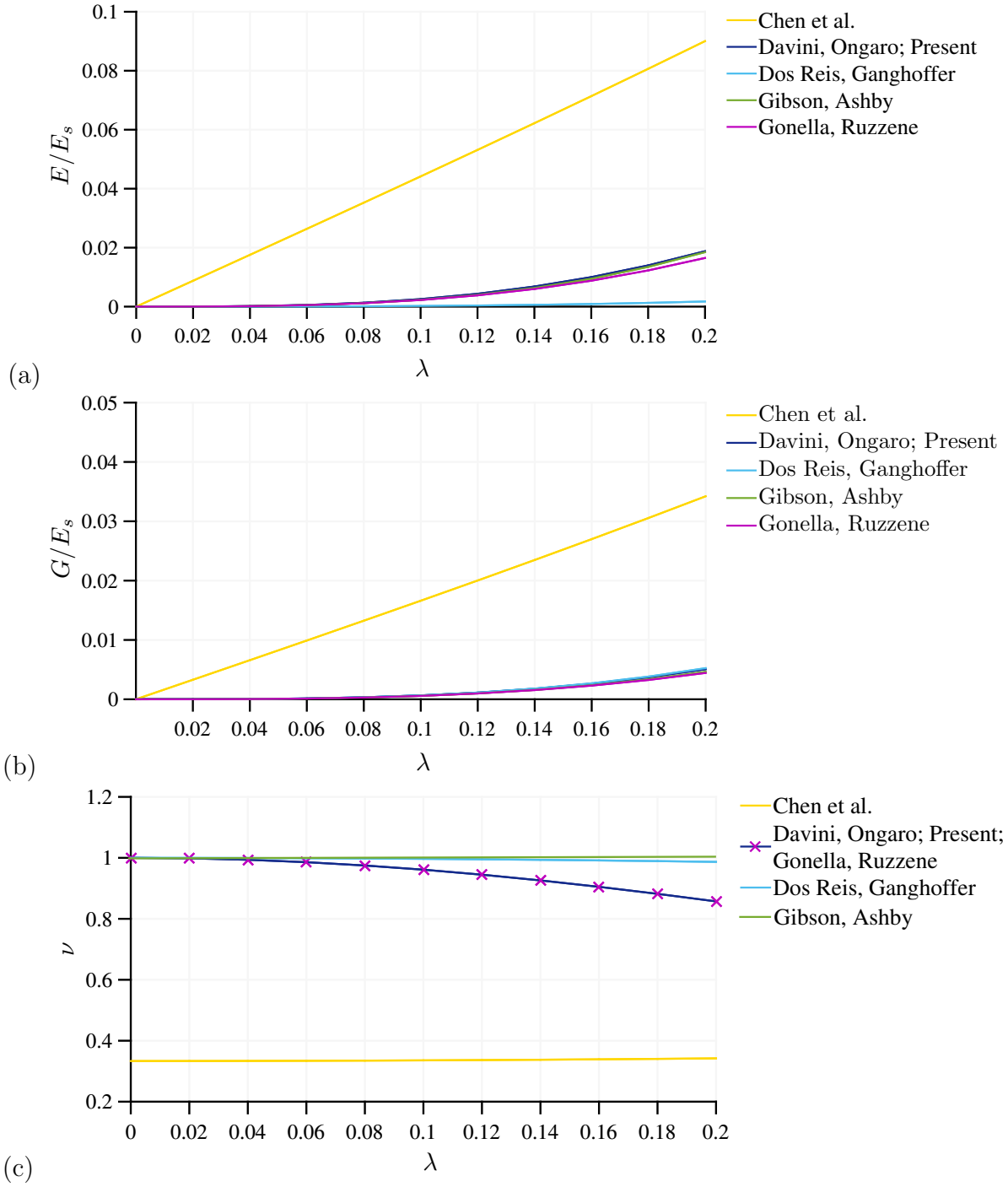

Figure 3.14: Comparison with the existing literature in the case of not-filled cellular materials: (a) normalised Young's modulus, (b) normalised shear modulus, (c) Poisson's ratio

Table 3.6 Comparison with the existing literature: not-filled honeycomb

Young's modulus	Shear modulus	Poisson's ratio
Chen *et al.* (1998)		
$\frac{E_{CH}}{E_s} = \frac{2\lambda(1+\lambda^2)}{\sqrt{3}\,(1-\nu_s^2)(3+\lambda^2)}$	$\frac{G_{CH}}{E_s} = \frac{\sqrt{3}\,\lambda(1+\lambda^2)}{12\,(1-\nu_s^2)}$	$\nu_{CH} = \frac{1+\lambda^2}{3+\lambda^2}$
Davini & Ongaro (2011)		
$\frac{E_{DO}}{E_s} = \frac{4\sqrt{3}\lambda^3}{3\,(1-\nu_s^2)(1+3\lambda^2)}$	$\frac{G_{DO}}{E_s} = \frac{\sqrt{3}\,\lambda^3}{3\,(1-\nu_s^2)(1+\lambda^2)}$	$\nu_{DO} = \frac{1-\lambda^2}{1+3\lambda^2}$
Dos Reis & Ganghoffer (2012a)		
$\frac{E_{DG}}{E_s} = \frac{4\sqrt{3}\lambda^3}{9\,(1-\nu_s^2)(4+\lambda^2)}$	$\frac{G_{DG}}{E_s} = \frac{4\sqrt{3}\,\lambda^3}{(1-\nu_s^2)(12+\lambda^2)}$	$\nu_{DG} = \frac{12-\lambda^2}{3(4+\lambda^2)}$
Gibson & Ashby (2001)		
$\frac{E_{GA}}{E_s} = \frac{4\lambda^3}{\sqrt{3}}$	$\frac{G_{GA}}{E_s} = \frac{\lambda^3}{\sqrt{3}}$	$\nu_{GA} = 1$
Gonella & Ruzzene (2008)		
$\frac{E_{GR}}{E_s} = \frac{4\sqrt{3}\lambda^3}{3(1+3\lambda^2)}$	$\frac{G_{GR}}{E_s} = \frac{\sqrt{3}\,\lambda^3}{3\,(1+\lambda^2)}$	$\nu_{GR} = \frac{1-\lambda^2}{1+3\lambda^2}$

expansions of the nodal degrees of freedom, displacements and rotations, provides the equivalent mechanical properties. If compared to Davini & Ongaro (2011), Gibson & Ashby (2001), Dos Reis & Ganghoffer (2012a) and Gonella & Ruzzene (2008), the method in Chen *et al.* (1998) ignores the connectivity of the beams and the equilibrium conditions at the nodes, leading to a much stiffer behavior (Figure 3.14).

3.6.2.2 Filled cellular materials

In the case of filled cellular materials, Table 3.7 shows that the effective elastic constants derived in Section 3.5.3 match those available in the literature, proposed in Murray *et al.* (2009) and Burlayenko & Sadowski (2010).

Specifically, Murray et al. (Murray *et al.*, 2009) focused on the in-plane Young's modulus, E_M, of a metallic honeycomb filled with a polymeric material. In Murray *et al.* (2009) the predictions are obtained through a finite element-based analysis of the unit cell, where the cell walls and the filler are modelled, respectively, as beam elements and plane-stress shell elements.

Regarding Burlayenko & Sadowski (2010), a three-dimensional finite element analysis is proposed to investigate the mechanics of aluminium honeycombs filled with a PVC foam. On the basis of the numerical model developed, the equivalent in-plane Young's moduli, $E_{1,B}$ and $E_{2,B}$, and shear modulus, G_B, are derived by the strain energy homogenization technique of periodic media, summarised by the following two steps.

In the first, three independent loading states are imposed to the unit cell: uniaxial compression in the $\boldsymbol{e}_1$ direction, uniaxial compression in the $\boldsymbol{e}_2$ direction, pure shear. The second consists in evaluating the corresponding strain energy density, U, and numerically differentiating U with respect to the volume average components of the strain, $\overline{\varepsilon}_{ij}$:

$$\frac{1}{E_{1,B}} = \frac{\partial^2 U}{\partial^2 \overline{\varepsilon}_{11}}, \qquad \frac{1}{E_{2,B}} = \frac{\partial^2 U}{\partial^2 \overline{\varepsilon}_{22}}, \qquad \frac{1}{G_B} = \frac{\partial^2 U}{2\,\partial^2 \overline{\varepsilon}_{12}}. \tag{3.121}$$

For sake of clarity, it should be noted that the values of the Winkler constant, K_w, listed in Table 3.7 are related to the Young's modulus of the filler in Murray *et al.* (2009), $E_{f,M}$, and in Burlayenko & Sadowski (2010), $E_{f,B}$, via Equation (3.24).

In conclusion, although there is a little amount of literature in the field of filled cellular materials with which to compare and contrast the findings of the present thesis, it can be said that what is available contains strong similarities and appears to lend credibility to the proposed theory.

3.7 Parametric analysis

By assuming E_s=79 GPa and ν_s=0.35 (aluminium alloy) as in the previous sections, Figure 3.15 illustrates the influence of $\lambda := h/\ell$ in the macroscopic elastic constants of the examined composite honeycomb.

In general, for fixed K_w, the normalised Young's modulus, E/E_s, and the normalised shear modulus, G/E_s, increase with increasing λ. Namely, when the cell walls become thick. For instance, E/E_s shows an increase of averagely more than 20% when λ varies from 0 to 0.2 (Figure 3.15a). A slightly different trend emerges in the case of G/E_s: a slow increase for small values of λ ($0 < \lambda < 0.1$), followed by a more significant increase for $\lambda > 0.1$ (Figure 3.15b). Specifically, in the latter case, even a small increase of λ provides a large increase of G/E_s. This makes varying λ a good design method to obtain a material with improved stiffness.

Regarding the influence of K_w, Figures 3.15a and 3.15b suggest that, for fixed λ, to an increase of K_w corresponds an increase of both E/E_s and G/E_s. This is consistent

Table 3.7 Comparison with the existing literature in the case of filled microstructure

Murray *et al.* (2009) E_s=70 GPa, ν_s=0.35, $\lambda = 0.1$		Present E_s=70 GPa, ν_s=0.35, $\lambda = 0.1$	
$E_{f,M}$ (GPa)	$E_{1,M} = E_{2,M}$ (GPa)	K_w (GPa)	$E_1 = E_2$ (GPa)
0.001	$0.3 \div 0.4$	0.001	0.35
0.01	$0.3 \div 0.4$	0.009	0.37
0.1	0.5	0.094	0.45
1	$1.2 \div 1.3$	0.94	1.3

Burlayenko & Sadowski (2010) E_s=72.2 GPa, ν_s=0.34, $\lambda = 0.0125$			Present E_s=72.2 GPa, ν_s=0.34, $\lambda = 0.0125$		
$E_{f,B}$ (GPa)	$E_{1,B} = E_{2,B}$ (MPa)	G_B (MPa)	K_w (GPa)	$E_1 = E_2$ (MPa)	G (MPa)
0.056	0.627	0.238	0.053	0.610	0.235
0.105	0.788	0.282	0.099	0.760	0.267
0.230	1.061	0.386	0.216	0.885	0.338

with the result that one expects by increasing the stiffness of the material filling the cells, i.e. the parameter K_w. Also, the higher K_w, the higher will be the increase. For make it more clear, let us focus on the normalised Young's modulus of Figure 3.15a. As it can be seen, increasing K_w from $10^{-4}E_s$ to $10^{-3}E_s$ provides an average increase of only 105% while, for K_w varying from $10^{-2}E_s$ to $10^{-1}E_s$, the increase is averagely of 180%. Thus, it can be said that not only λ but also K_w is an important parameter to improve the stiffness of low-weight cellular structures.

Finally, in terms of the influence of λ in the effective Poisson's ratio, ν, from Figure 3.15c it emerges that, for fixed K_w, an increase in λ results in an increase of ν, that is more significant for small values of K_w ($10^{-4}E_s, 10^{-3}E_s$). In other words, the bigger K_w, the smaller will be the influence of λ. In addition, when λ is fixed, Figure 3.15c shows a decrease of ν by increasing K_w. Specifically, increasing K_w from $10^{-3}E_s$ to $10^{-2}E_s$ leads to a significant decrease of ν, averagely of 170%. Conversely, the average decrease is of only 90% by varying K_w from $10^{-2}E_s$ to $10^{-1}E_s$.

Again, these results reveal the possibility to obtain a large control in the design of composite cellular materials through the variation of the geometric, λ, and mechanical,

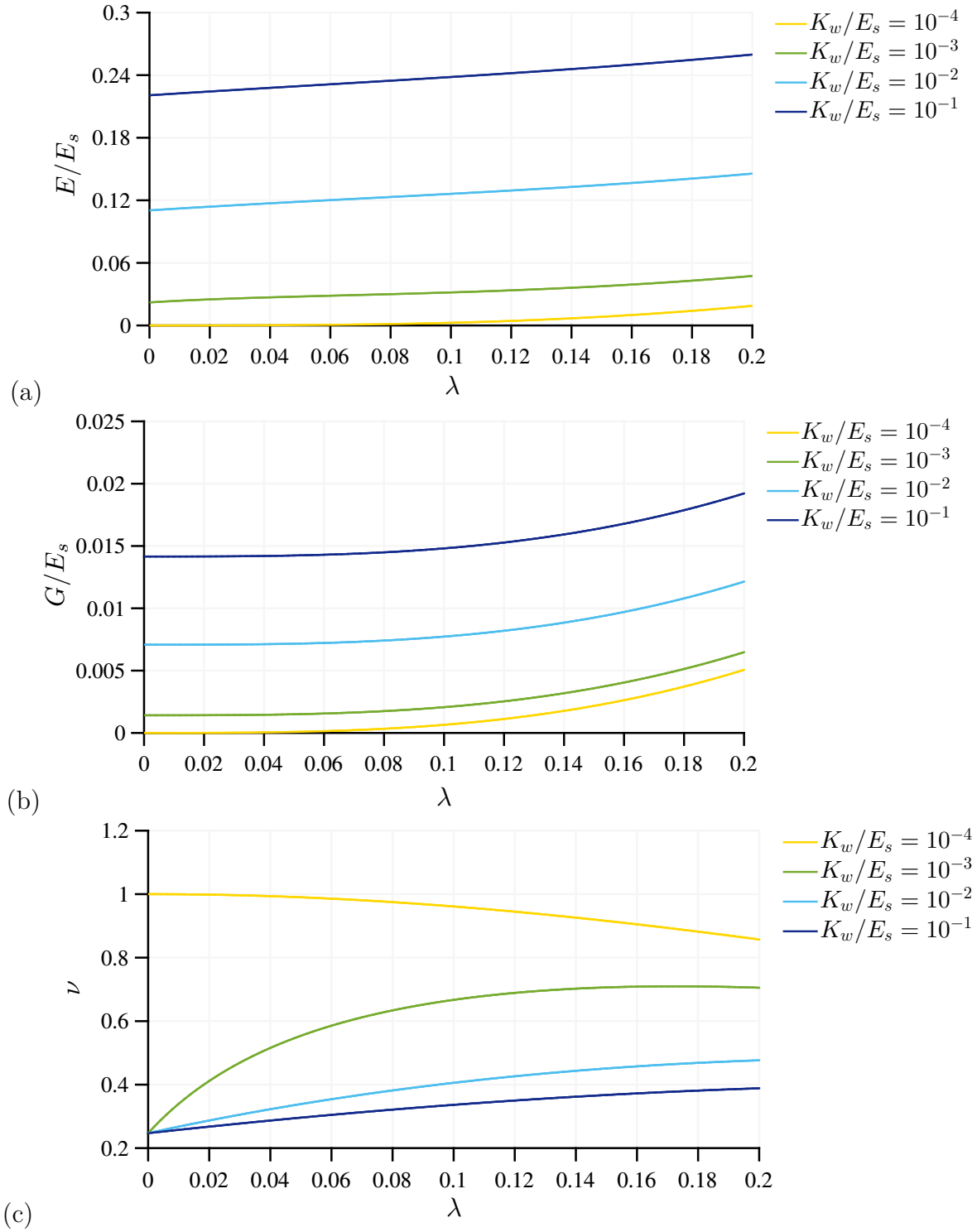

Figure 3.15: In-plane elastic constants versus the parameter λ for various K_w: (a) normalised Young's modulus, (b) normalised shear modulus, (c) Poisson's ratio

K_w, parameters of the microstructure. As seen, a wide range of mechanical properties can be easily achieved.

3.8 An application to the biological parenchyma tissue

The proposed theoretical model is inspired by the high efficiency of the biological composite structures that include, among others, the parenchyma tissue.

The parenchyma, briefly described in Section 3.1, is a plant tissue revealing a microstructure composed by thin-walled cells having the internal volumes filled with an incompressible fluid. As stated, the pressure exerted by the fluid, known as *turgor pressure*, is responsible for the strength and rigidity of the cell walls, leading to an improvement in the mechanical resistance of the whole cell (Van Liedekerke, 2010).

In the parenchyma, the fluid content plays a significant role in withstanding the external forces, but it is not the only factor. Load resistance also depends on the volume of intercellular spaces and on how closely the cells are packed together. Indeed, in densely packaged tissues, the freedom of the cell walls to deform is restrained and many experimental data indicate that bulky parenchyma cells are stiffer than their counterparts, although they are made of the same material (Cohen, 2011).

As pointed out in Zhu & Melrose (2003), the overall mechanical properties of the parenchyma tissue, effective moduli and stress-strain relations, are related to the characteristics of the individual components: cell walls, turgor pressure and cell-to-cell interactions.

A first attempt to describe the effects of the turgor pressure and the contribution of the cell walls' geometry on the macroscopic constants of the parenchyma is due to Nilsson et al. (Nilsson *et al.*, 1958). The authors, based on the analysis of the hydrostat, derived the Young's modulus of the whole tissue by analysing a single spherical cell, composed by a linear elastic material, subjected to infinitesimal deformations. The proposed relation,

$$E = 3\left[1 + \frac{7 - 5\nu_s}{20(1+\nu_s)}\right] p + \left[\left(\frac{3(7-5\nu_s)}{10(1-\nu_s^2)}\right)\frac{E_s\, h}{r}\right], \tag{3.122}$$

is a function of the turgor pressure, p, cell's radius, r, and cell walls' properties: thickness, h, Young's modulus, E_s, Poisson's ratio, ν_s. Despite the limiting assumptions behind, Equation (3.122) highlights a fundamental aspect of the parenchyma tissue, as well as of pressurised plant tissues in general. That is to say, the variable nature of the

tissue's stiffness, as both the turgor pressure and the walls' properties change with age and environmental constraints (Cohen, 2011; Niklas, 1992).

However, the mechanical behavior of the parenchyma is much more complex than one might think and Equation (3.122) fails to capture several other mechanical traits. For example, if subjected to an external load, the parenchyma tissue manifests properties that parallel those of elastic, plastic and viscoelastic solids. As a matter of fact, its resulting stress-strain diagram exhibits short-term elastic recovery, long-term plasticity, stress relaxation and creep (Cohen, 2011).

In addition, the physical properties of living tissues are very difficult to measure experimentally (Wu & Pitts, 1999).

Recalling that the stress is the applied force divided by the cross-sectional area through which the force is applied, it often emerges that, unlike ordinary solids, the stress-strain diagram of such tissues depends on the dimensions of the examined sample, preventing us the opportunity to obtain an accurate value of the mechanical properties (Niklas, 1992). In their study on the parenchyma, Falk et al. (Falk *et al.*, 1958) showed the dependence of the elastic modulus of the tissue on the cross-sectional area of the sample used in mechanical testing, even when the loading forces were normalised with respect to that variable. Specifically, increasing the cross-sectional area led to an increase in the elastic modulus. The reason is related to the more and more higher amount of cells involved in the test: the greater the number, the stiffer the parenchyma sample, as less cell walls are free to deform.

It clearly emerges that the analysis of the parenchyma and, more generally, of fluid-filled biological tissues, is extremely complicated without great simplifications and assumptions.

A question that arises is whether the results of our model could provide some useful information on the mechanical properties of such vegetative tissues.

Being a rigorous analysis well beyond our aim, and considering the small amount of available data, only the effective Young's modulus, E, is examined. Its value is given by Equation (3.87), reported here for ease of reading:

$$E = \frac{\left(13\,K_w\left(1-\nu_s^2\right)+16\lambda E_s\right)\left(51\left(1+\lambda^2\right)K_w\left(1-\nu_s^2\right)+208\lambda^3 E_s\right)}{4\sqrt{3}\left(1-\nu_s^2\right)\left(271\left(1+\lambda^2\right)K_w\left(1-\nu_s^2\right)+208\left(\lambda+3\lambda^3\right)E_s\right)}. \tag{3.123}$$

According to Equation (3.123), E is related to the cell walls' characteristics, Young's modulus, E_s, Poisson's ratio, ν_s and thinness ratio, λ, derived from the experimental published results. Regarding the Winkler foundation constant, K_w, the following additional considerations have to be made.

Restricting the analysis to the two-dimensional space and assuming, for simplicity, a microstructure composed by hexagonal cells, the parenchyma tissue is schematically illustrated in Figure 3.16.

Two configurations are considered: in the first, Figure 3.16a, the filling material is represented by a pressurised fluid, in the second, Figure 3.16b, by the Winkler model.

As in Section 3.3.1, a suitable relation between the inner pressure, p, and the constant K_w is provided by the energetic equivalence

$$W_{c,\,Winkler} \equiv W_{c,\,fluid}, \tag{3.124}$$

being

$$W_{c,\,Winkler} = W_{w,\,beams} + W_{f,\,Winkler} \tag{3.125}$$

and

$$W_{c,\,fluid} = W_{w,\,walls} + W_{f,\,fluid} \tag{3.126}$$

in turn, the elastic energy of the unit cell (Figure 3.16c) in the Winkler foundation model and in the fluid-filled configuration. Also, $W_{w,\,beams}$, $W_{f,\,Winkler}$ and $W_{w,\,walls}$, $W_{f,\,fluid}$ stand, respectively, for the elastic energies of the cell walls and of the filler in the two considered cases. It should be noted that in expressing the energy of a pressurised lattice as in Equation (3.126) it is implicitly assumed that the fluid phase acts as an external field on the cellular structure. Its contribution, given by the work done by the fluid from the undeformed area, A_0, to a generic deformed one, A, takes the form (Guiducci *et al.*, 2014)

$$W_{f,\,fluid} = \frac{1}{2}\, p \frac{A - A_0}{A_0}\, A_0 = \frac{1}{2}\, p\,(A - A_0). \tag{3.127}$$

By adopting the same notation and assumptions of Section 3.3.1 (see Appendix D for a detailed description), simple mathematical manipulations provide (Figure 3.16c)

$$W_{f,\,fluid} = \frac{1}{2}\, p\,(\mathbf{l}_2 \times \boldsymbol{e}_3 \cdot \mathbf{E}_f \mathbf{l}_1 + \boldsymbol{e}_3 \times \mathbf{l}_1 \cdot \mathbf{E}_f \mathbf{l}_2)\,, \tag{3.128}$$

with $\mathbf{l}_1$ and $\mathbf{l}_2$ the lattice vectors defined in Equation (3.3) and $\mathbf{E}_f$ the infinitesimal strain tensor introduced in Equation (3.14).

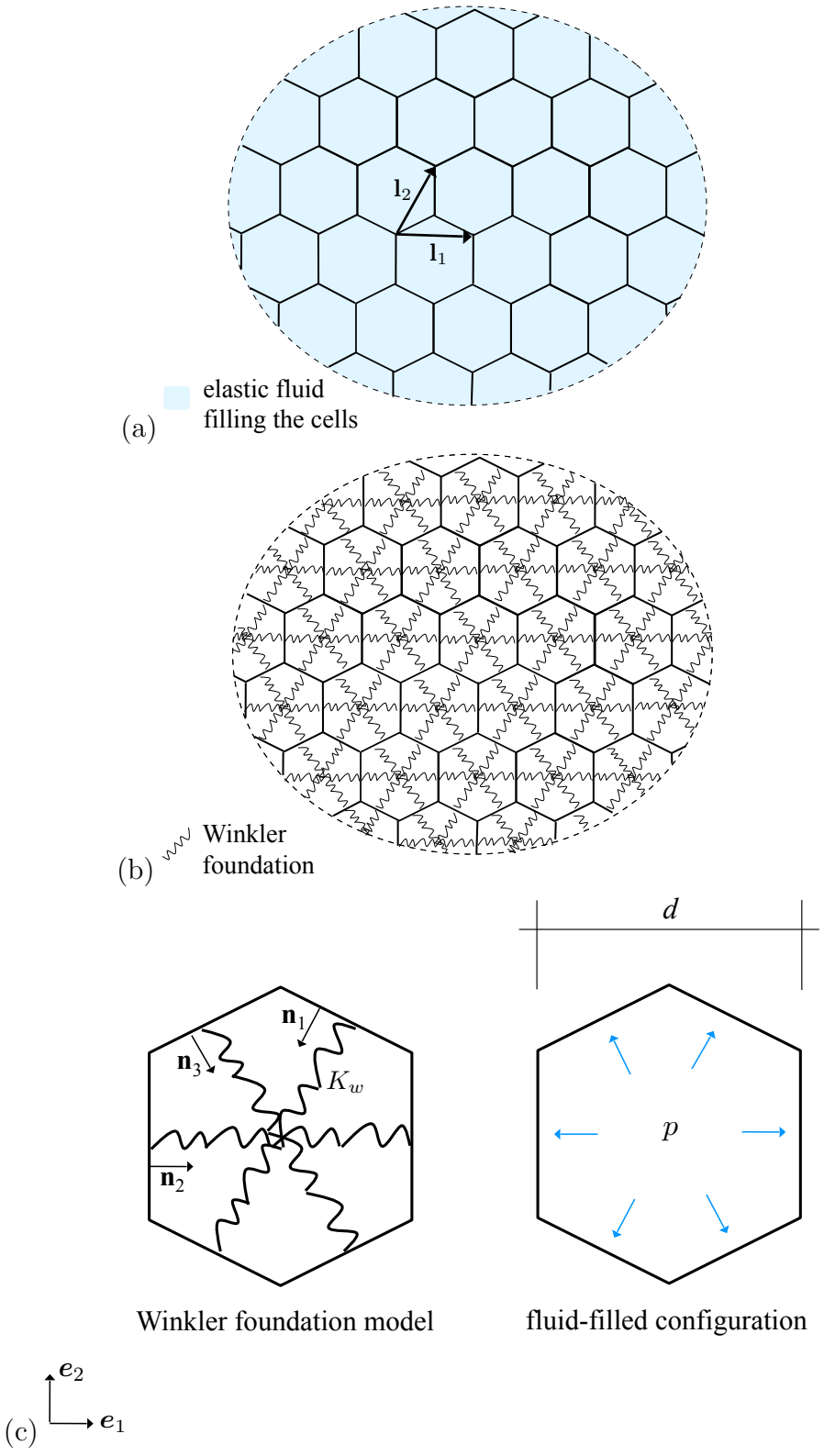

Figure 3.16: The parenchyma tissue: (a) the fluid-filled configuration, (b) the Winkler model, (c) the unit cell

Similarly, $W_{f,Winkler}$, obtained by summing the contribution of the springs in the $\mathbf{n}_i$ directions, is expressed by (cf. Equation (3.11))

$$W_{f,Winkler} = \sum_{i=1}^{3} \frac{1}{2} \Delta U_i \left(\mathbf{n}_i^T \mathbf{K}_w \mathbf{n}_i \right) \Delta U_i \equiv \sum_{i=1}^{3} \frac{1}{2} d \left(\mathbf{n}_i^T \mathbf{E}_f \mathbf{n}_i \right) \mathbf{n}_i^T \mathbf{K}_w \mathbf{n}_i \left(\mathbf{n}_i^T \mathbf{E}_f \mathbf{n}_i \right) d, \tag{3.129}$$

where ΔU_i and $\mathbf{K}_w$ are, in turn, the elongation and the stiffness matrix of the elastic springs, $d = \sqrt{3}\ell$.

From the hypothesis

$$W_{w,beams} \equiv W_{w,walls} \tag{3.130}$$

and the equivalence in Equation (3.124), it follows

$$W_{f,Winkler} \equiv W_{f,fluid} \tag{3.131}$$

or, in view of Equations (3.128) and (3.129),

$$\sum_{i=1}^{3} \frac{1}{2} d \left(\mathbf{n}_i^T \mathbf{E}_f \mathbf{n}_i \right) \mathbf{n}_i^T \mathbf{K}_w \mathbf{n}_i \left(\mathbf{n}_i^T \mathbf{E}_f \mathbf{n}_i \right) d = \frac{1}{2} p \left(\mathbf{l}_2 \times \boldsymbol{e}_3 \cdot \mathbf{E}_f \mathbf{l}_1 + \boldsymbol{e}_3 \times \mathbf{l}_1 \cdot \mathbf{E}_f \mathbf{l}_2 \right). \tag{3.132}$$

Finally, considering the deformation state

$$\mathbf{E}_f := \begin{bmatrix} 1 & 0 \\ 0 & 1 \end{bmatrix} \tag{3.133}$$

and substituting Equation (3.133) into Equation (3.132), lead to

$$K_w = \frac{\sqrt{3}}{3} p. \tag{3.134}$$

As summarised in Tables 3.8-3.10, three cases are investigated: the parenchyma tissue of the apple, Table 3.8, of the potato, Table 3.9, and of the carrot, Table 3.10.

Generally, the predictions of Equation (3.123) agree with the results of the other authors, derived from three-dimensional finite element simulations of an isolated parenchyma cell (Wu & Pitts, 1999), from experimental tests (Gibson, 2012; Georget *et al.*, 2003), or from simplified analytical models (Gibson *et al.*, 2010; Nilsson *et al.*, 1958).

The discrepancies that emerge are related to various factors.

Table 3.8 Young's modulus of the apple parenchyma tissue

	E (MPa)
Present $\lambda = 0.02 \div 0.2$ (by assumption) $p = 0.8$ MPa $\Rightarrow$K$_w = 0.47$ MPa E_s=52.8 MPa, ν_s=0.24 (Wu & Pitts, 1999)	$1 \div 1.6$
Gibson *et al.* (2010)	$0.31 \div 3.46$
Nilsson *et al.* (1958)	$0.9 \div 9.7$

Table 3.9 Young's modulus of the potato parenchyma tissue

	E (MPa)
Present $\lambda = 0.0087$ (Gibson, 2012) $p = 0.8$ MPa $\Rightarrow$K$_w = 0.47$ MPa $E_s = 500 \div 600$ MPa, ν_s=0.5 (Gibson, 2012)	$4 \div 4.2$
Gibson (2012)	$5 \div 6$
Nilsson *et al.* (1958)	$8 \div 9.6$
Experimental value (Gibson, 2012)	$3.5 \div 5.5$

Table 3.10 Young's modulus of the carrot parenchyma tissue

	E (MPa)
Present $\lambda = 0.02 \div 0.2$ $p = 0.8$ MPa $\Rightarrow$K$_w = 0.47$ MPa $E_s = 100$ MPa, ν_s=0.33 (Niklas, 1992)	$1.7 \div 2$
Georget *et al.* (2003)	$1.6 \div 14.2$
Nilsson *et al.* (1958)	$1.7 \div 18.6$
Experimental value (Georget *et al.*, 2003)	7 ± 1

Firstly, to the different cells' shape considered: hexagons in the present thesis, spheres in Wu & Pitts (1999) and Nilsson *et al.* (1958).

Secondly, to the approximated value of the cell walls' length, ℓ, and turgor pressure, p, assumed in Tables 3.8-3.10. ℓ, in particular, derives by considering the characteristics of the mature cell in Sanchis Gritsch & Murphy (2005), where the authors described the structure of the parenchyma cell at different stages of development. Regarding p, for simplicity, the value indicated by Georget et al. (Georget *et al.*, 2003) in the case of carrot parenchyma ($p = 0.8$ MPa), it is assigned to all the examined tissues.

However, Tables 3.8-3.10 reveal that the theory proposed in the present work could be applied in biology to gain some insights into the mechanics of composite tissues. This result is also confirmed in Chapter 5 by extending the analysis to composite cellular materials having a mutable elongated hexagonal microstructure.

4 | The elastic response of hierarchical composite cellular materials: synergy of hierarchy, material heterogeneity and cell topology

4.1 Introduction and state of the art

4.1.1 Introduction

Natural materials are typically built from a limited number of polymeric (e.g. proteins or polysaccharides) and ceramic (e.g. calcium salts or silica) components, having relatively poor intrinsic properties (Wegst *et al.*, 2015).

However, despite this limited toolbox, nature assembled an astounding range of structures, perfected over millions of years of evolution, that are able to combine the desirable properties of their building blocks and, often, perform significantly better than the sum of their parts (Wegst *et al.*, 2015; Mann, 2001). In most cases, the resulting systems offer unique combinations of mechanical properties that, in man-made materials, tend to be mutually exclusive.

Bone and nacre, for instance, are natural materials that combine strength and toughness at low weight, a distinctive quality that synthetic structural materials are still far from achieving. Indeed, strong materials are invariably brittle, whereas tough materials are frequently weak (Wegst *et al.*, 2015; Ritchie, 2011).

Other examples include bamboo and palm, two highly porous materials whose exceptional structural efficiency, in terms of mechanical performance per unit weight, fascinated a lot of scientists and engineers (Wegst, 2011; Wegst & Ashby, 2004). Such plants, in particular, are equally light, strong and flexible, three characteristics that in

engineered materials difficulty coexist: when high porosity is needed, it is usually at the expense of mechanical stability.

Contemporary characterisation and modelling tools allowed researchers to begin deciphering the intricate interplay of mechanisms that endow natural systems with their unusual properties. Unfortunately, identifying the salient strategies providing the astonishing combinations of stiffness, strength and toughness at low weight, is not a trivial undertaking and it is an open question how nature succeeded in doing this.

Some authors, however, analysed different types of natural materials and, after finding common design themes among them, suggested a number of possible techniques.

The majority of investigations conclude that hierarchy is nature's key of success (Fratzl, 2007; Pan, 2014; Gao, 2010; Chen & Pugno, 2013b). That is to say, the superior traits of natural structures stem from their complex hierarchical architecture spanning from the molecular to the macroscopic scale, in conjunction with the confluence of mechanisms that interact at multiple length scales. Hierarchy, in particular, allows the organism to be multifunctional and, through the optimisation of its architecture at each structural level, to perform both biological and mechanical functions to the best of its abilities (Fratzl & Weinkamer, 2007).

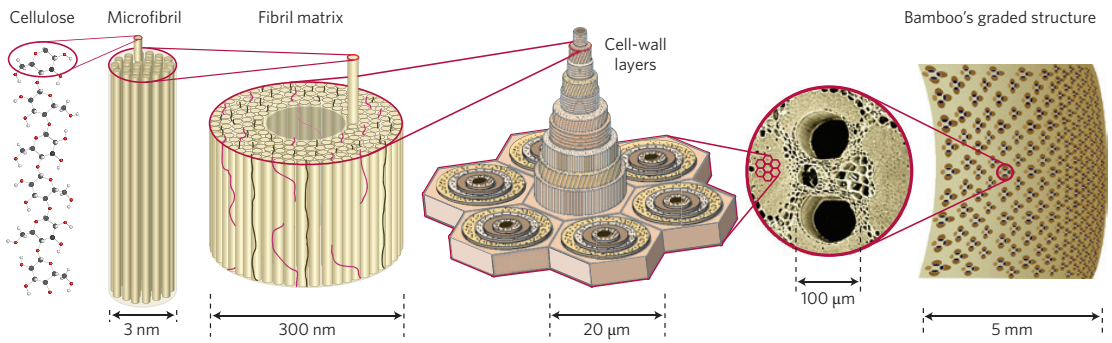

Figure 4.1: The hierarchical structure of bamboo, taken from Wegst et al. (2015)

The aforementioned bamboo, for example, is a hierarchical fibre-reinforced cellular material, composed of parallel cellulose fibres embedded in a lignin-hemicellulose matrix shaped into honeycomb-like cells (Wegst, 2011). The feature responsible for the high efficiency of the plant, in terms of flexural rigidity per unit weight, in the not-uniform distribution of the load-bearing fibres across the numerous length scales, in addition to a not constant cell walls' thickness (Figure 4.1). The plant, in particular, creates a gradient of density and modulus of fibres, with higher values of density where the stresses are larger (Wegst *et al.*, 2015). This solution leads to an optimised hierarchical architecture where the plant, to perform its functions, at each structural level uses the

smallest quantity of the most highly efficient cell walls' material. In other words, it can be said that, under a considerable number of constraints, every structural level is a local design optimum.

It clearly emerges that, in a system, hierarchy is reflected by three characteristics: multiscality, heterogeneity and anisotropy (Pan, 2014; Barthelat & Mirkhalaf, 2013). As a consequence, many mathematical laws and material sciences' principles, which assume isotropy and homogeneity, must be carefully applied when dealing with structural hierarchy.

4.1.2 State of the art

There is an enormous amount of literature focusing on the characterisation of a wide range of both biological and man-made hierarchical materials and it would be impossible to review the subject adequately. Consequently, in this introductory part we only consider the contributions related to the problem touched in the present thesis and we refer the interested reader to the recently published review articles Fratzl & Weinkamer (2007), Gibson (2012), Chen & Pugno (2013b), Pan (2014) and Wegst *et al.* (2015) and to the references therein for further discussions.

The pioneering work devoted to the analysis of hierarchical systems, fibre composites and cellular solids among others, is attributed to Lakes (Lakes, 1993), who recognised the importance of hierarchy in obtaining enhanced mechanical properties (e.g. stress attenuation, superplasticity, increased toughness).

The study was then extended by Bosia et al. (Bosia *et al.*, 2012), who introduced an analytical method to evaluate how hierarchy affects the structural strength of various hierarchical architectures of fibre bundles. The authors, by performing multiscale calculations, concluded that, in the case of different types of fibres, increasing the number of hierarchical levels led to an improvement in the material's strength.

In the context of cellular solids, Carpinteri and Pugno (Carpinteri & Pugno, 2008; Pugno & Carpinteri, 2008), Chen and Pugno (Chen & Pugno, 2013a; 2012), Haghpanah et al. (Haghpanah *et al.*, 2014), Fan et al. (Fan *et al.*, 2008) and Taylor et al. (Taylor *et al.*, 2012; 2011) investigated the role of hierarchy on the in-plane mechanical behavior of hierarchical honeycombs (Figure 4.2).

In particular, in Chen & Pugno (2012) and Haghpanah *et al.* (2014) the authors addressed the problem of elastic stability while in Carpinteri & Pugno (2008), Chen & Pugno (2013a), Fan *et al.* (2008) and Pugno & Carpinteri (2008) derived numerical and theoretical models, force or energy based, to describe the macroscopic strength, toughness and stiffness.

In addition, Zhao et al. (Zhao *et al.*, 2012) designed, fabricated and experimentally tested ultra-light hierarchical honeycombs with one level of hierarchy and woven textile sandwich walls (Figure 4.2b).

Another sandwich application was examined by Sun et al. (Sun *et al.*, 2014; Sun & Pugno, 2013), who suggested a multifunctional hierarchical honeycomb made of negative Poisson's ratio cell walls in order to achieve tunable stiffness (Figures 4.2f and 4.2g).

From these studies it emerges that hierarchy is detrimental to the specific stiffness. However, to avoid reducing the in-plane elastic properties, one effective strategy is to iteratively replace each three-edge node of a base hexagonal network with a smaller hexagon. Pioneered by Ajdari et al. (Ajdari *et al.*, 2012), this technique leads to a fractal-appearing structure, often called *self-similar hierarchical honeycomb*, up to 3.5 times stiffer than the not-hierarchical counterpart having the same mass (Figure 4.2h).

Specifically, a self-similar structure exhibits statistically similar characteristics when examined both locally, at the level of individual components, and globally, at the level of the whole system. In other words, the same general characteristic is independent of the scale at which the observation is made (Katz, 1999). This bio-inspired principle mimics the self-similar hierarchical design of biological systems, as the sticky foot of the Gecko (Chen & Pugno, 2013b), muscles and tendons (Galvanetto *et al.*, 2010; Fratzl, 2008) and the intriguing collagen (Figure 4.3), whose hierarchical organisation spans from the nano- to the macro-scale (Buehler, 2008).

In the last decade, due to the advent of additive manufacturing technologies, several attempts have been made to further explore the potential advantages of self-similar hierarchical structuring. Among them, starting from the study in Ajdari *et al.* (2012), Haghpanah et al. (Haghpanah *et al.*, 2013) presented a theoretical method to evaluate the in-plane stiffness and plastic collapse strength of first- and second-order self-similar hierarchical honeycombs, based on the classical plastic limit analysis (Chen *et al.*, 2007). With the benefits and insights afforded by the analytical machinery, the authors indicated possible ways to achieve optimised hierarchical structures of actual use, in terms of tailored combinations of stiffness and strength. For instance, how to lower the value of the stiffness while increasing the strength, in order to obtain a cellular material that is easily deformed but resistant to rupture.

An extension of the concepts of classical Fracture Mechanics to cracks propagating in a self-similar regime is discussed in Borodich (1999). The analysis focuses on scaling laws defining the transition between the properties belonging to different lengths of

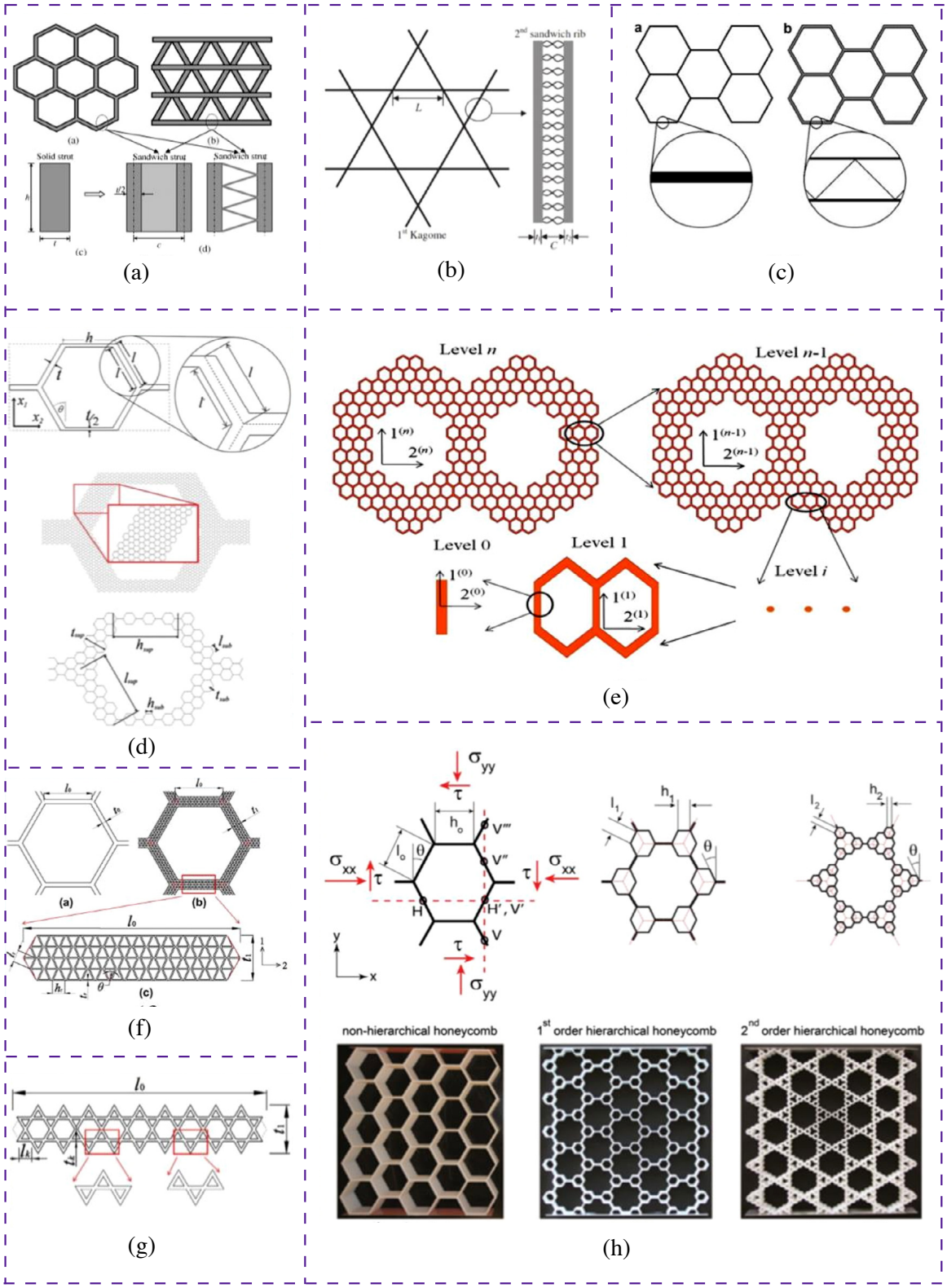

Figure 4.2: Hierarchical cellular materials examined in the literature: (a) Fan et al. (2008), (b) Zhao et al. (2012), (c), (d) Taylor et al. (2012; 2011), (e) Chen and Pugno (2013a; 2012), (f), (g) Sun & Pugno (2013), (h) Ajdari et al. (2012)

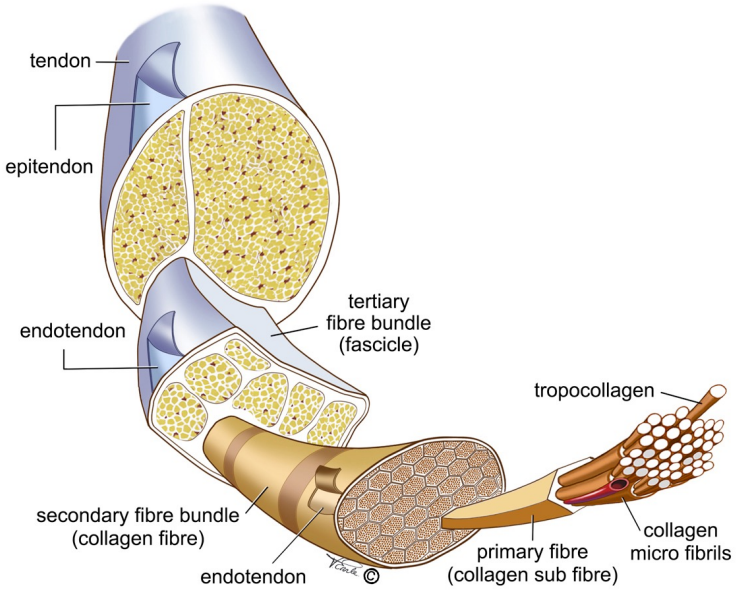

Figure 4.3: The hierarchical structure of tendon, taken from Earle (2013)

scale and it emerges that the fracture energy is an exponential function whose exponent is only related to the considered length of scale.

Finally, an attempt to numerically solve boundary value problems for self-similar domains structured on a large number of scales is reported in Soare & Picu (2007). The suggested finite element procedure employs modified shape functions in order to capture the complexity of the geometry at no additional computational cost.

Considering the abovementioned works, it can be said that, in the context of hierarchical cellular materials, a great variety of analytical and numerical techniques have been proposed and exhaustively discussed. Particular attention is given to avert the aforesaid detrimental effect on the specific stiffness and some possible ideas have been suggested. However, similarly to the not-hierarchical case addressed in Chapter 3, the available investigations are only concerned with hierarchical microstructures having empty cells.

Taking into account the doubtless benefits offered by the composite solutions in nature (cf. Section 3.1), this chapter provides an alternative technique to improve the specific stiffness of traditional honeycombs by structural hierarchy and material mixing. In particular, the study focuses on the potential value of adding hierarchy into two-dimensional composite cellular materials similar to that analysed in Chapter 3.

Two examples are considered: the self-similar hierarchical organisation and the case in which different levels have different cell topologies.

4.2 The hexagonal microstructure: analytical modelling

4.2.1 Basic concepts and assumptions

Let us consider the composite cellular material analysed in Chapter 3 and let us imagine to modify its architecture at successively smaller length scales. The modification, consisting of replacing each cell wall with a structural element having a hexagonal microstructure with filled cells (i.e., the same microstructure of the starting material), creates a novel class of hierarchical cellular materials, that will be referred to as *hierarchical composite cellular material*.

As illustrated in Figure 4.4, the substitution can be iterated to generate ever-finer structural detail while preserving the structure's sixfold symmetry, a sufficient condition for in-plane isotropy in the linear elastic regime (Christensen, 1987). In particular, Figure 4.4 shows a schematic of the geometrical replacements resulting in the level-$[n]$ hierarchical honeycomb, being n, the hierarchical order, defined as the number of levels of scale with recognised structure (Lakes, 1993).

For each level of hierarchy, i, two sets of parameters define the configuration:

$$\gamma^{[i-1]} := \left(\lambda^{[i-1]} := h^{[i-1]}/\ell^{[i-1]},\, K_w^{[i-1]},\, E_{walls}^{[i-1]},\, \nu_{walls}^{[i-1]},\, G_{walls}^{[i-1]}\right),$$

$$\gamma^{[i]} := \left(\lambda^{[i]} := h^{[i]}/\ell^{[i]},\, K_w^{[i]},\, E_{walls}^{[i]},\, \nu_{walls}^{[i]},\, G_{walls}^{[i]}\right),$$

$$i = 1, 2, ..., n. \tag{4.1}$$

The first, $\gamma^{[i-1]}$, describes the geometric, $\lambda^{[i-1]}$, and mechanical, $K_w^{[i-1]}$, $\nu_{walls}^{[i-1]}$, $E_{walls}^{[i-1]}$, $G_{walls}^{[i-1]}$, properties of the cell walls' microstructure (cf. Chapter 3), the level-$[i-1]$, while the second, $\gamma^{[i]}$, those of the underlying large architecture, the level-$[i]$.

By assuming that the size of the cell walls' microstructure is fine enough to be negligible with respect to the level-$[i]$ structure (Lakes, 1993), each cell arm can be treated as a continuum having Young's modulus, $E^{[i-1]}$, Poisson's ratio, $\nu^{[i-1]}$, and shear modulus, $G^{[i-1]}$, such that

$$E_{walls}^{[i]} \equiv E^{[i-1]}, \quad \nu_{walls}^{[i]} \equiv \nu^{[i-1]}, \quad G_{walls}^{[i]} \equiv G^{[i-1]}, \quad i = 1, 2, ..., n. \tag{4.2}$$

Accordingly, the effective elastic constants and stress-strain relations of the level-$[i]$ hierarchical honeycomb can be evaluated by adopting the same approach of Chapter 3. That is to say, by initially representing the composite microstructure as a sequence of Euler-Bernoulli beams on Winkler foundation and calculating the elastic energy of the unit cell, illustrated in Figure 4.4 by bold lines. Specifically, the latter quantity is obtained by summing the energetic contribution of the three elastic beams and those of the two sets of springs (Figure 4.4). Finally, the continuum model follows from the hypothesis that, in the limit, the discrete displacements and rotations of the nodes can be expressed in terms of the corresponding continuous fields (cf. Equation (3.71)).

It should be noted that, in the following, the description is abbreviated, as the present analysis is an extension of that presented in Chapter 3. In particular, for concision, only the effective elastic constants will be considered.

4.2.2 The equivalent continuum

4.2.2.1 Elastic constants

As it can be seen in Figure 4.4, the level-[1] hierarchical honeycomb coincides with the composite material examined in Chapter 3. Consequently, its Young's modulus, $E^{[1]}$, shear modulus, $G^{[1]}$, and Poisson's ratio, $\nu^{[1]}$, in the continuum approximation are given by

$$E^{[1]} = \frac{\left(13\, K_w^{[1]} v^{[0]} + 16\, \lambda^{[1]} E^{[0]}\right)\left(51\left(1+\lambda^{[1]\,2}\right) K_w^{[1]} v^{[0]} + 208 \lambda^{[1]\,3} E^{[0]}\right)}{4\sqrt{3}\, v^{[0]}\left(271\,(1+\lambda^{[1]\,2})\, K_w^{[1]} v^{[0]} + 208\,(\lambda^{[1]} + 3\lambda^{[1]\,3})\, E^{[0]}\right)}, \tag{4.3}$$

$$G^{[1]} = \frac{51\left(1+\lambda^{[1]\,2}\right) K_w^{[1]} v^{[0]} + 208 \lambda^{[1]\,3} E^{[0]}}{208\sqrt{3}\,(1+\lambda^{[1]\,2})\, v^{[0]}}, \tag{4.4}$$

$$\nu^{[1]} = \frac{67\left(1+\lambda^{[1]\,2}\right) K_w^{[1]} v^{[0]} - 208\,\lambda^{[1]}\left(\lambda^{[1]\,2}-1\right) E^{[0]}}{271\,(1+\lambda^{[1]\,2})\, K_w^{[1]} v^{[0]} + 208\,\lambda^{[1]}\,(1+3\lambda^{[1]\,2})\, E^{[0]}}, \tag{4.5}$$

with $K_w^{[1]}$ the Winkler foundation constant, $E^{[0]} \equiv E_s$ and $\nu^{[0]} \equiv \nu_s$, on order, the Young's modulus and Poisson's ratio of the cell walls, the level-[0], $\lambda^{[1]} := h^{[1]}/\ell^{[1]}$ the thinness ratio of the cell walls at level-[1]. In addition, to facilitate reading, $v^{[0]} := 1 - \nu^{[0]\,2}$.

The above relations, due to the assumptions in Equation (4.2), correspond to the cell walls' elastic moduli in the case of two levels of hierarchy, $n = 2$. Also, as stated,

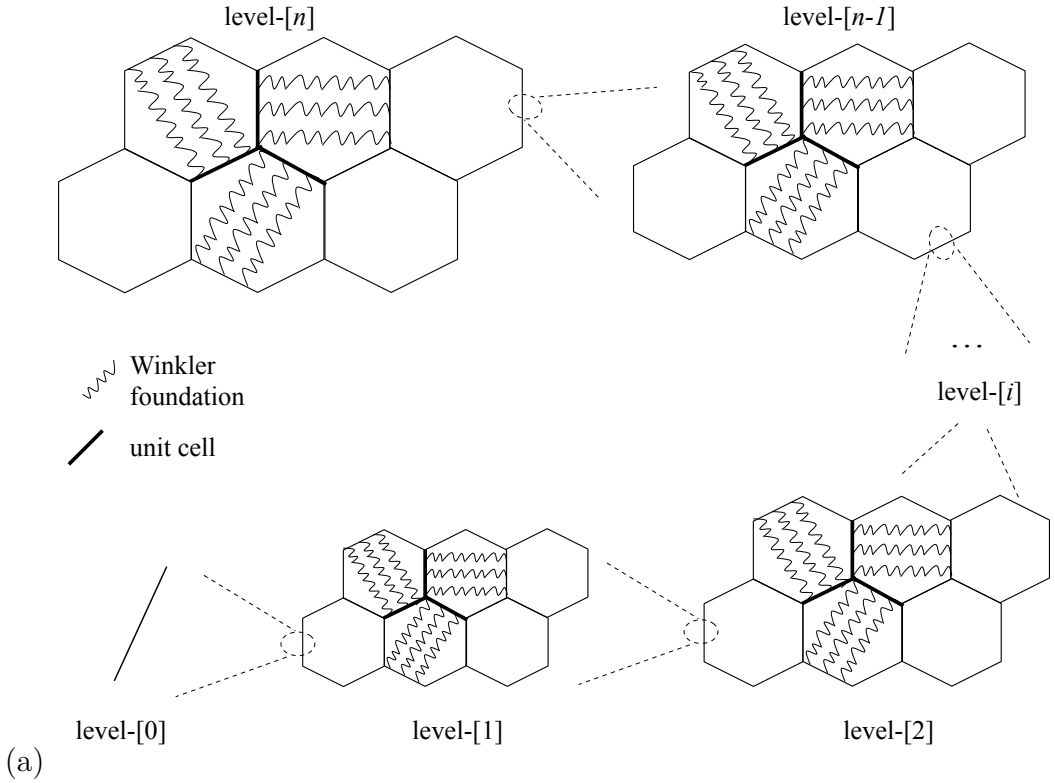

(a)

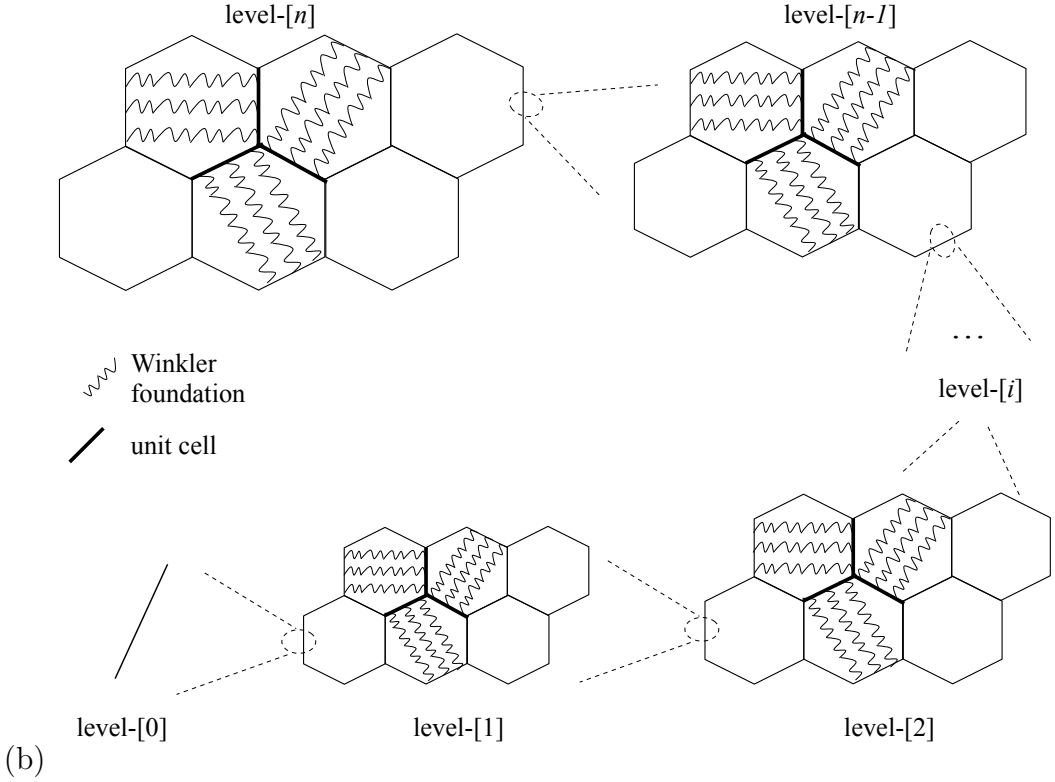

(b)

Figure 4.4: The hierarchical composite cellular material: (a) springs a, (b) springs b

the analysis adopted in Chapter 3 still applies and substituting $E^{[1]}$, $\nu^{[1]}$ for $E^{[0]}$, $\nu^{[0]}$ and $\lambda^{[2]} := h^{[2]}/\ell^{[2]}$, $K_w^{[2]}$ for $\lambda^{[1]}$, $K_w^{[1]}$ into Equations (4.3)-(4.5) provides the effective elastic constants of the level-[2] structure, $E^{[2]}$, $G^{[2]}$, $\nu^{[2]}$.

Analogous considerations lead to the Young's modulus, $E^{[n]}$, shear modulus, $G^{[n]}$, and Poisson's ratio, $\nu^{[n]}$, of the level-$[n]$ hierarchical honeycomb. In particular, replacing $E^{[0]}$, $\nu^{[0]}$ and $\lambda^{[1]}$, $K_w^{[1]}$ by $E^{[n-1]}$, $\nu^{[n-1]}$ and $\lambda^{[n]}$, $K_w^{[n]}$ into Equations (4.3)-(4.5) gives

$$E^{[n]} = \frac{\left(13K_w^{[n]}v^{[n-1]} + 16\lambda^{[n]}E^{[n-1]}\right)\left(51\left(1+\lambda^{[n]\,2}\right)K_w^{[n]}v^{[n-1]} + 208\lambda^{[n]\,3}E^{[n-1]}\right)}{4\sqrt{3}v^{[n-1]}\left(271\left(1+\lambda^{[n]\,2}\right)K_w^{[n]}v^{[n-1]} + 208\left(\lambda^{[n]}+3\lambda^{[n]\,3}\right)E^{[n-1]}\right)}, \tag{4.6}$$

$$G^{[n]} = \frac{51\left(1+\lambda^{[n]\,2}\right)K_w^{[n]}v^{[n-1]} + 208\lambda^{[n]\,3}E^{[n-1]}}{208\sqrt{3}\left(1+\lambda^{[n]\,2}\right)v^{[n-1]}}, \tag{4.7}$$

$$\nu^{[n]} = \frac{67\left(1+\lambda^{[n]\,2}\right)K_w^{[n]}v^{[n-1]} - 208\,\lambda^{[n]}\left(\lambda^{[n]\,2}-1\right)E^{[n-1]}}{271\left(1+\lambda^{[n]\,2}\right)K_w^{[n]}v^{[n-1]} + 208\,\lambda^{[n]}\left(1+3\lambda^{[n]\,2}\right)E^{[n-1]}}, \tag{4.8}$$

being $E^{[n-1]}$, $\nu^{[n-1]}$ and $\lambda^{[n]} := h^{[n]}/\ell^{[n]}$, in turn, the Young's modulus, Poisson's ratio and thinness ratio of the cell arms, $K_w^{[n]}$ the Winkler constant (Figure 4.4). Again, $v^{[n-1]} := 1 - \nu^{[n-1]\,2}$.

4.2.2.2 Density

Let us focus on the level-[1] structure in Figure 4.4.

From the rule of mixtures, the density of this composite configuration, $\rho^{[1]}$, takes the form

$$\rho^{[1]} = f^{[1]}\,\rho_f^{[1]} + \left(1 - f^{[1]}\right)\rho_s, \tag{4.9}$$

with $f^{[1]} := V_f^{[1]}/V_{tot}^{[1]}$ the porosity, $V_f^{[1]}$ and $V_{tot}^{[1]}$, respectively, the volume of the filling material and of the entire cell, ρ_s and $\rho_f^{[1]}$ the density of the cell walls, the first, and of the filler, the second (Figure 4.5).

Simple geometrical considerations provide

$$f^{[1]} = \frac{A_f^{[1]}\,b}{A_{tot}^{[1]}\,b} = \frac{\sqrt{3} - 2\,\lambda^{[1]}}{\sqrt{3}}, \tag{4.10}$$

where $A_{tot}^{[1]}$ and $A_f^{[1]}$ are, on order, the total area of the cell and of the filling material, b the width and $\lambda^{[1]}$ the quantity previously defined. Accordingly, by replacing Equation

(4.10) into Equation (4.9),

$$\rho^{[1]} = \left(\frac{\sqrt{3} - 2\,\lambda^{[1]}}{\sqrt{3}}\,\rho_f^{[1]} + \frac{2\,\lambda^{[1]}}{\sqrt{3}} \right) \rho_s \tag{4.11}$$

or, to simplify the notation,

$$\rho^{[1]} = a^{[1]}\rho_f^{[1]} + b^{[1]}\rho_s, \tag{4.12}$$

with

$$a^{[1]} := \frac{\sqrt{3} - 2\,\lambda^{[1]}}{\sqrt{3}}, \qquad b^{[1]} := \frac{2\,\lambda^{[1]}}{\sqrt{3}}. \tag{4.13}$$

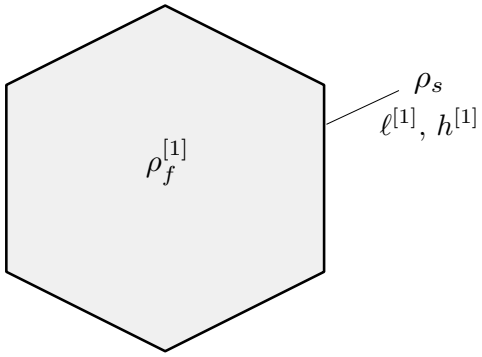

Figure 4.5: Density of the level-[1] *hierarchical structure*

In view of the hypothesis in Section 4.2.1, consisting in approximating each cell arm with an equivalent continuum, $\rho^{[1]}$ can also be treated as the cell walls' density in the case of two levels of hierarchy, $n = 2$. As a consequence,

$$\rho^{[2]} = a^{[2]}\rho_f^{[2]} + b^{[2]}\rho^{[1]} \tag{4.14}$$

gives the density of the level-[2] hierarchical composite, being $\rho_f^{[2]}$ the density of the filler, $a^{[2]}$ and $b^{[2]}$ derived by substituting $\lambda^{[2]} := h^{[2]}/\ell^{[2]}$ for $\lambda^{[1]}$ into Equations (4.13).

Similarly, in the case of n levels of hierarchy, the density is expressed by

$$\rho^{[n]} = a^{[n]}\rho_f^{[n]} + b^{[n]}\rho^{[n-1]}, \tag{4.15}$$

with $\rho_f^{[n]}$ and $\rho^{[n-1]}$, in turn, the density of the filling material and of the cell walls, $a^{[n]}$ and $b^{[n]}$ obtained as before.

4.2.2.3 Stiffness-to-density rato

In practical applications, the stiffness-to-density ratio is an important parameter, often used to optimise the structural design and reduce cost. The utility of the stiffness-to-density ratio, also known as *specific stiffness*, is to find materials with high stiffness at low weight, ideal candidates for the construction of airplane wings, bridges, masts or bicycle frames, among others. Wegst and Ashby (Wegst & Ashby, 2004), for example, analysed the mechanical efficiency of many natural materials and plotted the so-called *Ashby's maps*, a common method for choosing the best material for a given application.

Regarding the hierarchical composite material examined in the present thesis, a closed-form expression for the specific stiffness can be obtained from the relations in Sections 4.2.2.1 and 4.2.2.2. Specifically, for the level-$[n]$ structure, Equations (4.6)-(4.8) and (4.15) lead to

$$\frac{E^{[n]}}{\rho^{[n]}} = \frac{E^{[n]}}{a^{[n]}\rho_f^{[n]} + b^{[n]}\rho^{[n-1]}}, \tag{4.16}$$

$$\frac{G^{[n]}}{\rho^{[n]}} = \frac{G^{[n]}}{a^{[n]}\rho_f^{[n]} + b^{[n]}\rho^{[n-1]}}. \tag{4.17}$$

4.2.2.4 Parametric analysis

According to the above formulation, this section aims at understanding how the microstructure's parameters affect the macroscopic elastic moduli in the case of structural hierarchy.

The analysis involves a three-level hierarchical honeycomb having a hexagonal microstructure with filled cells at all levels.

The starting element of the hierarchical structure, the level-[0] in Figure 4.4, has Young's modulus E_s, Poisson's ratio ν_s and thinness ratio λ. For simplicity, it is assumed that the self-similar condition (Chen & Pugno, 2012)

$$\lambda^{[i]} \equiv \lambda, \qquad i = 1, 2, 3, \tag{4.18}$$

holds true.

Similarly, the hypothesis that the density of the filling material, $\rho_f^{[i]}$, is the same at all levels, provides

$$\rho_f^{[i]} \equiv \rho_f = \alpha\, \rho_s, \qquad i = 1, 2, 3, \tag{4.19}$$

with α a positive constant depending on the material inside the cells. If the filler is a standard hexagonal honeycomb, as commonly happens in nature (Gibson & Ashby,

2001), the classical relations (Gibson & Ashby, 2001)

$$\frac{\rho_f^{[i]}}{\rho_{s,f}} = \frac{2}{\sqrt{3}}\,\lambda_f^{[i]}, \qquad \frac{E_f^{[i]}}{E_{s,f}} = \frac{4}{\sqrt{3}}\,\lambda_f^{[i]\,3}, \qquad i = 1,2,3 \tag{4.20}$$

provide its (effective) Young's modulus, $E_f^{[i]}$, and density, $\rho_f^{[i]}$, as a function of the cell walls' properties, i.e., the thinness ratio, $\lambda_f^{[i]}$, the density, $\rho_{s,f}$, and the Young's modulus, $E_{s,f}$.

By taking into account the result of the energetic equivalence in Section 3.3.1 (cf. Equation (3.24)),

$$K_w^{[i]} = \frac{8}{5\sqrt{3}}\,E_f^{[i]}, \qquad i = 1,2,3, \tag{4.21}$$

together with the assumption

$$\rho_{s,f} \equiv \rho_s, \qquad E_{s,f} \equiv E_s, \tag{4.22}$$

simple mathematical manipulations give

$$K_w^{[i]} = \frac{4\sqrt{3}}{5}\,E_s \left(\frac{\rho_f^{[i]}}{\rho_s}\right)^3, \qquad i = 1,2,3, \tag{4.23}$$

a suitable relation between the Winkler constant, $K_w^{[i]}$, and the filler's density. Finally, in view of Equation (4.19),

$$K_w^{[i]} \equiv K_w = \frac{4\sqrt{3}}{5}\,\alpha^3\,E_s, \qquad i = 1,2,3, \tag{4.24}$$

equation on which the present study is based.

In particular, four values of α are considered: 0.4, 0.2, 0.1, 0.05, leading to $K_w = (10^{-1}E_s, 10^{-2}E_s, 10^{-3}E_s, 10^{-4}E_s)$, respectively. It is also assumed $E_s = 79$ GPa, $\nu_s = 0.35$, $\rho_s = 2900$ kg/m^3 (aluminum alloy) (Gibson *et al.*, 2010).

The outcome of the analysis is summarised in Figure 4.6, where the specific stiffness, $E^{[3]}/\rho^{[3]}$ and $G^{[3]}/\rho^{[3]}$, and Poisson's ratio, $\nu^{[3]}$, are plotted versus the parameter λ.

In terms of the stiffness-to-density ratio, Figures 4.6a and 4.6b suggest that, for fixed K_w, an increase in λ provides an increase in $E^{[3]}/\rho^{[3]}$ and $G^{[3]}/\rho^{[3]}$, which is more significant for $\lambda < 0.1$. As a matter of fact, for $\lambda > 0.1$ the increase in $E^{[3]}/\rho^{[3]}$ is averagely of 1%, while for $\lambda < 0.1$ the average increase is more than 15% (Figure 4.6a). A similar trend emerges in the case of $G^{[3]}/\rho^{[3]}$: an increase of only 10% for $\lambda > 0.1$, larger one (20%) when $\lambda < 0.1$ (Figure 4.6b).

In addition, when λ is fixed, Figures 4.6a and 4.6b illustrate an improvement in the specific stiffness by increasing K_w. In particular, as expected, for high values of K_w ($10^{-1}\,E_s$, $10^{-2}\,E_s$) the increase in both $E^{[3]}/\rho^{[3]}$ and $G^{[3]}/\rho^{[3]}$ is higher than that occurring for small ones ($10^{-3}\,E_s$, $10^{-4}\,E_s$). That is to say, the higher the stiffness of the material filling the cells, the higher will be the resulting hierarchical composite. For example, $E^{[3]}/\rho^{[3]}$ shows an average increase of more than 180% when the parameter K_w varies from $10^{-2}\,E_s$ to $10^{-1}\,E_s$.

To summarise, it can be said that the presented graphs illustrate the large range of achievable specific stiffness permitted by varying the geometrical, λ, and mechanical, K_w, parameters of the microstructure.

A similar consideration can be derived by focusing on the Poisson's ratio, $\nu^{[3]}$, plotted in Figure 4.6c. Generally, for fixed K_w, increasing λ provides a decrease in $\nu^{[3]}$, that is more evident for high values of λ. For instance, when $K_w = 10^{-4}\,E_s$, varying λ from 0.05 to 0.1 leads to a decrease of average 60% while, for $0.1 < \lambda < 0.2$, the decrease is averagely of 130%.

Regarding the influence of the Winkler constant, it emerges that, for small values of λ ($\lambda < 0.05$), $\nu^{[3]}$ is not affected by K_w, being $\nu^{[3]} = 0.3332$ regardless of K_w. Conversely, when the beams become more and more thicker ($0.05 < \lambda < 0.2$), even a small increase of K_w leads to a high increase in $\nu^{[3]}$. Indeed, as Figure 4.6c illustrates, varying K_w from $10^{-3}\,E_s$ to $10^{-2}\,E_s$ provides an increase of 35% at $\lambda = 0.15$ and of 90% at $\lambda = 0.2$. This finding, that could be of actual use, reveals the possibility to obtain optimised hierarchical structures having desirable and, perhaps, actively tailorable properties. In particular, for particular values of λ ($\lambda < 0.05$), it is possible to improve the specific stiffness of the material, by varying K_w, but without modifying its Poisson's ratio.

4.2.3 Filled vs not-filled cells

To throughly analyse the influence of the microstructure's properties in the specific stiffness of a hierarchical cellular material, this section deals with a self-similar hierarchical honeycomb having three levels of hierarchy and a hexagonal architecture at all levels.

Similarly to Section 4.2.2.4, the cell walls are made of aluminium alloy with $E_s = 79$ GPa, $\nu_s = 0.35$, $\rho_s = 2900$ kg/m^3 (Gibson *et al.*, 2010). The cells, initially empty as in the traditional hierarchical honeycomb (Chen & Pugno, 2012), are then alternately filled with an elastic medium at some levels while leaving empty the others.

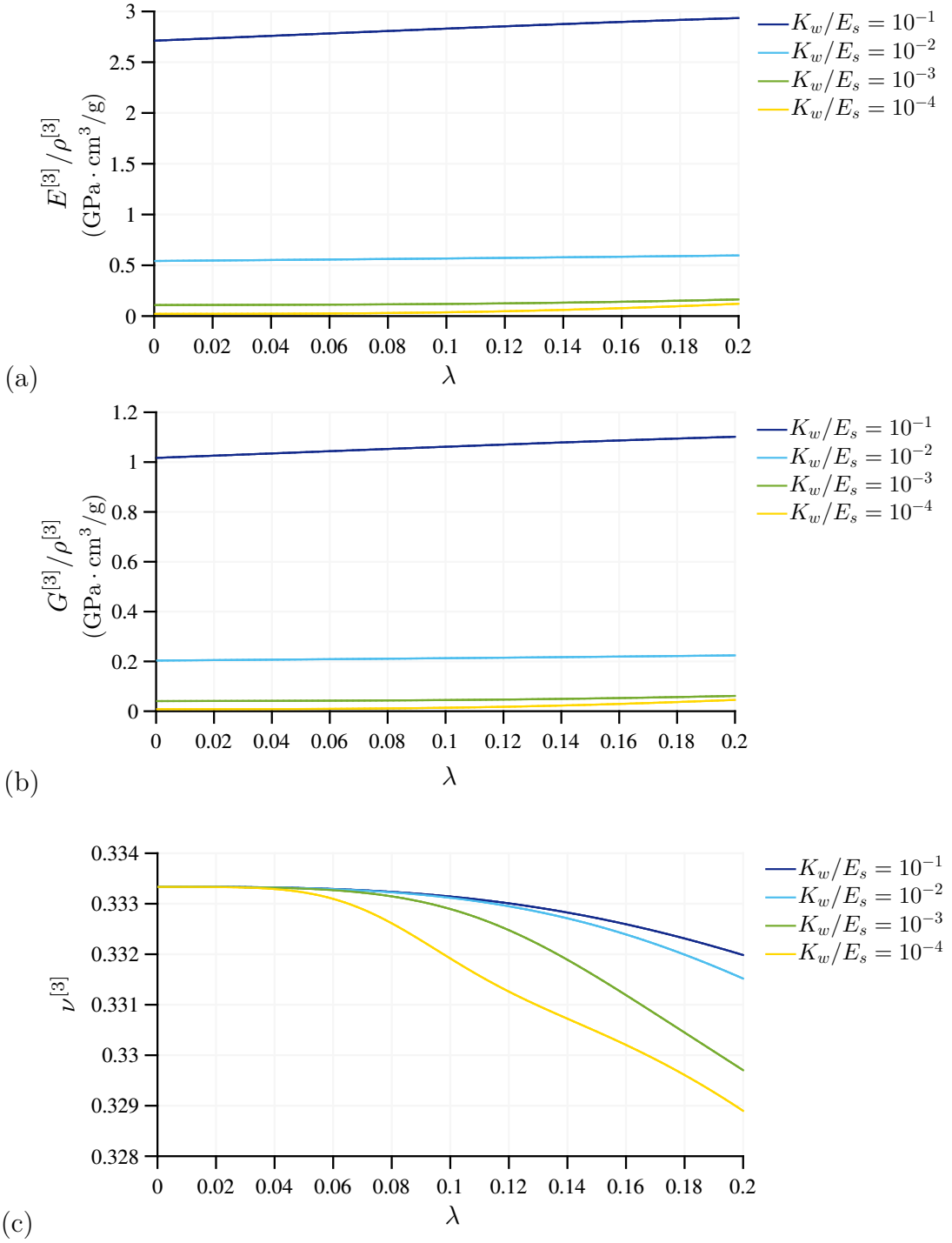

Figure 4.6: The influence of λ in the (a), (b) specific stiffness and (c) Poisson's ratio of a three-level hierarchical composite cellular material

Table 4.1 Hierarchical configurations considered

	level-[1]	level-[2]	level-[3]
configuration k=1	not-filled cells	not-filled cells	not-filled cells
configuration k=2	filled cells	not-filled cells	not-filled cells
configuration k=3	filled cells	filled cells	not-filled cells
configuration k=4	filled cells	not-filled cells	filled cells
configuration k=5	not-filled cells	filled cells	not-filled cells
configuration k=6	not-filled cells	filled cells	filled cells
configuration k=7	not-filled cells	not-filled cells	filled cells
configuration k=8	filled cells	filled cells	filled cells

The investigated configurations, listed in Table 4.1, reveal that the stiffness-to-density ratio of a hierarchical composite honeycomb is affected not only by the parameters λ, E_s, ν_s, K_w, but also by having filled cells at one level rather than at another.

For example, let us consider the configurations $k = 2$, $k = 5$ and $k = 7$, with filled cells at only one level: the first, the second and the third, respectively (Table 4.1). It emerges that the resulting specific stiffness, $\left(E^{[3]}/\rho^{[3]}\right)_k$ and $\left(G^{[3]}/\rho^{[3]}\right)_k$, normalised by the specific stiffness of the standard hierarchical honeycomb (i.e., configuration $k = 1$), $\left(E^{[3]}/\rho^{[3]}\right)_{k=1}$ and $\left(G^{[3]}/\rho^{[3]}\right)_{k=1}$, have different values in the three examined cases (Table 4.2). In particular, the presence of the filler at small levels, as in configurations $k = 2$ and $k = 5$, makes the corresponding hierarchical structure 70% and 65% less stiff than the structure in configuration $k = 7$, where the elastic medium fills the cells at higher levels. As pointed out in Gao (2010), it can be said that, in terms of macroscopic mechanical behavior, the smaller the level, the less important is the presence of the filling material. This result is confirmed by focusing on configurations $k = 3$, $k = 4$ and $k = 6$, having filled cells at two levels: the first and the second, the first and the third, the second and the third, in turn (Table 4.1). As expected, the maximum and the minimum value of normalised specific stiffness occurs, on order, in the case of configurations $k = 6$ and $k = 3$. Again, the effective properties of the hierarchical composite honeycomb are less affected by having filled cells at small levels, i.e., configuration $k = 3$, rather than at larger ones, i.e., configurations $k = 4$ and $k = 6$.

Moreover, Table 4.3 suggests that the specific stiffness of a traditional hierarchical honeycomb can be significantly improved by filling its cells at all levels (i.e., configu-

Table 4.2 Filled vs not-filled: normalised specific stiffness with $K_w = 10^{-2}\, E_s$

$\left(E^{[3]}/\rho^{[3]}\right)_k / \left(E^{[3]}/\rho^{[3]}\right)_{k=1}$				
	$\lambda = 0.2$	$\lambda = 0.1$	$\lambda = 0.05$	$\lambda = 0.02$
configuration k=2	1.21	1.20	1.18	1.18
configuration k=3	1.28	1.24	1.20	1.20
configuration k=4	1.92	1.86	1.86	1.85
configuration k=5	1.26	1.24	1.21	1.21
configuration k=6	2.70	2.70	2.50	2.50
configuration k=7	1.92	1.87	1.87	1.86
configuration k=8	3.30	3.30	3.20	3.20
$\left(G^{[3]}/\rho^{[3]}\right)_k / \left(G^{[3]}/\rho^{[3]}\right)_{k=1}$				
	$\lambda = 0.2$	$\lambda = 0.1$	$\lambda = 0.05$	$\lambda = 0.02$
configuration k=2	1.25	1.23	1.20	1.20
configuration k=3	1.31	1.28	1.23	1.22
configuration k=4	2.10	2.00	1.92	1.90
configuration k=5	1.29	1.27	1.24	1.24
configuration k=6	3.10	3.00	2.90	2.90
configuration k=7	2.20	2.10	1.94	1.92
configuration k=8	3.80	3.60	3.60	3.40

Table 4.3 The level-[3] *hierarchical cellular material: comparison between the composite configuration and the traditional one*

$(E^{[3]}/\rho^{[3]})_{k=8}/(E^{[3]}/\rho^{[3]})_{k=1}$				
	$\lambda = 0.2$	$\lambda = 0.1$	$\lambda = 0.05$	$\lambda = 0.02$
$K_w = 10^{-4}\,E_s$	1.35	1.12	1.10	1.16
$K_w = 10^{-3}\,E_s$	1.83	1.65	1.62	1.53
$K_w = 10^{-2}\,E_s$	3.30	3.30	3.20	3.20
$K_w = 10^{-1}\,E_s$	4.71	4.32	4.31	4.11
$(G^{[3]}/\rho^{[3]})_{k=8}/(G^{[3]}/\rho^{[3]})_{k=1}$				
	$\lambda = 0.2$	$\lambda = 0.1$	$\lambda = 0.05$	$\lambda = 0.02$
$K_w = 10^{-4}\,E_s$	1.43	1.14	1.13	1.17
$K_w = 10^{-3}\,E_s$	1.82	1.81	1.74	1.60
$K_w = 10^{-2}\,E_s$	3.80	3.60	3.60	3.40
$K_w = 10^{-1}\,E_s$	5.41	5.33	5.11	5.02

ration $k = 8$). Specifically, an improvement up to 5 times is observed by varying the filler's stiffness, K_w, from $10^{-4}\,E_s$ to $10^{-1}\,E_s$ (Table 4.3).

4.2.4 Optimal values

Motivated by the increasing trend in the maximum values of specific stiffness observed for the level-[3] composite hierarchical honeycomb in comparison with the traditional counterpart, one question that arises is whether introducing additional levels of hierarchy leads to a further improvement.

As illustrated in Figures 4.7 and 4.8, where the analysis is extended up to the level-[6] hierarchical order, the answer is affirmative, provided that the filler is stiffer than a critical value. In particular, only for $K_w = 10^{-1}\,E_s$ adding the fourth order of hierarchy provides an enhancement in the specific stiffness of a three-level hierarchical honeycomb. Conversely, introducing the fifth and the sixth level does not result in a significant improvement (Figure 4.8).

However, the significance of the present investigation is more evident when examining the effects of adding hierarchical levels to the level-[1] composite honeycomb. That is to say, in contrast to the classical cellular materials where hierarchy is detrimental for the specific stiffness (Chen & Pugno, 2013a; 2012), in the cell-filled configuration increasing the number of hierarchical levels leads to an increase in the stiffness-to-

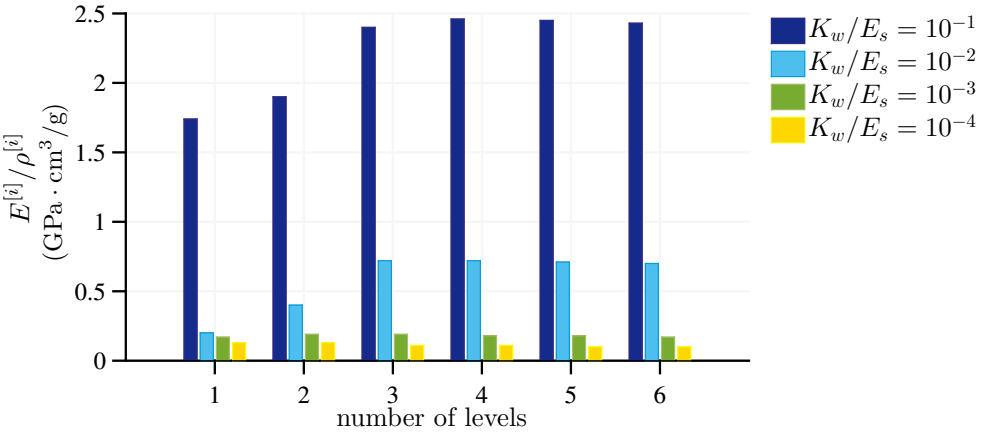

Figure 4.7: Stiffness-to-density ratio vs levels of hierarchy, with $\lambda = 0.1$

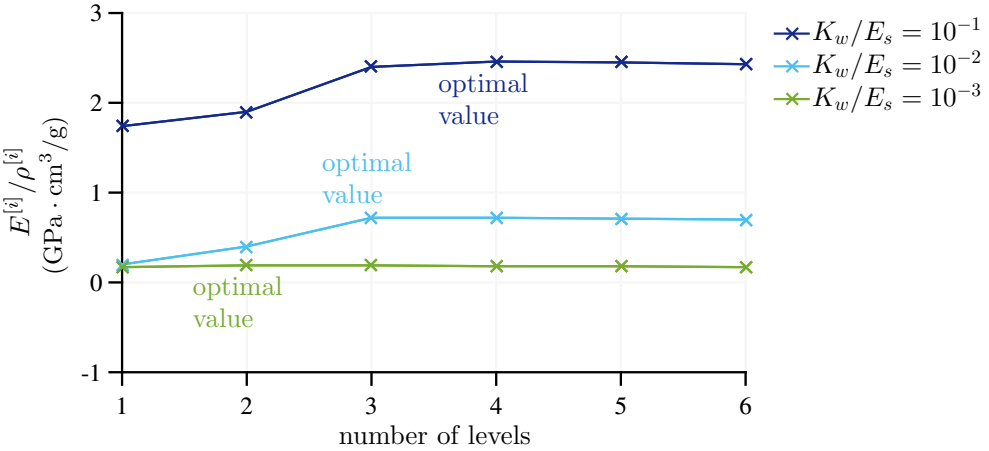

Figure 4.8: Stiffness-to-density ratio vs levels of hierarchy, optimal values in the case of $\lambda = 0.1$

density ratio (Figure 4.7). Nevertheless, high values of K_w, $10^{-1}\,E_s$ and $10^{-2}\,E_s$, provide an higher improvement than that which occurs for $K_w = 10^{-3}\,E_s$. Conversely, when $K_w = 10^{-4}\,E_s$, the specific stiffness decreases by increasing the hierarchical levels, as in the traditional honeycomb.

Thus, in accordance with Bosia *et al.* (2012), it can be concluded that both hierarchy and material heterogeneity are necessary to obtain improved stiffness. In addition, an optimal number of hierarchical levels naturally emerges: level-[4] for $K_w = 10^{-1}\,E_s$, level-[3] for $K_w = 10^{-2}\,E_s$, level-[2] for $K_w = 10^{-3}\,E_s$ (Figure 4.8).

It should be noted that Figures 4.7 and 4.8 are based on an aluminium honeycomb ($E_s = 79$ GPa, $\nu_s = 0.35$, $\rho_s = 2900$ kg/m^3) with $\lambda = 0.1$, assumption that does not affect the outcome of the analysis, being minimum the effect of λ on the stiffness-to-density ratio (cf. Figure 4.6a). Also, as in Sections 4.2.2.4 and 4.2.3, the self-similar conditions in Equations (4.18), (4.19) and (4.24) are adopted.

However, beyond the specific improvements afforded by the particular hierarchical structure examined, this comprehensive study may suggest new avenues for the understanding and development of novel bioinspired materials via structural hierarchy and material mixing.

4.3 Different levels with different cell topologies

As noted in the previous sections, the effective elastic constants of a hierarchical composite honeycomb are generally affected by the geometric and mechanical properties of the microstructure at each level. It also emerged that, in terms of specific stiffness, having filled cells at one level rather than at another plays an important role.

To go further in this direction and to examine more closely how the microstructure's parameters can be optimised to improve the macroscopic performance of the material, this section deals with a three-level hierarchical structure having different cell topologies at each level: the hexagonal, the square and the equilateral triangular.

Similarly to Sections 4.2.2.4-4.2.4, in the considered architectures, listed in Table 4.4 and schematised in Figure 4.9, the cell walls have Young's modulus E_s=79 GPa, Poisson's ratio ν_s=0.35, density $\rho_s = 2900$ kg/m^3 (aluminium alloy) and the self-similar conditions still apply.

The outcome of the study reveals that the examined configurations are not isotropic, being the derived macroscopic moduli, Young's modulus, $E_k^{[3]}$, shear modulus, $G_k^{[3]}$,

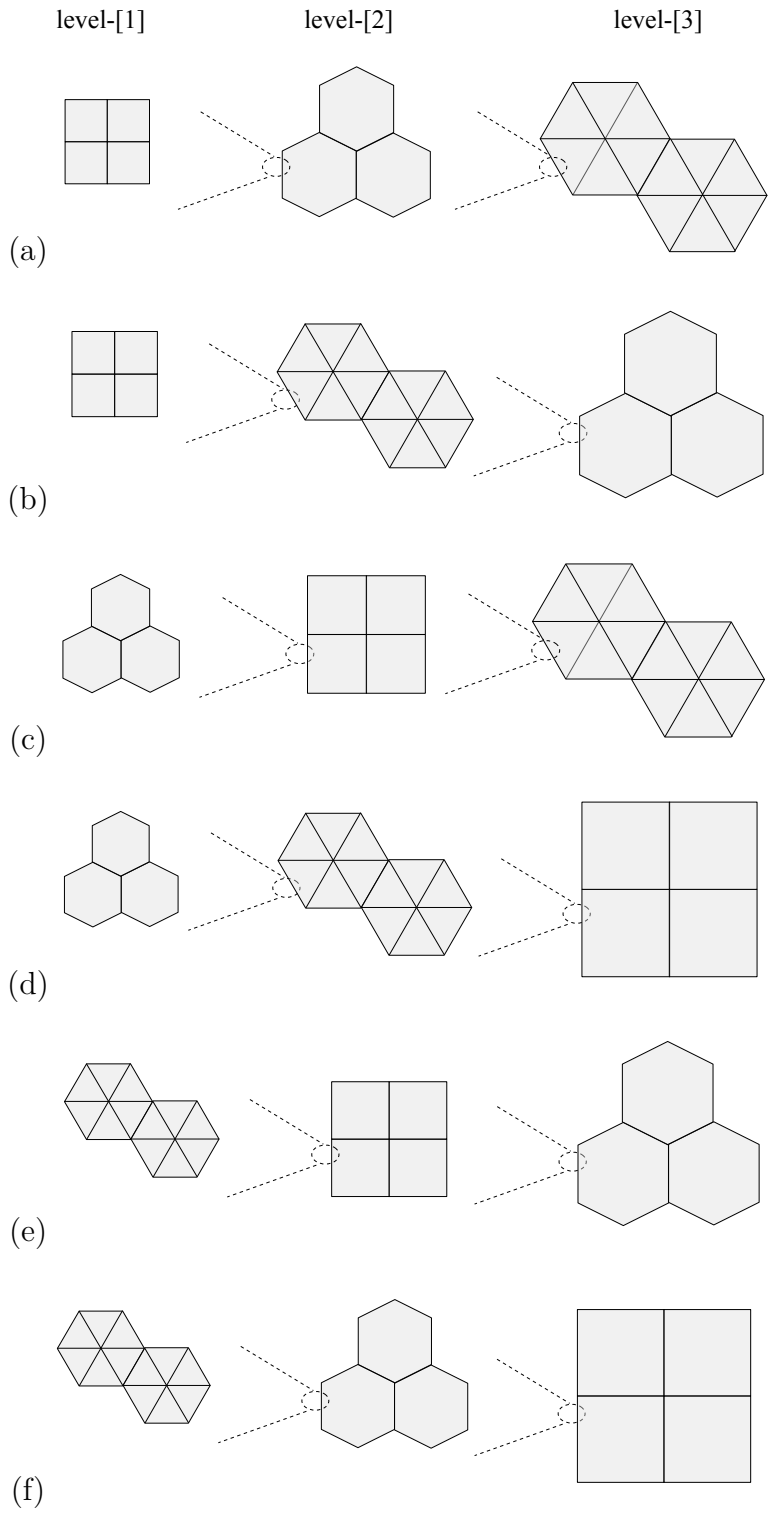

Figure 4.9: Different levels with different cell topologies, schematic representation of the considered configurations: (a) $k = 9$, (b) $k = 10$, (c) $k = 11$, (d) $k = 12$, (e) $k = 13$, (f) $k = 14$

Table 4.4 Hierarchical configurations with different cell topologies

	level-[1]	level-[2]	level-[3]
configuration k=9	square	hexagonal	triangular
configuration k=10	square	triangular	hexagonal
configuration k=11	hexagonal	square	triangular
configuration k=12	hexagonal	triangular	square
configuration k=13	triangular	square	hexagonal
configuration k=14	triangular	hexagonal	square

and Poisson's ratio, $\nu_k^{[3]}$, directionally dependent and such that the classical relation

$$G_k^{[3]} = \frac{E_k^{[3]}}{2\left(1+\nu_k^{[3]}\right)}, \tag{4.25}$$

is not satisfied.

Thus, to provide a more complete description, the mechanical response associated with different orientations is investigated: 0°, 30°, 45°, 60°, measured counterclockwise from $\boldsymbol{e}_1, \boldsymbol{e}_2$ (Figure 4.10). The corresponding elastic constants, plotted in Figures 4.11-4.14 as a function of K_w, are denoted by $(\cdot)_{0^\circ}^{[3]}$, $(\cdot)_{30^\circ}^{[3]}$, $(\cdot)_{45^\circ}^{[3]}$ and $(\cdot)_{60^\circ}^{[3]}$, respectively.

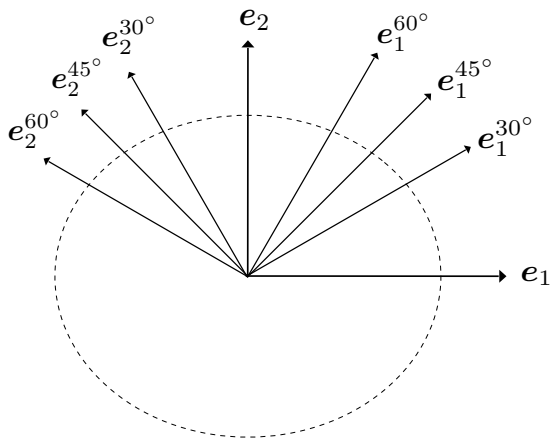

Figure 4.10: Mechanical response associated with different orientations

A common feature in the proposed graphs is the increase in the specific stiffness provided by increasing K_w but, as expected, different results come from the six considered cases.

For example, it emerges that having a hexagonal, configurations $k = 10$ and $k = 13$, or a square, configurations $k = 12$ and $k = 14$, microstructure at the third level leads to the highest values of $(E^{[3]}_{0^\circ}/\rho^{[3]})_k$ (Figure 4.11a) while, in terms of $(G^{[3]}_{0^\circ}/\rho^{[3]})_k$, configurations $k = 12$ and $k = 14$ are the least performant (Figure 4.11b). Conversely, configurations $k = 10$ and $k = 13$ could be the best solution to obtain a hierarchical material with superior shear modulus, $(G^{[3]}_{0^\circ})_k$, and minimum weight. Also, Figure 4.11b reveals the existence of a particular value of K_w, $K^*_w = 0.76 \times 10^{-3}\, E_s$, such that

$$\left(\frac{G^{[3]}_{0^\circ}}{\rho^{[3]}}\right)_{k=9,11} > \left(\frac{G^{[3]}_{0^\circ}}{\rho^{[3]}}\right)_{k=10,13} \quad \text{for } K_w < K^*_w, \tag{4.26}$$

$$\left(\frac{G^{[3]}_{0^\circ}}{\rho^{[3]}}\right)_{k=9,11} < \left(\frac{G^{[3]}_{0^\circ}}{\rho^{[3]}}\right)_{k=10,13} \quad \text{for } K_w > K^*_w. \tag{4.27}$$

That is to say, small values of K_w, $K_w < K^*_w$, make the hierarchical organisations $k = 9$ and $k = 11$ stiffer than those in configurations $k = 10$ and $k = 13$. An opposite trend emerges for $K_w > K^*_w$.

As illustrated in Figures 4.12-4.14, the specific stiffness associated with the axis rotated by 30°, 45° and 60° exhibits very low values if compared to the plots in Figure 4.11. The reason is that, due to the alignment of the cell walls in the loading direction, the stiffness of the square microstructure is higher in the $\boldsymbol{e}_1$ and $\boldsymbol{e}_2$ orientations, rather than in the other ones, where the values are very low. However, neglecting this quantitative aspect, the previous considerations still apply. Namely, in terms of $(E^{[3]}_{30^\circ}/\rho^{[3]})_k$ and $(G^{[3]}_{30^\circ}/\rho^{[3]})_k$, configurations $k = 10$, $k = 13$ and $k = 12$, $k = 14$ have, on order, the highest and the lowest values (Figure 4.12). Conversely, regarding Figures 4.13 and 4.14, the hierarchical architectures with a triangular microstructure at the third level, i.e., configurations $k = 9$ and $k = 11$, are less stiff than those having a hexagonal architecture as cases $k = 10$ and $k = 13$.

Finally, Figures 4.11c, 4.12c, 4.13c and 4.14c suggest that the effect of K_w on the effective Poisson's ratio is generally minimal, with the exception of configurations $k = 9$ and $k = 11$, where an increase in K_w provides a decrease in $(\nu^{[3]}_{(\cdot)})_k$. As before, different values can be observed by considering different directions. In addition, it should be noted that configurations $k = 12$ and $k = 14$ are not plotted in Figures 4.11c, 4.13c and 4.14c as their Poisson's ratio vanish (see Appendix B).

These findings, unique in exploring a new class of complex hierarchical materials with tailored parameters at each level, in the practical context could assist the designer in the selection of the cell topology that best suits a given requirement.

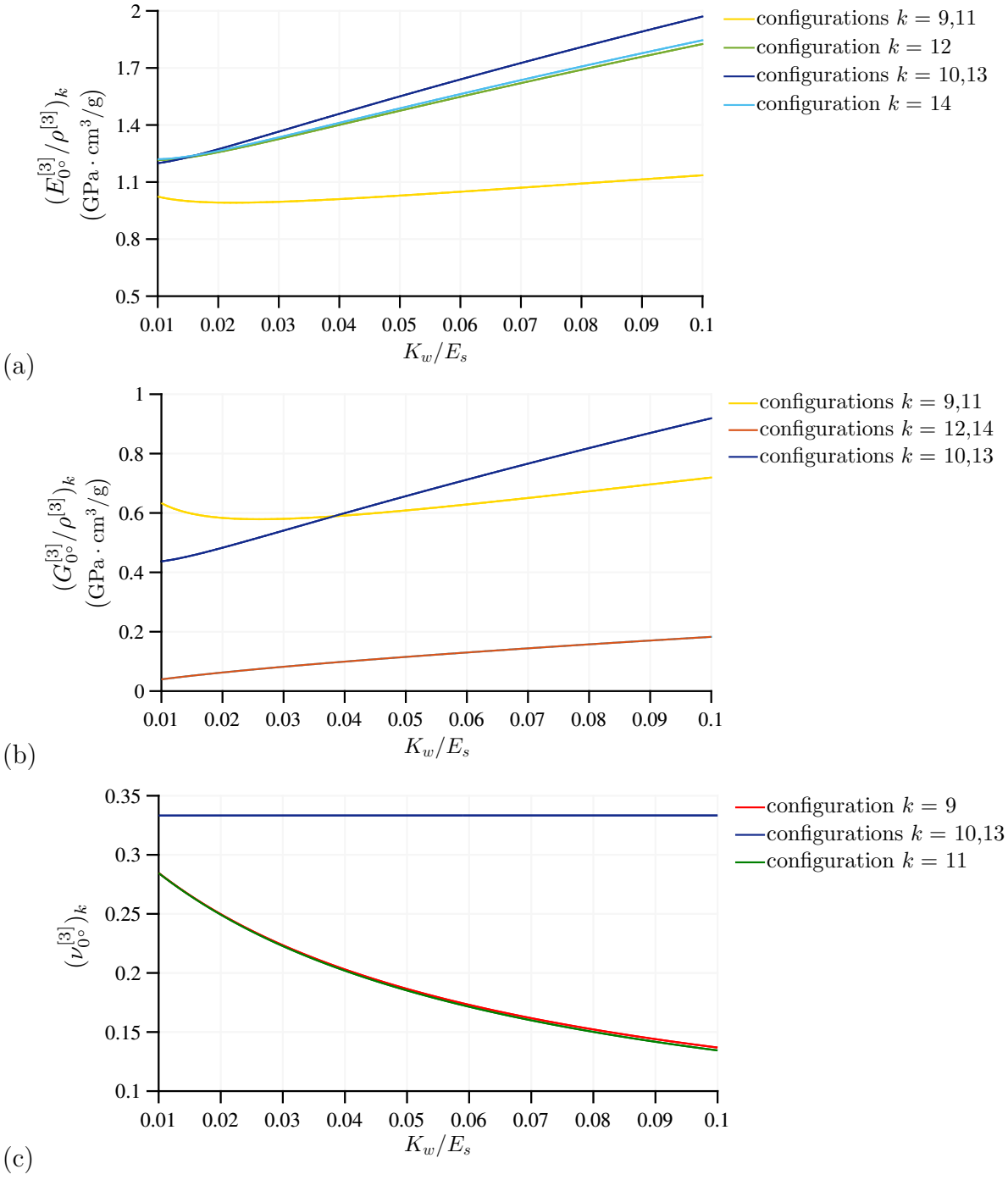

Figure 4.11: The hierarchical honeycomb with different cell topologies: influence of K_w in the (a), (b) specific stiffness and (c) Poisson's ratio associated with the axis $(\boldsymbol{e}_1, \boldsymbol{e}_2)$ in the case of λ=0.02

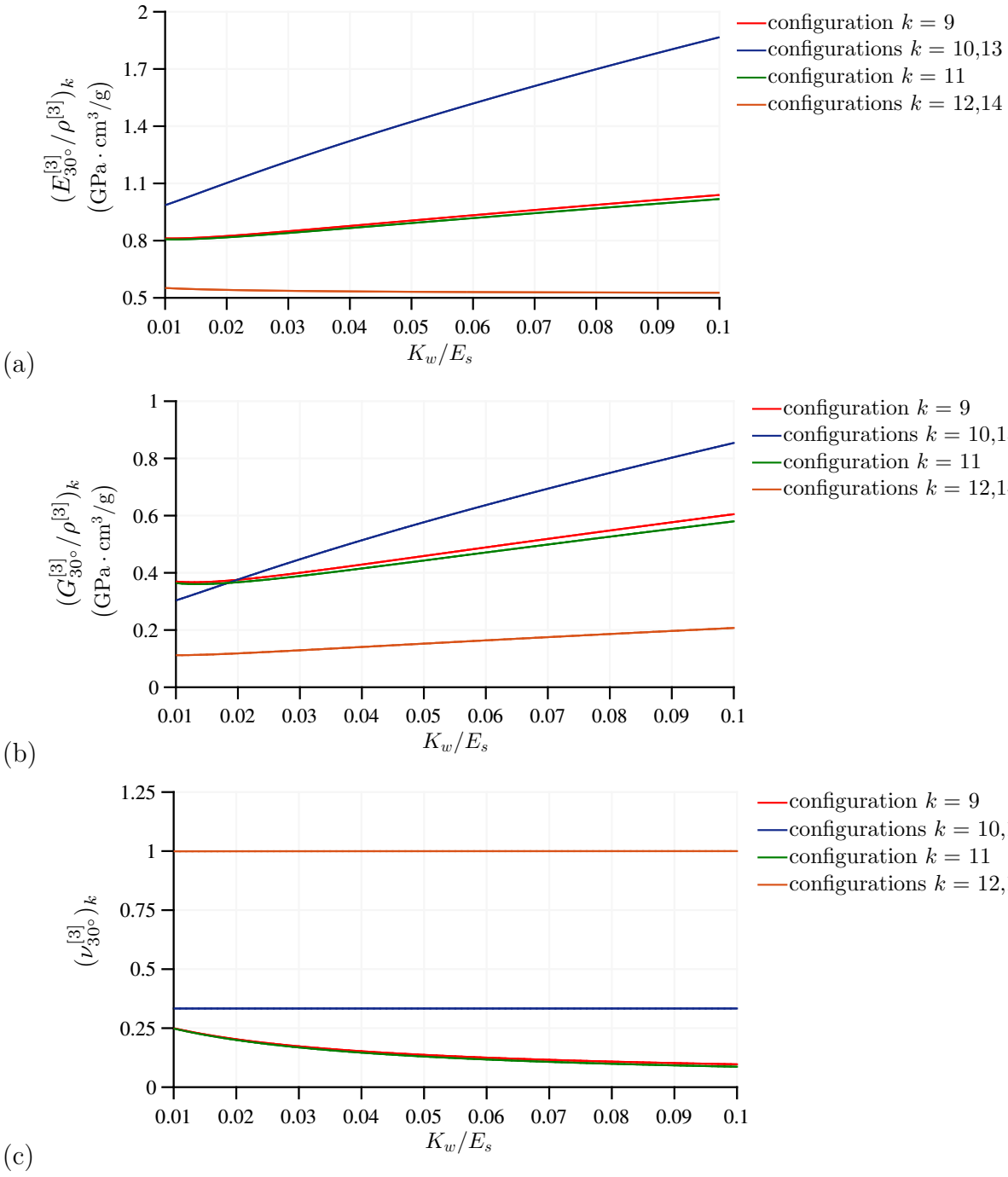

Figure 4.12: The hierarchical honeycomb with different cell topologies: influence of K_w in the (a), (b) specific stiffness and (c) Poisson's ratio associated with the axis rotated counterclockwise by 30° from $(\boldsymbol{e}_1, \boldsymbol{e}_2)$ in the case of λ=0.02

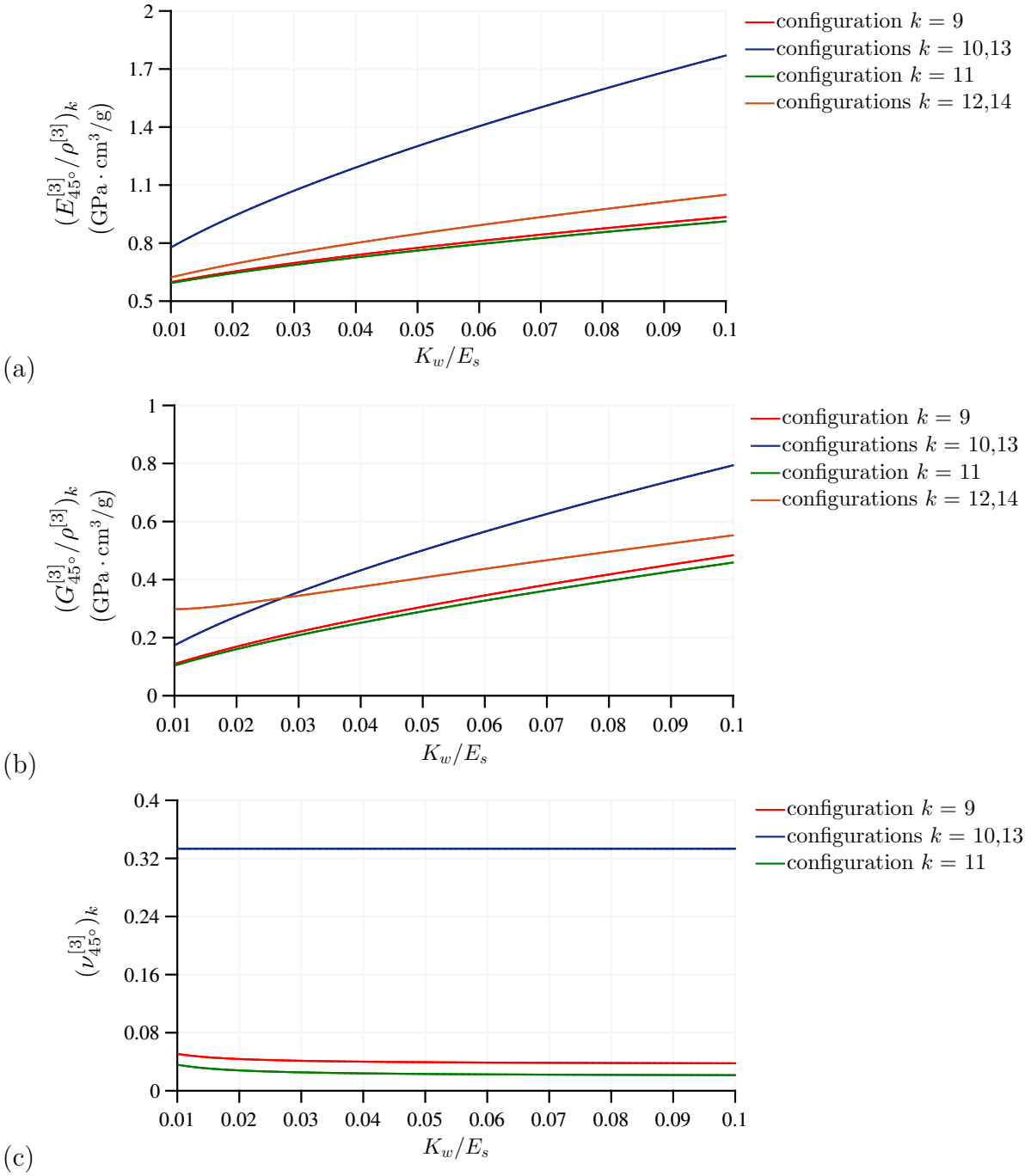

Figure 4.13: The hierarchical honeycomb with different cell topologies: influence of K_w in the (a), (b) specific stiffness and (c) Poisson's ratio associated with the axis rotated counterclockwise by 45° from $(\boldsymbol{e}_1, \boldsymbol{e}_2)$ in the case of λ=0.02

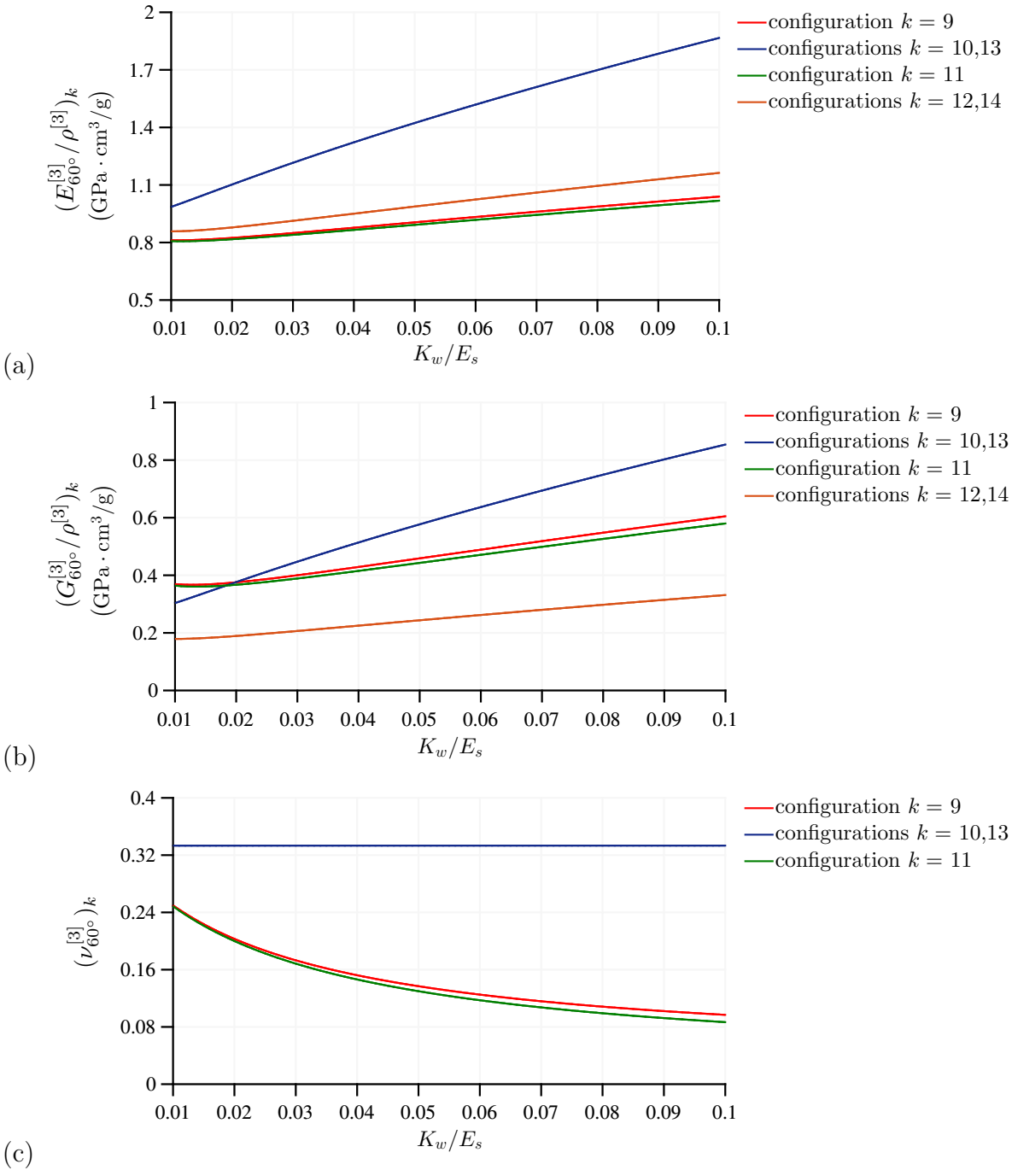

Figure 4.14: The hierarchical honeycomb with different cell topologies: influence of K_w in the (a), (b) specific stiffness and (c) Poisson's ratio associated with the axis rotated counterclockwise by 60° from $(\boldsymbol{e}_1, \boldsymbol{e}_2)$ in the case of λ=0.02

5 | Mutable cellular materials: theoretical model and homogenization of the discrete system

5.1 Introduction

As pointed out in Chapter 3, cellular structures having the internal volumes of the cells filled with fluids, fibers or other bulk materials are very common in nature. This composite solution has been credited with playing an important role in the mechanical efficiency of biological systems.

In the previously examined parenchyma tissue, for instance, the pressure exerted by the fluid within the cells against the cell walls leads to an improvement in the load-bearing capacity of the tissue.

Another example, concerning the nature's wonders of design, is the hygroscopic keel tissue of the ice plant *Delosperma nakurense* (Figure 5.1).

The ice plant grows in the arid regions of Africa and, to prevent the premature dispersion of the seeds, adapted its anatomy and material architecture to the unfavourable environmental conditions. As Figure 5.1a shows, the plant produced a special seed capsule where, in the dry state, five petal-like sections, the protective valves, cover the seed compartment as a box-like lid. When it rains, the valves, unfolding backwards, reveal a seed compartment partitioned in five seed chambers from which, within few minutes, most of the seeds are splashed out by the falling water (Lockyer, 1932). Then, when the capsule dries up, the valves return to the original position.

The specialised organ promoting this sophisticated origami-like movement mechanism for seed dispersal is the hygroscopic keel tissue composed, in the dry state, by a network of elongated cells filled with a swelling cellulosic inner (CIL). Due to the high adsorption and desorption capability of the CIL, the influx/efflux of water into the

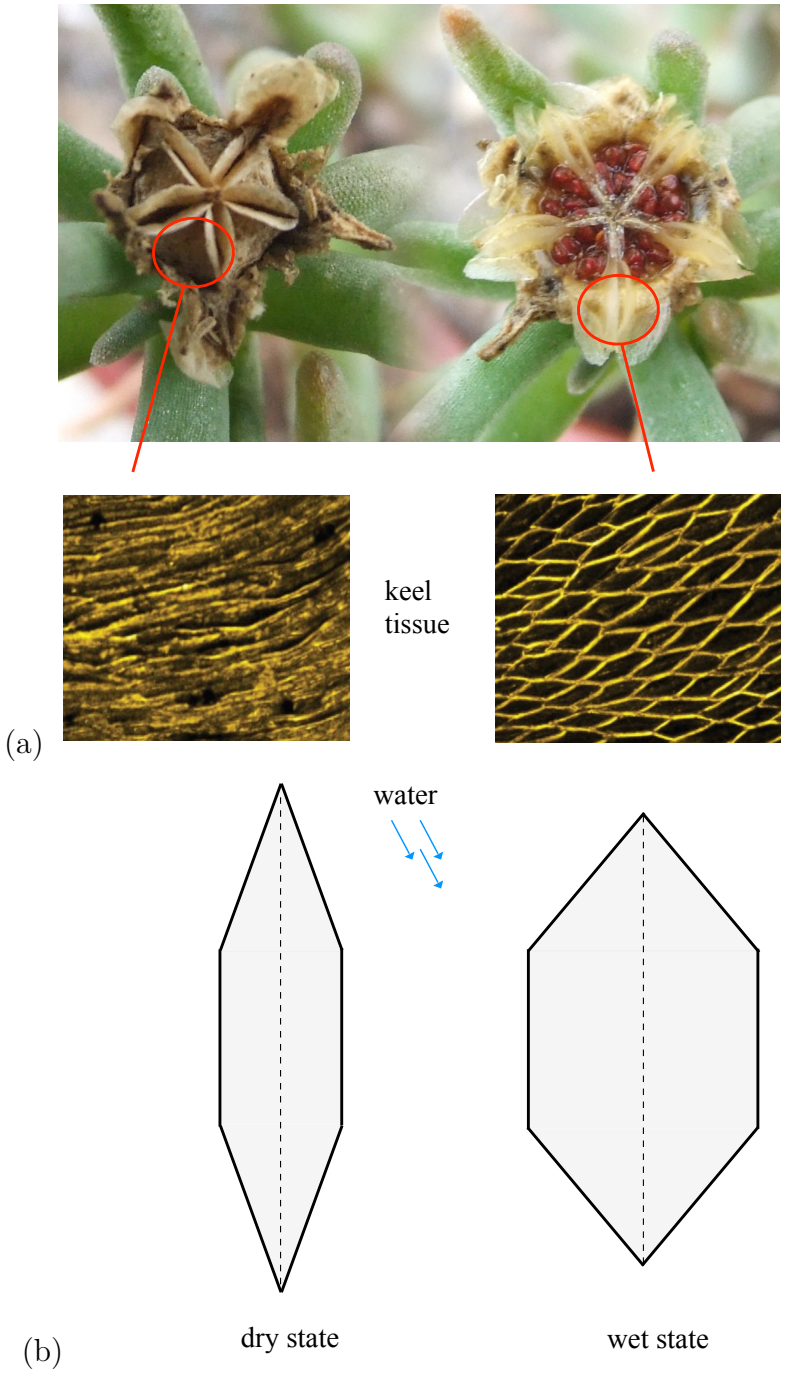

Figure 5.1: (a) The seed capsule, taken from Grootscholten (2005), and the keel tissue, taken from Guiducci et al. (2014), of the ice plant Delosperma nakurense in the dry (left) and wet (right) state, (b) the schematic representation of the keel tissue

cells leads to a volume increase/decrease of the CIL, resulting in cells having the ability to open and close upon wetting/drying cycles. From this point of view, experimental observations (Guiducci *et al.*, 2014) reveal that the filler contains a soft inclusion, having Young's modulus $E_{incl} \approx 0$, that behaves like an elongated thin septum partitioning the internal volume of the cell. Consequently, the cell walls' coupling effect due to the presence of the filling material is compromised (cf. Section 3.2) and this particular configuration, where the cell walls act independently from each other, could facilitate the reversible expansion/contraction of the cells (Figure 5.1b). It follows a reversible change in the original geometry and stiffness of the whole tissue, that is thus able to combine load bearing and morphing functions (Burgert & Fratzl, 2009; Guiducci *et al.*, 2015; Li & Wang, 2017).

Existing studies investigated the morphology and composition of the keel tissue, although under different assumptions, techniques and scope.

Among them, Guiducci et al. (Guiducci *et al.*, 2014) represented this intriguing tissue as a honeycomb-like structure internally pressurised by a fluid phase. Their attention was focused on describing the mechanical aspects related to the hygroscopic actuation of the ice plant but the finite element-based analysis performed confirmed the improvement in the macroscopic stiffness of the keel provided by the filler. Similar results are presented in Guiducci *et al.* (2015), where the aforementioned concepts are generalised to pressurised honeycombs with L-shaped and Tetris tiles-like cells.

By shifting our attention from plant biology to plant-inspired morphing engineered systems, Vos et al. (Vos & Barrett, 2011; Vos *et al.*, 2011) developed a pressure adaptive honeycomb (PAH) by inserting air pouches into a conventional honeycomb having a hexagonal texture. Specifically, when pressurised, the pouches expand in volume and induce a change in the cells' shape and effective stiffness. Regarding the latter, the authors experimentally demonstrated the central role played by the inner pressure in providing extra rigidity to the whole system.

In addition, Khire et al. (Khire *et al.*, 2006) evaluated the variable stiffness of a honeycomb-type inflatable structure by means of finite element simulations and it emerged that the overall rigidity primarily came from the internal pressure.

Referring the interested reader to Dumais & Forterre (2012), Forterre (2013), Martone *et al.* (2010) and Razghandi *et al.* (2014) for a systematic and comprehensive review on the engineering aspects of plant-inspired morphing systems, it can be said that over the last decade there has been a steady rise of interests in applying the principles of reversible plant movements to create synthetic mutable materials (Li &

Wang, 2017). In particular, such adaptive systems are able to autonomously alter their external shape and can advance the state of the art of many applications.

For example, high performance aircrafts can benefit from integrative morphing wings to control their flights paths without sacrificing the aerodynamic streamline and fuel economy (Vasista & Tong Land Wong, 2012). Also, kinetic architectures capable of altering their internal configurations can provide extra freedoms for indoor environment control and human-building interaction (Fortmeyer & Linn, 2014). Finally, sensing devices and soft robots can exploit the shape changing materials for miniaturisation (Guiducci *et al.*, 2015).

It is widely recognised that a full understanding of the interplay between their architecture and mechanical performance would facilitate the design of new materials, providing an efficient, alternative route to the time-consuming experimental investigations for predicting their macroscopic response.

However, in the context of mutable materials, little is known about the relation between the mechanics of the underlying microstructure and macroscopic properties. Specifically, a continuum model has not been derived and explicit formulas for the effective elastic constants and constitutive equations are currently not available in the literature. It clearly emerges that this limitedly explored research area needs further efforts in order to offer concrete and relevant tools to engineers for developing future generations of mutable materials and structures having the attractive characteristics of plants.

To provide a contribution in this direction, and considering the main topic of the present thesis (i.e., composite cellular materials), this chapter presents a continuum model for two-dimensional mutable cellular materials inspired by the keel tissue of the ice plant. That is to say, a composite honeycomb having a mutable hexagonal architecture composed by elongated hexagonal cells filled with an elastic medium.

5.2 Mathematical description of the discrete system

5.2.1 Geometry

The examined material can be conceived as an interconnected network of discrete elements whose extreme nodes are identified by the two shifted lattices

$$L_1(\ell) := \left\{ \mathbf{X} \in \mathbb{R}^2 : \mathbf{X} = n^1 \mathbf{l}_1 + n^2 \mathbf{l}_2 \,, \text{with}\, (n^1, n^2) \in \mathbb{Z}^2 \right\} \tag{5.1}$$

and

$$L_2(\ell) := \mathbf{s} + L_1(\ell). \tag{5.2}$$

Similarly to Section 3.2.1, $\mathbf{l}_1$, $\mathbf{l}_2$ and $\mathbf{s}$ denote, in turn, the lattice vectors and the shift vector. In Cartesian components, they are given by (Figure 5.2)

$$\mathbf{l}_1 = \begin{bmatrix} 2\,\ell\cos\theta \\ 0 \end{bmatrix}, \quad \mathbf{l}_2 = \begin{bmatrix} \ell\cos\theta \\ \ell(1+\sin\theta) \end{bmatrix}, \quad \mathbf{s} = \begin{bmatrix} \ell\cos\theta \\ \ell\sin\theta \end{bmatrix}, \tag{5.3}$$

with ℓ and θ, respectively, the length (the lattice size) and inclination of the cell walls.

5.2.2 The unit cell

The lattice vectors define the unit cell of the periodic array, composed by the line elements 0-1, 0-2, 0-3, treated as Euler-Bernoulli beams on Winkler foundation (cf. Section 3.3), connecting the external nodes 1, 2, 3 to the central point 0 (Figure 5.2b).

Each beam is supported by two sets of springs: the springs a, in the $-\boldsymbol{\eta}_2^e$ direction (Figure 5.3a), and the springs b, in the direction of $\boldsymbol{\eta}_2^e$ (Figure 5.3b), anchored at the nodes of the lattice L_3 defined by

$$L_3(\ell) := 2\,\mathbf{s} + L_1(\ell). \tag{5.4}$$

In both cases, the reactions of the springs are not orthogonal to the beams but, for symmetry reasons, the tangential components cancel each other out. As we will see in Section 5.2.3, this allows using the stiffness matrix $\mathbf{k}_{wf}^e$ defined in Equation (3.48) to evaluate the elastic energy of the beams 0-1, 0-2 and 0-3.

Also, as illustrated in Figure 5.2a, the nodes of L_3 are connected to those of the lattice L_2 by means of the line elements 0-4, 0-5, 0-6, represented by the vectors

$$\mathbf{b}_4 = \mathbf{s}, \qquad \mathbf{b}_5 = -\mathbf{l}_1 - \mathbf{s}, \qquad \mathbf{b}_6 = (\mathbf{s} - \mathbf{l}_2)/2. \tag{5.5}$$

From a mechanical point of view, they are modelled as Euler-Bernoulli beams whose stiffness is assumed to be much smaller than that of the beams composing the principal lattices L_1 and L_2 (i.e., the cell walls). Consequently, in evaluating the elastic energy of the unit cell (cf. Section 5.2.3), the contribution of 0-4, 0-5, 0-6 can be neglected with respect to 0-1, 0-2, 0-3 composing the skeleton of the cells.

It is noteworthy that, as mentioned in Section 5.2.1, the examined composite honeycomb is inspired by the keel tissue of the ice plant, where a thin septum partitioning

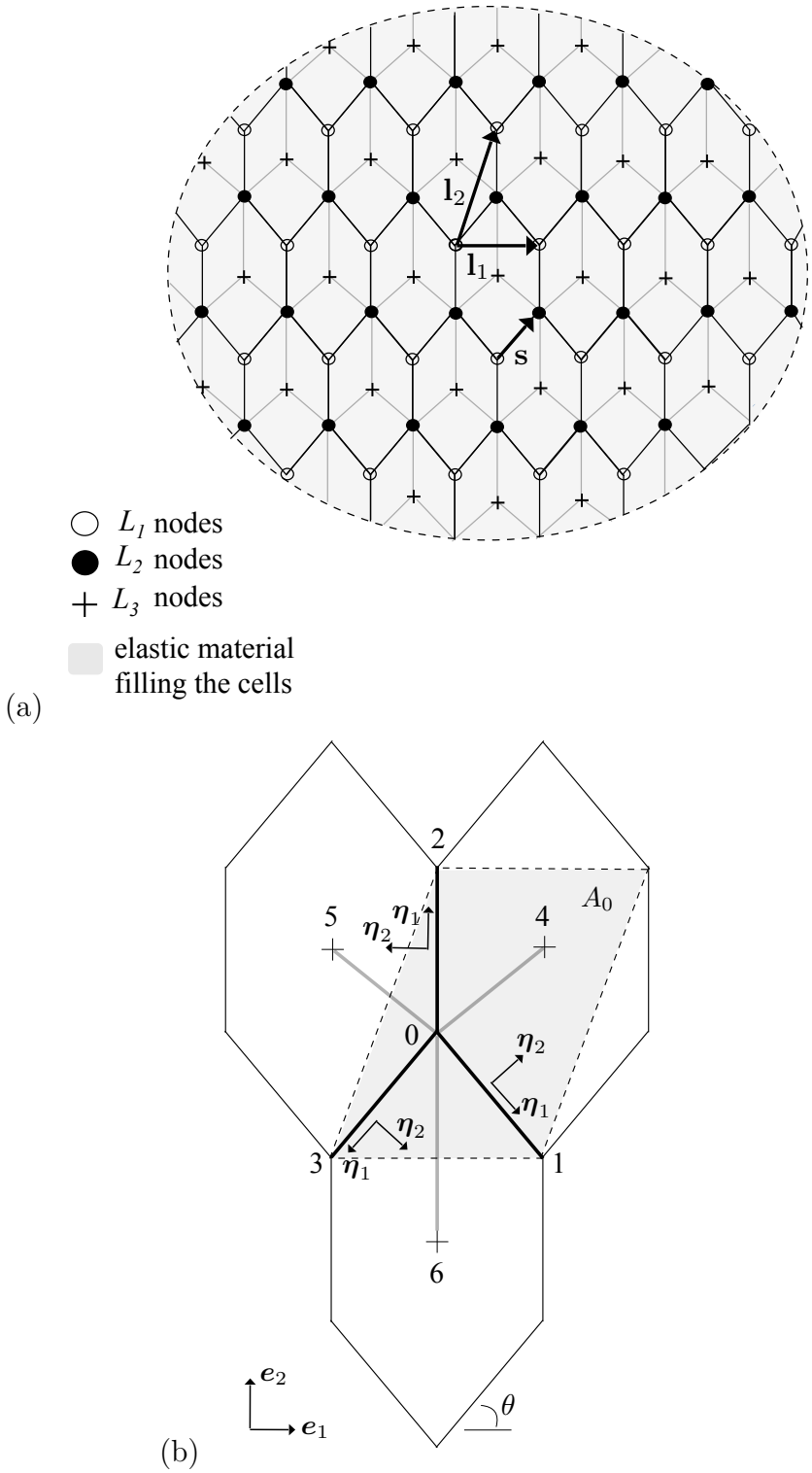

Figure 5.2: The mutable composite honeycomb: (a) the hexagonal microstructure, (b) the unit cell

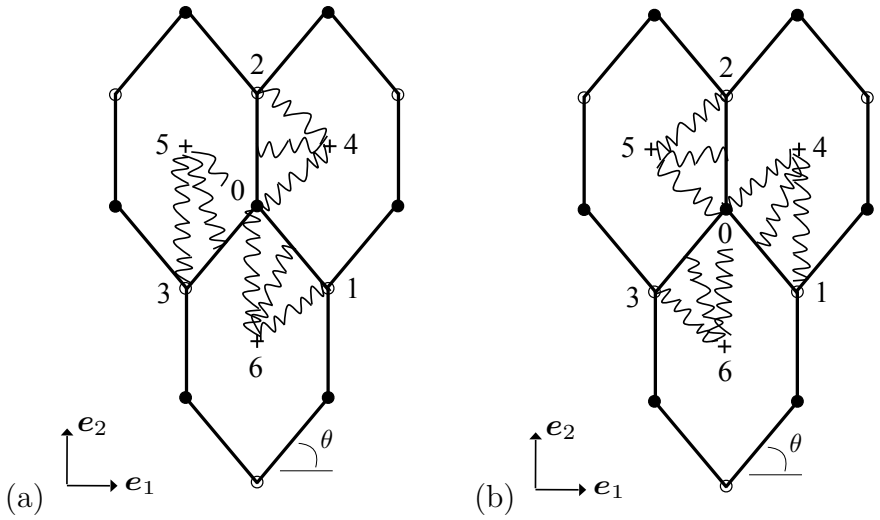

Figure 5.3: The two sets of springs supporting the elastic beams in the mutable composite honeycomb: (a) springs a, (b) springs b

the internal volume of the cells compromises the cell walls' coupling effect due to the presence of the filler.

Since the theoretical model described in Chapter 3, where the springs connect two opposite beams, does not adequately represent the examined configuration, in the present chapter the missing coupling effect caused by the septum is modelled by anchoring the springs at the nodes of L_3, where it is assumed located the "discontinuity" of the filler. This condition, offering a viable way to analytically represent the investigated microstructure, is not too limiting since a rigorous study of the biological tissue does not coincide with our scope; we are interested in exploring general concepts and highlighting qualitative/quantitative effects arising from the considered problem, rather than focusing on a specific behavior.

5.2.3 Elastic energy

In view of the previous assumptions, the elastic energy of the unit cell, W, is obtained by considering the contribution of the beams 0-1, 0-2, 0-3. In particular, by following the procedure described in Section 3.4, the elastic energy of each beam takes the form

$$w^e = w_b^e + w_{wf}^{e,a} + w_{wf}^{e,b}, \tag{5.6}$$

where $w_{wf}^{e,a}$, $w_{wf}^{e,b}$ and w_b^e, respectively related to the elongation of the springs and to the axial and bending deformations of the beam, are expressed in Equations (3.34)-(3.36).

Similarly, as it can be seen in Figure 5.2b, the first node of each beam coincides with the central point 0, where it is imposed the balance of forces and moments. This condition guarantees the equilibrium of the examined cell and allows us to condense the degrees of freedom of 0, leading to

$$W = W_b + W^a_{wf} + W^b_{wf} \equiv W\left(\tilde{\mathbf{D}}, \boldsymbol{\Delta}\tilde{\mathbf{D}}^a, \boldsymbol{\Delta}\tilde{\mathbf{D}}^b\right), \tag{5.7}$$

where W_b, W^a_{wf}, W^b_{wf} are given in Equations (3.57)-(3.59) and

$$\tilde{\mathbf{D}} := \begin{bmatrix} \mathbf{D}_1 \\ \mathbf{D}_2 \\ \mathbf{D}_3 \end{bmatrix} = \begin{bmatrix} U_1 & V_1 & \varphi_1 & U_2 & V_2 & \varphi_2 & U_3 & V_3 & \varphi_3 \end{bmatrix}^T, \tag{5.8}$$

$$\boldsymbol{\Delta}\tilde{\mathbf{D}}^a := \begin{bmatrix} \boldsymbol{\Delta}\mathbf{D}^a_1 \\ \boldsymbol{\Delta}\mathbf{D}^a_2 \\ \boldsymbol{\Delta}\mathbf{D}^a_3 \end{bmatrix} = \begin{bmatrix} \Delta U^a_1 & \Delta V^a_1 & \Delta\varphi^a_1 & \Delta U^a_2 & \Delta V^a_2 & \Delta\varphi^a_2 & \Delta U^a_3 & \Delta V^a_3 & \Delta\varphi^a_3 \end{bmatrix}^T, \tag{5.9}$$

$$\boldsymbol{\Delta}\tilde{\mathbf{D}}^b := \begin{bmatrix} \boldsymbol{\Delta}\mathbf{D}^b_1 \\ \boldsymbol{\Delta}\mathbf{D}^b_2 \\ \boldsymbol{\Delta}\mathbf{D}^b_3 \end{bmatrix} = \begin{bmatrix} \Delta U^b_1 & \Delta V^b_1 & \Delta\varphi^b_1 & \Delta U^b_2 & \Delta V^b_2 & \Delta\varphi^b_2 & \Delta U^b_3 & \Delta V^b_3 & \Delta\varphi^b_3 \end{bmatrix}^T, \tag{5.10}$$

are, in turn, the global vectors of nodal displacements and elongation of the springs (cf. Section 3.4.2). In particular,

$$\boldsymbol{\Delta}\,\mathbf{D}^a_1 = \begin{bmatrix} \mathbf{D}_1 - \mathbf{D}_6 \end{bmatrix} = \begin{bmatrix} \mathbf{U}_1 - \mathbf{U}_6 \\ \varphi_1 - \varphi_6 \end{bmatrix}, \tag{5.11}$$

$$\boldsymbol{\Delta}\,\mathbf{D}^a_2 = \begin{bmatrix} \mathbf{D}_2 - \mathbf{D}_4 \end{bmatrix} = \begin{bmatrix} \mathbf{U}_2 - \mathbf{U}_4 \\ \varphi_2 - \varphi_4 \end{bmatrix}, \tag{5.12}$$

$$\boldsymbol{\Delta}\,\mathbf{D}^a_3 = \begin{bmatrix} \mathbf{D}_3 - \mathbf{D}_5 \end{bmatrix} = \begin{bmatrix} \mathbf{U}_3 - \mathbf{U}_5 \\ \varphi_3 - \varphi_5 \end{bmatrix} \tag{5.13}$$

and

$$\boldsymbol{\Delta}\,\mathbf{D}^b_1 = \begin{bmatrix} \mathbf{D}_1 - \mathbf{D}_4 \end{bmatrix} = \begin{bmatrix} \mathbf{U}_1 - \mathbf{U}_4 \\ \varphi_1 - \varphi_4 \end{bmatrix}, \tag{5.14}$$

$$\boldsymbol{\Delta}\,\mathbf{D}_2^b = \left[\ \mathbf{D}_2 - \mathbf{D}_5\ \right] = \left[\begin{array}{c} \mathbf{U}_2 - \mathbf{U}_5 \\ \varphi_2 - \varphi_5 \end{array}\right], \tag{5.15}$$

$$\boldsymbol{\Delta}\,\mathbf{D}_3^b = \left[\ \mathbf{D}_3 - \mathbf{D}_6\ \right] = \left[\begin{array}{c} \mathbf{U}_3 - \mathbf{U}_6 \\ \varphi_3 - \varphi_6 \end{array}\right], \tag{5.16}$$

with

$$\mathbf{U}_i := \left[\ U_i \quad V_i\ \right]^T. \tag{5.17}$$

With reference to the equilibrium conditions of the anchorage points 4, 5, 6, in addition to those enhanced in Figure 5.2b, i.e., 0-1, 0-2 and 0-3, the springs of other walls are anchored to the nodes 4, 5, 6. Nevertheless, it is not necessary to include such additional beams in the unit cell and impose the equilibrium of forces in 4, 5, 6 since the forces brought to the anchorage points by the springs balance with one another because of the symmetry of the hexagonal cells.

5.3 The homogenized model

5.3.1 Elastic energy

As in Section 3.5, the homogenized model follows by writing the nodal degrees of freedom in Equation (5.7) in terms of the gradient of the two continuous fields of displacements and rotations $\hat{\mathbf{U}}(\cdot)$ and $\hat{\varphi}(\cdot)$:

$$\mathbf{U}_j := \left[\begin{array}{c} U_j \\ V_j \end{array}\right] = \hat{\mathbf{U}}_0 \,+\, \nabla\hat{\mathbf{U}}\,\mathbf{b}_j, \qquad \varphi_j = \hat{\varphi}_0 \,+\, \nabla\hat{\varphi}\,\mathbf{b}_j, \qquad j = 1, 2, ..., 6. \tag{5.18}$$

Substituting Equations (5.18) into Equation (5.7) and dividing the resulting expression by the area of the unit cell, $A_0 = 2\ell^2\cos\theta(1+\sin\theta)$, lead to the strain energy density of the limit problem:

$$w \equiv w\left(\varepsilon_{\alpha\beta}, (\omega - \hat{\varphi}), \hat{\varphi}_{,\alpha} = 0\right), \tag{5.19}$$

revealing that the equivalent continuum is not-polar (more details are provided in Appendix E).

5.3.2 Constitutive equations

The constitutive equations of the limit continuum have a structure identical to the relations in (3.86).

Again, simple mathematical manipulations reveal that the stress tensor is not-symmetric, being its symmetric, $\sigma_{\gamma\delta}^{sym}$, and skew-symmetric, $\sigma_{\gamma\delta}^{skw}$, parts given by

$$\sigma_{11} = \frac{C_\ell c\left(\varepsilon_{11}\left(24c^4 D_\ell + c^2\left(C_\ell \ell^2 + 48 D_\ell s^2\right) + 12 D_\ell s^2 f_{14}\right) + s f_0\left(C_\ell \ell^2 - 12 D_\ell\right)\varepsilon_{22}\right)}{\ell f_0\left(24c^2 D_\ell + C_\ell \ell^2 f_{14}\right)}$$

$$+ \frac{K_w c\left(\varepsilon_{11} f_1 - \varepsilon_{22} f_2\right)}{104 f_0 f_3},$$

$$\sigma_{22} = \frac{C_\ell\left(C_\ell \ell^2 s^2 f_0 \varepsilon_{22} + c^2\left(s\left(C_\ell \ell^2 - 12 D_\ell\right)\varepsilon_{11} + 12 D_\ell f_0 \varepsilon_{22}\right)\right)}{c\ell\left(24c^2 D_\ell + C_\ell \ell^2 f_{14}\right)} + \frac{K_w\left(\varepsilon_{22} f_4/c - \varepsilon_{11} c f_2\right)}{104 f_0 f_3},$$

$$\sigma_{12}^{sym} = \sigma_{21}^{sym} = \frac{3 D_\ell c\left(C_\ell \ell^2\left(4 s f_0\left(s f_0 + 3\right) + 3 + 4c^2\left(2s + f_{14}\right)\right) - 24 D_\ell s f_0\right)\varepsilon_{12}}{2\ell^3 f_0\left(2 C_\ell \ell^2 c^2 + 3 D_\ell\left(4 s f_0 + 3\right)\right)}$$

$$+ \frac{6 D_\ell\left(3c^4 D_\ell + C_\ell \ell^2 c^6 + 3 D_\ell s^2 f_0^2\right)\varepsilon_{12}}{\ell^3 f_0 c\left(2 C_\ell \ell^2 c^2 + 3 D_\ell\left(4 s f_0 + 3\right)\right)} + \frac{K_w\, f_5\, \varepsilon_{12}}{208 c f_0 f_3},$$

$$\sigma_{12}^{skw} = -\sigma_{21}^{skw} = \frac{9\, D_\ell\left(\omega - \hat{\varphi}\right)}{c\,\ell^3\left(3 + 4 s f_0\right)},$$

$$\sigma_{12} = \sigma_{12}^{sym} + \sigma_{12}^{skw}, \quad \sigma_{21} = \sigma_{21}^{sym} + \sigma_{21}^{skw}, \tag{5.20}$$

with C_ℓ and D_ℓ the tensile and bending stiffness of the beams (cf. Equation (3.45)), K_w the Winkler foundation constant, $\varepsilon_{\alpha\beta}$ and ω the infinitesimal strains and infinitesimal rotation. Also, to simplify the notation, c and s stand, respectively, for $\cos\theta$ and $\sin\theta$, while $f_i = f_i(\cos\theta, \sin\theta)$ are the polynomial expressions listed in Appendix E.

5.3.3 Elastic moduli

The derivation presented in Section 3.5.3 to predict the effective elastic constants of the composite honeycomb with a regular hexagonal microstructure can be applied to the case of the mutable architecture.

As expected, the macroscopic elastic moduli are a function of the angle θ, via the terms $c := \cos\theta$, $s := \sin\theta$ and the polynomials $f_i = f_i(\cos\theta, \sin\theta)$, as well as of the

geometric and mechanical properties of the cell walls, i.e., thinness ratio, $\lambda := h/\ell$, Young's modulus, E_s, Poisson's ratio, $v := (1-\nu_s^2)$:

$$E_1 = \frac{c\left(K_w c^2\left(4\lambda^3 f_8 E_s + K_w v f_6\left(f_{14}+2\lambda^2 c^2\right)\right) + 4\lambda E_s\left(104\lambda^3 E_s f_{10}/f_0 + f_7 K_w v\right)/v\right)}{4\left(f_9 K_w v\left(2\lambda^2 c^2 + f_{14}\right) + 104\lambda f_{10} E_s\left(\lambda^2 c^2 + s^2\right)\right)},$$

$$\nu_{12} = -\frac{c^2\left(K_w v f_2\left(2\lambda^2 c^2 + f_{14}\right) + 104\lambda\left(\lambda^2-1\right) E_s f_{11}\right)}{K_w v f_4\left(2\lambda^2 c^2 + f_{14}\right) + 104\lambda f_0 E_s\left(\lambda^2 c^2 + s^2\right) f_{11}/s},$$

$$E_2 = \frac{4\lambda E_s\left(104\lambda^3 E_s f_{10}/f_0 + f_7 K_w v\right)/v + K_w c^2\left(4\lambda^3 E_s f_8 + K_w v f_6\left(f_{14}+2\lambda^2 c\right)\right)}{4 f_0 c\left(K_w v f_1\left(2\lambda^2 c^2 + f_{14}\right) + 104\lambda^3 f_3 E_s\left(s^2\left(3+2c^2\right) + 2c^4 + c^2\right)\right)},$$

$$\nu_{21} = -\frac{K_w v f_2\left(2\lambda^2 c^2 + f_{14}\right) + 104\lambda\left(\lambda^2-1\right) f_{11} E_s}{K_w v f_1\left(2\lambda^2 c^2 + f_{14}\right) + 104\lambda^3 E_s f_3\left(s^2\left(3+2c^2\right) + 2c^4 + c^2\right)},$$

$$G = \frac{1}{416 f_0 c}\left(\frac{104\lambda^3 E_s\left(c^2\left(2\lambda^2 + f_{13}\right) - 2\lambda^2 s f_0 + f_{12}\right)}{v\left(\lambda^2\left(4 f_0 s + 3\right) + 8c^2\right)} + \frac{K_w f_{11}}{f_{10}}\right), \tag{5.21}$$

with E_1, ν_{12} and E_2, ν_{21} denoting, in turn, the Young's modulus and corresponding Poisson's ratio in the $\boldsymbol{e}_1$ and $\boldsymbol{e}_2$ direction, G the shear modulus.

The analysis of the derived quantities reveals the system isotropy only in the particular case $\theta = 30°$ (i.e., regular hexagons), being

$$\begin{aligned}
E_1 = E_2 \equiv E &= \frac{(13\,K_w(1-\nu_s^2) + 32\lambda E_s)(17(1+\lambda^2)K_w(1-\nu_s^2) + 104\lambda^3 E_s)}{2\sqrt{3}(1-\nu_s^2)(305(1+\lambda^2)K_w(1-\nu_s^2) + 416(\lambda+3\lambda^3)E_s)},\\
\nu_{12} = \nu_{21} \equiv \nu &= \frac{33(1+\lambda^2)K_w(1-\nu_s^2) - 416\lambda(\lambda^2-1)E_s}{305(1+\lambda^2)K_w(1-\nu_s^2) + 416\lambda(1+3\lambda^2)E_s},\\
G &= \frac{17(1+\lambda^2)K_w(1-\nu_s^2) + 104\lambda^3 E_s}{104\sqrt{3}(1+\lambda^2)(1-\nu_s^2)},
\end{aligned} \tag{5.22}$$

such that

$$G = \frac{E}{2\left(1+\nu\right)}. \tag{5.23}$$

5.4 Application of the theory to the keel tissue of the ice plant

5.4.1 Comparison with the available data

Let us express the stress-strain relations in Equations (5.20) by using the Voigt notation (cf. Section 3.6.1)

$$\begin{bmatrix} \sigma_{11} \\ \sigma_{22} \\ \sigma_{12} \end{bmatrix} = \begin{bmatrix} C_{11} & C_{12} & C_{13} \\ C_{21} & C_{22} & C_{23} \\ C_{31} & C_{32} & C_{33} \end{bmatrix} \begin{bmatrix} \varepsilon_{11} \\ \varepsilon_{22} \\ 2\,\varepsilon_{12} \end{bmatrix}, \tag{5.24}$$

where

$$\begin{aligned}
C_{11} &= \frac{C_\ell c\left(24c^4 D_\ell + c^2\left(C_\ell \ell^2 + 48 D_\ell s^2\right) + s\left(12 D_\ell s f_{14}\right)\right)}{\ell f_0\left(24c^2 D_\ell + C_\ell \ell^2 f_{14}\right)} + \frac{K_w c f_1}{104 f_0 f_3}, \\
C_{22} &= \frac{C_\ell\left(C_\ell \ell^2 s^2 + 12 D_\ell c^2\right) f_0}{c\ell\left(24c^2 D_\ell + C_\ell \ell^2 f_{14}\right)} + \frac{K_w f_4/c}{104 f_0 f_3}, \\
C_{12} = C_{21} &= \frac{C_\ell c s\left(C_\ell^2 - 12 D_\ell\right)}{\ell\left(24c^2 D_\ell + C_\ell \ell^2 f_{14}\right)} - \frac{K_w c f_2}{104 f_0 f_3}, \\
C_{33} &= \frac{3 D_\ell\left(C_\ell \ell^2\left(4 s f_0\left(s f_0 + 3\right) + 3\right) - 24 D_\ell s f_0\right)}{2\ell^3 f_0\left(2 C_\ell \ell^2 c^2 + 3 D_\ell\left(4 s f_0 + 3\right)\right)} \\
&\quad + \frac{3 D_\ell\left(2c^4\left(C_\ell \ell^2\left(2 s f_0 + 1\right) + 3 D_\ell\right) + 2 C_\ell \ell^2 c^6 + 6 D_\ell s^2 f_0^2\right)}{\ell^3 f_0 c\left(2 C_\ell \ell^2 c^2 + 3 D_\ell\left(4 s f_0 + 3\right)\right)} + \frac{K_w f_5}{208 c f_0 f_3}, \\
C_{13} &= C_{23} = C_{31} = C_{32} = 0
\end{aligned} \tag{5.25}$$

are the components of the effective stiffness tensor obtained in Section 5.3.2.

Even though a detailed analysis of the hygroscopic keel tissue does not coincide with our scope, in order to verify the validity of the adopted modelling technique, the C_{ij} constants in Equations (5.25) are compared to the solutions available in the literature. For this purpose, we have considered the work by Guiducci et al. (Guiducci *et al.*, 2014), where the effective stiffness of the keel tissue, represented as a pressurised honeycomb, is derived by numerical homogenization and theoretical modelling based on the Born rule.

As Table 5.1 summarises, four configurations are investigated, characterised by different values of cell walls' inclination, θ, and inner pressure, p.

Table 5.1 A practical application to the keel tissue of the ice plant: comparison with the existing literature

Guiducci *et al.* (2014) E_s=1 GPa, ν_s=0.3, $\lambda = 0.07$					
$\theta(^\circ)$	p (MPa)	C_{22} (GPa)	C_{11} (GPa)	C_{33} (GPa)	$C_{12} = C_{21}$ (GPa)
75	0	0.1÷0.3	0.002	0.004÷0.012	0.028
48	2.5	0.03	0.020÷0.027	0.03÷0.086	0.020÷0.026
47	5	0.025	0.03÷0.05	0.03÷0.086	0.015
46	6	0.02	0.03÷0.04	0.02÷0.096	0.02
Present E_s=1 GPa, ν_s=0.3, $\lambda = 0.07$					
$\theta(^\circ)$	K_w (MPa)	C_{22} (GPa)	C_{11} (GPa)	C_{33} (GPa)	$C_{12} = C_{21}$ (GPa)
75	0	0.15	0.002	0.004	0.025
48	1.33	0.028	0.02	0.04	0.018
47	2.35	0.022	0.046	0.057	0.014
46	3.25	0.02	0.04	0.054	0.019

Notwithstanding the different strategies adopted, Table 5.1 reveals that the agreement is generally very good, being the discrepancy between the two estimates of averagely 1.5 %.

From this point of view, the source of difference is mainly related to geometric and mechanical aspects. The first can be attributed to the different cells' shape considered, diamond-shaped cells in Guiducci *et al.* (2014) and elongated hexagons in the present thesis; the second to the different way in which the interaction between the filler and the cell walls is mimicked.

In particular, the aim of Guiducci et al. (Guiducci *et al.*, 2014) was to explore the hygroscopic actuation of the ice plant and special attention was given to the swelling of the hygroscopic material (CIL) inside the cells of the keel tissue due to the adsorption of water. Consequently, to better describe the relation between water content and swelling properties, in Guiducci *et al.* (2014) the CIL is replaced by a fluid domain occupying the cavities of the cells, whose walls are thus subjected to a uniform hydrostatic pressure, p.

In spite of this, the comparison in Table 5.1 confirms the validity of our model for evaluating the effective elastic properties of biological tissues having a mutable hexagonal architecture.

In addition, the advantage of the proposed theory is that an explicit relation between the inner pressure, p, and the Winkler foundation constant, K_w, can be obtained by extending the energetic equivalence in Section 3.8 to the case of elongated cells. Specifically, it emerges (cf. Appendix D for more details)

$$K_w(p) = \frac{\cos\theta\,(1+\sin\theta)}{2\cos^2\theta + \sin\theta\,(1+\sin\theta)}\,p, \tag{5.26}$$

relation on which Table 5.1 is based.

5.4.2 Optimal values of pressure and cell walls' inclination

One question that arises is if there exist an optimal value of p, $\tilde{p}$, that maximises the area of the hexagonal cell, A_0, expressed by

$$A_0(p) = 2\ell^2\cos\theta\cdot(1+\sin\theta), \tag{5.27}$$

with ℓ and $\theta = \theta(p)$, in turn, the length and inclination of the cell walls.

As known from mathematics, $\tilde{p}$ can be found by evaluating the stationary points of the differentiable function in Equation (5.27) and, in particular, by focusing on the points $\tilde{\theta}$ where the first derivative of Equation (5.27),

$$\frac{\partial A_0}{\partial\theta} = \frac{\partial A_0}{\partial\sin\theta}\frac{\mathrm{d}\sin\theta}{\mathrm{d}\theta} + \frac{\partial A_0}{\partial\cos\theta}\frac{\mathrm{d}\cos\theta}{\mathrm{d}\theta} = 2\ell^2(\cos^2\theta - \sin^2\theta - \sin\theta), \tag{5.28}$$

vanishes.

As illustrated in Figure 5.4, the stationary point located at $\theta \equiv \tilde{\theta} = 30°$ identifies the maximum of Equation (5.27) and the corresponding value of p, derived from Guiducci *et al.* (2014), is given by $\tilde{p} \approx 15$ MPa. It should be noted that, for simplicity, in Figure 5.4 we have assumed $\ell = 1$ mm, being the outcome of the analysis not affected by the particular value of cell walls' length considered.

5.4.3 The smart mechanism of the biological tissue

A schematic representation of the smart mechanism of the keel tissue is illustrated in Figure 5.5 and it can be described as follows.

Initially, in the dry state at zero pressure, the tissue is composed by elongated cells characterised by an high value of θ, $\theta_0 \equiv \theta(p=0) \approx 75°$ (Guiducci *et al.*, 2014), and minimum capability to absorb water (Figure 5.5a). When it starts raining, the filler

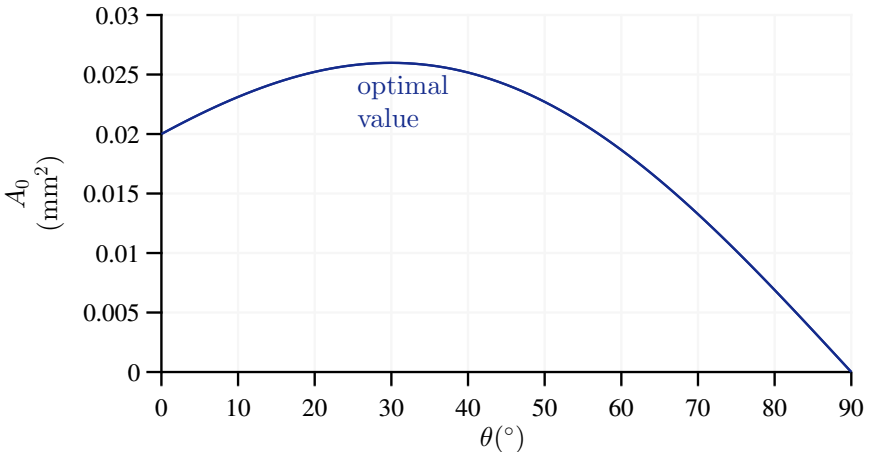

Figure 5.4: An application to the hygroscopic keel tissue: optimal value of θ

absorbs more and more large amounts of water, leading to an increase in the inner pressure and, consequently, to a decrease in θ. In particular, decreasing θ provides an increase in A_0 (cf. Figure 5.4), as well as an increase in the absorption capability (Figure 5.5b). At $\theta = 30°$, the stationary condition of maximum absorption is reached (Figure 5.5c). Then, when the rain stops, the pressure inside the cells decreases, as the absorbed water starts to evaporate (Figure 5.5d). It follows an increase in θ and a decrease in A_0, until the original configuration is restored (Figure 5.5e).

5.4.4 Parametric analysis

From a macroscopic point of view, a variation in the cell walls' inclination, θ, and inner pressure, p, strongly affects the effective stiffness of the biological keel tissue.

To examine such influence, let us focus on the in-plane elastic and shear moduli given in Equations (5.21) and let us assume $E_s = 1$ GPa, $\nu_s = 0.3$, $\lambda := h/\ell = 0.07$, typical values of the lignified cell walls of the keel tissue (Guiducci *et al.*, 2014).

The results are presented in Figures 5.6 and 5.7, where the macroscopic constants are plotted as a function of $\theta = \theta(p)$. It should be noted that the curves are obtained by substituting Equation (5.26) into Equations (5.21).

As it can be seen in Figure 5.6, in the dry state (i.e., $\theta \equiv \theta_0 \approx 75°$) the elastic response of the keel tissue is strongly anisotropic and it emerges that E_2/E_s is bigger than E_1/E_s by roughly one order of magnitude. Then, Figures 5.6a and 5.6b suggest that a decrease in θ, provided by the increase in the inner pressure due to the influx of water, leads to an increase in E_1/E_s and to a decrease in E_2/E_s. This is not surprising since the smaller the angle θ, the more elongated in the $\boldsymbol{e}_1$ direction will

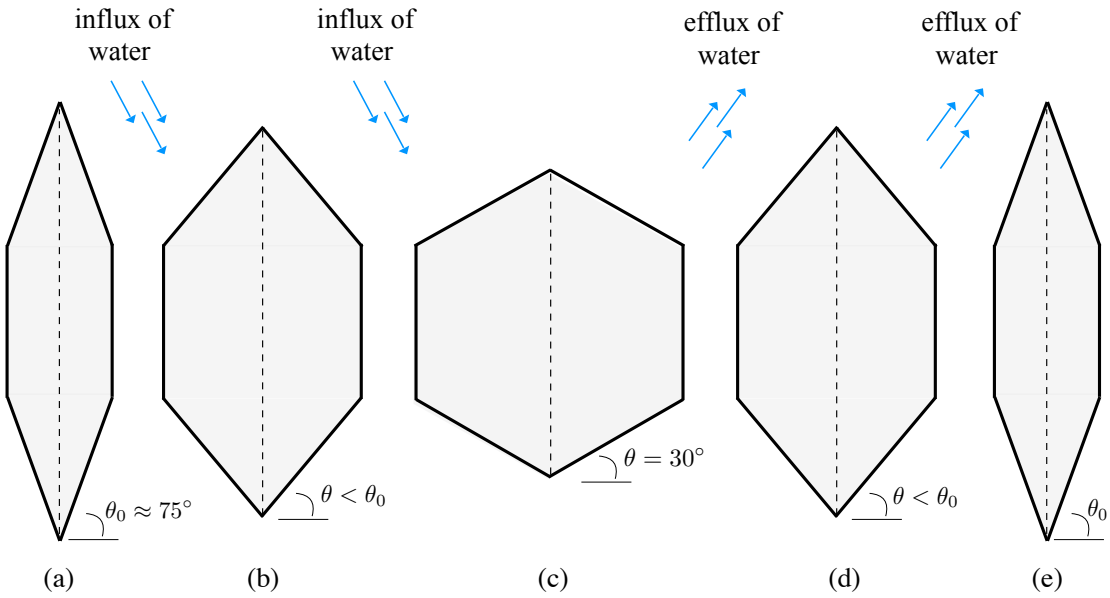

Figure 5.5: The smart mechanism of the hygroscopic keel tissue: (a) dry state, (b) when it starts raining, the filler absorbs water leading to an increase in the absorption capability, (c) stationary condition, maximum absorption, (d) the rain stops and the water absorbed starts to evaporate, until (e) the original configuration is restored

be the resulting cell. Consequently, the smaller θ, the higher E_1. In the stationary condition of maximum absorption, at $\theta = 30°$, the tissue exhibits a completely isotropic behavior, with $E_1 = E_2$. Also, at $\theta = 30°$, Figures 5.6a and 5.6b reveal that E_1/E_s and E_2/E_s have, respectively, their maximum and minimum values. Finally, due to the efflux of adsorbed water, a decrease in p provides an increase in θ, followed by a decrease in E_1/E_s and an increase in E_2/E_s.

Conversely, Figure 5.7 shows that the normalised shear modulus, G/E_s, is less affected by the variation of θ. In particular, the maximum value of G/E_s occurs in the dry state, at $\theta \equiv \theta_0 \approx 75°$, while G/E_s attains its minimum when $\theta = 30°$.

In addition, to provide a more complete description, in Figures 5.6 and 5.7 two additional values of λ are explored: $\lambda = 0.01$ (i.e., slender beams) and $\lambda = 0.2$ (i.e., thick beams). Interestingly, it can be observed that the above considerations apply irrespective of the considered value of thinness ratio, λ.

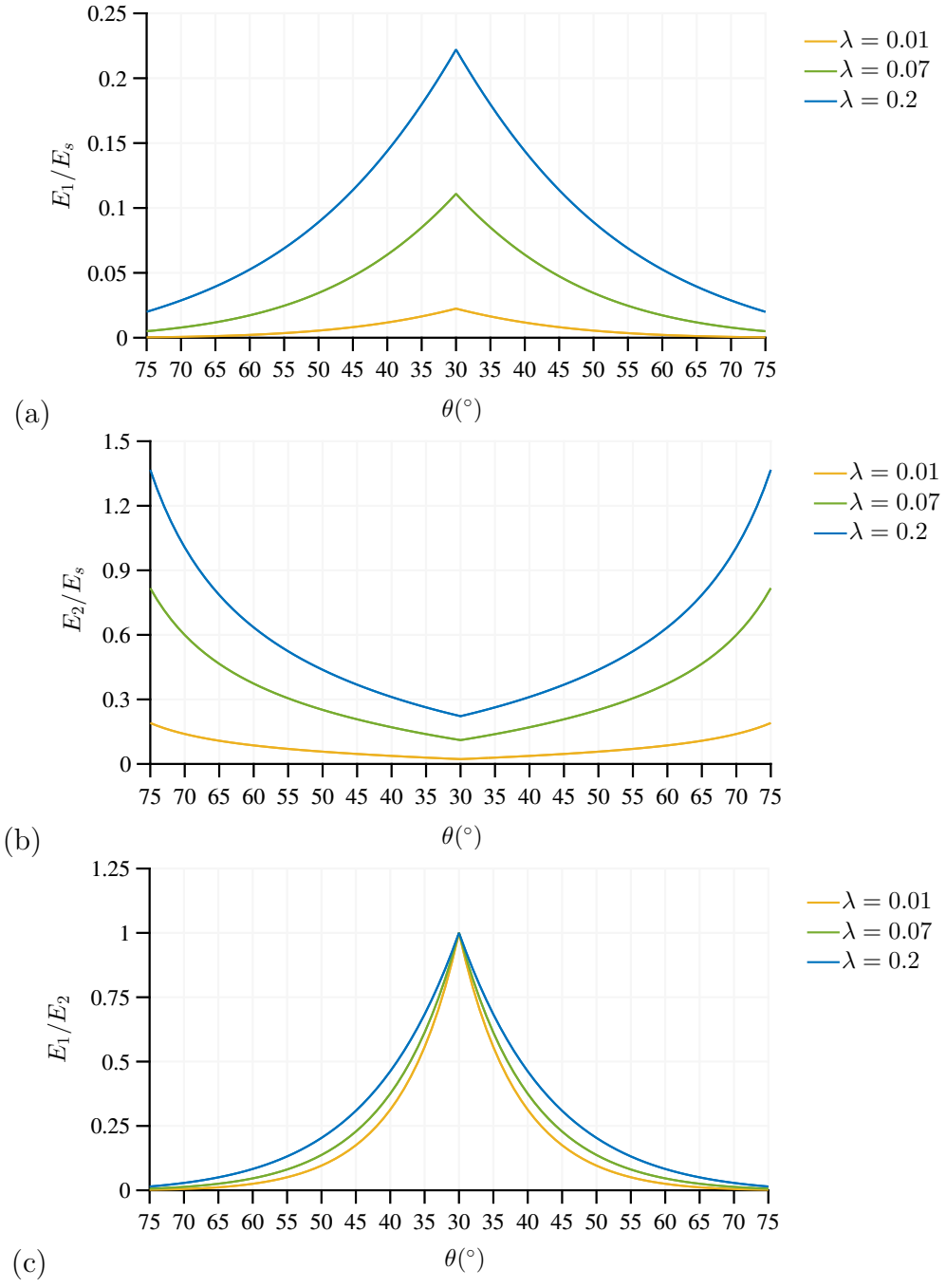

Figure 5.6: The effective elastic constants of the mutable honeycomb as a function of θ: (a), (b) normalised Young's moduli and (c) corresponding elastic anisotropy ratio

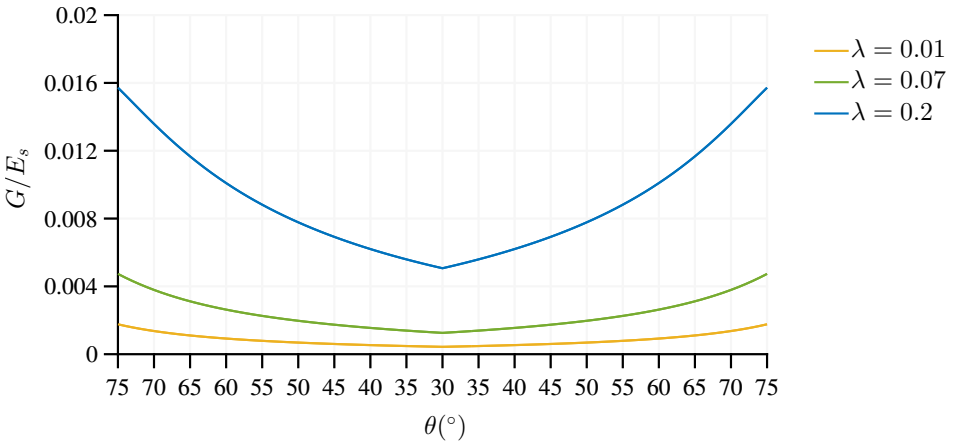

Figure 5.7: The normalised shear modulus of the mutable honeycomb as a function of θ

6 | A new class of cellular materials inspired by the ancient Japanese art of kirigami

6.1 Motivation

The ability of the biological systems to adapt their shape and properties in response to external stimuli has gained a rising interest in recent years, as a rich source of bio-inspired design of smart materials.

In the previous chapter we have investigated the mechanics of the so-called *mutable honeycomb*, inspired by the keel tissue of the ice plant, where the adsorption/desorption of water, in conjunction with the swelling of the cellulosic inner layer (CIL) inside the lumen of the cells, leads to a change in the cells' shape and effective stiffness of the whole tissue.

As stated, various authors transferred the physical principles behind the shape changing characteristics of the plants into synthetic materials, providing enhanced performance and novel functionalities in different fields, such as architecture (Tibbits & Cheung, 2012), robotics (Petralia & Wood, 2010; Cappello *et al.*, 2015) or aeronautics. In the context of cellular materials, such mutable features are usually replicated by pressurising the cells of traditional honeycombs, for example by inserting inflatable air pouches into the cells and varying their inner pressure (Vos & Barrett, 2011).

An alternative strategy to obtain a mutable honeycomb is based on the *kirigami* technique, a variation of the ancient Japanese art of *origami*.

6.2 Origami, kirigami and their applications in engineering: state of the art

Origami, from *ori* meaning *folding* and *kami* meaning *paper*, consists in transforming a simple sheet of paper into a strong, lightweight and flexible three-dimensional structure by applying a prescribed sequence of folds (Tachi, 2010).

Within the past 50 years, a great deal of efforts has gone into exploring the breadth of attainable origami structures and these results have been extended far beyond the art itself. Indeed, origami is currently finding many engineering applications and the recent advances in computer science, number theory and computational geometry have paved the way for powerful new analysis and design techniques based on origami concepts.

From the engineering point of view, the use of origami has two significant features: the capability of producing a foldable/deployable structure and the provision, at the same time, of a reinforcement function.

In optics, for instance, these two characteristics inspired the Foldscope (Cybulski *et al.*, 2014), a minimalistic microscope that can be assembled from a flat sheet of paper and several other small components in under ten minutes. Although it costs less than a dollar, this device, which is small enough to fit in a pocket (70x20x2 mm^3) and weighs less than 9 g, can provide 2000x magnification and sub-micron resolution.

Origami also inspired a novel class of biomedical devices, specifically designed for accessing the hard-to-reach areas of the human body in a minimally invasive way (Kuribayashi *et al.*, 2006), and improved the performance of many industrial products, as in the case of the robotic systems, capable of complex tasks, that can be printed on planar sheets and subsequently folded into some final state (Onal *et al.*, 2011).

This low-cost and extremely fast manufacturing process having, as stated, great advantages such as rigidity in the folded configuration and flat-foldability to facilitate storage and transportation, has been employed in architecture to develop a foldable hallway connecting two offsets and uniquely-sized openings between buildings (Tachi, 2010).

Deployable shelters, used primary for disaster relief and military operational bases, represent an additional origami-inspired application, whose key traits include lightweight frames, insulation toward energy efficiency in heating and cooling, high volume expansion ratio and rigid foldability (Thrall & Quaglia, 2014; Martinez-Martin & Thrall, 2014; Chen & Feng, 2012).

Another closely related example is Foldcore (Eidini & Paulino, 2015), a zigzag-shaped sandwich panel core based on the Miura-ori geometry, a classic origami folding pattern whose main constituents are parallelogram facets connected along fold lines (commonly used for folding and unfolding maps). Foldcore, in particular, differently from the conventional honeycomb cores often characterised by accumulation of humidity, complicated manufacture process and vulnerability against impact loads (Liu *et al.*, 2015), possesses a number of intriguing properties, as open ventilation channels, superior energy absorption capability and impact strength, in-plane auxetic behavior.

It is worth noting that, being not limited to any material or scale, the origami technique shows large potential for manufacturing on very small scales. As a matter of fact, in recent studies it has been explored the folding behavior of mono- and multilayer graphene sheets (Cranford *et al.*, 2009; Lee *et al.*, 2008; Booth *et al.*, 2008), providing a starting point for *graphene origami*, an emerging method that can be used in the implementation of wearable, flexible and foldable electronic devices, such as smartphones, tablets, watches or microscopic robots.

It can be said that the above examples encompass the majority of current research in the promising field of origami applied to engineering.

However, not only origami, but also the related art of *kirigami* (Castle *et al.*, 2014), allowing the paper to be cut, is currently receiving broad attention from scientists and engineers, that are adapting this technique to different two-dimensional starting materials to create structures from the macro- to the microscale (Wang-Iverson *et al.*, 2011; Hawkes *et al.*, 2010). The kirigami cuts, in particular, help determine the final three-dimensional shapes and, differently from the origami, alleviate stresses that could otherwise cause the material to fracture. In addition, kirigami can make a sheet of paper stretchable just by adding parallel cuts dividing it into an array of thin strips with short cross connections. Then, when the paper is pulled perpendicular to the cuts, they open up and allow the sheet to stretch, while the strips buckle into a tilted wavy arrangement (Figure 6.1).

Notably, Blees et al. (Blees *et al.*, 2014) built a version of this springy structure out of a graphene sheet (Figure 6.2) and their experiments revealed that the so-called *graphene kirigami* had extremely high elongation limits ($\sim 240\%$) and mechanical robustness if compared to the uncut graphene.

Similar results are proposed in Shyu *et al.* (2015), where it emerges that graphene oxide polyvinyl alcohol (GO-PVA) nanocomposite sheets acquire unusual high extensibility after microscale kirigami patterning, opening up a wide range of novel

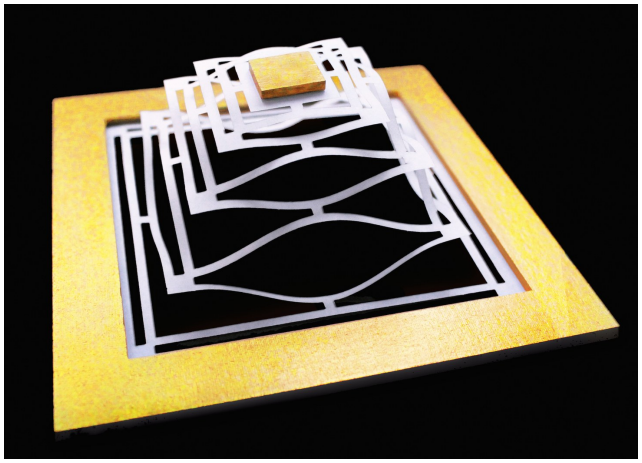

Figure 6.1: An example of kirigami, taken from Blees et al. (2014)

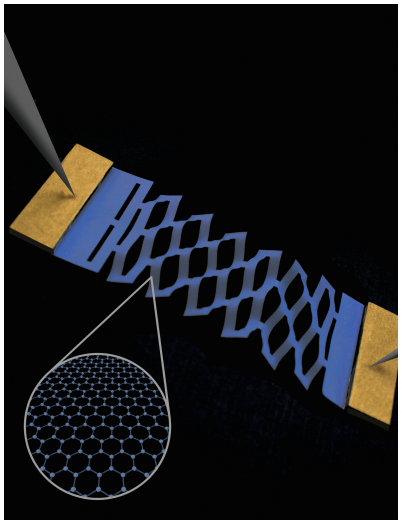

Figure 6.2: The graphene kirigami, taken from Blees et al. (2014)

technological solutions for stretchable electronics and optoelectronics devices, among other possible applications.

As demonstrated in a patent filed by Dean in 1921 (Dean, 1921), kirigami principles can also be exploited to create a hexagonal honeycomb configuration, as the cuts in the sheet material open up into hexagonal holes, coinciding with the honeycomb cells.

Moreover, by considering the space filling models of classical geometries, Saito et al. (Saito *et al.*, 2014) developed a mathematical definition of the cutting patterns leading to kirigami honeycombs and cellular structures with complex functional geometries, together with the associated manufacturing technique.

Taking into account the results in Saito *et al.* (2014), Neville et al. (Neville *et al.*, 2017; 2016; 2014) reported how a class of kirigami honeycombs showed large shape and volume deformations. This result provides a potential platform for unusual multifunctional and shape-changing materials that could be used for morphing airframe components or space deployable structures applications. The authors, in particular, started by creating a pattern of cuts into a flat sheet of thermoplastic polymer, which was then corrugated and folded repeatedly to give a honeycomb architecture. Interestingly, the finite element simulations in Neville *et al.* (2017) reveal that relatively small changes in the fold angle lead to a "Poisson's switch", that is a transition from positive to negative values of the Poisson's ratio of the resulting material.

Recently, Zhang et al. (Zhang *et al.*, 2015) and Zheng et al. (Zheng *et al.*, 2016) explored the mechanical behavior of sophisticated three-dimensional mesostructures obtained from multilayered two-dimensional precursors with a predefined pattern of cuts via the kirigami approach. In accordance with the abovementioned works, the studies in Zhang *et al.* (2015) and Zheng *et al.* (2016) prove the ability of the kirigami technique to increase the ultimate strain and to prevent the unpredictable local failures of the final material.

Finally, kirigami has also been a subject of intense scientific investigations in the biological field, since several natural systems (e.g. birds' wings) have periodic polyhedral designs that could easily be reproduced in terms of kirigami techniques (Sareh & Rossiter, 2015).

However, despite the important scientific interest in the novel field of kirigami applications in engineering, there still remains a large domain to be investigated. In particular, one of the key issues of the kirigami approach, consisting in establishing a relation between the arrangement of the cuts and the overall mechanical response, have not been explored. Such relation, if available, could be useful for designing commercial,

engineering or artistic kirigami structures with tunable properties and the intention of the following sections is to make a contribution to this open field of research.

6.3 The kirigami honeycomb

6.3.1 Basic idea

The basic idea of the kirigami honeycomb, illustrated in Figures 6.3 and 6.4, consists in cutting and stretching a single sheet of starting material of length A_1, height A_2 and unitary width. As it can be seen (Figure 6.4), the stretch causes the cuts to open, leading to a sequence of honeycombs with different geometric and mechanical properties. In particular, the final configuration is closely related to the length, l_c, and distance, d_c, of the cuts, as well as to the considered value of stretch, given by (Barbieri *et al.*, 2017)

$$\alpha := 1 + \frac{\bar{u}}{A_2}, \tag{6.1}$$

with $\bar{u}$ the applied displacement (Figure 6.3).

As the following sections will explain more in detail, the cuts pattern plays an important role in determining the elongation limit of the sheet material and, consequently, the maximum value of attainable α. Thus, only a particular set of kirigami honeycombs can be obtained from a given arrangement of cuts.

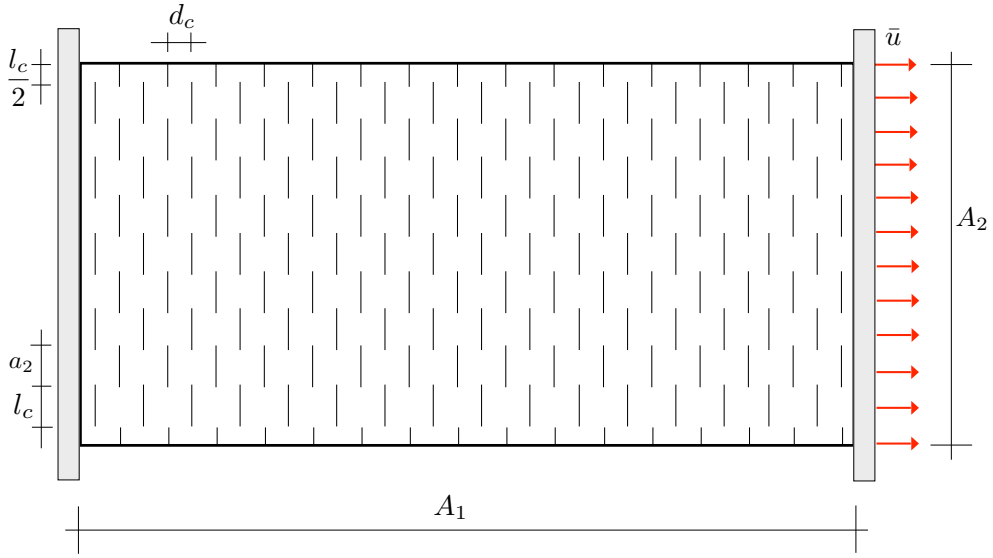

Figure 6.3: The kirigami honeycomb: schematic representation of the pattern of cuts indicating the most relevant geometric parameters

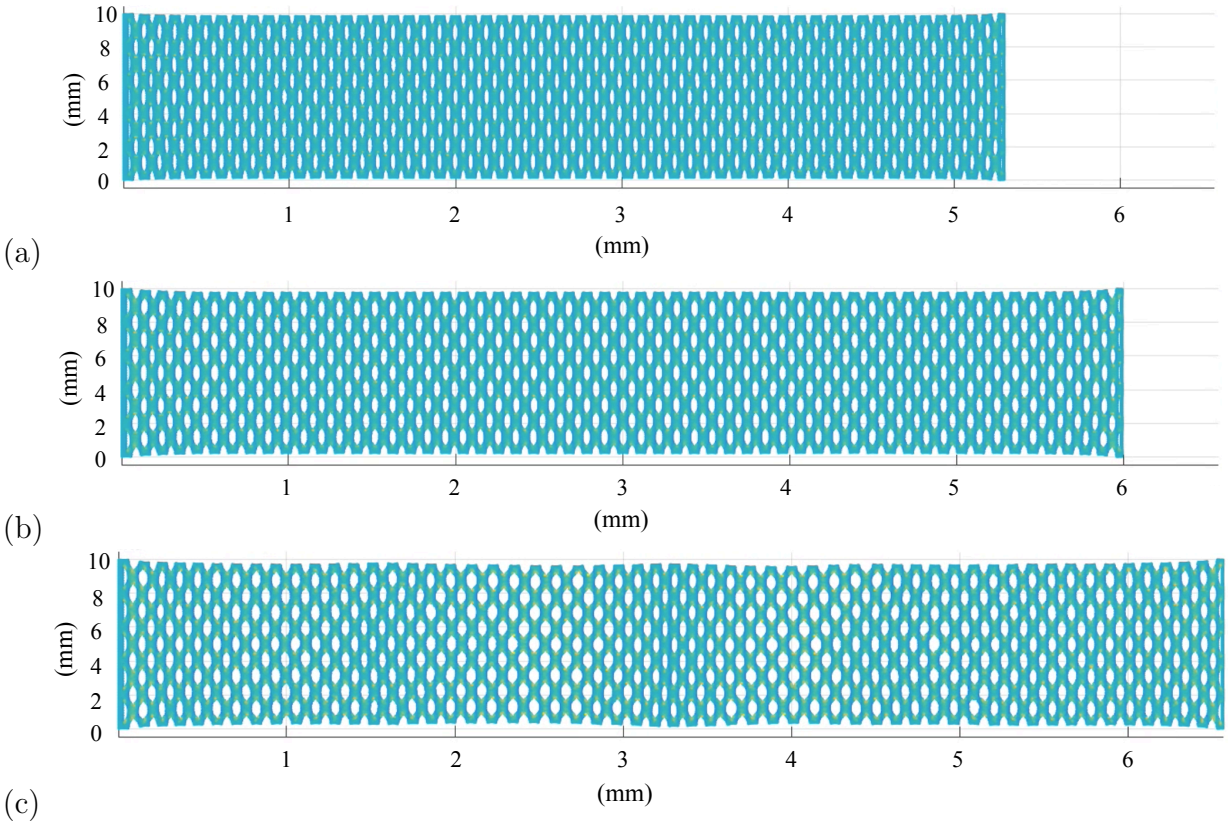

Figure 6.4: The kirigami honeycomb: snapshots of the configurations corresponding to the applied stretch of (a) $\alpha = 1.5$, (b) $\alpha = 1.7$, (c) $\alpha = 1.9$

For the sake of clear disclosure, it should be noted that the numerical simulations in Figure 6.4, performed by the *J-integral*-based arc length solver proposed in Barbieri *et al.* (2017), concern a kirigami honeycomb obtained from a rubber sheet material with

$$A_1 = 340\,\text{mm}, \quad A_2 = 100\,\text{mm}, \quad l_c = 12\,\text{mm}, \quad d_c = 3\,\text{mm}, \quad a_2 = 8\,\text{mm}. \tag{6.2}$$

Finally, in terms of mechanical properties, the following values are adopted: Young's modulus E_s=2.5 MPa and Poisson's ratio $\nu_s = 0.5$ (Gibson & Ashby, 2001), fracture energy G_c=10 kJ/m^2 (Barbieri *et al.*, 2017).

6.3.2 Effective properties

From a theoretical point of view, it is possible to derive explicit formulas for the effective elastic constants (i.e., Young's moduli, Poisson's ratios, shear modulus) of the kirigami honeycombs obtained at each deformation state by means of the strategy presented in the previous chapters. Namely, by representing each deformed configuration as a sequence of discrete elements forming a periodic array of mutable hexagonal cells (cf. Chapter 5).

In particular, let us focus on Figure 6.5, illustrating a portion of the α-kirigami honeycomb provided by subjecting the patterned sheet in Figure 6.3 to the generic stretch α.

Its continuum description follows by analysing the unit cell of the periodic arrangement (Figure 6.5b), identified by the lattice vectors

$$\mathbf{l}_1 = \begin{bmatrix} 2\,\ell_\alpha \cos\theta_\alpha \\ 0 \end{bmatrix}, \quad \mathbf{l}_2 = \begin{bmatrix} \ell_\alpha \cos\theta_\alpha \\ \ell_\alpha \sin\theta_\alpha + h_\alpha \end{bmatrix}, \quad \mathbf{s} = \begin{bmatrix} \ell_\alpha \cos\theta_\alpha \\ \ell_\alpha \sin\theta_\alpha \end{bmatrix}, \tag{6.3}$$

and composed by the elements 0-1, 0-2, 0-3 treated as Euler-Bernoulli beams.

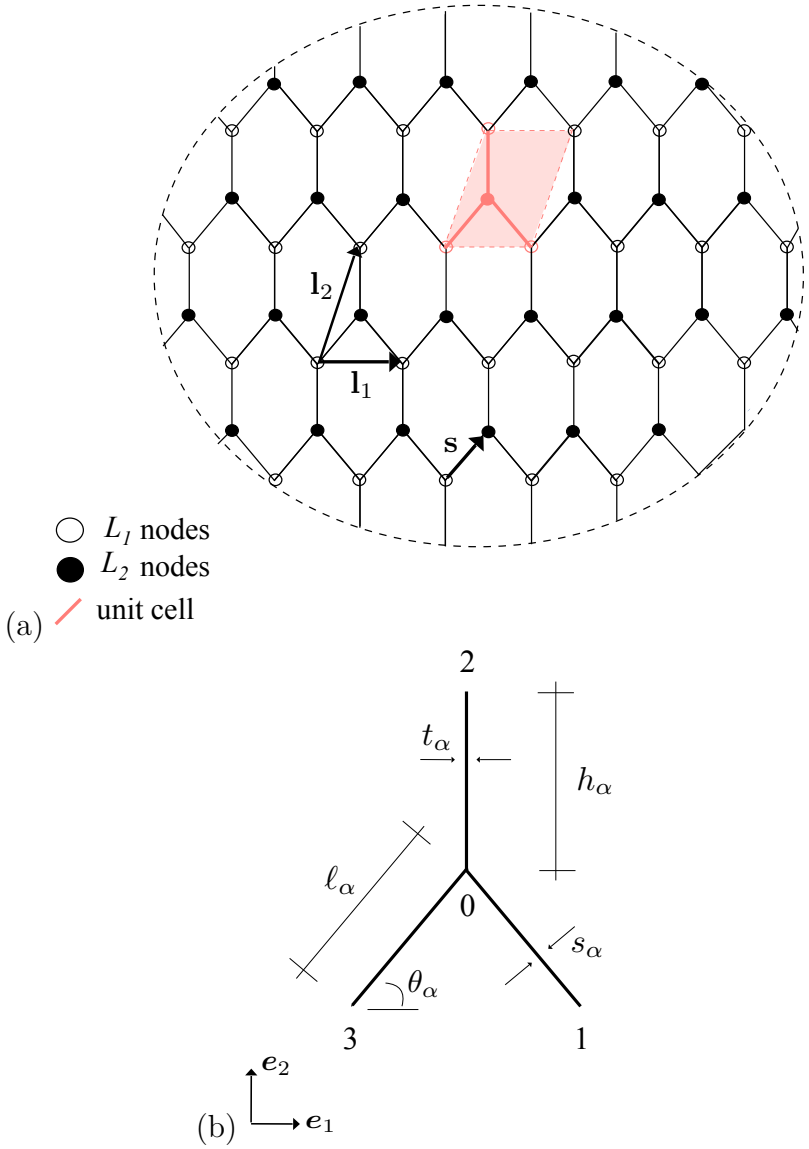

Figure 6.5: (a) The kirigami honeycomb in the theoretical description, (b) the unit cell and its geometric parameters

Again, by applying the energetic approach described in Section 3.4, it emerges that the macroscopic elastic moduli of the α-kirigami honeycomb take the form

$$E_{1,\alpha} = \frac{c_\alpha\,\lambda_{s\alpha}^3\,E_s}{f_{2\alpha}\,(c_\alpha^2\,\lambda_{s\alpha}^2 + s_\alpha^2)\,(1-\nu_s^2)},$$

$$E_{2,\alpha} = \frac{\beta_\alpha\,\lambda_{s\alpha}^3\,f_{2\alpha}\,E_s}{c_\alpha\,(2\lambda_{s\alpha}^2 + \beta_\alpha\,(c_\alpha^2 + \lambda_{s\alpha}^2\,s_\alpha^2))\,(1-\nu_s^2)},$$

$$\nu_{12,\alpha} = -\frac{c_\alpha^2\,s_\alpha\,(\lambda_{s\alpha}^2-1)}{f_{2\alpha}\,(c_\alpha^2\,\lambda_{s\alpha}^2 + s_\alpha^2)},$$

$$\nu_{21,\alpha} = -\frac{\beta_\alpha\,s_\alpha\,f_{2\alpha}\,(\lambda_{s\alpha}^2-1)}{2\lambda_{s\alpha}^2 + \beta_\alpha\,(c_\alpha^2 + \lambda_{s\alpha}^2\,s_\alpha^2)},$$

$$G_\alpha = \frac{\lambda_{s\alpha}^3\,\beta_\alpha^3\,(c_\alpha^4\,(\lambda_{s\alpha}^2\,f_{1\alpha} + \delta_\alpha^2\,(20+8s_\alpha^2)) + f_{1\alpha}\,\lambda_{s\alpha}^2\,s_\alpha^2 f_{2\alpha}^2)\,E_s}{4c_\alpha\,f_{2\alpha}\,(8f_{1\alpha}\,c_\alpha^2 + \lambda_{s\alpha}^2\,f_{3\alpha})\,(1-\nu_s^2)}$$

$$+\frac{\lambda_{s\alpha}^3\,c_\alpha\,(4+\beta_\alpha^6\,\delta_\alpha^2\,(\delta_\alpha^2 - 2\,(\lambda_{s\alpha}^2-2)\,s_\alpha\,f_{2\alpha}) + 4\beta_\alpha^3\,(s_\alpha\,(f_{5\alpha} - \lambda_{s\alpha}^2\,f_{2\alpha}) + f_{4\alpha}))\,E_s}{4\,f_{2\alpha}\,(8f_{1\alpha}\,c_\alpha^2 + \lambda_{s\alpha}^2\,f_{3\alpha})\,(1-\nu_s^2)}, \tag{6.4}$$

with $E_{1,\alpha}$, $E_{2,\alpha}$ and $\nu_{12,\alpha}$, $\nu_{21,\alpha}$ the Young's moduli and Poisson's ratios in the $\boldsymbol{e}_1$ and $\boldsymbol{e}_2$ directions, G_α the shear modulus.

The derived expressions reveal that the equivalent properties are closely related to the geometric parameters of the considered configuration (subscript α) via the terms $\beta_\alpha := \lambda_{t\alpha}/\lambda_{s\alpha}$ and $\delta_\alpha := h_\alpha/\ell_\alpha$, with $\lambda_{t\alpha} := t_\alpha/h_\alpha$ and $\lambda_{s\alpha} := s_\alpha/\ell_\alpha$ denoting, respectively, the thinness ratio of the vertical and inclined cell walls, $c_\alpha := \cos\theta_\alpha$, $s_\alpha := \sin\theta_\alpha$ and the polynomials $f_{i,\alpha} = f_{i,\alpha}(c_\alpha, s_\alpha, \lambda_{t\alpha}, \lambda_{s\alpha})$, with θ_α the shape angle (see Appendix F for a detailed discussion).

In Figure 6.6 it is interesting to see the vast range of effective constants that the kirigami honeycomb structures can be designed with, just by changing the value of the applied stretch, α.

Regarding the normalised Young's moduli, Figure 6.6a illustrates that varying α from 1 to 1.9 (the maximum value that the material can withstand before fracture)

Table 6.1 Geometric parameters of the kirigami honeycombs corresponding to different values of stretch

α	h_α (mm)	ℓ_α (mm)	$\lambda_{t\alpha}$	$\lambda_{s\alpha}$	$\theta_\alpha(^\circ)$
1.1	5.17	3.32	0.29	0.48	84.4
1.2	5.13	3.38	0.29	0.47	78.8
1.3	5.08	3.43	0.30	0.47	73.3
1.4	5.04	3.49	0.30	0.46	67.7
1.5	5.00	3.54	0.30	0.45	62.2
1.6	4.96	3.59	0.30	0.45	56.7
1.7	4.92	3.65	0.30	0.44	51.1
1.8	4.88	3.70	0.31	0.43	45.5
1.9	4.84	3.76	0.31	0.43	40.1

results in an increase in $E_{1\alpha}/E_s$ and to a decrease in $E_{2\alpha}/E_s$. Specifically, the honeycombs corresponding to small values of stretch ($\alpha < 1.3$) exhibit a strongly anisotropic mechanical behavior and it emerges that $E_{2\alpha}$ is approximately 20 times higher than $E_{1\alpha}$. This result is determined by the particular geometry of the honeycombs, composed, as it can be seen in Figure 6.4a, by hexagonal cells strongly elongated in the $\boldsymbol{e}_2$ direction. Conversely, increasing the value of α leads to a decrease in the shape angle θ_α, providing a more and more regular hexagonal honeycomb with $E_{1\alpha}$ approaching $E_{2\alpha}$ (Figures 6.6a and 6.6c).

Similar considerations apply in the case of the normalised shear modulus, G_α/E_s. As illustrated in Figure 6.6b, varying α from 1 to 1.9 could be a good design method for decreasing G_α/E_s of 150%.

6.4 Cuts pattern and effective properties

The scenario described in Figure 6.6 shows that a great number of kirigami honeycombs with substantially different mechanical properties can be obtained just by changing the value of the applied stretch, α.

To go one step further in the analysis, in this section we aim at investigating how the effective elastic constants of the kirigami honeycombs are affected not only by the value of α, but also by the characteristics of the cuts (i.e., distance, d_c, and length, l_c).

Along the lines of the previous example, the discussion involves a kirigami-style structure made of rubber with the alternating pattern of cuts illustrated in Figure 6.3 and such that

$$A_1 = 340\,\text{mm}, \quad A_2 = 100\,\text{mm}. \tag{6.5}$$

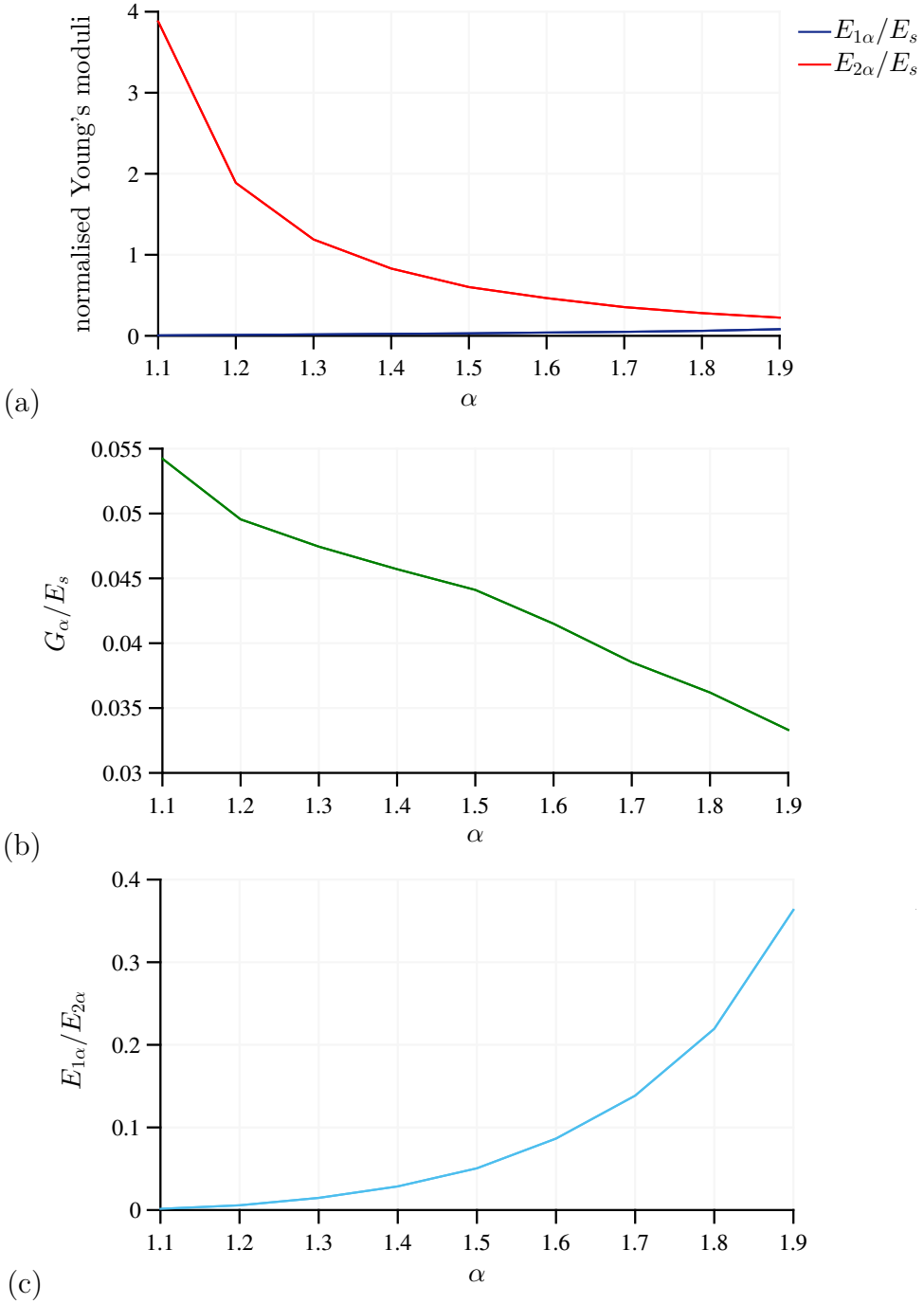

Figure 6.6: The effective elastic constants of the kirigami honeycomb: (a) normalised Young's moduli, (b) normalised shear modulus and (c) corresponding elastic anisotropy ratio

Table 6.2 The role of cuts pattern on the effective properties of the kirigami honeycomb: examined configurations

	d_c (mm)	l_c (mm)
K1	7.5	15
K2	4.5	15
K3	6.5	20
K4	6.5	15

As summarised in Table 6.2, four different configurations are considered: K1 and K2, where the cuts have different spacing but same length, K3 and K4, with cuts having different length but same spacing.

Figures 6.7 and 6.8 illustrate that the cuts pattern dictates the range of attainable kirigami honeycombs since, as anticipated in Section 6.3.1, the elongation limit of the sheet material is strongly affected by the position of the cuts.

In particular, in the case of cuts having same length, l_c, but different spacing, d_c, it emerges that small values of d_c lead to a more stretchable material and, consequently, to a wider range of kirigami honeycombs. Also, the honeycombs corresponding to closer cuts (i.e., configuration K2) are characterised by a smaller value of the thinness ratio (Table 6.3), providing smaller values of Young's moduli and shear modulus. As expected, independently of d_c, the kirigami honeycombs obtained by applying small ($\alpha < 1.8$) or high ($\alpha > 2.7$) values of stretch display a strongly anisotropic mechanical behavior (Figure 6.8b), being their cells strongly elongated in the $\boldsymbol{e}_2$ direction, in the first case, or approaching a brick-like arrangement, in the second (Table 6.3). Interestingly, the analysis reveals that the values of α providing a more regular honeycomb, with $E_{1\alpha} = E_{2\alpha}$, are different in the two examined cases: $\alpha = 2.55$ for the configuration K1, $\alpha = 2.7$ for the configuration K2.

A similar trend can be found by comparing the configurations K3 and K4, where the cuts have same spacing but different length. As it can be seen in Figure 6.8b, notwithstanding the value of l_c, when α is small the cellular structures exhibit large anisotropy, with $E_{2\alpha}$ much higher than $E_{1\alpha}$ (Figure 6.7b). Then, an increase in α leads to a decrease in the shape angle θ_α (Table 6.4), providing a set of honeycomb structures with a more and more isotropic behavior. However, it should be mentioned that longer cuts (i.e., configuration K3) result in a more stretchable sheet material, which implies a wider range of attainable kirigami honeycombs.

In addition, Figures 6.7b and 6.8a show that the effective Young's moduli and shear modulus of the kirigami honeycombs are less affected by the values of l_c rather than

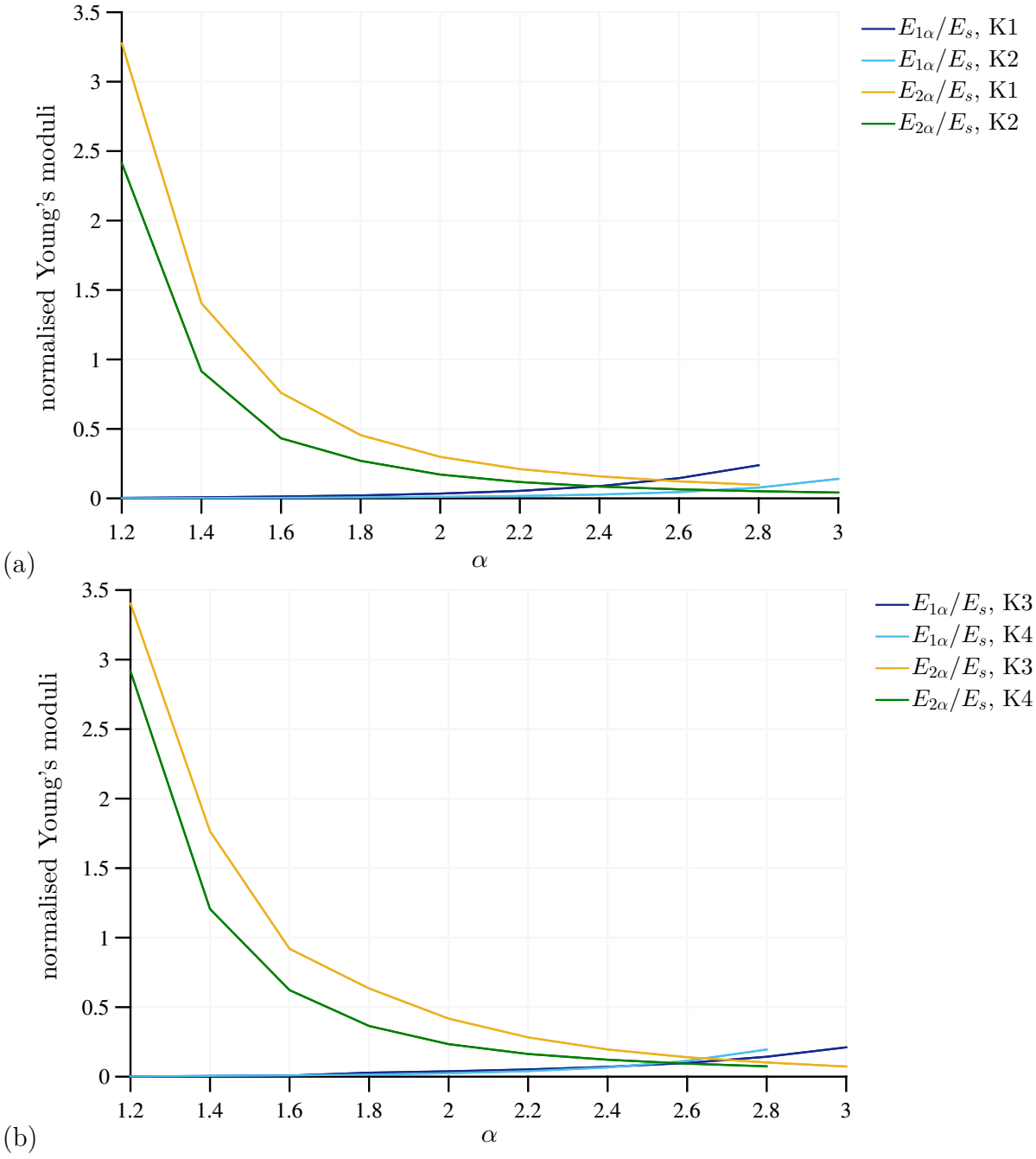

Figure 6.7: The role of cuts pattern on the normalised Young's moduli of the kirigami honeycomb in the case of (a) cuts with different spacing but same length and (b) cuts with same spacing but different length

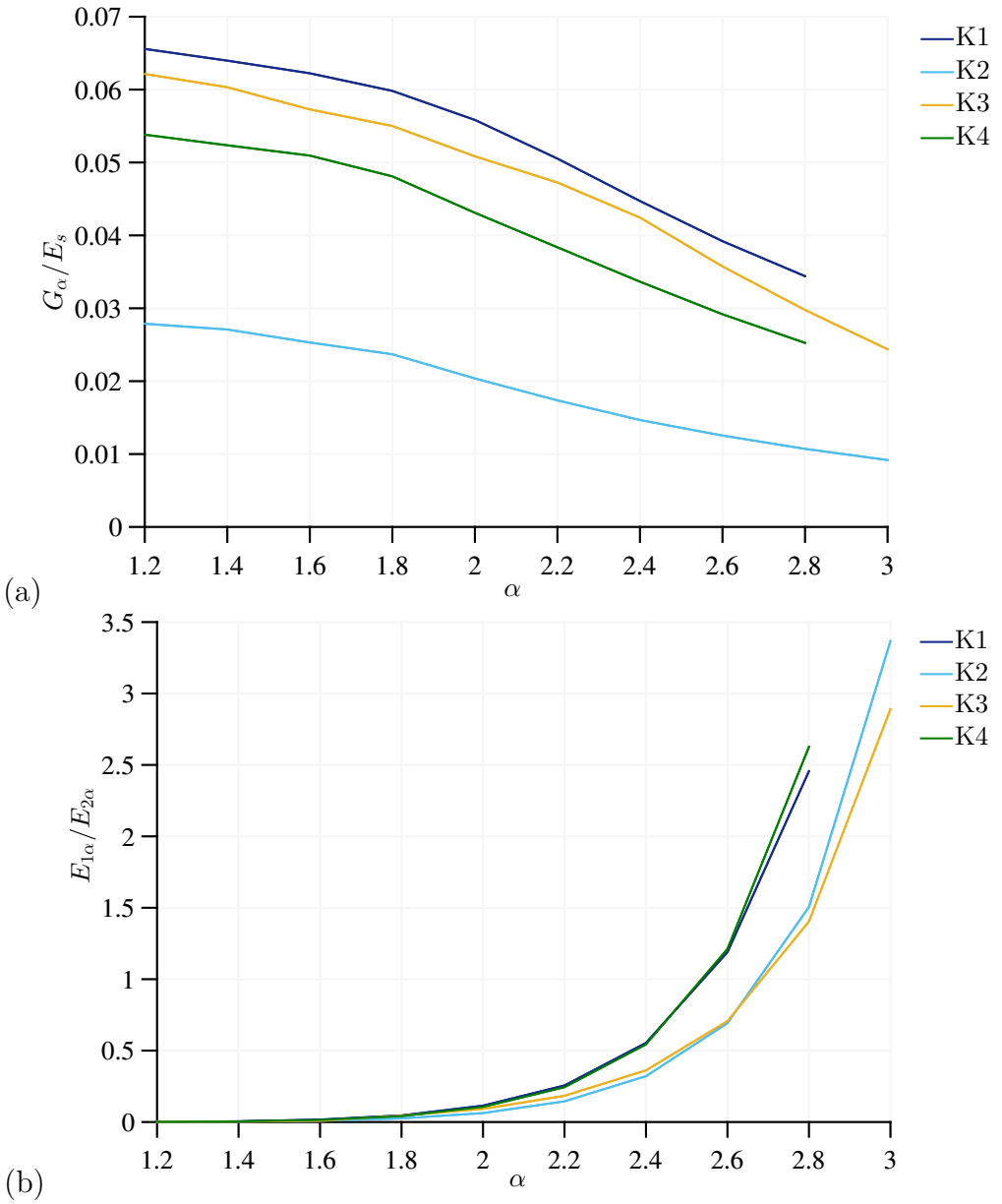

Figure 6.8: Cuts pattern and effective properties of the kirigami honeycomb: (a) normalised shear modulus, (b) elastic anisotropy ratio

Table 6.3 Geometric parameters of the kirigami honeycombs corresponding to different values of stretch in the case of cuts with same length but different spacing

K1					
α	h_α (mm)	ℓ_α (mm)	$\lambda_{t\alpha}$	$\lambda_{s\alpha}$	$\theta_\alpha(^\circ)$
1.2	7.92	5.22	0.48	0.35	82.1
1.4	7.80	5.39	0.47	0.35	74.3
1.6	7.67	5.56	0.45	0.36	66.1
1.8	7.55	5.73	0.44	0.37	58.2
2	7.43	5.90	0.43	0.37	50.4
2.2	7.29	6.07	0.42	0.38	42.3
2.4	7.17	6.24	0.41	0.38	34.5
2.6	7.05	6.41	0.40	0.39	26.4
2.8	6.92	6.58	0.39	0.40	18.5
K2					
α	h_α (mm)	ℓ_α (mm)	$\lambda_{t\alpha}$	$\lambda_{s\alpha}$	$\theta_\alpha(^\circ)$
1.2	8.31	5.47	0.29	0.25	82.8
1.4	8.17	5.65	0.28	0.25	75.6
1.6	8.04	5.83	0.27	0.26	68.5
1.8	7.91	6	0.27	0.26	61.2
2	7.78	6.18	0.26	0.27	54.2
2.2	7.65	6.36	0.25	0.27	47.1
2.4	7.52	6.54	0.25	0.28	39.9
2.6	7.38	6.71	0.24	0.28	32.7
2.8	7.25	6.89	0.23	0.29	25.6
3	7.12	7.07	0.23	0.29	18.4

those of d_c. As a matter of fact, the curves corresponding to the configurations K3 and K4 are more close to each other, if compared to those corresponding to K1 and K2.

This knowledge, in conjunction with the previous findings, increases the potentials of the kirigami technique to contribute significantly to the development of new structural and functional materials. Ideally, this technique can be adopted to obtain a great number of honeycombs having a wide range of desirable properties just by changing the characteristics of the starting sheet material and tailoring the cuts pattern and applied stretch.

Table 6.4 Geometric parameters of the kirigami honeycombs corresponding to different values of stretch in the case of cuts with same spacing but different length

K3					
α	h_α (mm)	ℓ_α (mm)	$\lambda_{t\alpha}$	$\lambda_{s\alpha}$	$\theta_\alpha(^\circ)$
1.2	8.08	5.33	0.44	0.31	82.5
1.4	7.96	5.49	0.43	0.31	75.8
1.6	7.83	5.67	0.42	0.32	68.3
1.8	7.7	5.85	0.40	0.43	61.4
2	7.57	6.02	0.39	0.42	54.2
2.2	7.44	6.19	0.38	0.41	47.6
2.4	7.31	6.37	0.37	0.39	39.9
2.6	7.19	6.54	0.36	0.38	32.8
2.8	7.05	6.72	0.35	0.37	25.5
3	6.93	6.89	0.34	0.36	18.7
K4					
α	h_α (mm)	ℓ_α (mm)	$\lambda_{t\alpha}$	$\lambda_{s\alpha}$	$\theta_\alpha(^\circ)$
1.2	7.77	5.11	0.44	0.31	82.5
1.4	7.64	5.28	0.43	0.32	74.1
1.6	7.52	5.45	0.41	0.32	66.4
1.8	7.39	5.61	0.4	0.33	58.2
2	7.27	5.78	0.39	0.33	50.2
2.2	7.15	5.95	0.38	0.34	42.3
2.4	7.03	6.12	0.37	0.34	34.4
2.6	6.91	6.28	0.36	0.35	26.7
2.8	6.79	6.45	0.35	0.36	18.5

7 | Conclusions and outlook

7.1 Conclusions

Modern engineering applications demand ever-increasing structural performances, with materials that are stronger, tougher, lighter and multifunctional.

Since simple homogeneous materials are not able to fulfil these requirements, researchers drove their attention towards the development of new structural materials, filling the gaps and pushing the limits of the Ashby's materials performance maps. Often, biological systems served as a source of inspiration, as in the case of cellular materials.

Commonly observed in nature, cellular materials offer useful combinations of structural properties and low weight, yielding the possibility of coexistence of what used to be antagonistic physical properties within a single material. Due to their peculiar characteristics, they are very promising for engineering applications in a variety of industries including aerospace, automotive, marine and constructions. However, their use is conditional upon the development of appropriate constitutive models for revealing the complex relations between microstructure parameters and macroscopic behavior. From this point of view, a great variety of analytical and numerical techniques have been proposed and exhaustively discussed in recent years.

The majority of works concern cellular structures with empty cells but, in reality, in many natural systems the cells are filled with fluids or other bulk materials to better resist external stimuli.

This thesis, taking into account the doubtless advantages offered by the aforementioned composite configurations and to provide a contribution in this limitedly investigated research area, deals with the analysis of composite cellular materials biologically inspired and describes the mathematical formulation and modelling technique leading to a continuum model.

Initially, inspired by the biological parenchyma tissue, the attention is focused on a regular hexagonal microstructure having the cells filled with an elastic medium. In the

framework of linear elasticity and by modelling the microstructure as a sequence of Euler-Bernoulli beams on Winkler foundation, an energetic approach provides closed-form expressions for the macroscopic elastic constants and stress-strain relations. In particular, the treatment of the problem is simplified by introducing the classical shape functions of the Finite Element Method in order to represent the displacements within each beam in terms of its end values of displacements and rotation. This allows to write the elastic energy of the discrete system as a quadratic function of them. Finally, assuming the Born rule and expressing the variables defined to represent the nodal degrees of freedom as a function of the gradient of the two continuous fields of displacements and rotation give the continuum model. The predicted results are verified by means of numerical simulations and by comparison with the available data in the literature. In both cases, it emerges a very good agreement. In addition, the application of the theoretical model to estimate the effective stiffness of the biological parenchyma tissue reveals that the proposed modelling strategy could be useful to gain some qualitative/quantitative information on the mechanical properties of natural systems.

The assumption of the Born rule, in conjunction with an energetic approach, is also employed to investigate the mechanics of mutable cellular materials composed by mutable elongated hexagonal cells filled with an elastic medium. The problem is inspired by the peculiar behavior of the hygroscopic keel tissue of the ice plant *Delosperma nakurense*, where the adsorption/desorption of water, together with the swelling of the cellulosic inner layer (CIL) inside the lumen of the cells, leads to a reversible change in the cells' shape and effective stiffness of the whole tissue. Similarly to the previous case, the system is conceived as an interconnected network of Euler-Bernoulli beams on Winkler foundation and the homogenized model follows by introducing the affine interpolants of nodal displacements and rotation. Even though a detailed analysis of the keel tissue is well beyond our scope, the derived quantities, constitutive equations and elastic moduli in the macroscopic description, are in accordance with those obtained by the other authors, where the biological tissue is represented as a pressurised honeycomb. In particular, an energetic equivalence gives an explicit relation between the inner pressure and the Winkler foundation constant. Optimal values of pressure and cell walls' inclination also emerge.

Then, inspired by the complex organisation of many natural systems, the thesis investigates the effects of introducing structural hierarchy into a two-dimensional composite cellular material. Interestingly, in contrast to the traditional cellular materials with empty cells, it emerges an improvement in the specific stiffness, provided that the

filler is stiffer than a critical value. Specifically, two cases are considered: the self-similar configuration and the case in which different levels have different cell topologies. In the first, the analytical expressions for the in-plane elastic constants derived reveal the system isotropy as for the not-filled hierarchical cellular structures, while, in the second, indicate a synergy of hierarchy, material heterogeneity and cell topology in obtaining improved stiffness.

Finally, due to the steady rise of interest in applying the principles of reversible plant movements to create synthetic mutable materials with unusual functionalities, the last part of the thesis presents a novel strategy to obtain a honeycomb with mutable cells. The technique is based on *kirigami*, a variation of the Japanese art of *origami*, and consists in cutting and stretching a flat sheet of starting material, leading to a sequence of honeycombs with different geometric and mechanical properties. One of the key issues of the kirigami approach, that is obtaining a relation between the pattern of cuts and the overall mechanical response, is explored for the first time. Notably, the study shows that a great number of honeycombs can be obtained just by changing the position of the cuts and the applied stretch.

As a conclusion, with respect to the published works, the novelties of the present thesis can be summarised as follows.

Firstly, the beam on Winkler foundation has never been applied to investigate the mechanics of composite cellular materials. Despite the simplifications introduced, the obtained results are found to be in very good agreement with the published data.

Secondly, the explicit formulas derived offer a full understanding of the interplay between the macroscopic properties and the underlying microstructure of both engineering and biological composite cellular materials, suggesting an alternative route to the time-consuming experimental investigations for predicting their macroscopic response.

Thirdly, the analysis provides a contribution into the role of structural hierarchy on the in-plane elastic properties of composite cellular materials, as well as some possible ways to improve low-weight cellular structures by mixing different materials and varying the cell topology.

Finally, it presents the potentials of the kirigami technique in creating a vast range of honeycombs with tailored features and a relation between the arrangement of the cuts and the mechanical properties is derived.

7.2 Future perspectives

Based on the present thesis, a number of directions for further research can be formulated. The main issues can be summarised as follows.

The proposed work deals with the in-plane analysis of composite cellular materials to derive explicit formulas for their effective elastic constants and stress-strain relations. Thus, a first possible extension consists in exploring also the out-of-plane behavior and taking into account other possible deformation and failure mechanism, such as buckling, plasticity or debonding. The environmental effects, e.g. temperature, on the mechanical properties could also be included to provide a more comprehensive model and to offer a further advance in the field of composite cellular structures.

As stated, the analytical predictions are verified by means of numerical simulations and by comparison with the results available in the literature. Mechanical experiments could be conducted to further testify the validity of the suggested approach.

Mechanical experiments, together with additional numerical simulations, could also be done in the case of the kirigami honeycomb to investigate, for example, different types of sheet material, larger samples or more complicated cuts patterns (e.g. inclined or hierarchical cuts).

Negative Poisson's ratio materials are undoubtedly fascinating, mainly because of their counterintuitive mechanical behavior. A possible way for further research would be to derive a continuum model for composite cellular materials having auxetic microstructures. Besides, the association of auxetics with hierarchy would probably give rise to some interesting new composites.

A | Continuum modelling of the composite honeycomb with equilateral triangular microstructure

A.1 The discrete system

As in Chapter 3, a sequence of Euler-Bernoulli beams on Winkler foundation represents the triangular composite microstructure in the discrete description.

The unit cell of the periodic configuration (Figure A.1) is composed by the the six beams 0-1, 0-2, 0-3, 0-4, 0-5, 0-6 connecting the external nodes 1, 2, 3, 4, 5, 6 to the central one, 0. In the global reference system ($\boldsymbol{e}_1$, $\boldsymbol{e}_2$), the beams are described by the vectors (Figure A.1c)

$$\begin{gathered}\mathbf{b}_1 = \begin{bmatrix} \ell & 0 \end{bmatrix}^T, \quad \mathbf{b}_2 = \begin{bmatrix} \frac{\ell}{2} & \frac{\sqrt{3}\,\ell}{2} \end{bmatrix}^T, \quad \mathbf{b}_3 = \begin{bmatrix} -\frac{\ell}{2} & \frac{\sqrt{3}\,\ell}{2} \end{bmatrix}^T, \\ \mathbf{b}_4 = -\mathbf{b}_1, \qquad \mathbf{b}_5 = -\mathbf{b}_2, \qquad \mathbf{b}_6 = -\mathbf{b}_3,\end{gathered} \tag{A.1}$$

respectively.

The elastic energy of the unit cell, W, is obtained by summing the energetic contribution of the beams it consists, given by

$$w^e = \frac{w_b^e + w_{wf}^{e,a} + w_{wf}^{e,b}}{2}, \tag{A.2}$$

with

$$w_b^e := \frac{1}{2}\left(\mathbf{d}^e\right)^T \cdot \mathbf{k}_b^e \mathbf{d}^e \tag{A.3}$$

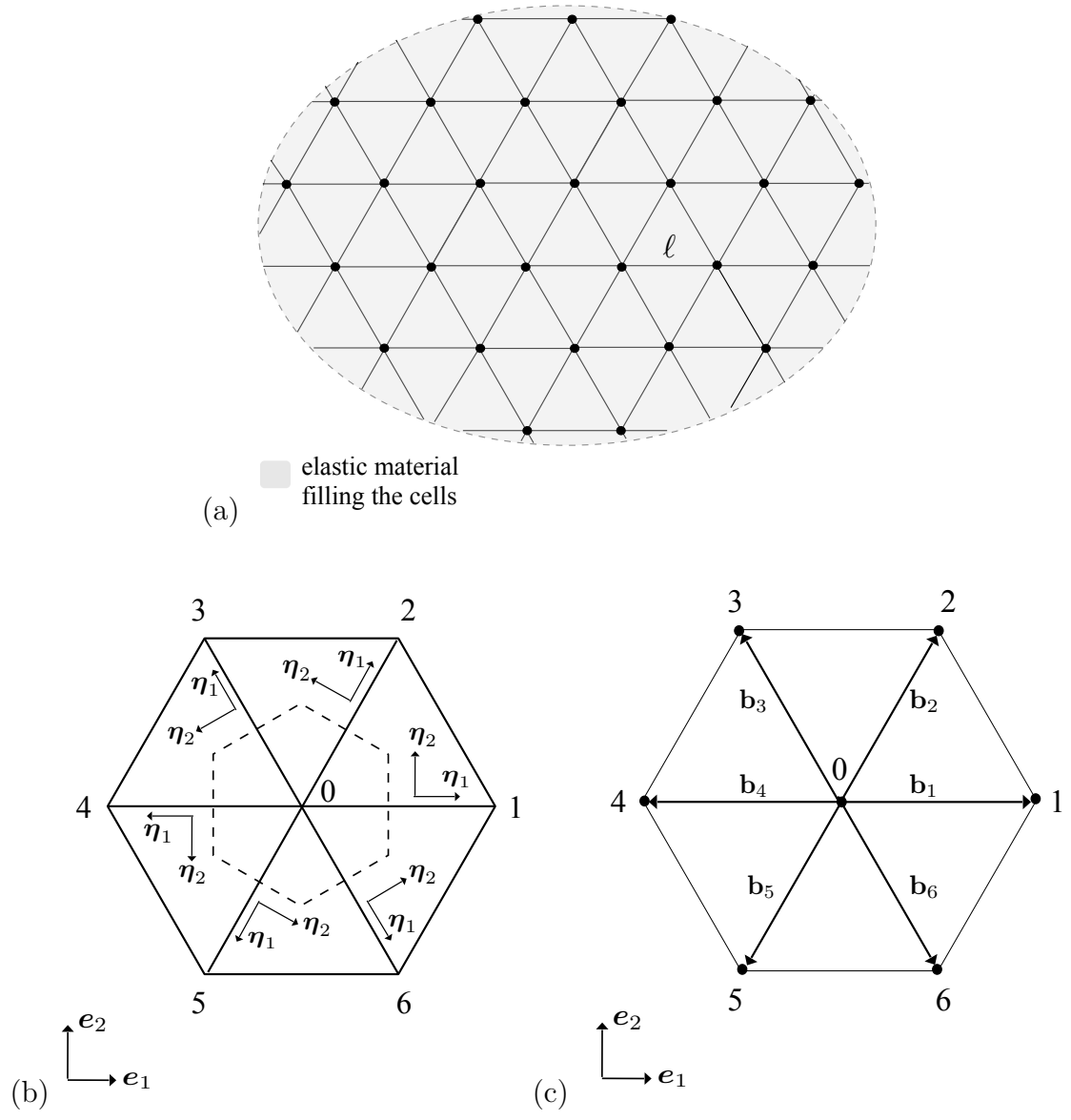

Figure A.1: (a) The equilateral triangular microstructure, (b) the unit cell and (c) the $\mathbf{b}_i$ *vectors*

due to the axial and bending deformations of the beam,

$$w_{wf}^{e,a} := \frac{1}{2} \left(\boldsymbol{\Delta}\mathbf{d}^{e,a}\right)^T \cdot \mathbf{k}_{wf}^{e} \boldsymbol{\Delta}\mathbf{d}^{e,a} \tag{A.4}$$

and

$$w_{wf}^{e,b} := \frac{1}{2} \left(\boldsymbol{\Delta}\mathbf{d}^{e,b}\right)^T \cdot \mathbf{k}_{wf}^{e} \boldsymbol{\Delta}\mathbf{d}^{e,b}, \tag{A.5}$$

related to the elongation of the springs a (Figure A.2a),

$$\boldsymbol{\Delta}\mathbf{d}^{e,a} := \left[\begin{array}{c} \boldsymbol{\Delta}\mathbf{d}_i^a \\ \boldsymbol{\Delta}\mathbf{d}_j^a \end{array} \right] = \left[\begin{array}{cccccc} \Delta u_i^a & \Delta v_i^a & \Delta \varphi_i^a & \Delta u_j^a & \Delta v_j^a & \Delta \varphi_j^a \end{array} \right]^T, \tag{A.6}$$

the first, and of the springs b (Figure A.2b),

$$\boldsymbol{\Delta}\mathbf{d}^{e,b} := \left[\begin{array}{c} \boldsymbol{\Delta}\mathbf{d}_i^b \\ \boldsymbol{\Delta}\mathbf{d}_j^b \end{array} \right] = \left[\begin{array}{cccccc} \Delta u_i^b & \Delta v_i^b & \Delta \varphi_i^b & \Delta u_j^b & \Delta v_j^b & \Delta \varphi_j^b \end{array} \right]^T, \tag{A.7}$$

the second.

Specifically, for the beams 0-1, 0-2, 0-3, 0-4, 0-5, 0-6, the terms in Equations (A.6) and (A.7) are expressed by (Figure A.3),

$$\boldsymbol{\Delta}\,\mathbf{d}^{1,a} = \left[\begin{array}{c} \boldsymbol{\Delta}\,\mathbf{d}_0^a \\ \boldsymbol{\Delta}\,\mathbf{d}_1^a \end{array} \right] = \left[\begin{array}{c} \mathbf{u}_0 - \mathbf{u}_6 \\ \varphi_0 - \varphi_6 \\ \mathbf{u}_1 - \mathbf{u}_6 \\ \varphi_1 - \varphi_6 \end{array} \right], \quad \boldsymbol{\Delta}\,\mathbf{d}^{1,b} = \left[\begin{array}{c} \boldsymbol{\Delta}\,\mathbf{d}_0^b \\ \boldsymbol{\Delta}\,\mathbf{d}_1^b \end{array} \right] = \left[\begin{array}{c} \mathbf{u}_0 - \mathbf{u}_2 \\ \varphi_0 - \varphi_2 \\ \mathbf{u}_1 - \mathbf{u}_2 \\ \varphi_1 - \varphi_2 \end{array} \right], \tag{A.8}$$

$$\boldsymbol{\Delta}\,\mathbf{d}^{2,a} = \left[\begin{array}{c} \boldsymbol{\Delta}\,\mathbf{d}_0^a \\ \boldsymbol{\Delta}\,\mathbf{d}_2^a \end{array} \right] = \left[\begin{array}{c} \mathbf{u}_0 - \mathbf{u}_1 \\ \varphi_0 - \varphi_1 \\ \mathbf{u}_2 - \mathbf{u}_1 \\ \varphi_2 - \varphi_1 \end{array} \right], \quad \boldsymbol{\Delta}\,\mathbf{d}^{2,b} = \left[\begin{array}{c} \boldsymbol{\Delta}\,\mathbf{d}_0^b \\ \boldsymbol{\Delta}\,\mathbf{d}_2^b \end{array} \right] = \left[\begin{array}{c} \mathbf{u}_0 - \mathbf{u}_3 \\ \varphi_0 - \varphi_3 \\ \mathbf{u}_2 - \mathbf{u}_3 \\ \varphi_2 - \varphi_3 \end{array} \right], \tag{A.9}$$

$$\boldsymbol{\Delta}\,\mathbf{d}^{3,a} = \left[\begin{array}{c} \boldsymbol{\Delta}\,\mathbf{d}_0^a \\ \boldsymbol{\Delta}\,\mathbf{d}_3^a \end{array} \right] = \left[\begin{array}{c} \mathbf{u}_0 - \mathbf{u}_2 \\ \varphi_0 - \varphi_2 \\ \mathbf{u}_1 - \mathbf{u}_2 \\ \varphi_1 - \varphi_2 \end{array} \right], \quad \boldsymbol{\Delta}\,\mathbf{d}^{3,b} = \left[\begin{array}{c} \boldsymbol{\Delta}\,\mathbf{d}_0^b \\ \boldsymbol{\Delta}\,\mathbf{d}_3^b \end{array} \right] = \left[\begin{array}{c} \mathbf{u}_0 - \mathbf{u}_4 \\ \varphi_0 - \varphi_4 \\ \mathbf{u}_3 - \mathbf{u}_4 \\ \varphi_3 - \varphi_4 \end{array} \right], \tag{A.10}$$

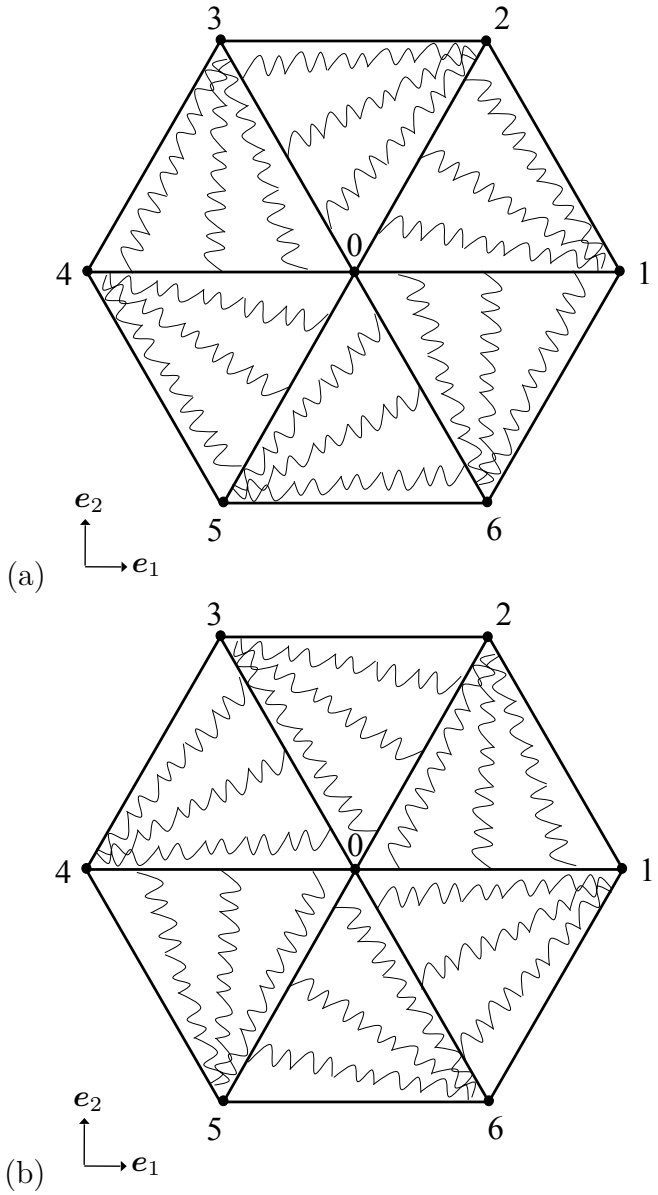

Figure A.2: Equilateral triangular microstructure: (a) springs a, (b) springs b

$$\boldsymbol{\Delta}\,\mathbf{d}^{4,a} = \begin{bmatrix} \boldsymbol{\Delta}\,\mathbf{d}_0^a \\ \boldsymbol{\Delta}\,\mathbf{d}_4^a \end{bmatrix} = \begin{bmatrix} \mathbf{u}_0 - \mathbf{u}_3 \\ \varphi_0 - \varphi_3 \\ \mathbf{u}_4 - \mathbf{u}_3 \\ \varphi_4 - \varphi_3 \end{bmatrix}, \quad \boldsymbol{\Delta}\,\mathbf{d}^{4,b} = \begin{bmatrix} \boldsymbol{\Delta}\,\mathbf{d}_0^b \\ \boldsymbol{\Delta}\,\mathbf{d}_4^b \end{bmatrix} = \begin{bmatrix} \mathbf{u}_0 - \mathbf{u}_5 \\ \varphi_0 - \varphi_5 \\ \mathbf{u}_4 - \mathbf{u}_5 \\ \varphi_4 - \varphi_5 \end{bmatrix}, \tag{A.11}$$

$$\boldsymbol{\Delta}\,\mathbf{d}^{5,a} = \begin{bmatrix} \boldsymbol{\Delta}\,\mathbf{d}_0^a \\ \boldsymbol{\Delta}\,\mathbf{d}_5^a \end{bmatrix} = \begin{bmatrix} \mathbf{u}_0 - \mathbf{u}_4 \\ \varphi_0 - \varphi_4 \\ \mathbf{u}_5 - \mathbf{u}_4 \\ \varphi_5 - \varphi_4 \end{bmatrix}, \quad \boldsymbol{\Delta}\,\mathbf{d}^{5,b} = \begin{bmatrix} \boldsymbol{\Delta}\,\mathbf{d}_0^b \\ \boldsymbol{\Delta}\,\mathbf{d}_5^b \end{bmatrix} = \begin{bmatrix} \mathbf{u}_0 - \mathbf{u}_6 \\ \varphi_0 - \varphi_6 \\ \mathbf{u}_5 - \mathbf{u}_6 \\ \varphi_5 - \varphi_6 \end{bmatrix}, \tag{A.12}$$

$$\boldsymbol{\Delta}\,\mathbf{d}^{6,a} = \begin{bmatrix} \boldsymbol{\Delta}\,\mathbf{d}_0^a \\ \boldsymbol{\Delta}\,\mathbf{d}_6^a \end{bmatrix} = \begin{bmatrix} \mathbf{u}_0 - \mathbf{u}_5 \\ \varphi_0 - \varphi_5 \\ \mathbf{u}_6 - \mathbf{u}_5 \\ \varphi_6 - \varphi_5 \end{bmatrix}, \quad \boldsymbol{\Delta}\,\mathbf{d}^{6,b} = \begin{bmatrix} \boldsymbol{\Delta}\,\mathbf{d}_0^b \\ \boldsymbol{\Delta}\,\mathbf{d}_6^b \end{bmatrix} = \begin{bmatrix} \mathbf{u}_0 - \mathbf{u}_1 \\ \varphi_0 - \varphi_1 \\ \mathbf{u}_6 - \mathbf{u}_1 \\ \varphi_6 - \varphi_1 \end{bmatrix}. \tag{A.13}$$

Also, in Equation (A.2), the factor 1/2 takes into account that each member is shared between two adjacent cells and contributes only half of its strain energy to the representative cell.

The forces and couples acting at the extreme nodes of the beams,

$$\mathbf{f}^e := \begin{bmatrix} \mathbf{f}_i \\ \mathbf{f}_j \end{bmatrix} = \begin{bmatrix} f_{xi} & f_{yi} & m_i & f_{xj} & f_{yj} & m_j \end{bmatrix}^T, \tag{A.14}$$

are obtained from

$$\mathbf{f}^e = \mathbf{f}_b^e + \mathbf{f}_{wf}^{e,a} + \mathbf{f}_{wf}^{e,b}, \tag{A.15}$$

with $\mathbf{f}_b^e$, typical of the Euler-Bernoulli beam, and $\mathbf{f}_{wf}^{e,a}$, $\mathbf{f}_{wf}^{e,b}$, related to the elastic springs, provided by Equations (3.50)-(3.52).

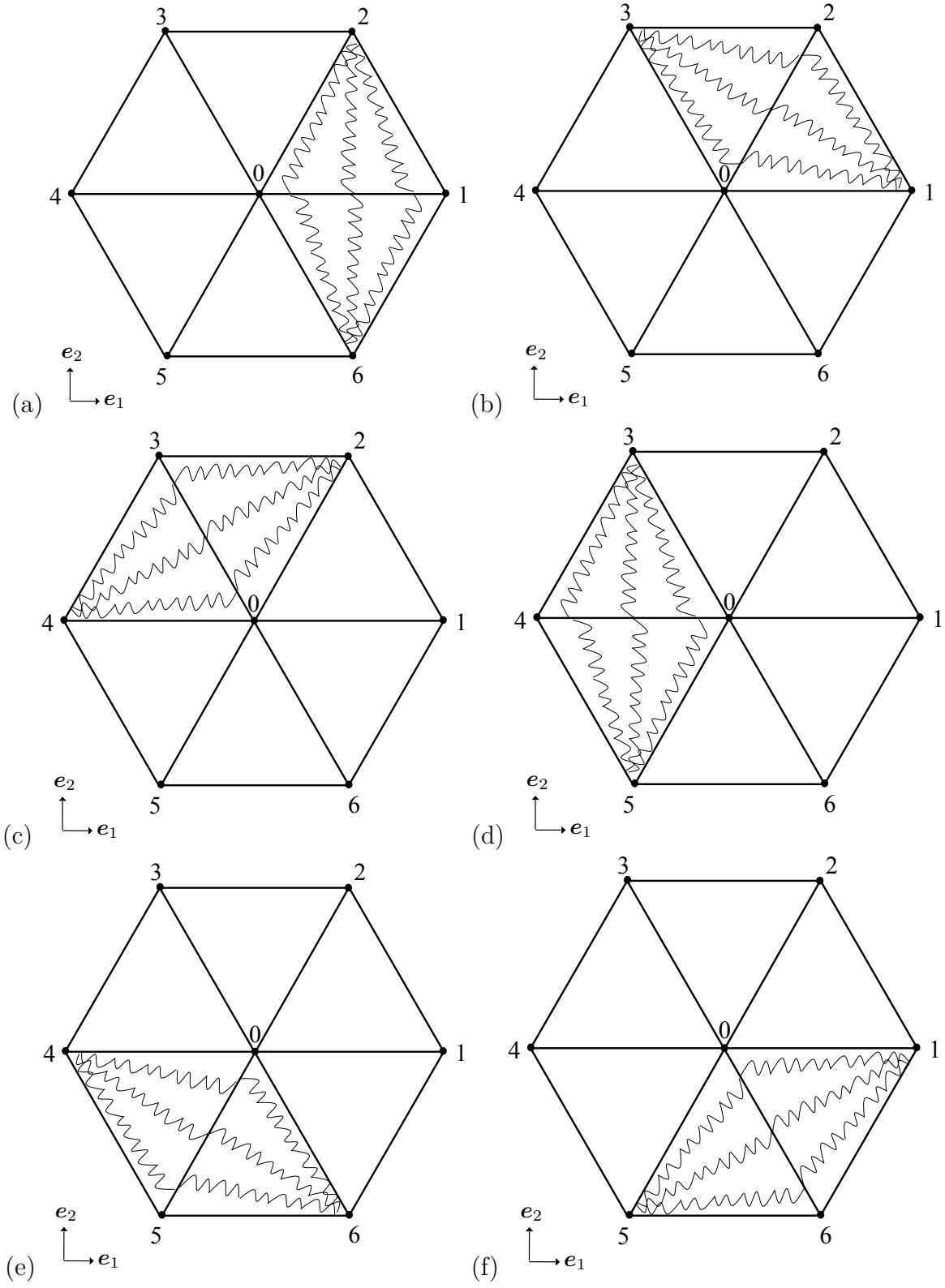

Figure A.3: The unit cell with focus on springs in the equilateral triangular microstructure: (a) beam 0-1, (b) beam 0-2, (c) beam 0-3, (d) beam 0-4, (e) beam 0-5, (f) beam 0-6

From Figure A.1b it is not difficult to see that the first node of each beam coincides with the central point 0. Consequently, as already discussed in Section 3.4.2,

$$\mathbf{f}^e = \begin{bmatrix} \mathbf{f}_0 \\ \mathbf{f}_j \end{bmatrix} = \begin{bmatrix} \mathbf{k}_{b,01}\,\mathbf{d}_j + \mathbf{k}_{b,00}\,\mathbf{d}_0 \\ \mathbf{k}_{b,11}\,\mathbf{d}_j + \mathbf{k}_{b,10}\,\mathbf{d}_0 \end{bmatrix} + \begin{bmatrix} \mathbf{k}_{wf,01}\,\boldsymbol{\Delta}\mathbf{d}_j^a + \mathbf{k}_{wf,00}\,\boldsymbol{\Delta}\mathbf{d}_0^a \\ \mathbf{k}_{wf,11}\,\boldsymbol{\Delta}\mathbf{d}_j^a + \mathbf{k}_{wf,10}\,\boldsymbol{\Delta}\mathbf{d}_0^a \end{bmatrix} + \begin{bmatrix} \mathbf{k}_{wf,01}\,\boldsymbol{\Delta}\mathbf{d}_j^b + \mathbf{k}_{wf,00}\,\boldsymbol{\Delta}\mathbf{d}_0^b \\ \mathbf{k}_{wf,11}\,\boldsymbol{\Delta}\mathbf{d}_j^b + \mathbf{k}_{wf,10}\,\boldsymbol{\Delta}\mathbf{d}_0^b \end{bmatrix}, \quad \text{(A.16)}$$

where $\mathbf{k}_{b,ij}$ and $\mathbf{k}_{wf,ij}$ are the matrices defined in Equations (3.55).

Furthermore, by expressing Equation (A.16) in the global reference system, imposing the balance of forces and moments in 0 and condensing the corresponding degrees of freedom, it emerges

$$W = W\left(\tilde{\mathbf{D}}, \boldsymbol{\Delta}\tilde{\mathbf{D}}^a, \boldsymbol{\Delta}\tilde{\mathbf{D}}^b\right) \equiv W\left(\mathbf{D}_j, \boldsymbol{\Delta}\mathbf{D}_j^a, \boldsymbol{\Delta}\mathbf{D}_j^b\right), \quad j = 1, 2, ..., 6, \quad \text{(A.17)}$$

being

$$\tilde{\mathbf{D}} := \begin{bmatrix} \mathbf{D}_1 \\ \vdots \\ \mathbf{D}_6 \end{bmatrix} = \begin{bmatrix} U_1 & V_1 & \varphi_1 & ... & U_6 & V_6 & \varphi_6 \end{bmatrix}^T \quad \text{(A.18)}$$

the vector of nodal displacements and

$$\boldsymbol{\Delta}\tilde{\mathbf{D}}^a := \begin{bmatrix} \boldsymbol{\Delta}\mathbf{D}_1^a \\ \vdots \\ \boldsymbol{\Delta}\mathbf{D}_6^a \end{bmatrix} = \begin{bmatrix} \Delta U_1^a & \Delta V_1^a & \Delta\varphi_1^a & ... & \Delta U_6^a & \Delta V_6^a & \Delta\varphi_6^a \end{bmatrix}^T, \quad \text{(A.19)}$$

$$\boldsymbol{\Delta}\tilde{\mathbf{D}}^b := \begin{bmatrix} \boldsymbol{\Delta}\mathbf{D}_1^b \\ \vdots \\ \boldsymbol{\Delta}\mathbf{D}_6^b \end{bmatrix} = \begin{bmatrix} \Delta U_1^b & \Delta V_1^b & \Delta\varphi_1^b & ... & \Delta U_6^b & \Delta V_6^b & \Delta\varphi_6^b \end{bmatrix}^T \quad \text{(A.20)}$$

the elongation of the springs in the global reference (cf. Section 3.4.2).

A.2 The equivalent continuum

A.2.1 Elastic energy

Similarly to Section 3.5, the continuum model is obtained by writing the nodal degrees of freedom in Equations (A.18)-(A.20) as a function of the equivalent fields of displacement, $\hat{\mathbf{U}}(\cdot)$, and rotation, $\hat{\varphi}(\cdot)$:

$$\mathbf{U}_j := \begin{bmatrix} U_j \\ V_j \end{bmatrix} = \hat{\mathbf{U}}_0 + \nabla\hat{\mathbf{U}}\,\mathbf{b}_j, \qquad \varphi_j = \hat{\varphi}_0 + \nabla\hat{\varphi}\,\mathbf{b}_j, \qquad j = 1, 2, ..., 6, \tag{A.21}$$

where $\hat{\mathbf{U}}_0$ and $\hat{\varphi}_0$ are the values of $\hat{\mathbf{U}}(\cdot)$ and $\hat{\varphi}(\cdot)$ at the central point of the cell in the limit problem $\ell \to 0$.

Again, substituting Equations (A.21) into Equation (A.17) and dividing the resulting expression by the area of the unit cell, $A_0 = \sqrt{3}\ell^2/2$, provide the strain energy density in the continuum form:

$$\begin{aligned} w = & \frac{\sqrt{3}\left(C_\ell^2\ell^2\left(3\varepsilon_{11}^2 + 4\varepsilon_{12}^2 + 2\varepsilon_{11}\varepsilon_{22} + 3\varepsilon_{22}^2\right) + 48C_\ell D_\ell\left(\varepsilon_{11}^2 + \varepsilon_{22}^2 + 2\varepsilon_{12}^2\right)\right)}{96D_\ell\ell + 8C_\ell\ell^3} \\ & + \frac{6\sqrt{3}\left(D_\ell^2\left(3\varepsilon_{11}^2 + 12\varepsilon_{12}^2 - 6\varepsilon_{11}\varepsilon_{22} + 3\varepsilon_{22}^2\right) + D_\ell\left(12D_\ell + C_\ell\ell^2\right)\left(\omega - \hat{\varphi}\right)^2\right)}{12D_\ell\ell^3 + C_\ell\ell^5} \\ & + \frac{39K_w\left(59\left(\varepsilon_{11}^2 + \varepsilon_{22}^2\right) + 96\varepsilon_{12}^2 + 22\varepsilon_{11}\varepsilon_{22}\right)}{4480\sqrt{3}}. \end{aligned} \tag{A.22}$$

As it can be seen, in the limit $\ell \to 0$ the contribution of the microrotation gradients, $\hat{\varphi}_{,\alpha}$, is missing (cf. Section 3.5.1), leading to a not-polar equivalent continuum. It should be noted that in Equation (A.22) the same notation of Section 3.5 has been adopted.

A.2.2 Constitutive equations

Referring to Section 3.5.2 for a more detailed description, the explicit formulas for the constitutive equations are derived by

$$\sigma_{\gamma\delta} := \frac{\partial w}{\partial \hat{U}_{\gamma,\delta}} = \frac{\partial w}{\partial \varepsilon_{\gamma\delta}} + \frac{1}{2}\frac{\partial w}{\partial \omega}\, e_{\gamma\delta} \equiv \sigma_{\gamma\delta}^{sym} + \sigma_{\gamma\delta}^{skw}, \quad \gamma, \delta = 1, 2, \tag{A.23}$$

with $\sigma_{\gamma\delta}^{sym}$ and $\sigma_{\gamma\delta}^{skw}$, in turn, the symmetric and skew-symmetric parts of the Cauchy stress tensor.

In particular, it emerges

$$\begin{aligned}
\sigma_{11} &= \left(\frac{9\,(C_\ell \ell^2 + 4D_\ell)}{4\sqrt{3}\ell^3} + \frac{767K_w}{2240\sqrt{3}}\right)\varepsilon_{11} + \left(\frac{3\,(C_\ell \ell^2 - 12D_\ell)}{4\sqrt{3}\ell^3} + \frac{143K_w}{2240\sqrt{3}}\right)\varepsilon_{22},\\
\sigma_{22} &= \left(\frac{9\,(C_\ell \ell^2 + 4D_\ell)}{4\sqrt{3}\ell^3} + \frac{767\,K_w}{2240\sqrt{3}}\right)\varepsilon_{22} + \left(\frac{3\,(C_\ell \ell^2 - 12D_\ell)}{4\sqrt{3}\ell^3} + \frac{143\,K_w}{2240\sqrt{3}}\right)\varepsilon_{11},\\
\sigma_{12}^{sym} &= \sigma_{21}^{sym} = \left(\frac{3\,(C_\ell \ell^2 + 12D_\ell)}{2\sqrt{3}\ell^3} + \frac{39\,K_w}{140\sqrt{3}}\right)\varepsilon_{12},\\
\sigma_{12}^{skw} &= -\sigma_{21}^{skw} = \frac{12\sqrt{3}\,D_\ell}{\ell^3}\,(\omega - \hat{\varphi})\,,\\
\sigma_{12} &= \sigma_{12}^{sym} + \sigma_{12}^{skw}, \quad \sigma_{21} = \sigma_{21}^{sym} + \sigma_{21}^{skw}.
\end{aligned} \tag{A.24}$$

A.2.3 Elastic constants

Simple mathematical manipulations provide the elastic constants of the equivalent continuum (cf. Section 3.5.3).

The Young's modulus and corresponding Poisson's ratio in the $\boldsymbol{e}_1$ and $\boldsymbol{e}_2$ direction are given, respectively, by

$$E_1 := \frac{\sigma_{11}}{\varepsilon_{11}} = \frac{\sqrt{3}\,(13\,K_w(1-\nu_s^2) + 32E_s\lambda)\,(39\,K_w(1-\nu_s^2) + 70E_s\lambda\,(1+\lambda^2))}{2(1-\nu_s^2)\,(767K_w(1-\nu_s^2) + 560E_s\lambda\,(3+\lambda^2))}, \tag{A.25}$$

$$\nu_{12} := -\frac{\varepsilon_{22}}{\varepsilon_{11}} = \frac{143K_w(1-\nu_s^2) - 560_s\,(\lambda^2-1)}{767K_w(1-\nu_s^2) + 560_s\,(\lambda^2+3)}, \tag{A.26}$$

and

$$E_2 := \frac{\sigma_{22}}{\varepsilon_{22}} = E_1 \equiv E, \qquad \nu_{21} := -\frac{\varepsilon_{11}}{\varepsilon_{22}}\nu_{12} \equiv \nu, \tag{A.27}$$

with $\lambda := h/\ell$ denoting the thinness ratio.

Finally, the effective shear modulus takes the form

$$G := \frac{\sigma_{12}^{sym}}{2\varepsilon_{12}} = \frac{\sqrt{3}\,(39K_w(1-\nu_s^2) + 70_s\,(\lambda^2+1))}{280(1-\nu_s^2)}. \tag{A.28}$$

A.3 Numerical implementation and validation of the theoretical results

A procedure similar to that proposed in Section 3.6.1 can be employed to verify the analytical results.

That is to say, by considering a 75x50 mm domain discretized in a number of gradually smaller equilateral triangular cells, modelled as a sequence of Euler-Bernoulli beams having $E_s = 79$ GPa, $\nu_s = 0.35$ and $h = 0.1\ell$, supported by elastic springs of stiffness $K_w = 10^{-2}E_s$. The three examined load conditions, uniaxial compression in the $\boldsymbol{e}_1$ direction, uniaxial compression in the $\boldsymbol{e}_2$ direction and pure shear, are simulated by applying forces of the same intensity at the unconstrained boundary nodes of the domain.

The solution of the corresponding boundary value problems and the calculation of the displacements and derived quantities along the beams provide the homogenized stiffness components, given by the ratio between the average volume strain,

$$\overline{\varepsilon}_{ij}^{(\cdot)} := \frac{1}{V}\int_V \varepsilon_{ij}^{(\cdot)}\, dV, \qquad i,j = 1,2, \tag{A.29}$$

and the applied stress, $\overline{\sigma}_{ij}$.

In particular, denoting with S_{ij} the components of the homogenized compliance tensor (cf. Section 3.6.1), in the case of horizontal and vertical compression it emerges, on order,

$$S_{11} = \frac{\overline{\varepsilon}_{11}^{(1)}}{\overline{\sigma}_{11}} \equiv \frac{1}{E_1}, \qquad S_{21} = \frac{\overline{\varepsilon}_{22}^{(1)}}{\overline{\sigma}_{11}} \equiv -\frac{\nu_{21}}{E_1}, \qquad S_{31} = \frac{2\,\overline{\varepsilon}_{12}^{(1)}}{\overline{\sigma}_{11}} \tag{A.30}$$

and

$$S_{12} = \frac{\overline{\varepsilon}_{11}^{(2)}}{\overline{\sigma}_{22}} \equiv -\frac{\nu_{21}}{E_2}, \qquad S_{22} = \frac{\overline{\varepsilon}_{22}^{(2)}}{\overline{\sigma}_{22}} \equiv \frac{1}{E_2}, \qquad S_{32} = \frac{2\,\overline{\varepsilon}_{12}^{(2)}}{\overline{\sigma}_{22}} \tag{A.31}$$

while, for pure shear,

$$S_{13} = \frac{\overline{\varepsilon}_{11}^{(3)}}{\overline{\sigma}_{12}}, \qquad S_{23} = \frac{\overline{\varepsilon}_{22}^{(3)}}{\overline{\sigma}_{12}}, \qquad S_{33} = \frac{2\,\overline{\varepsilon}_{12}^{(3)}}{\overline{\sigma}_{12}} \equiv \frac{1}{G}. \tag{A.32}$$

Tables A.1 and A.2 summarise the results of the analysis: Table A.1 in terms of the S_{ij} constants, Table A.2 in terms of the elastic moduli.

Initially, the convergence study performed reveals that the numerical solutions fast converge by refining the mesh. As it can be seen, a 750x500 cells discretization is sufficient to get converged results.

Table A.1 Equilateral triangular microstructure: comparison between the analytical and numerical approach, S_{ij} constants (GPa^{-1})

No. cells	ℓ (mm)	S_{11}	S_{22}	S_{33}	S_{12}	S_{21}	$S_{13}, S_{23}, S_{31}, S_{32}$
15x10	5	0.094	0.094	0.238	-0.03	-0.03	0
75x50	1	0.095	0.094	0.239	-0.03	-0.03	0
100x100	0.5	0.095	0.095	0.240	-0.03	-0.03	0
300x200	0.25	0.095	0.095	0.241	-0.03	-0.03	0
375x250	0.2	0.095	0.095	0.243	-0.03	-0.03	0
600x400	0.125	0.095	0.095	0.251	-0.03	-0.03	0
750x500	0.1	0.095	0.095	0.251	-0.03	-0.03	0
Analytical results		0.096	0.096	0.254	-0.03	-0.03	0

Table A.2 Equilateral triangular microstructure: comparison between the analytical and numerical approach, elastic moduli

No. cells	ℓ (mm)	E_1 (GPa)	E_2 (GPa)	G (GPa)	ν_{12}	ν_{21}
15x10	5	10.59	10.61	4.19	0.38	0.37
75x50	1	10.57	10.59	4.17	0.36	0.35
100x100	0.5	10.56	10.58	4.16	0.35	0.35
300x200	0.25	10.54	10.56	4.15	0.33	0.34
375x250	0.2	10.53	10.55	4.11	0.33	0.33
600x400	0.125	10.53	10.54	3.99	0.33	0.33
750x500	0.1	10.53	10.54	3.99	0.33	0.33
Analytical results		10.46	10.46	3.94	0.33	0.33

In addition, Tables A.1 and A.2 suggest a good agreement between the theoretical and numerical predictions, with an average difference of 1.5% between the two estimates. Similarly to the case of the hexagonal honeycomb (cf. Section 3.6.1), the difference could be related to the Saint-Venant border effect that, contrary to the numerical simulations, it is not captured by the proposed theory. This aspect, however, considering the outcome of the present study, slightly affect the prediction ability of the theoretical model.

Finally, for the sake of completeness, it should be said that the analytical values in Tables A.1 and A.2 are calculated by substituting

$$\begin{aligned} C_{11} = C_{22} &= \frac{3\sqrt{3}\,(C_\ell \ell^2 + 4D_\ell)}{4\,\ell^3} + \frac{767\,K_w}{2240\sqrt{3}}, \\ C_{12} = C_{21} &= \frac{\sqrt{3}\,(C_\ell \ell^2 - 12D_\ell)}{4\,\ell^3} + \frac{143\,K_w}{2240\sqrt{3}}, \\ C_{33} &= \frac{\sqrt{3}\,(C_\ell \ell^2 + 12D_\ell)}{2\,\ell^3} + \frac{39\,K_w}{140\sqrt{3}}, \\ C_{13} = C_{23} = \; & C_{31} = C_{32} = 0, \end{aligned} \tag{A.33}$$

obtained in Section A.2.2, into the Equations (3.98).

B | A continuum model for the composite honeycomb with square microstructure

A continuum model for the composite honeycomb with square microstructure can be obtained by adopting the same procedure described in Chapter 3 for the regular hexagonal texture. Thus, for the sake of conciseness and clarity, in the following sections only the main results will be reported and explanations will be provided only where substantial modifications are required.

B.1 The composite square microstructure: geometric description and energetics of the discrete system

B.1.1 Geometry

Figure B.1 schematically illustrates the composite square microstructure, Figure B.1a, and its unit cell, Figure B.1b. The latter is composed by the line elements 0-1, 0-2, 0-3, 0-4, treated as Euler-Bernoulli beams elastically supported by a Winkler foundation, that link the central node 0 to the external joints 1, 2, 3, 4. In the global coordinate system ($\boldsymbol{e}_1$, $\boldsymbol{e}_2$), the elastic beams are represented by the vectors (Figure B.1c)

$$\mathbf{b}_1 = \begin{bmatrix} \ell & 0 \end{bmatrix}^T, \qquad \mathbf{b}_2 = \begin{bmatrix} 0 & \ell \end{bmatrix}^T, \qquad \mathbf{b}_3 = -\mathbf{b}_1, \qquad \mathbf{b}_4 = -\mathbf{b}_2, \tag{B.1}$$

respectively. Finally, $A_0 = \ell^2$ gives the area of the unit cell (Figure B.1b).

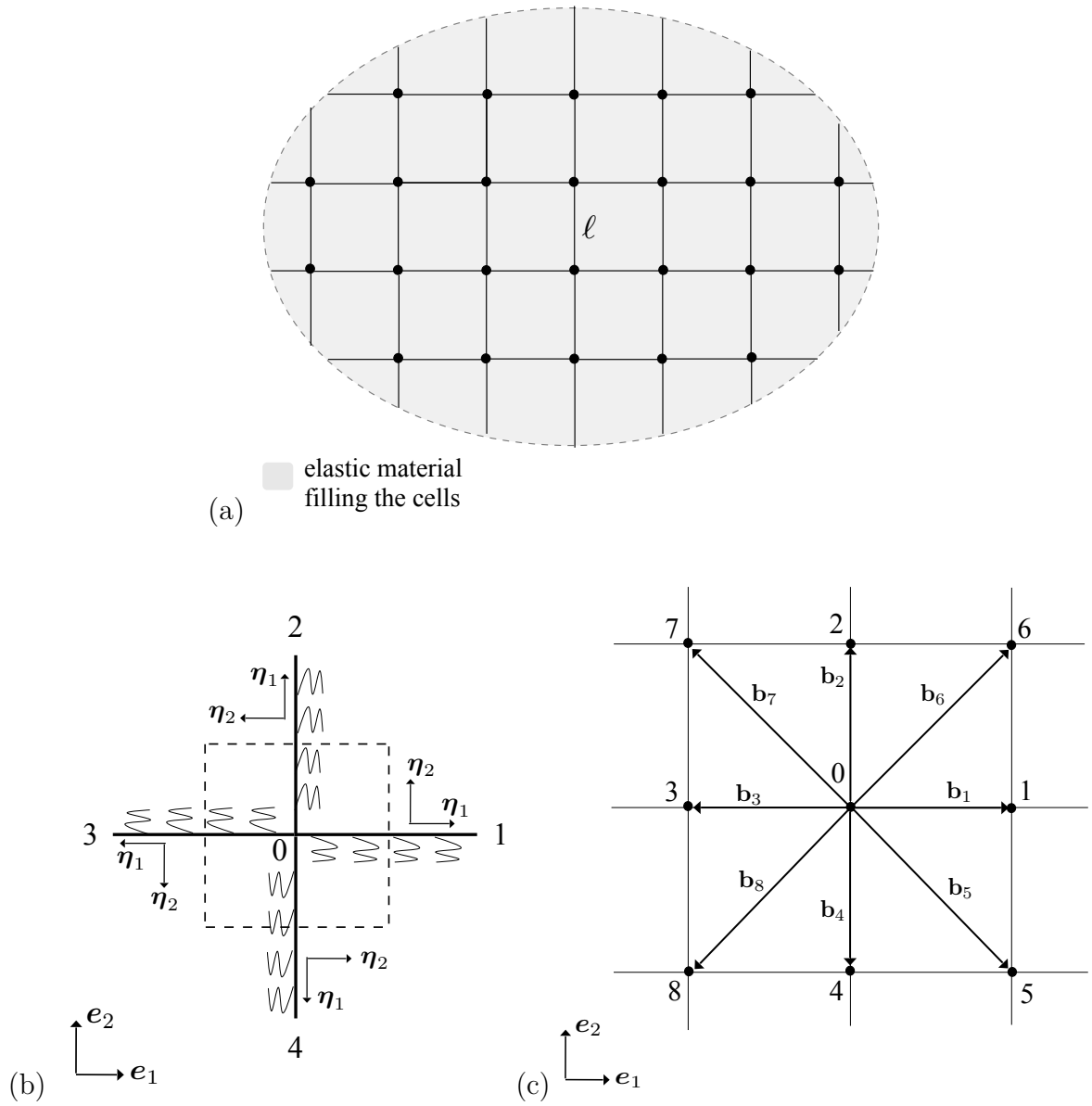

Figure B.1: The composite honeycomb with square microstructure: (a) geometric description, (b) unit cell and (c) $\mathbf{b}_i$ *vectors*

B.1.2 Energetics

As it can be seen in Figure B.2, in the examined lattice the beams are connected to the corresponding one by two sets of springs: the springs a, in the $-\boldsymbol{\eta}_2$ direction (Figure B.2a), and the springs b, in the $\boldsymbol{\eta}_2$ direction (Figure B.2b).

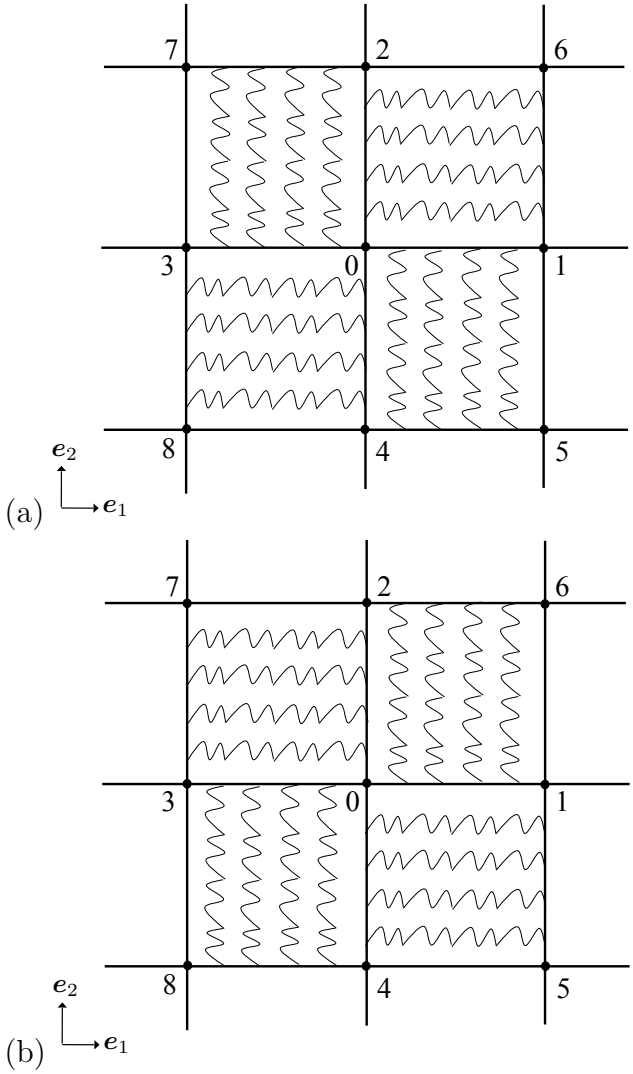

Figure B.2: The square microstructure: (a) springs a, (b) springs b

Also, being the springs shared between two opposite beams,

$$w^e = w_b^e + \frac{1}{2}\, w_{wf}^{e,a} + \frac{1}{2}\, w_{wf}^{e,b} \tag{B.2}$$

gives the elastic energy of each structural component (cf. Equation (3.33)). With the same notation of Section 3.4, in Equation (B.2) w_b^e stands for the elastic energy of the

Table B.1 The elongation of the springs in the square microstructure: indices i, j, k, l, m

	i	j	k	l	m
beam 0-1	1	4	5	2	6
beam 0-2	2	1	6	3	7
beam 0-3	3	2	7	4	8
beam 0-4	4	3	8	1	5

classical Euler-Bernoulli beam, while $w_{wf}^{e,a}$ and $w_{wf}^{e,b}$ are a function of the elongation of the springs, expressed by (Figure B.3)

$$\boldsymbol{\Delta}\,\mathbf{d}^{i,a} = \begin{bmatrix} \boldsymbol{\Delta}\,\mathbf{d}_0^a \\ \boldsymbol{\Delta}\,\mathbf{d}_i^a \end{bmatrix} = \begin{bmatrix} \mathbf{u}_0 - \mathbf{u}_j \\ \varphi_0 - \varphi_j \\ \mathbf{u}_i - \mathbf{u}_k \\ \varphi_i - \varphi_k \end{bmatrix}, \quad \boldsymbol{\Delta}\,\mathbf{d}^{i,b} = \begin{bmatrix} \boldsymbol{\Delta}\,\mathbf{d}_0^b \\ \boldsymbol{\Delta}\,\mathbf{d}_i^b \end{bmatrix} = \begin{bmatrix} \mathbf{u}_0 - \mathbf{u}_l \\ \varphi_0 - \varphi_l \\ \mathbf{u}_i - \mathbf{u}_m \\ \varphi_i - \varphi_m \end{bmatrix}, \tag{B.3}$$

where the indices i, j, k, l, m are provided in Table B.1.

In terms of the elastic energy of the unit cell, W, calculated from the contribution of the constituent beams, it should be noted that only half of each member is within the elementary cell. Thus, in evaluating W, only $w^e/2$ will be considered. In addition, similarly to the case of the hexagonal lattice, imposing the equilibrium of forces and moments in 0 and performing a condensation of the corresponding degrees of freedom, lead to

$$W = W\left(\tilde{\mathbf{D}}, \boldsymbol{\Delta}\tilde{\mathbf{D}}^a, \boldsymbol{\Delta}\tilde{\mathbf{D}}^b\right) \tag{B.4}$$

with

$$\tilde{\mathbf{D}} := \begin{bmatrix} \mathbf{D}_1 \\ \vdots \\ \mathbf{D}_4 \end{bmatrix} = \begin{bmatrix} U_1 & V_1 & \varphi_1 & \dots & U_4 & V_4 & \varphi_4 \end{bmatrix}^T \tag{B.5}$$

and

$$\boldsymbol{\Delta}\tilde{\mathbf{D}}^a := \begin{bmatrix} \boldsymbol{\Delta}\mathbf{D}_1^a \\ \vdots \\ \boldsymbol{\Delta}\mathbf{D}_4^a \end{bmatrix} = \begin{bmatrix} \Delta U_1^a & \Delta V_1^a & \Delta\varphi_1^a & \dots & \Delta U_4^a & \Delta V_4^a & \Delta\varphi_4^a \end{bmatrix}^T, \tag{B.6}$$

$$\boldsymbol{\Delta}\tilde{\mathbf{D}}^b := \begin{bmatrix} \boldsymbol{\Delta}\mathbf{D}_1^b \\ \vdots \\ \boldsymbol{\Delta}\mathbf{D}_4^b \end{bmatrix} = \begin{bmatrix} \Delta U_1^b & \Delta V_1^b & \Delta\varphi_1^b & \dots & \Delta U_4^b & \Delta V_4^b & \Delta\varphi_4^b \end{bmatrix}^T, \tag{B.7}$$

in turn, the vectors of nodal displacements and elongation of the springs expressed in the global reference $(\boldsymbol{e}_1, \boldsymbol{e}_2)$.

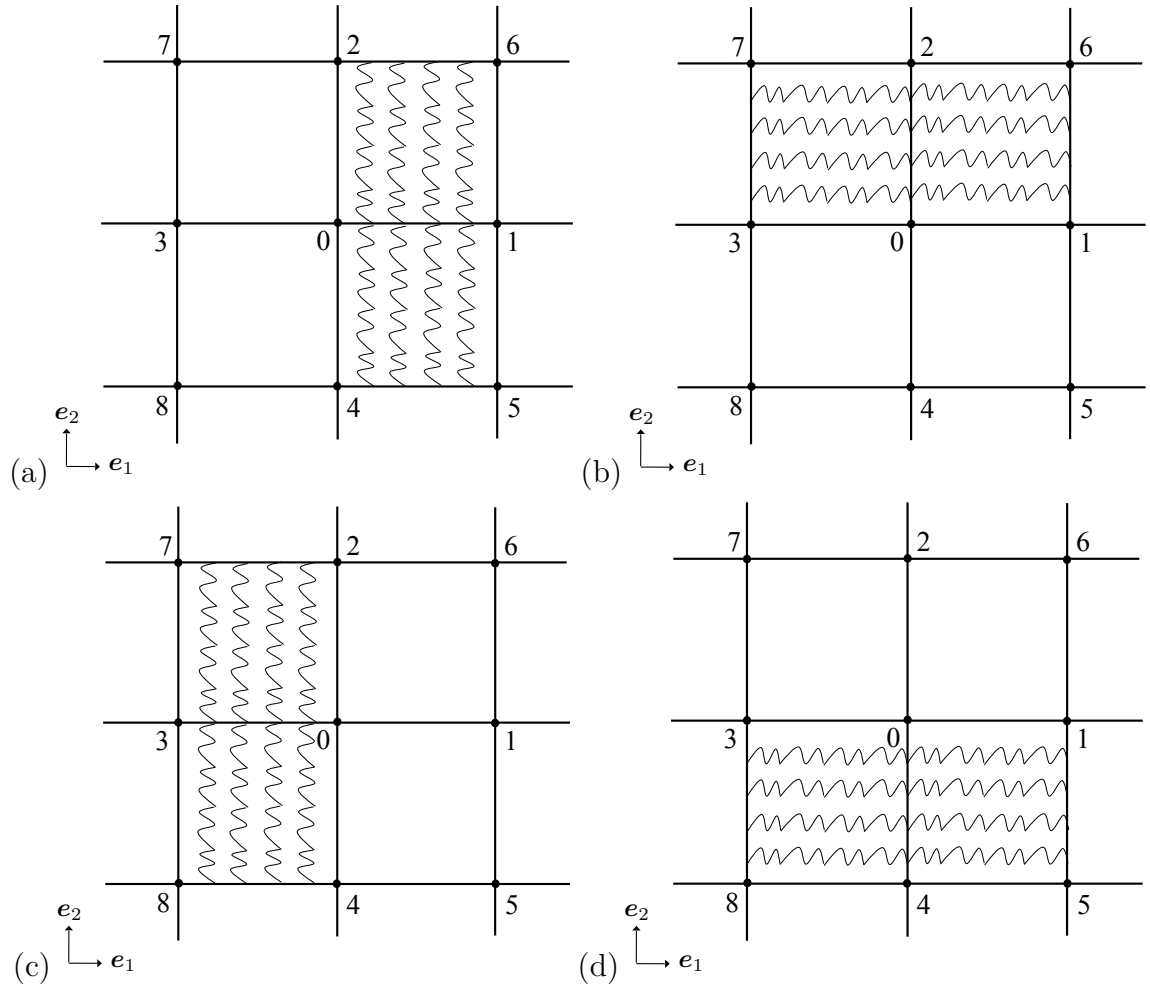

Figure B.3: The unit cell with focus on springs in the square microstructure: (a) beam 0-1, (b) beam 0-2, (c) beam 0-3, (d) beam 0-4

B.2 The continuum model

B.2.1 Elastic energy

As in Section 3.5, the continuum model follows from the hypothesis that in the limit $\ell \to 0$ there exist the two equivalent, continuous fields of displacements, $\hat{\mathbf{U}}(\cdot)$, and microrotation, $\hat{\varphi}(\cdot)$. In particular, writing the discrete variables in Equation (B.4) in terms of the gradients of $\hat{\mathbf{U}}(\cdot)$ and $\hat{\varphi}(\cdot)$ (cf. Equation (3.71)) and dividing the

obtained expression by A_0, give the strain energy density of the equivalent (not-polar) continuum:

$$w = \frac{C_\ell \ell^2 \left(\varepsilon_{11}^2 + \varepsilon_{22}^2\right) + 24 D_\ell \left(\varepsilon_{12}^2 + \left(\omega - \hat{\varphi}\right)^2\right) + K_w \ell^3 \left(\varepsilon_{11}^2 + \varepsilon_{22}^2\right)}{2\,\ell^3}. \tag{B.8}$$

Again,

$$C_\ell := \frac{E_s\, h}{1-\nu_s^2} \qquad \text{and} \qquad D_\ell := \frac{E_s\, h^3}{12(1-\nu_s^2)} \tag{B.9}$$

denote, respectively, the axial and bending stiffness of the beams, having thickness h, length l, Young's modulus E_s and Poisson's ratio ν_s.

B.2.2 Constitutive equations

The explicit formulas for the macroscopic constitutive equations are a consequence of Equation (B.8).

It emerges that the resulting stress tensor is not-symmetric and its components,

$$\sigma_{\gamma\delta} := \frac{\partial w}{\partial \hat{U}_{\gamma,\delta}} = \frac{\partial w}{\partial \varepsilon_{\gamma\delta}} + \frac{1}{2}\frac{\partial w}{\partial \omega}\, e_{\gamma\delta} \equiv \sigma_{\gamma\delta}^{sym} + \sigma_{\gamma\delta}^{skw}, \quad \gamma,\delta = 1,2, \tag{B.10}$$

are

$$\begin{aligned}
\sigma_{11} &= \left(\frac{C_\ell}{\ell} + K_w\right)\varepsilon_{11},\\
\sigma_{22} &= \left(\frac{C_\ell}{\ell} + K_w\right)\varepsilon_{22},\\
\sigma_{12}^{sym} &= \sigma_{21}^{sym} = \left(\frac{3\left(C_\ell \ell^2 + 12 D_\ell\right)}{2\sqrt{3}\ell^3} + \frac{39\, K_w}{140\sqrt{3}}\right)\varepsilon_{12},\\
\sigma_{12}^{skw} &= -\sigma_{21}^{skw} = \frac{12 D_\ell}{\ell^3}\varepsilon_{12},\\
\sigma_{12} &= \sigma_{12}^{sym} + \sigma_{12}^{skw}, \quad \sigma_{21} = \sigma_{21}^{sym} + \sigma_{21}^{skw}.
\end{aligned} \tag{B.11}$$

B.2.3 Elastic constants

If applied to the square microstructure, the approach presented in Section 3.5.3 provides

$$E_1 = E_2 \equiv E = \frac{E_s\,\lambda}{(1-\nu_s^2)} + K_w,$$

$$\nu_{12} = \nu_{21} \equiv \nu = 0, \tag{B.12}$$

$$G = \frac{E_s\,\lambda^3}{2\,(1-\nu_s^2)},$$

where E_1, ν_{12} and E_2, ν_{21} are, respectively, the effective Young's modulus and Poisson's ratio in the $\boldsymbol{e}_1$ and $\boldsymbol{e}_2$ direction, G the effective shear modulus and $\lambda := h/\ell$ the thinness ratio. As expected, the analysis reveals that

$$G \neq \frac{E}{2\,(1+\nu)}, \tag{B.13}$$

being the equivalent continuum not-isotropic.

In particular, the classic transformations equations for stress and strain, in conjunction with simple mathematical manipulations, lead to the macroscopic elastic constants associated with different directions:

$$E_\theta = \frac{\lambda^3 E_s\,(K_w\,(1-\nu_s^2) + \lambda E_s)}{(1-\nu_s^2)\,(\lambda^3 E_s\,(c^4+s^4) + 2c^2s^2\,(K_w\,(1-\nu_s^2) + \lambda E_s))},$$

$$\nu_\theta = \frac{2c^2s^2\,(K_w\,(1-\nu_s^2) + \lambda E_s - \lambda^3 E_s)}{\lambda^3 E_s\,(c^4+s^4) + 2c^2s^2\,(K_w\,(1-\nu_s^2) + \lambda E_s)}, \tag{B.14}$$

$$G_\theta = \frac{\lambda^3 E_s\,(K_w\,(1-\nu_s^2) + \lambda E_s)}{4\,(1-\nu_s^2)\left(\left(c^2-s^2\right)^2 K_w\,(1-\nu_s^2) + \lambda\,(c^4 + 2c^2\,(2\lambda^2-1)\,s^2 + s^4)\,E_s\right)},$$

with E_θ, ν_θ, G_θ, in turn, the Young's modulus, Poisson's ratio and shear modulus associated with the axis rotated counterclockwise through an angle of θ from $(\boldsymbol{e}_1, \boldsymbol{e}_2)$. In addition, to simplify the notation, c and s stand for $\cos\theta$, the first, and $\sin\theta$, the second.

Finally, in the case of $K_w = 0$ (i.e., not-filled honeycomb), it emerges that Equations (B.12) exactly match those available in the literature, proposed by Gibson and Ashby (cf. Equation (2.6)) and by Gonnella and Ruzzene (Gonnella & Ruzzene, 2008), listed

as

$$E_{1,GR} = E_{2,GR} \equiv E_{GR} = E_s\,\lambda,$$

$$\nu_{12,GR} = \nu_{21,GR} \equiv \nu_{GR} = 0, \tag{B.15}$$

$$G_{GR} = \frac{E_s\,\lambda^3}{2}.$$

B.3 Validation of the theory: comparison between the theoretical predictions and the numerical results

Tables B.2 and B.3 present the results of the numerical simulations, with reference to the elastic moduli (Table B.3) and S_{ij} constants, components of the homogenized compliance tensor (Table B.2). As explained in Section 3.6.1, the simulations are conducted on a 50x50 mm domain subjected to different types of load conditions: uniaxial compression in the $\boldsymbol{e}_1$ direction, uniaxial compression in the $\boldsymbol{e}_2$ direction, pure shear. In terms of geometric and mechanical properties of the cell walls, modelled as Euler-Bernoulli beams on Winkler foundation, it is assumed $h = 0.1\ell$, $E_s = 79$ GPa, $\nu_s = 0.35$ and $K_w = 10^{-2}E_s$.

Again, the mesh density (i.e., the number of square cells discretizing the domain) is increased until the results converge satisfactory. In particular, in the examined case, convergence is achieved at 500x500 cells discretization.

Finally, it should be noted that the numerical solutions are obtained by applying the computational homogenization scheme described in Section 3.6.1, where both the elastic moduli and S_{ij} constants are given by the ratio between the average volume strain, $\overline{\varepsilon}_{ij}^{(\cdot)}$, and the applied stress, $\overline{\sigma}_{ij}$ (cf. Equations (3.111), (3.113) and (3.115)).

Generally, it can be said that the numerical results are in very good agreement with the theoretical predictions, derived by substituting

$$C_{11} = C_{22} = \frac{C_\ell}{\ell} + K_w,$$

$$C_{33} = \frac{12D_\ell}{\ell^3}, \tag{B.16}$$

$$C_{12} = C_{21} = C_{13} = C_{23} = C_{31} = C_{32} = 0,$$

Table B.2 Square microstructure: comparison between the analytical and numerical approach, S_{ij} constants (GPa^{-1})

No. cells	ℓ (mm)	S_{11}	S_{22}	S_{33}	$S_{12}, S_{21}, S_{13}, S_{23}, S_{31}, S_{32}$
10x10	5	0.1094	0.1093	19.61	0
50x50	1	0.1095	0.1096	20.83	0
100x100	0.5	0.1097	0.1098	21.74	0
200x200	0.25	0.1098	0.110	22.22	0
250x250	0.2	0.110	0.110	22.22	0
400x400	0.125	0.110	0.110	22.22	0
500x500	0.1	0.110	0.110	22.22	0
Analytical results		0.111	0.111	22.22	0

Table B.3 Square microstructure: comparison between the analytical and numerical approach, elastic moduli

No. cells	ℓ (mm)	E_1 (GPa)	E_2 (GPa)	G (GPa)	ν_{12}, ν_{21}
10x10	5	9.14	9.15	4.19	0
50x50	1	9.13	9.12	4.17	0
100x100	0.5	9.11	9.10	4.16	0
200x200	0.25	9.10	9.09	4.15	0
250x250	0.2	9.08	9.08	4.11	0
400x400	0.125	9.08	9.07	3.99	0
500x500	0.1	9.08	9.07	3.99	0
Analytical results		9.00	9.00	3.94	0

calculated in Section B.2.2, into Equations (3.98). Specifically, the two estimates differ of averagely 1%, revealing the validity of the proposed theory in investigating the mechanics of composite materials with square microstructure.

C | From the local to the global reference system

C.1 Degrees of freedom

Let us focus on the e-th Euler-Bernoulli beam on Winkler foundation element in Figure C.1 and let us denote with

$$\mathbf{d}^e := \begin{bmatrix} \mathbf{d}_i \\ \mathbf{d}_j \end{bmatrix} = \begin{bmatrix} u_i & v_i & \varphi_i & u_j & v_j & \varphi_j \end{bmatrix}^T \tag{C.1}$$

and

$$\boldsymbol{\Delta}\mathbf{d}^{e,a} := \begin{bmatrix} \boldsymbol{\Delta}\mathbf{d}_i^a \\ \boldsymbol{\Delta}\mathbf{d}_j^a \end{bmatrix} = \begin{bmatrix} \Delta u_i^a & \Delta v_i^a & \Delta \varphi_i^a & \Delta u_j^a & \Delta v_j^a & \Delta \varphi_j^a \end{bmatrix}^T, \tag{C.2}$$

$$\boldsymbol{\Delta}\mathbf{d}^{e,b} := \begin{bmatrix} \boldsymbol{\Delta}\mathbf{d}_i^b \\ \boldsymbol{\Delta}\mathbf{d}_j^b \end{bmatrix} = \begin{bmatrix} \Delta u_i^b & \Delta v_i^b & \Delta \varphi_i^b & \Delta u_j^b & \Delta v_j^b & \Delta \varphi_j^b \end{bmatrix}^T, \tag{C.3}$$

respectively, the vectors of nodal displacements and elongation of the springs (cf. Section 3.4.1) expressed in the local reference system ($\boldsymbol{\eta}_1^e$, $\boldsymbol{\eta}_2^e$).

Similarly, let

$$\mathbf{D} := \begin{bmatrix} \mathbf{D}_I \\ \mathbf{D}_J \end{bmatrix} = \begin{bmatrix} U_I & V_I & \varphi_I & U_J & V_J & \varphi_J \end{bmatrix}^T \tag{C.4}$$

and

$$\boldsymbol{\Delta}\mathbf{D}^a := \begin{bmatrix} \boldsymbol{\Delta}\mathbf{D}_I^a \\ \boldsymbol{\Delta}\mathbf{D}_J^a \end{bmatrix} = \begin{bmatrix} \Delta U_I^a & \Delta V_I^a & \Delta \varphi_I^a & \Delta U_J^a & \Delta V_J^a & \Delta \varphi_J^a \end{bmatrix}^T, \tag{C.5}$$

$$\boldsymbol{\Delta}\mathbf{D}^b := \left[\begin{array}{c} \boldsymbol{\Delta}\mathbf{D}^b_I \\ \boldsymbol{\Delta}\mathbf{D}^b_J \end{array} \right] = \left[\begin{array}{cccccc} \Delta U^b_I & \Delta V^b_I & \Delta\varphi^b_I & \Delta U^b_J & \Delta V^b_J & \Delta\varphi^b_J \end{array} \right]^T \tag{C.6}$$

be the corresponding vectors referred to the global coordinate system ($\boldsymbol{e}_1$, $\boldsymbol{e}_2$).

The relation between the local and the global quantities can be easily obtained by introducing the transformation matrix

$$\mathbf{Q}^e := \left[\begin{array}{cccccc} \boldsymbol{\eta}^e_{\mathbf{1}} \cdot \boldsymbol{e}_1 & \boldsymbol{\eta}^e_{\mathbf{1}} \cdot \boldsymbol{e}_2 & 0 & 0 & 0 & 0 \\ \boldsymbol{\eta}^e_{\mathbf{2}} \cdot \boldsymbol{e}_1 & \boldsymbol{\eta}^e_{\mathbf{2}} \cdot \boldsymbol{e}_2 & 0 & 0 & 0 & 0 \\ 0 & 0 & 1 & 0 & 0 & 0 \\ 0 & 0 & 0 & \boldsymbol{\eta}^e_{\mathbf{1}} \cdot \boldsymbol{e}_1 & \boldsymbol{\eta}^e_{\mathbf{1}} \cdot \boldsymbol{e}_2 & 0 \\ 0 & 0 & 0 & \boldsymbol{\eta}^e_{\mathbf{2}} \cdot \boldsymbol{e}_1 & \boldsymbol{\eta}^e_{\mathbf{2}} \cdot \boldsymbol{e}_2 & 0 \\ 0 & 0 & 0 & 0 & 0 & 1 \end{array} \right] \tag{C.7}$$

that rotates the axis ($\boldsymbol{e}_1$, $\boldsymbol{e}_2$) into ($\boldsymbol{\eta}^e_1$, $\boldsymbol{\eta}^e_2$):

$$\mathbf{D}^e = (\mathbf{Q}^e)^T \, \mathbf{d}^e, \qquad \boldsymbol{\Delta}\, \mathbf{D}^{e,a} = (\mathbf{Q}^e)^T \, \boldsymbol{\Delta}\, \mathbf{d}^{e,a}, \qquad \boldsymbol{\Delta}\, \mathbf{D}^{e,b} = (\mathbf{Q}^e)^T \, \boldsymbol{\Delta}\, \mathbf{d}^{e,b}. \tag{C.8}$$

C.2 Stiffness matrices

Addressing the interested reader to Huebner *et al.* (2001) for a comprehensive treatment, in terms of the stiffness matrices, the above relations take the form

$$\mathbf{K}^e_b = (\mathbf{Q}^e)^T \, \mathbf{k}^e_b \, \mathbf{Q}^e, \qquad \mathbf{K}^e_{wf} = (\mathbf{Q}^e)^T \, \mathbf{k}^e_{wf} \, \mathbf{Q}^e, \tag{C.9}$$

where $\mathbf{k}^e_b$, $\mathbf{k}^e_{wf}$ and $\mathbf{K}^e_b$, $\mathbf{K}^e_{wf}$ are, in turn, the local and global stiffness matrices of the classical Euler-Bernoulli beam and Winkler foundation.

C.3 Forces and couples

Finally, the global vector of forces and couples is given by (cf. Section 3.4.1)

$$\mathbf{F}^e = \mathbf{K}^e_b \, \mathbf{D}^e + \frac{1}{2} \mathbf{K}^e_{wf} \, \boldsymbol{\Delta}\, \mathbf{D}^{e,a} + \frac{1}{2} \mathbf{K}^e_{wf} \, \boldsymbol{\Delta}\, \mathbf{D}^{e,b}, \tag{C.10}$$

with

$$\mathbf{F}^e := \left[\begin{array}{c} \mathbf{F}_I \\ \mathbf{F}_J \end{array} \right] = \left[\begin{array}{cccccc} F_{XI} & F_{YI} & M_I & F_{XJ} & F_{YJ} & M_J \end{array} \right]^T. \tag{C.11}$$

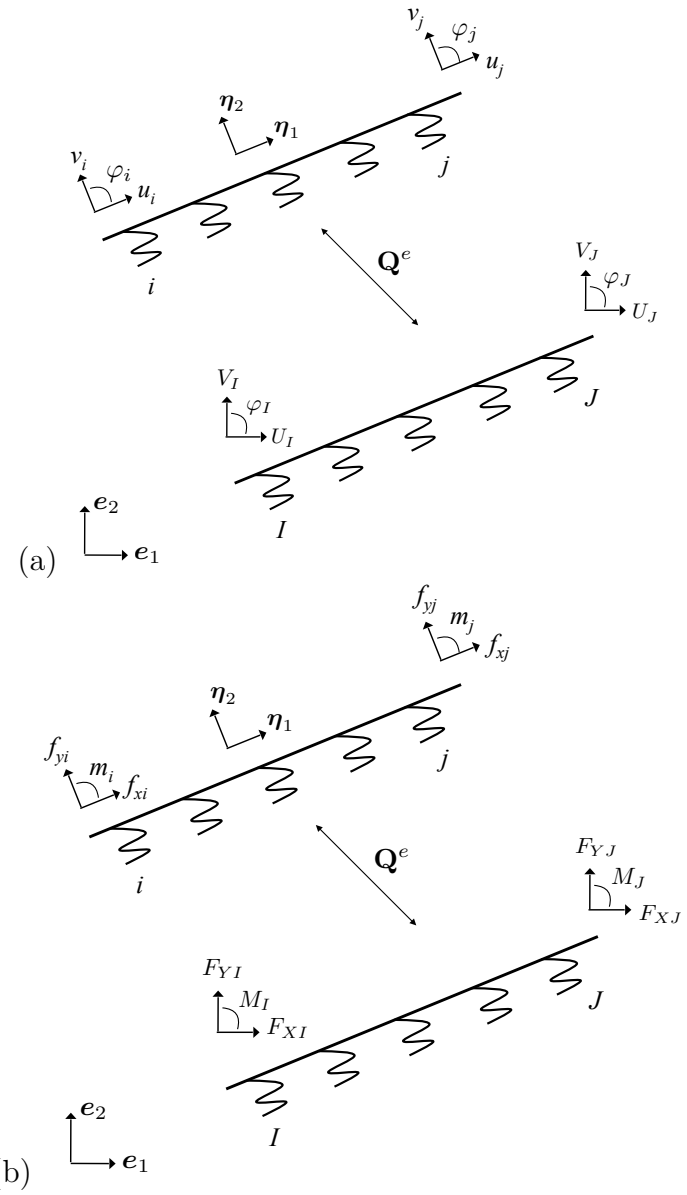

Figure C.1: From the local to the global reference system: (a) degrees of freedom, (b) forces and couples

D | Application of the theory to the biological pressurised tissues: relation between the Winkler foundation constant and the cells' inner pressure

As mentioned in Section 3.8, the application of our theory to the pressurised tissues in biology, i.e., the parenchyma tissue and the hygroscopic keel tissue of the ice plant, requires a suitable relation between the Winkler foundation constant of our model, K_w, and the biological cells' inner pressure, p.

Such relation can be obtained by considering the energetic equivalence in Equation (3.124), provided here for ease of reading:

$$W_{c,\,Winkler} \equiv W_{c,\,fluid}, \tag{D.1}$$

with

$$W_{c,\,Winkler} = W_{w,\,beams} + W_{f,\,Winkler} \tag{D.2}$$

and

$$W_{c,\,fluid} = W_{w,\,walls} + W_{f,\,fluid}, \tag{D.3}$$

respectively, the elastic energy of the unit cell in the case of Winkler foundation model (Figure D.1a) and fluid-filled configuration (Figure D.1b).

By assuming that the elastic energy of the cell walls is the same in the two considered configurations,

$$W_{w,\,beams} \equiv W_{w,\,walls}, \tag{D.4}$$

Equation (D.1) reduces to

$$W_{f,\,Winkler} \equiv W_{f,\,fluid}. \tag{D.5}$$

The first term,

$$W_{f,\,Winkler} = \sum_{i=1}^{3} \frac{1}{2}\,\Delta U_i \left(\mathbf{n}_i^T \mathbf{K}_w \mathbf{n}_i\right) \Delta U_i \equiv \sum_{i=1}^{3} \frac{1}{2}\, d_i\, (\mathbf{n}_i^T \mathbf{E}_f \mathbf{n}_i) \mathbf{n}_i^T\, \mathbf{K}_w \mathbf{n}_i \left(\mathbf{n}_i^T \mathbf{E}_f \mathbf{n}_i\right)\, d_i, \tag{D.6}$$

is a function of the elongation of the springs in the $\mathbf{n}_i$ direction, given by

$$\Delta U_i \equiv \Delta\, d_i = (\mathbf{n}_i^T \mathbf{E}_f \mathbf{n}_i) d_i, \qquad i = 1, 2, 3, \tag{D.7}$$

with

$$\mathbf{E}_f := \begin{bmatrix} \varepsilon_{11} & \varepsilon_{12} \\ \varepsilon_{12} & \varepsilon_{22} \end{bmatrix} \tag{D.8}$$

the infinitesimal strain vector,

$$\mathbf{n}_1 = \begin{bmatrix} -\sin\theta \\ -\cos\theta \end{bmatrix}, \qquad \mathbf{n}_2 = \begin{bmatrix} 1 \\ 0 \end{bmatrix}, \qquad \mathbf{n}_3 = \begin{bmatrix} \sin\theta \\ -\cos\theta \end{bmatrix} \tag{D.9}$$

and (Figure D.1c)

$$d_1 = d_3 = \ell\,\sqrt{2 + 2\sin\theta}, \qquad d_2 = 2\ell\,\cos\theta. \tag{D.10}$$

In addition,

$$W_{f,\,fluid} = \frac{1}{2}\, p \frac{A - A_0}{A_0}\, A_0 = \frac{1}{2}\, p\, (A - A_0) \tag{D.11}$$

is related to the variation in the area of the cell, expressed by

$$A - A_0 = \|\mathbf{l}_1^* \times \mathbf{l}_2^*\| - \|\mathbf{l}_1 \times \mathbf{l}_2\|, \tag{D.12}$$

being

$$\mathbf{l}_1 = \begin{bmatrix} 2\ell\cos\theta \\ 0 \end{bmatrix}, \qquad \mathbf{l}_2 = \begin{bmatrix} \ell\cos\theta \\ \ell\,(1 + \sin\theta) \end{bmatrix} \tag{D.13}$$

and

$$\mathbf{l}_1^* := \mathbf{l}_1 + (\mathbf{U}_5 - \mathbf{U}_3) = \mathbf{l}_1 + \mathbf{E}_f \mathbf{l}_1, \qquad \mathbf{l}_2^* := \mathbf{l}_2 + (\mathbf{U}_1 - \mathbf{U}_3) = \mathbf{l}_2 + \mathbf{E}_f \mathbf{l}_2, \tag{D.14}$$

in turn, the lattice vectors in the undeformed and deformed configuration, $\mathbf{U}_i$ the displacements of the i-th node (Figure D.1c). In particular, simple mathematical

manipulations provide

$$\begin{aligned}
&\|\mathbf{l}_1^* \times \mathbf{l}_2^*\| = \| \left(\mathbf{l}_1 + (\mathbf{U}_5 - \mathbf{U}_3)\right) \times \left(\mathbf{l}_2 + (\mathbf{U}_1 - \mathbf{U}_3)\right) \| \\
&= \|\mathbf{l}_1 \times \mathbf{l}_2 + (\mathbf{U}_5 - \mathbf{U}_3) \times \mathbf{l}_2 + \mathbf{l}_1 \times (\mathbf{U}_1 - \mathbf{U}_3) + o\left(\|\mathbf{U}\|^2\right) \| \\
&= \sqrt{\|\mathbf{l}_1 \times \mathbf{l}_2\|^2 + 2\left(\mathbf{l}_1 \times \mathbf{l}_2\right) \cdot \left((\mathbf{U}_5 - \mathbf{U}_3) \times \mathbf{l}_2\right) + 2\left(\mathbf{l}_1 \times \mathbf{l}_2\right) \cdot \mathbf{l}_1 \times (\mathbf{U}_1 - \mathbf{U}_3) + o\left(\|\mathbf{U}\|^2\right)} \\
&\approx \|\mathbf{l}_1 \times \mathbf{l}_2\| \sqrt{1 + \frac{2\left(\mathbf{l}_1 \times \mathbf{l}_2\right)}{\|\mathbf{l}_1 \times \mathbf{l}_2\|} \cdot (\mathbf{U}_5 - \mathbf{U}_3) \times \frac{\mathbf{l}_2}{\|\mathbf{l}_1 \times \mathbf{l}_2\|} + \frac{2\left(\mathbf{l}_1 \times \mathbf{l}_2\right)}{\|\mathbf{l}_1 \times \mathbf{l}_2\|} \cdot \frac{\mathbf{l}_1}{\|\mathbf{l}_1 \times \mathbf{l}_2\|} \times (\mathbf{U}_1 - \mathbf{U}_3)}.
\end{aligned} \tag{D.15}$$

By taking into account that

$$\frac{\mathbf{l}_1 \times \mathbf{l}_2}{\|\mathbf{l}_1 \times \mathbf{l}_2\|} = \boldsymbol{e}_3 \tag{D.16}$$

and considering the relations in Equation (D.14), it emerges

$$\begin{aligned}
\|\mathbf{l}_1^* \times \mathbf{l}_2^*\| &\approx \|\mathbf{l}_1 \times \mathbf{l}_2\| \left(1 + \boldsymbol{e}_3 \cdot (\mathbf{U}_5 - \mathbf{U}_3) \times \frac{\mathbf{l}_2}{\|\mathbf{l}_1 \times \mathbf{l}_2\|} + \boldsymbol{e}_3 \cdot \frac{\mathbf{l}_1}{\|\mathbf{l}_1 \times \mathbf{l}_2\|} \times (\mathbf{U}_1 - \mathbf{U}_3)\right) \\
&= \|\mathbf{l}_1 \times \mathbf{l}_2\| \left(1 + \frac{\mathbf{l}_2 \times \boldsymbol{e}_3}{\|\mathbf{l}_1 \times \mathbf{l}_2\|} \cdot \mathbf{E}_f \mathbf{l}_1 + \frac{\boldsymbol{e}_3 \times \mathbf{l}_1}{\|\mathbf{l}_1 \times \mathbf{l}_2\|} \cdot \mathbf{E}_f \mathbf{l}_2\right).
\end{aligned} \tag{D.17}$$

Substituting Equation (D.17) into Equation (D.12) leads to

$$A - A_0 = \mathbf{l}_2 \times \boldsymbol{e}_3 \cdot \mathbf{E}_f \mathbf{l}_1 + \boldsymbol{e}_3 \times \mathbf{l}_1 \cdot \mathbf{E}_f \mathbf{l}_2 \tag{D.18}$$

and

$$W_{f,\,fluid} = \frac{1}{2} p \left(A - A_0\right) = \frac{1}{2} p \left(\mathbf{l}_2 \times \boldsymbol{e}_3 \cdot \mathbf{E}_f \mathbf{l}_1 + \boldsymbol{e}_3 \times \mathbf{l}_1 \cdot \mathbf{E}_f \mathbf{l}_2\right). \tag{D.19}$$

The equivalence in (D.5), together with standard calculations, gives

$$K_w(p) = p \, \frac{\cos\theta \left(1 + \sin\theta\right) \left(\varepsilon_{11} + \varepsilon_{22}\right)}{2 \left(\varepsilon_{11} \left(1 + \sin^3\theta\right) + \varepsilon_{22} \left(1 + \sin\theta\right) \cos^2\theta\right)} \tag{D.20}$$

that, when the deformation state is described by

$$\boldsymbol{E}_f := \begin{bmatrix} 1 & 0 \\ 0 & 1 \end{bmatrix}, \tag{D.21}$$

provides

$$K_w(p) = p\,\frac{\cos\theta\,(1+\sin\theta)}{(1+\sin^3\theta)+(1+\sin\theta)\cos^2\theta}. \tag{D.22}$$

Regarding the angle θ, inclination of the cell walls (Figure D.1), two cases are considered. In the first, dealing with the parenchyma tissue, $\theta = 30°$ (cf. Section 3.8) while in the second, related to the hygroscopic keel tissue, the values of $\theta = \theta(p)$ are derived from Guiducci *et al.* (2014) (cf. Section 5.4).

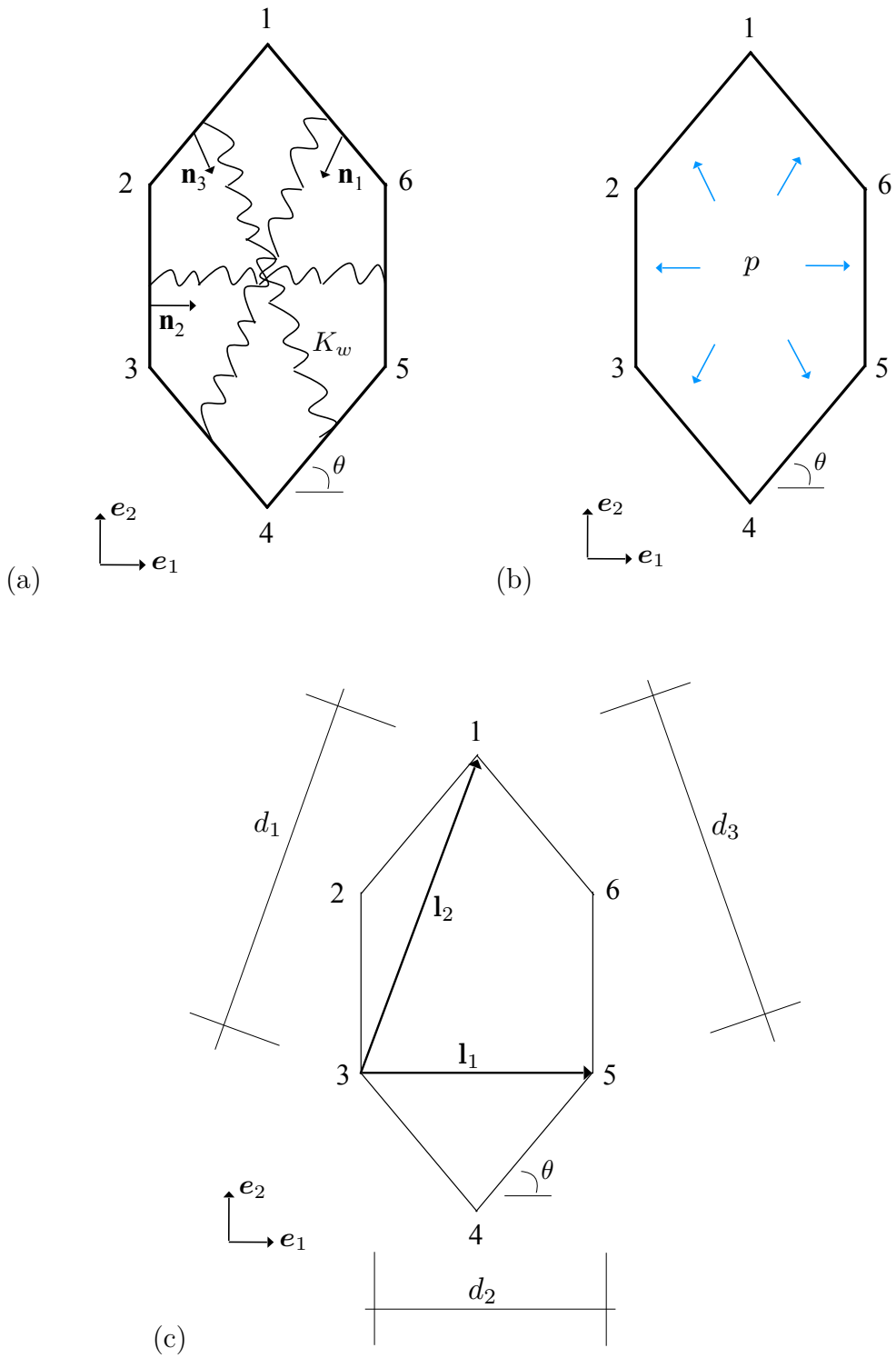

Figure D.1: Application of the theory to the biological tissues: (a) Winkler foundation model, (b) pressurised cell, (c) $\mathbf{l}_i$ *vectors and geometrical parameters* d_i

E | A continuum model for mutable cellular materials: elastic energy and polynomial expressions f_i

E.1 Elastic energy

By adopting the same notation of Section 5.3, the analysis reveals that the limit continuum has the following elastic energy density:

$$
\begin{aligned}
w = & \frac{\varepsilon_{11}^2\, C_\ell c^2 \left(24c^4 D_\ell + 12 D_\ell s^2 f_{14} + c^2\left(C_\ell \ell^2 + 48 D_\ell s^2\right)\right) + \varepsilon_{22}^2\, C_\ell f_0^2 \left(12c^2 D_\ell + C_\ell \ell^2 s^2\right)}{2\ell f_0 \left(24c^2 D_\ell + C_\ell \ell^2 f_{14}\right) c} \\
& + \frac{3 D_\ell \varepsilon_{12}^2 \left(4 C_\ell c^6 \ell^2 + 12 D_\ell f_{15}^2 + 4c^4\left(3D_\ell + C_\ell \ell^2 f_{16}\right) + c^2\left(C_\ell \ell^2 f_{13} - 24 D_\ell f_{15}\right)\right)}{2c\ell^3 f_0 \left(2C_\ell c^2 \ell^2 + 3D_\ell\left(3 + 4 f_{15}\right)\right)} \\
& + \frac{\varepsilon_{11}\varepsilon_{22}\, C_\ell c \left(C_\ell \ell^2 - 12 D_\ell\right) s}{24c^2 D_\ell + C_\ell \ell^2 f_{14}} + \frac{9 D_\ell \left(\omega - \hat{\varphi}\right)^2}{c\ell^3\left(3 + 4 f_{15}\right)} \\
& + \frac{K_w \left(c\left(\varepsilon_{11}^2 f_1 - \varepsilon_{11}\varepsilon_{22} f_2\right) + \varepsilon_{22}^2 f_4 / c + \varepsilon_{12}^2 f_5\right)}{208 f_0 f_3}.
\end{aligned}
\tag{E.1}
$$

Again, to simplify the notation, $c := \cos\theta$, $s := \sin\theta$ and $f_i = f_i(\cos\theta, \sin\theta)$ are the polynomials given in the following section.

E.2 The polynomials f_i

$$
\begin{aligned}
f_0 &= 1 + s, \\
f_1 &= 11518 + s\left(13520 + s\left(23761 + 24\left(540 + 617s\right)s\right)\right), \\
f_2 &= s\left(\left(8s\left(1851s + 8\right) - 1901\right)s - 9412\right) + 1352, \\
f_3 &= 347 + 484s + 452s^2, \\
f_4 &= \left(\left(s\left(8s\left(1851s - 1604\right) + 9721\right) + 9464\right)s + 20280\right)c^2, \\
f_5 &= s^2\left(\left(\left(8s\left(1851s - 2222\right) + 21585\right)s + 22836\right)s + 35114\right) \\
&\quad + \left(8s\left(1851s + 1958\right) + 10969\right)c^4 + 6\left(\left(8s\left(44 - 617s\right) + 2063\right)s + 4158\right)sc^2, \\
f_6 &= 25688 + s\left(9464 + s\left(24093 + 4s\left(581 + 8207s\right)\right)\right), \\
f_7 &= s^2 f_0^2\, f_1 + c^2\, f_4 + 2c^2 s f_0\, f_2, \\
f_8 &= 11518 + 2\, f_4\left(1 + s^2\right) + 33852s + 98719s^2 \\
&\quad + 2s^3\left(s\left(59222 + s\left(s\left(9721 + 8s\left(1851s - 1604\right)\right)9464\right)\right)53046\right), \\
f_9 &= f_0\, f_4, \\
f_{10} &= f_0^3\, f_4, \\
f_{11} &= s f_0\, f_3, \\
f_{12} &= \left(8s f_0 + 4\right)c^4 + 4c^6, \\
f_{13} &= 4s f_0\left(s + s^2 + 3\right) + 3, \\
f_{14} &= 1 + 2s^2, \\
f_{15} &= s f_0, \\
f_{16} &= 1 + 2s f_0.
\end{aligned}
\tag{E.2}
$$

In the particular case of regular hexagonal microstructure, i.e., $\theta = 30°$, the above expressions are:

$$\begin{aligned}
&f_0 = 3/2, && f_1 = 107055/4, && f_2 = -11583/4,\\
&f_3 = 702, && f_4 = 321165/16, && f_5 = 35802,\\
&f_6 = 77571/2, && f_7 = 53703/2, && f_8 = 249561/2,\\
&f_9 = 963495/32, && f_{10} = 9477/4, && f_{11} = 1053/2,\\
&f_{12} = 117/16, && f_{13} = 57/4, && f_{14} = 3/2,\\
&f_{15} = 3/4, && f_{16} = 5/2.
\end{aligned} \tag{E.3}$$

Accordingly, the elastic energy density in Equation (E.1) and the constitutive equations presented in Section 5.3.2 take the form:

$$\begin{aligned}
w = &\frac{(\varepsilon_{11}^2+\varepsilon_{22}^2)\,(C_\ell^2\ell^4+36D_\ell C_\ell\ell^2)+2\varepsilon_{11}\varepsilon_{22}(C_\ell^2\ell^4-12D_\ell C_\ell\ell^2)+96D_\ell C_\ell\ell^2\varepsilon_{12}^2}{4\sqrt{3}\ell^3(12D_\ell+C_\ell\ell^2)}\\
&+\frac{3D_\ell\,(\omega-\hat{\varphi})^2}{\sqrt{3}\ell^3}+\frac{K_w\,(305\,(\varepsilon_{11}^2+\varepsilon_{22}^2)+544\,\varepsilon_{12}^2+66\,\varepsilon_{11}\varepsilon_{22})}{1664\sqrt{3}}
\end{aligned} \tag{E.4}$$

and

$$\begin{aligned}
&\sigma_{11}=\sigma_{11}^{sym}=\frac{(C_\ell^2\ell^2+36D_\ell C_\ell)\varepsilon_{11}+(C_\ell^2\ell^2-12D_\ell C_\ell)\varepsilon_{22}}{2\sqrt{3}\,\ell(12D_\ell+C_\ell\ell^2)}+\frac{K_w(305\varepsilon_{11}+33\varepsilon_{22})}{832\sqrt{3}},\\
&\sigma_{22}=\sigma_{22}^{sym}=\frac{(C_\ell^2\ell^2+36D_\ell C_\ell)\varepsilon_{22}+(C_\ell^2\ell^2-12D_\ell C_\ell)\varepsilon_{11}}{2\sqrt{3}\,\ell(12D_\ell+C_\ell\ell^2)}+\frac{K_w(305\varepsilon_{22}+33\varepsilon_{11})}{832\sqrt{3}},\\
&\sigma_{12}^{sym}=\sigma_{21}^{sym}=\frac{48D_\ell C_\ell\varepsilon_{12}}{2\sqrt{3}\,\ell(12D_\ell+C_\ell\ell^2)}+\frac{17K_w\,\varepsilon_{12}}{52\sqrt{3}},\\
&\sigma_{12}^{skw}=-\sigma_{21}^{skw}=\frac{\sqrt{3}\,D_\ell\,(\omega-\hat{\varphi})}{\ell^3},\\
&\sigma_{12}=\sigma_{12}^{sym}+\sigma_{12}^{skw},\qquad \sigma_{21}=\sigma_{21}^{sym}+\sigma_{21}^{skw}.
\end{aligned} \tag{E.5}$$

F | The kirigami honeycomb: elastic energy and constitutive equations of the limit continuum

As stated in Section 6.3, a sequence of kirigami honeycombs can be obtained by cutting and stretching a sheet of starting material. In particular, let us consider the α-kirigami honeycomb, corresponding to the application of the generic stretch α.

As anticipated, its continuum description follows from the analysis of the unit cell of the periodic array, illustrated in Figure F.1 for ease of reading, together with the energetic approach presented in Section 3.4. Specifically, the equivalent continuum is characterised by the following elastic energy and constitutive equations.

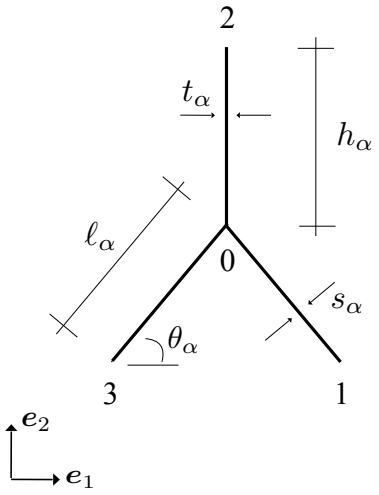

Figure F.1: Continuum modelling of the α-kirigami honeycomb: the unit cell

F.1 Elastic energy

$$
\begin{aligned}
w = & \frac{\lambda_{s\alpha} E_s \left(\beta_\alpha f_{2\alpha}^2 \left(c_\alpha^2 \lambda_{s\alpha}^2 + s_\alpha^2\right) \varepsilon_{22}^2 + c_\alpha^2 \left(\beta_\alpha \left(c_\alpha^2 + \lambda_{s\alpha}^2 s_\alpha^2\right) + 2\lambda_{s\alpha}^2\right) \varepsilon_{11}^2\right)}{2c_\alpha \left(1-\nu_s^2\right) \left(\beta_\alpha + 2\left(c_\alpha^2 \lambda_{s\alpha}^2 + s_\alpha^2\right) f_{2\alpha}\right)} \\
& + \frac{E_s \lambda_{s\alpha}^3 c_\alpha^2 \left(4\beta_\alpha^3 \left(f_{4\alpha} + s_\alpha f_{8\alpha}\right) + 4 + \beta_\alpha^6 \delta_\alpha^2 \left(\delta_\alpha^2 - 2s_\alpha \left(\lambda_{s\alpha}^2 - 2\right) f_{2\alpha}\right)\right) \varepsilon_{12}^2}{2c_\alpha \left(1-\nu_s^2\right) \left(f_{2\alpha} \left(8 f_{1\alpha} c_\alpha^2 + \lambda_{s\alpha}^2 f_{3\alpha}\right)\right)} \\
& + \frac{E_s \lambda_{s\alpha}^3 \left(f_{6\alpha} + \beta_\alpha^3 c_\alpha^4 \left(2\lambda_{s\alpha}^2 + \delta_\alpha^2 f_{9\alpha}\right) + \beta_\alpha^3 f_{1\alpha} \lambda_{s\alpha}^2 s_\alpha^2 f_{2\alpha}^2\right) \varepsilon_{12}^2}{2c_\alpha \left(1-\nu_s^2\right) \left(f_{2\alpha} \left(8 f_{1\alpha} c_\alpha^2 + \lambda_{s\alpha}^2 f_{3\alpha}\right)\right)} \\
& + \frac{\lambda_{s\alpha}^3 E_s \left(f_{6\alpha} + \beta_\alpha^3 f_{1\alpha} \lambda_{s\alpha} \left(1 + \delta_\alpha s_\alpha\right)^2 + f_{7\alpha}\right) \left(\omega - \hat{\varphi}\right)^2}{2c_\alpha \left(1-\nu_s^2\right) \left(f_{2\alpha} \left(8 f_{1\alpha} c_\alpha^2 + \lambda_{s\alpha}^2 f_{3\alpha}\right)\right)} \\
& - \frac{\lambda_{s\alpha} E_s \left(f_{2\alpha} \beta_\alpha c_\alpha \left(\lambda_{s\alpha}^2 - 1\right) s_\alpha\right) \varepsilon_{11} \varepsilon_{22}}{\left(1-\nu_s^2\right) \left(\beta_\alpha + 2\left(c_\alpha^2 \lambda_{s\alpha}^2 + s_\alpha^2\right) f_{2\alpha}\right)},
\end{aligned}
\tag{F.1}
$$

where $\lambda_{t\alpha} := t_\alpha / h_\alpha$ and $\lambda_{s\alpha} := s_\alpha / \ell_\alpha$ are, in turn, the thinness ratio of the vertical and inclined cell walls, $\beta_\alpha := \lambda_{t\alpha} / \lambda_{s\alpha}$ and $\delta_\alpha := h_\alpha / \ell_\alpha$. Also, to simplify the notation, $c_\alpha := \cos\theta_\alpha$, $s_\alpha := \sin\theta_\alpha$ and $f_{i,\alpha} = f_{i,\alpha}(c_\alpha, s_\alpha, \lambda_{t\alpha}, \lambda_{s\alpha})$ are the polynomials listed in Section F.3. Finally, θ_α states for the shape angle (Figure F.1).

F.2 Constitutive equations

The stress-strain relations, derived from (cf. Section 3.5.2)

$$
\sigma_{\gamma\delta} := \frac{\partial w}{\partial \varepsilon_{\gamma\delta}} + \frac{1}{2} \frac{\partial w}{\partial \omega} e_{\gamma\delta} \equiv \sigma_{\gamma\delta}^{sym} + \sigma_{\gamma\delta}^{skw}, \quad \gamma, \delta = 1, 2,
\tag{F.2}
$$

are

$$
\begin{aligned}
\sigma_{11} &= \frac{c_\alpha \lambda_{s\alpha} \left(\beta_\alpha \left(\varepsilon_{11} \left(c_\alpha^2 + \lambda_{s\alpha}^2 s_\alpha^2\right) + s_\alpha \left(\varepsilon_{22} \left(1 - \lambda_{s\alpha}^2\right) f_{2\alpha}\right)\right) + 2\varepsilon_{11} \lambda_{s\alpha}^2\right) E_s}{f_{2\alpha} \left(\beta_\alpha + 2\left(c_\alpha^2 \lambda_{s\alpha}^2 + s_\alpha^2\right)\right) \left(1 - \nu_s^2\right)}, \\
\sigma_{22} &= \frac{\beta_\alpha \lambda_{s\alpha} \left(\varepsilon_{22} \left(c_\alpha^2 \lambda_{s\alpha}^2 + s_\alpha^2\right) f_{2\alpha} + s_\alpha c_\alpha^2 \left(1 - \lambda_{s\alpha}^2\right) \varepsilon_{11}\right) E_s}{c_\alpha \left(\beta_\alpha + 2\left(c_\alpha^2 \lambda_{s\alpha}^2 + c_\alpha^2\right)\right) \left(1 - \nu_s^2\right)},
\end{aligned}
\tag{F.3}
$$

$$\sigma_{12}^{sym} = \frac{\lambda_{s\alpha}^3 E_s \left(c_\alpha^2 \left(4 + \beta_\alpha^6 \delta_\alpha^2 \left(\delta_\alpha^2 - 2 f_{2\alpha} \left(\lambda_{s\alpha}^2 - 2\right) s_\alpha\right)\right) + f_{6\alpha} + \beta_\alpha^3 f_{1\alpha} \lambda_{s\alpha}^2 s_\alpha^2 f_{2\alpha}^2\right) \varepsilon_{12}}{2 c_\alpha f_{2\alpha} \left(8 f_{1\alpha} c_\alpha^2 + \lambda_{s\alpha}^2 f_{3\alpha}\right) \left(1 - \nu_s^2\right)}$$

$$+ \frac{\lambda_{s\alpha}^3 E_s \beta_\alpha^3 \left(c_\alpha^3 \left(2\lambda_{s\alpha}^2 + \delta_\alpha^2 f_{9\alpha}\right) + 4 c_\alpha \left(f_{4\alpha} - \delta_\alpha \left(\lambda_{s\alpha}^2 - 14\right) s_\alpha - \left(\lambda_{s\alpha}^2 - 8\right) s_\alpha^2\right)\right) \varepsilon_{12}}{2 f_{2\alpha} \left(8 f_{1\alpha} c_\alpha^2 + \lambda_{s\alpha}^2 f_{3\alpha}\right) \left(1 - \nu_s^2\right)},$$

$$\sigma_{12}^{skw} = -\sigma_{21}^{skw} = \frac{2\lambda_{s\alpha}^3 E_s}{\sqrt{3}\left(1 + \lambda_{s\alpha}^2\right)\left(1 - \nu_s^2\right)} \left(\omega - \hat{\varphi}\right),$$

$$\sigma_{12} = \sigma_{12}^{sym} + \sigma_{12}^{skw}, \qquad \sigma_{21} = \sigma_{12}^{sym} + \sigma_{21}^{skw}. \tag{F.4}$$

F.3 The polynomials $f_{i\alpha}$

$$f_{1\alpha} = 2 + \beta_\alpha^3 \delta_\alpha^2,$$

$$f_{2\alpha} = \delta_\alpha + s_\alpha,$$

$$f_{3\alpha} = \beta_\alpha^6 \, \delta_\alpha^2 + 4 s_\alpha^2 + 4\beta_\alpha^3 \left(2 + 3\delta_\alpha s_\alpha + 2\delta_\alpha^2 s_\alpha^2\right),$$

$$f_{4\alpha} = \delta_\alpha^2 \left(2 + 3 s_\alpha^2 + 2 s_\alpha^4\right),$$

$$f_{5\alpha} = 14\delta_\alpha + 8 s_\alpha, \tag{F.5}$$

$$f_{6\alpha} = 8\beta_\alpha^3 \, \delta_\alpha^2 \, c_\alpha^6,$$

$$f_{7\alpha} = 4\beta_\alpha^3 \, \delta_\alpha^2 \, c_\alpha^4 \left(4 s_\alpha^2 - 3\right) + c_\alpha^2 \left(4 + \beta_\alpha^6 \delta_\alpha^4 + 4\beta_\alpha^3 \delta_\alpha^2 \left(2 - 3 s_\alpha^2 + 2 s_\alpha^4\right)\right),$$

$$f_{8\alpha} = 14\delta_\alpha + s_\alpha \left(8 - \lambda_{s\alpha}^2 s_\alpha f_{2\alpha}\right),$$

$$f_{9\alpha} = 12 + \beta_\alpha^3 \, \lambda_{s\alpha}^2 + 16 s_\alpha^2.$$

F.4 The particular case $\theta_\alpha = 30°$, $\beta_\alpha = \delta_\alpha = 1$

In the particular case of regular hexagonal microstructure, with $\beta_\alpha = \delta_\alpha = 1$ and $\theta_\alpha = 30°$, the expressions in Equation (F.5) are given by

$$\begin{aligned} &f_{1\alpha} = 3, && f_{2\alpha} = 3/2, && f_{3\alpha} = 18, \\ &f_{4\alpha} = 23/8, && f_{5\alpha} = 18, && f_{6\alpha} = 27/8, \\ &f_{7\alpha} = 27/8, && f_{8\alpha} = 18 - 3\lambda_\alpha^2/8, && f_{9\alpha} = 16 + \lambda_\alpha^2, \end{aligned} \tag{F.6}$$

with $\lambda_{s\alpha} = \lambda_{t\alpha} \equiv \lambda_\alpha$.

Consequently, the elastic energy density in Equation (F.1) and the constitutive relations in Equations (F.3) and (F.4) are now expressed by:

$$w = \frac{\lambda_\alpha E_s \left(\left(1 + 3\lambda_\alpha^2\right) \left(\varepsilon_{11}^2 + \varepsilon_{22}^2\right) + 8\varepsilon_{12}^2 \lambda_\alpha^2 - 2\varepsilon_{11}\varepsilon_{22} \left(\lambda_\alpha^2 - 1\right) \right)}{4\sqrt{3} \left(1 + \lambda_\alpha^2\right) \left(1 - \nu_s^2\right)} + \frac{\lambda_\alpha^3 E_s \left(\omega - \hat{\varphi}\right)^2}{4\sqrt{3} \left(1 - \nu_s^2\right)} \tag{F.7}$$

and

$$\begin{aligned} \sigma_{11} &= \frac{\lambda_\alpha E_s \left(\varepsilon_{11} + \varepsilon_{22} + \lambda_\alpha^2 \left(3\varepsilon_{11} - \varepsilon_{22}\right)\right)}{2\sqrt{3} \left(1 + \lambda_\alpha^2\right) \left(1 - \nu_s^2\right)}, \\ \sigma_{22} &= \frac{\lambda_\alpha E_s \left(\varepsilon_{11} + \varepsilon_{22} + \lambda_\alpha^2 \left(3\varepsilon_{22} - \varepsilon_{11}\right)\right)}{2\sqrt{3} \left(1 + \lambda_\alpha^2\right) \left(1 - \nu_s^2\right)}, \\ \sigma_{12}^{sym} &= \frac{2\lambda_\alpha^3 E_s}{\sqrt{3} \left(1 + \lambda_\alpha^2\right) \left(1 - \nu_s^2\right)} \varepsilon_{12}, \\ \sigma_{12}^{skw} &= -\sigma_{21}^{skw} = \frac{\lambda_\alpha^3 E_s}{4\sqrt{3} \left(1 - \nu_s^2\right)} \left(\omega - \hat{\varphi}\right), \\ \sigma_{12} &= \sigma_{12}^{sym} + \sigma_{12}^{skw}, \qquad \sigma_{21} = \sigma_{12}^{sym} + \sigma_{21}^{skw}. \end{aligned} \tag{F.8}$$

Finally, the elastic moduli listed in Equations (6.4) take the form

$$
\begin{aligned}
E_{1,\alpha} = E_{2,\alpha} \equiv E_\alpha &= \frac{4\lambda_\alpha^3 E_s}{\sqrt{3}\,(3\lambda_\alpha^2+1)\,(1-\nu_s^2)}, \\
\nu_{12,\alpha} = \nu_{21,\alpha} \equiv \nu_\alpha &= \frac{1-\lambda_\alpha^2}{3\lambda_\alpha^2+1}, \\
G_\alpha &= \frac{\lambda_\alpha^3 E_s}{\sqrt{3}\,(\lambda_\alpha^2+1)\,(1-\nu_s^2)},
\end{aligned}
\tag{F.9}
$$

relations that coincide with the published results (cf. Section 3.6.2, Table 3.6).

References

Adams, D. F. & Doner, D. R. (1967) Transverse normal loading of a unidirectional composite. *Journal of Composite Materials*, **1** (2), 152–164.

Aizenberg, J., Weaver, J. C., Thanawala, M. S., Sundar, V. C., Morse, D. E. & Fratzl, P. (2005) Skeleton of Euplectella sp.: Structural Hierarchy from the Nanoscale to the Macroscale. *Science*, **309** (5732), 275–278.

Ajdari, A., Jahromi, B. H., Papadopoulos, J., Hashemi, H. N. & Vaziri, A. (2012) Hierarchical honeycombs with tailorable properties. *International Journal of Solids and Structures*, **49**, 1413–1419.

Altenbach, H. & Oechsner, A. (2010) *Cellular and Porous Materials in Structures and Processes*. Udine, CISM.

Alzebdeh, K. & Ostoja-Starzewski, M. (1999) On a spring-Network Model and Effective Elastic Moduli of granular Materials. *Journal of Applied Mechanics*, **66**, 172–180.

Ashby, M. F. (2006) The properties of foams and lattices. *Philosophical Transactions of the Royal Society A*, **364**, 15–30.

Avramidis, I. E. & Morfidis, K. (2006) Bending of beams on three-parameter elastic foundation. *International Journal of Solids and Structures*, **43**, 357–375.

Barbieri, E., Ongaro, F. & Pugno, N. M. (2017) A J-integral-based arc-length solver for brittle and ductile crack propagation in finite deformation-finite strain hyperelastic solids with an application to graphene kirigami. *Computer Methods in Applied Mechanics and Engineering*, **315**, 713–743.

Barthelat, F. & Mirkhalaf, M. (2013) The quest for stiff, strong and tough hybrid materials: an exhaustive exploration. *Journal of the Royal Society Interface*, **10**, 1–11.

Bazant, Z. P. (1971) Micropolar medium as model for buckling of grid frameworks. *Developments in Mechanics*, **6**, 587–594.

Bazant, Z. P. & Christensen, M. (1972) Analogy between micropolar continuum and grid frameworks under initial stress. *International Journal of Solids and Structures*, **8**, 327–346.

Bensoussan, A., Lions, J. L. & Papanicolaou, G. (1978) *Asymptotic Analysis for Periodic Structures*. Berlin, North-Holland.

Bhushan, B. (2009) Biomimetics: lessons from nature-an overview. *Philosophical Transactions of the Royal Society A*, **367**, 1445–1486.

Bitzer, T. (1994) Honeycomb marine applications. *Journal of Reinforced Plastics and Composites*, **13**, 355–360.

Bixler, G. D. & Bhushan, B. (2012) Bioinspired rice leaf and butterfly wing surface structures combining shark skin and lotus effects. *Soft Matter*, **8** (44), 11271–11284.

Blees, M., Rose, P., Barnard, A., Roberts, S. & McEuen, P. L. (2014) Graphene Kirigami. *Nature*, **524**, 204–212.

Booth, T. J., Blake, P., Nair, R. R., Jiang, D., Hill, E. W., Bangert, U., Bleloch, A., Gass, M., Novoselov, K. S., Katsnelson, M. I. & Geim, A. K. (2008) Macroscopic graphene membranes and their extraordinary stiffness. *Nano Letters*, **8**, 2442–2446.

Borodich, F. M. (1999) Fractals and fractal scaling in fracture mechanics. *International Journal of Fracture*, **64**, 239–259.

Bosia, F., Abdalrahman, T. & Pugno, N. M. (2012) Investigating the role of hierarchy on the strength of composite materials: evidence of a crucial synergy between hierarchy and material mixing. *Nanoscale*, **4**, 1200–1207.

Bouchitte, G. & Suquet, P. (1991) Homogenization, plasticity and yield design. In: Dal Maso, G. & Dell'Antonio, G. F. (eds), *Composite Media and Homogenization Theory: An International Centre for Theoretical Physics Workshop, Trieste, Italy, January 1990*, Birkhauser, pp. 107–133.

Braides, A. (2002) Γ-*Convergence for Beginners*. Oxford, Oxford University Press.

Brockenborough, J. R., Suresh, S. & Wienecke, H. A. (1991) Deformation of metal-matrix composites with continuous fibers: geometrical effects of fiber distribution and shape. *Acta Metallurgica et Materialia*, **39**, 735–752.

Bruce, D. M. (2003) Mathematical modelling of the cellular mechanics of plants. *Philosophical Transactions of the Royal Society B*, **358**, 1437–1444.

de Bruijn, N. G. (1981) Algebraic theory of Penrose's non-periodic tilings of the plane. *Indagationes Mathematicae (Proceedings)*, **84** (1), 53–66.

Buehler, M. J. (2008) Nanomechanics of collagen fibrils under varying cross-link densities: Atomistic and continuum studies. *Journal of the Mechanical Behavior of Biomedical Materials I*, **41**, 59–67.

Burgert, I. & Fratzl, P. (2009) Actuation systems in plants as prototypes for bioinspired devices. *Philosophical Transactions of the Royal Society A*, **367**, 1541–1557.

Burlayenko, V. N. & Sadowski, T. (2010) Effective elastic properties of foam-filled honeycomb cores of sandwich panels. *Composite Structures*, **92**, 2890–2900.

Caillerie, D., Mourad, A. & Raoult, A. (2006) Discrete Homogenization in Graphene Sheet Modeling. *Journal of Elasticity*, **84**, 33–68.

Cappello, L., Pirrera, A. & Weaver, P. M. (2015) A series elastic composite actuator for soft arm exosuits. In: *IEEE International Conference on Rehabilitation Robotics (ICORR), Singapore, August 2015*, IEEE, pp. 61–66.

Carpinteri, A. & Pugno, N. (2008) Mechanics of hierarchical materials. *International Journal of Fracture*, **150**, 221–226.

Castle, T., Cho, Y., Gong, X., Jung, E., Sussman, D. M., Yang, S. & Kamien, R. D. (2014) Making the cut: Lattice kirigami rules. *Physical Review Letters*, **113**, 245–502.

Chen, C. N. (1998) Solution of beam on elastic foundation by DQEM. *Journal of Engineering Mechanics*, **124**, 1381–1384.

Chen, Y. & Feng, J. (2012) Folding of a type of deployable origami structures. *International Journal of Structural Stability and Dynamics*, **12** (6), 12500541–125005417.

Chen, W. F., Han, D. J. & Han, D. (2007) *Plasticity for structural engineers*. Plantation, J. Ross Publication.

Chen, J. Y., Huang, Y. & Ortiz, M. (1998) Fracture analysis of cellular materials: a strain gradient model. *Journal of the Mechanics and Physics of Solids*, **46** (5), 789–828.

Chen, Q. & Pugno, N. M. (2012) In-plane elastic buckling of hierarchical honeycomb materials. *European Journal of Mechanics - A/Solids*, **34**, 120–129.

Chen, Q. & Pugno, N. M. (2013a) In-plane elastic properties of hierarchical nano-honeycombs: The role of the surface effect. *European Journal of Mechanics - A/Solids*, **37**, 248–255.

Chen, Q. & Pugno, N. M. (2013b) Biomimetic mechanisms of natural hierarchical materials: a review. *Journal of the Mechanical Behavior of Biomedical Materials*, **19**, 3–33.

Christensen, R. M. (1987) Sufficient symmetry conditions for isotropy of the elastic moduli tensor. *Journal of Applied Mechanics*, **54**, 772–777.

Christensen, R. M. (2000) Mechanics of cellular and other low-density materials. *International Journal of Solids and Structures*, **37**, 93–104.

Cybulski, J. S., Clements, J. & Prakash, M. (2014) Foldscope: origami-based paper microscope. *PLOS ONE*, **9** (6), 1–11.

Cohen, Y. B. (2005) Biomimetics: mimicking and inspired-by biology. In: *Proceedings of the SPIE Smart Structures Conference, 7-10 March 2005, San Diego, USA*, SPIE, pp. 1–8.

Cohen, Y. B. (2011) *Biomimetics: Nature-Based Innovation*. Boca Raton, CRC Press.

Cranford, S., Sen, D. & Buehler, M. J. (2009) Meso-origami: folding multilayer graphene sheets. *Applied Physics Letters*, **95** (12), 1231211–1231213.

Cundy, H. M. & Rolett, A. P. (1961) *Mathematical models*. Oxford, Clarendon Press.

Dal Maso, G. (1993) *An introduction to* Γ*-convergence*. Boston, Birkauser.

Davini, C. & Ongaro, F. (2011) A Homogenized Model for Honeycomb cellular materials. *Journal of Elasticity*, **104**, 205–226.

Dawson, M. A. & Gibson, L. J. (2007) Optimization of cylindrical shells with compliant cores. *International Journal of Solids and Structures*, **44**, 1145–1160.

Dean, H. B. (1921) *Artificial Honeycomb.* Patent US1.

Deshpande, V. S., Ashby, M. F. & Fleck, N. A. (2001) Foam topology: bending versus stretching dominated architectures. *Acta Materialia*, **49**, 1035–1040.

Dinev, D. (2012) Analytical solution of beam on elastic foundation by singularity functions. *Engineering MECHANICS*, **19** (6), 381–392.

D'Mello, R. J. & Waas, A. M. (2013) In-plane crush response and energy absorption of circular cell honeycomb filled with elastomer. *Composite structures*, **106**, 491–501.

Dos Reis, F. & Ganghoffer, J. F. (2012a) Construction of micropolar continua from the asymptotic homogenization of beam lattices. *Computers & Structures*, **112-113**, 354–363.

Dos Reis, F. & Ganghoffer, J. F. (2012b) Equivalent mechanical properties of auxetic lattices from discrete homogenization. *Computational Materials Science*, **51**, 314–321.

Drugan, W. J. & Willis, J. R. (1996) A micromechanics-based nonlocal constitutive equations and estimates of representative volume element size for elastic composites. *Journal of the Mechanics and Physics of Solids*, **44**, 497–524.

Dumais, J. & Forterre, Y. (2012) Vegetable dynamics: the role of water in plant movements. *Annual Review of Fluid Mechanics*, **44**, 453–478.

Earle, V. (2013) Vicky Earle - Medical Illustration.
Available from: http://vearlemedicalart.com [Accessed 15th November 2016].

Eidini M. & Paulino, G. H. (2015) Unraveling metamaterial properties in zigzag-base folded sheets. *Science Advances*, **1** (8), e1500224.

Eisenberger, M. & Yankelevsky, D. Z. (1985) Exact stiffness matrix for beams on elastic foundation. *Computers & Structures*, **21**, 1335–1359.

Eremeyev, V. A., Lebedev, L. P. & Altenbach, H. (2013) *Foundations of Micropolar Mechanics.* Berlin, Springer.

Ericksen, J. L. (2008) On the Cauchy-Born Rule. *Mathematics and Mechanics of Solids*, **13**, 199–220.

Eringen, A. C. (1966) Linear Theory of Micropolar Elasticity. *Journal of Mathematics and Mechanics*, **15** (6), 909–923.

Eringen, A. C. (1968) Theory of Micropolar elasticity. In: Liebowitz, H. (ed.), *Fracture II*, New York, Academic Press, pp. 662–729.

Falk, S., Hertz, C. H. & Virgin, H. I. (1958) On the relation between turgor pressure and tissue rigidity. Experiments on resonance frequency and tissue rigidity. *Physiologia Plantarum*, **11**, 802–817.

Fan, H. L., Jin, F. N. & Fang, D. N. (2008) Mechanical properties of hierarchical cellular materials. Part I: Analysis. *Composites Science and Technology*, **68**, 3380–3387.

Forterre, Y. (2013) Slow, fast and furious: understanding the physics of plant movements. *Journal of Experimental Botany*, **64**, 4745–4760.

Fortmeyer, R. & Linn, C. (2014) *Kinetic Architecture: Designs for Active Envelopes*. Australia, Images Publishing.

Fratzl, P. (2007) Biomimetic materials research: what can we really learn from nature's structural materials. *Journal of The Royal Society Interface*, **4**, 637–642.

Fratzl, P. (2008) *Collagen: Structure and Mechanics. An Introduction*. Berlin, Springer.

Fratzl, P. & Weinkamer, R. (2007) Nature's hierarchical materials. *Progress in Materials Science*, **52** (8), 1263–1334.

Fratzl, P. & Weinkamer, R. (2011) Mechanical adaptation of biological materials. The examples of bone and wood. *Materials Science and Engineering C*, **31**, 1164–1173.

Fleck, N. A., Deshpande, V. S. & Ashby, M. F. (2010) Micro-architectured materials: past, present and future. *Proceedings of the Royal Society of London A*, **466**, 2495–2516.

Galvanetto, U. & Ferri Aliabadi, M. H. (2010) *Multiscale Modeling in Solid Machanics. Computational Approaches*. London, Imperial College Press.

Gao, H. (2010) Learning from Nature about Principles of Hierarchical Materials. In: *3rd International Nanoelectronics Conference (INEC), Hong Kong, China, 3-8 January 2010*, IEEE.

Georget, D. M. R., Smith, A. C. & Waldron, K. W. (2003) Modelling of carrot tissue as a fluid-filled foam. *Journal of Materials Science*, **38**, 1933–1938.

Gibson, L. J. (1989) Modelling the Mechanical Behavior of Cellular Materials. *Materials Science and Engineering A*, **110**, 1–36.

Gibson, L. J. (2005) Biomechanics of cellular solids. *Journal of Biomechanics*, **38**, 377–399.

Gibson, L. J. (2012) The hierarchical structure and mechanics of plant materials. *Journal of the Royal Society Interface*, **9**, 2749–2766.

Gibson, L. J. & Ashby, M. F. (2001) *Cellular Solids. Structure and Properties*. Cambridge, Cambridge University Press.

Gibson, L. J., Ashby, M. F. & Harley, B. A. (2010) *Cellular Materials in Nature and Medicine*. Cambridge, Cambridge University Press.

Gibson, L. J., Ashby, M. F., Schajer, G. S. & Robertson, C. I. (1982) The Mechanics of Two-dimensional Cellular Materials. *Proceedings of the Royal Society of London A*, **382**, 25–42.

Gonella, S. & Ruzzene, M. (2008) Homogenization and equivalent in-plane properties of two-dimensional periodic lattices. *International Journal of Solids and Structures*, **45**, 2897–2915.

Gordon, R., Losic, D., Tiffany, M. A., Nagy, S. S. & Sterrenburg, F. A. S. (2008) The Glass Menagerie: diatoms for novel applications in nanotechnology. *Trends in Biotechnology*, **27** (2), 116–127.

Grootscholten, C. (2005) Cok Grootscholten Succulent World ...
Available from: https://grootscholten.fotki.com [Accessed 5th May 2017].

Guiducci, L., Fratzl, P., Brechet, Y. J. M. & Dunlop, J. W. C. (2014) Pressurized honeycombs as soft-actuators: a theoretical study. *Journal of The Royal Society Interface*, **11** (98), 20140458.

Guiducci, L., Weaver, J. C., Brechet, Y. J. M., Fratzl, P. & Dunlop, J. W. C. (2015) The Geometric Design and Fabrication of Actuating Cellular Structures. *Advanced Materials Interfaces*, **2**, 1500011.

Gusev, A. A. (1997) Representative volume element size for elastic composites: a numerical study. *Journal of the Mechanics and Physics of Solids*, **45**, 1449–1459.

Haghpanah, B., Oftadeh, R., Papadopoulos, J. & Vaziri, A. (2013) Self-similar hierarchical honeycombs. *Proceedings of the Royal Society of London A*, **469**, 5322–5334.

Haghpanah, B., Papadopoulos, J., Mousanezhad, D. & Hashemi, H. N. (2014) Buckling of regular, chiral and hierarchical honeycombs under a general macroscopic stress state. *Proceedings of the Royal Society of London A*, **470**, 20130856.

Harrington, M. (2011) Origami in seed capsules.
Available from: https://www.mpg.de/4346926/biomimetic_origami_seed [Accessed 1st March 2016].

Harrington, M. J., Razghandi, K., Ditsch, F., Guiducci, L., Rueggeberg, M., Dunlop, J. W. C., Fratzl, P., Neinhuis, C. & Burgert, I. (2011) Origami-like unfolding of hydro-actuated ice plant seed capsules. *Nature Communications*, **2**, 337.

Hawkes, E., An, B., Benbernou, N. M., Tanaka, H., Kim, S., Demaine, E. D., Rus, D. & Wood, R. J. (2010) Programmable matter by folding. *Proceedings of the National Academy of Sciences of the United States of America*, **107**, 12441–12445.

Hetenyi, M. (1946) *Beams on elastic foundation*. Baltimore, Waverly Press.

Hosur, V. & Bhavikatti, S. S. (1996) Influence lines for bending moments in beams on elastic foundations. *Computers & Structures*, **58**, 1225–1231.

Huebner, K. H., Dewhirst, D. L., Smith, D. E. & Byrom, T. G. (2001) *The Finite Element Method for Engineers*. New York, Wiley.

Hutchinson, R. G. & Fleck, N. A. (2005) Micro-architectured cellular solids-the hunt for statically determinate periodic trusses. *ZAMM - Journal of Applied Mathematics and Mechanics*, **85**, 607–617.

Janco, R. (2010) Solution Methods for Beam and Frames on Elastic Foundation Using the Finite Element Method. In: *International Scientific Conference on Mechanical*

Structures and Foundation Engineering (MSFE), Ostrava, Czech Republic, 13 September 2010.

Jenkins, C. H. M. (2012) *Bio-Inspired Engineering.* New York, Momentum Press.

Jeronimidis, G. & Atkins, A. G. (1995) Mechanics of biological materials and structures - Nature's lessons for the engineer. *Journal of Mechanical Engineering Science*, **209**, 221–235.

Kanit, T., Forest, S., Galliet, I., Mounoury, V. & Jeulin, D. (2003) Determination of the size of the representative volume element for random composites: statistical and numerical approach. *International Journal of Solids and Structures*, **40**, 3647–3679.

Karkon, M. & Karkon, H. (2016) New element formulation for free vibration analysis of Timoshenko beam on Pasternak elastic foundation. *Asian Journal of Civil Engineering*, **17** (4), 427–442.

Katz, J. S. (1999) The self-similar science system. *Research Policy*, **28**, 501–517.

Kemp, M. (2004) Structural intuitions and metamorphic thinking in art, architecture and science. In: *Metamorph - 9th International Architecture Exhibition Focus*, Fondazione La Biennale di Venezia, pp. 30–43.

Kerr, A. B. (1964) Elastic and viscoelastic foundation models. *Journal of Applied Mechanics*, **31**, 491–498.

Khire, R. A., Dessel, S. V., Messac, A. & Mullur, A. A. (2006) Study of a honeycomb-type rigidified inflatable structure for housing. *Journal of Structural Engineering*, **132**, 1664–1672.

Kraynik, A. M., Neilsen, M. K., Reinelt, D. A. & Warren, W. E., (1998) Foam micromechanics. In: *Foams and Emulsions: Proceedings of the NATO Advanced Study Institute on Foams, Emulsions and Cellular Materials*, Cargese, Corsica, Kluwer.

Kumar, R. S. & McDowell, D. L. (2004) Generalized continuum modeling of 2-D periodic cellular solids. *International Journal of Solids and Structures*, **41**, 7399–7422.

Kuo, Y. H. & Lee, S. Y. (1994) Deflection of nonuniform beams resting on a nonlinear elastic foundation. *Computers & Structures*, **51**, 513–519.

Kuribayashi, K., Tsuchiya, K., You, Z., Tomus, D., Umemoto, M., Ito, T. & Sasaki, M. (2006) Self-deployable origami stent grafts as a biomedical application of Ni-rich TiNi shape memory alloy foil. *Materials Science & Engineering*, **419**, 131–137.

Lakes, R. (1993) Materials with structural hierarchy. *Nature*, **361**, 511–515.

Lee, C., Wei, X., Kysar, J. W. & Hone, J. (2008) Measurement of the elastic properties and intrinsic strength of monolayer graphene. *Science*, **321**, 385–388.

Li, S. & Wang, K. W. (2017) Plant-inspired adaptive structures and materials for morphing and actuation: a review. *Bioinspiration & Biomimetics*, **12**, 011001.

Liu, S., Lu, G., Chen, Y. & Leong, Y. W. (2015) Deformation of the Miura-ori patterned sheet. *International Journal of Mechanical Sciences*, **99**, 130–142.

Lockwood, E. H. & Macmillan, R. H. (1978) *Geometric symmetry*. Cambridge, Cambridge University Press.

Lockyer, S. (1932) Seed dispersal from hygroscopic Mesembryanthemum fruits, Bergeranthus scapigerus, and Dorotheanthus bellidiformis, with a note on Carpanthea pomeridiana. *Annals of Botany*, **46**, 323–342.

Mann, S. (2001) *Biomineralization: Principles and Concepts in Bioinorganic Materials Chemistry*. Oxford, Oxford University Press.

Martinez-Martin, F. J. & Thrall, A. P. (2014) Honeycomb core sandwich panels for origami-inspired deployable shelters: Multi-objective optimization for minimum weight and maximum energy efficiency. *Engineering Structures*, **69**, 158–167.

Martone, P. T., Boller, M., Burgert, I., Dumais, J., Edwards, J., Mach, K., Rowe, N., Rueggeberg, M., Seidel, R. & Speck, T. (2010) Mechanics without muscle: biomechanical inspiration from the plant world. *Integrative and Comparative Biology*, **50**, 888–907.

Mattheck, C. & Kubler, H. (1995) *The internal optimization of trees*. Berlin, Springer.

Meyers, M. A., Chen, P. Y., Lin, A. Y. M. & Seki, Y. (2008) Biological materials: Structure and mechanical properties. *Progress in Materials Science*, **53**, 1–206.

Michel, J. C., Moulinec, H., & Suquet, P. (1999) Effective properties of composite materials with periodic microstructure: a computational approach. *Computer Methods in Applied Mechanics and Engineering*, **172**, 109–143.

Milwich, M., Speck, T., Speck, O., Stegmaier, T. & Planck, H. (2006) Biomimetics and technical textiles: solving engineering problems with the help of nature's wisdom. *American Journal of Botany*, **93**, 1295–1305.

Moulinec, H. & Suquet, P. (1995) A FFT-based numerical method for computing the mechanical properties of composites from images of their microstructure. In: *Microstructure - Property Interactions in Composite Materials*, Zurich, Switzerland, Kluwer Academic Publishers, pp. 235–246.

Moulinec, H. & Suquet, P. (1997) A numerical method for computing the overall response of nonlinear composites with complex microstructure. *Computer Methods in Applied Mechanics and Engineering*, **157**, 69–94.

Murray, G., Gandhi, F. & Hayden, E. (2012) Polymer Filled Honeycombs to Achieve a Structural Material with Appreciable Damping. *Journal of Intelligent Material Systems and Structures*, **23** (6), 703–718.

Needleman, A. (1972) Void growth in an elastic plastic medium. *Journal of Applied Mechanics*, **39**, 964–970.

Nemat-Nasser, S. & Hori, M. (1993) *Micromechanics: Overall Properties of Heterogenous Materials*. Amsterdam, North Holland Publishing.

Neville, R. M., Pirrera, A. & Scarpa, F. (2014) Open shape morphing honeycombs through kirigami. In: *Proceedings of the ASME Conference on Smart Materials, Adaptive Structures and Intelligent Systems, 8-10 September 2014, Newport, Rhode Island, USA*, ASME.

Neville, R. M., Scarpa, F. & Pirrera, A. (2016) Shape morphing Kirigami mechanical metamaterials. *Scientific Reports*, **6**, 31067.

Neville, R. M., Chen, J., Guo, X., Zhang, F., Wang, W., Dobah, Y., Scarpa, F., Leng, J. & Peng, H. X. (2017) A Kirigami shape memory polymer honeycomb concept for deployment. *Smart Materials and Structures*, **26** (5), 05LT03.

Niklas, K. J. (1989) Mechanical Behavior of Plant Tissues as Inferred from the Theory of Pressurized Cellular Solids. *American Journal of Botany*, **76** (6), 929–937.

Niklas, K. J. (1992) *Plant Biomechanics: An Engineering Approach to Plant Form and Function*. Chicago, University of Chicago Press.

Nilsson, S., Hertz, C. & Falk, S. (1958) On the relation between turgor pressure and tissue rigidity. Theoretical calculations on model systems. *Physiologia Plantarum*, **11**, 818–837.

Noor, A. K. (1988) Continuum modelling for repetitive lattice structures. *Applied Mechanics Reviews*, **41**, 285–296.

Onal, C. D., Wood, R. J. & Rus, D. (2011) Towards printable robotics: Origami-inspired planar fabrication of three-dimensional mechanisms. In: *Proceedings of the International Conference on Robotics and Automation (ICRA), Shanghai, China, 9-13 May 2011*.

Ostoya-Starzewski, M. (2002) Lattice models in micromechanics. *Applied Mechanics Reviews*, **55**, 35–60.

Pan, N. (2014) Exploring the significance of structural hierarchy in material systems - A review. *Applied Physics Reviews*, **1**, 021302.

Pellegrino, C., Galvanetto, U. & Schrefler, B. A. (1999) Numerical homogenization of periodic composite materials with non-linear material components. *International Journal for Numerical Methods in Engineering*, **46**, 1609–1637.

Perano, K. J. (1983) *Application of micropolar elasticity to the finite element continuum analysis of articulated structures*. Ph.D. dissertation, University of California, Davis, USA.

Petralia, M. & Wood, R. (2010) Fabrication and analysis of dielectric-elastomer minimum-energy structures for highly-deformable soft robotic systems. In: *Proceedings of the IEEE/RSJ International Conference on Intelligent Robots and Systems (IROS), Taipei, Taiwan, 18-22 October 2010*, pp. 2357–2363.

Popper, K.R. (1965) *Conjectures and Refutations: The Growth of Scientific Knowledge*. New York, Harper Torchbooks.

Ptaszny, J. & Fedelinski, P. (2011) Numerical homogenization by using the fast multipole boundary element method. *Archives of civil and mechanical engineering*, **11**, 181–193.

Pugno, N. & Carpinteri, A. (2008) Design of micro-nanoscale bio-inspired hierarchical materials. *Philosophical Magazine Letters*, **88**, 397–405.

Razzaq, A. (2016) Study solutions website.
Available from: http://istudy.pk/parenchyma [Accessed 12th March 2017].

Razaqpur, A. G. & Shah, K. R. (1991) Exact analysis of beams on two-parameter elastic foundations. *International Journal of Solids and Structures*, **27**, 435–454.

Razghandi, K., Turcaud, S. & Burgert, I. (2014) *Nonlinear Elasticity and Hysteresis: fluid-solid coupling in porous media*. Weinheim, Wiley.

Ritchie, R. O. (2011) The conflicts between strength and toughness. *Nature Materials*, **10**, 817–822.

Sab, K. (1992) On the homogenization and the simulation of random materials. *European Journal of Mechanics - A/Solids*, **11**, 585–607.

Saito, K., Pellegrino, S. & Nojima, T. (2014) Manufacture of arbitrary cross-section composite honeycomb cores based on origami techniques. *Journal of Mechanical Design*, **136** (5), 051011.

Sanchez, C., Arribart, H. & Giraud Guille, M. M. (2005) Biomimetism and bioinspiration as tools for the design of innovative materials and systems. *Nature Materials*, **4**, 277–288.

Sanchez-Palencia, E. (1974) Comportement local et macroscopique d'un type de milieux physiques hrogs. *International Journal of Engineering Science*, **12**, 331–351.

Sanchis Gritsch, C. & Murphy, R. J. (2005) Ultrastructure of Fibre and Parenchyma Cell Walls During Early Stages of Culm Development in *Dendrocalamus asper*. *Annals of Botany*, **95**, 619–629.

Sareh, S. & Rossiter, J. (2015) Kirigami artificial muscles with complex biologically inspired morphologies. *Smart Materials and Structures*, **22** (1), 014004.

Sen, Y. L., Huei, Y. K. & Yee, H. K. (1990) Elastic static deflection of a non-uniform Bernoulli-Euler beam with general elastic end restraints. *Computers & Structures*, **36**, 91–97.

Shah, G. V. & Sitti, M. (2004) Modelling and Design of Biomimetic Adhesives Inspired by Gecko Foot-Hairs. In: *Proceedings of the IEEE International Conference on Robotics and Biomimetics (ROBIO), Shenyang, China, 22-26 August 2004*, pp. 873–878.

Shyu, T. C., Damasceno, P. F., Dodd, P. M., Lamoureux, A., Xu, L., Shlian, M., Shtein, M., Glotzer, S. C. & Kotov, N. A. (2015) A kirigami approach to engineering elasticity in nanocomposites through patterned defects. *Nature materials*, **14**, 785–790.

Soare, M. A. & Picu, R. C. (2007) An approach to solving mechanics problems for materials with multiscale self-similar microstructure. *International Journal of Solids and Structures*, **44**, 7877–7890.

Sun, C. T. & Vaidya, R. S. (1996) Prediction of composite properties from a representative volume element. *Composites Science and Technology*, **56**, 171–179.

Sun, Y., Chen, Q. & Pugno, N. (2014) Elastic and transport properties of the tailorable multifunctional hierarchical honeycombs. *Composite Structures*, **107**, 698–710.

Sun, Y. & Pugno, N. (2013) In plane stiffness of multifunctional hierarchical honeycombs with negative Poisson's ratio sub-structures. *Composite Structures*, **106**, 681-689.

Tachi, T. (2010) Geometric considerations for the design of rigid origami structures. In: *Proceedings of the International Association for Shell and Spatial Structures (IASS) Symposium, Shanghai, China, 8-12 November 2010*, **12**, pp. 458–460.

Taylor, C. M., Smith, C. W., Miller, W. & Evans, K. E. (2011) The effects of hierarchy on the in-plane elastic properties of honeycombs. *International Journal of Solids and Structures*, **48**, 1330–1339.

Taylor, C. M., Smith, C. W., Miller, W. & Evans, K. E. (2010) Functional grading in hierarchical honeycombs: density specific elastic performance. *Composite Structures*, **94**, 2296–2305.

Terada, K. & Kikuchi, N. (2001) A class of general algorithms for multi-scale analyses of heterogeneous media. *Computer Methods in Applied Mechanics and Engineering*, **190**, 5427–5464.

Terada, K., Hori, M., Kyoya, T., Kikuchi, N. (2000) Simulation of the multi-scale convergence in computational homogenization approaches. *International Journal of Solids and Structures*, **37**, 2285–2311.

Thompson, A. W. (1992) *On growth and form - the complete revised edition.* New York, Dover Publications.

Thrall, A. P. & Quaglia, C. P. (2014) Accordion shelters: a historical review of origami-like deployable shelters developed by the US military. *Engineering Structures*, **59**, 686–692.

Tibbits, S. & Cheung, K. (2012) Programmable materials for architectural assembly and automation. *Assembly Automation*, **32**, 216–225.

Tsiatas, G. C. (2014) A new efficient method to evaluate exact stiffness and mass matrices of non-uniform beams resting on an elastic foundation. *Archive of Applied Mechanics*, **84**, 615–623.

Vallabhan, C. V. G. & Das, Y. C. (1991) A refined model for beams on elastic foundations. *International Journal of Solids and Structures*, **5**, 629–637.

Van Liedekerke, P., Ghysels, P., Tijskens, E., Samaey, G., Smeedts, B., Roose, D. & Ramon, H. (2010) A particle-based model to simulate the micromechanics of single-plant parenchyma cells and aggregates. *Physical Biology*, **7** (2), 026006.

Vasista, S. & Tong Land Wong, K. C. (2012) Realization of morphing wings: a multidisciplinary challenge. *Journal of Aircraft*, **49**, 11–28.

Vincent, J. F. V., Bogatyreva, O. A., Bogatyrev, N. R, Bowyer, A. & Pahl, A. K. (2006) Biomimetics: its practice and theory. *Journal of The Royal Society Interface*, **3**, 471–482.

Vos, R. & Barrett, R. (2011) Mechanics of pressure-adaptive honeycomb and its application to wing morphing. *Smart Materials & Structures*, **20**, 94010.

Vos, R., Barrett R. & Romkes A. (2011) Mechanics of pressure-adaptive honeycomb. *Journal of Intelligent Material Systems and Structures*, **22**, 1041–1055.

Wang, X. L. & Stronge, W. J. (1999) Micropolar Theory of Two-Dimensional Stresses in Elastic Honeycomb. *Proceedings of the Royal Society of London*, **455**, 2091–2116.

Wang-Iverson, P., Lang, R. J. & Yim, M. (2011) *Origami 5: Fifth International Meeting of Origami Science, Mathematics, and Education*. Boca Raton, CRC Press.

Warner, M., Thiel, B. L. & Donald, A. M. (2000) The elasticity and failure of fluid-filled cellular solids: Theory and experiment. *Proceedings of the National Academy of Sciences of the United States of America*, **97** (4), 1370–1375.

Warren, W. E. & Byskov, E. (2002) Three-fold symmetry restrictions on two-dimensional micropolar materials. *European Journal of Mechanics - A/Solids*, **21**, 779–792.

Warren, W. E & Kryanik, A. M. (1997) Linear elastic behavior of a low-density Kelvin foam with open cells. *Journal of Applied Mechanics*, **64**, 787–794.

Wegst, U. G. K. (2011) Bending efficiency through property gradients in bamboo, palm and wood-based composites. *Journal of the Mechanical Behavior of Biomedical Materials*, **4**, 744–755.

Wegst, U. G. K. & Ashby, M. F. (2004) The mechanical efficiency of natural materials. *Philosophical Magazine*, **84**, 2167–2181.

Wegst, U. G., Bai, H., Saiz, E., Tomsia, A. P. & Ritchie, R. O. (2015) Bioinspired structural materials. *Nature Materials*, **14**, 23–36.

Wilson, S. (1990) A new face of aerospace honeycomb. *Materials and Design*, **11**, 323–326.

Wu, N., Pitts, M. J. (1999) Development and validation of a finite element model of an apple fruit cell. *Postharvest Biology and Technology*, **16**, 1–8.

Xu, M., Paci, J. T., Oswald, J. & Belytschko, T. (2012) A constitutive equation for graphene based on density functional theory. *International Journal of Solids and Structures*, **49**, 2582–2589.

Zhang, P., Ma, L., Fan, F., Zeng, Z., Peng, C., Loya, P. E., Liu, Z., Gong, Y., Zhang, J. & Zhang, X. (2014) Fracture toughness of graphene. *Nature Communications*, **5**, 3782.

Zhang, Y., Yan, Z., Nan, K., Xiao, D., Liu, Y., Luan, H., Fu, H., Wang, X., Yang, Q. & Wang, J. (2015) A mechanically driven form of Kirigami as a route to

3D mesostructures in micro/nanomembranes. *Proceedings of the National Academy of Sciences of the United States of America*, **112**, 11757–11764.

Zhao, L., Zheng, Q., Fan, H. & Jin, F. (2012) Hierarchical composite honeycombs. *Materials & Design*, **40**, 124–129.

Zheng, Y., Fan, Z., Fei, L., Han, M., Ou, D., Liu, Y., Lin, Q., Guo, X., Fu, H., Xie, Z., Gao, M., Huang, Y., Kim, J. H., Qiu, Y., Nan, K., Kim, J., Gutruf, P., Luo, H., Zhao, A., Hwang, K. C., Huang, Y., Zhang, Y. & Rogers, J. A. (2016) Mechanical assembly of complex, 3D mesostructures from releasable multilayers of advanced materials. *Science Advances*, **2**, 1–11.

Zhu, H. X. & Melrose, J. R. (2003) A Mechanics Model for the Compression of Plant and Vegetative Tissues. *Journal of Theoretical Biology*, **221**, 89–101.

Zienkiewicz, O. C. (1977) *The finite element method.* London, McGraw-Hill.

Journal publications

Ongaro, F., De Falco, P., Pugno, N. M. & Barbieri, E. (2016) Mechanics of filled cellular materials. *Mechanics of materials*, **97**, 26–47.

Ongaro, F., Pugno, N. M. & Barbieri, E. (2016) The in-plane elastic properties of hierarchical composite cellular materials: synergy of hierarchy, material heterogeneity and cell topologies at different levels. *Mechanics of materials*, **103**, 135–147.

Barbieri, E., Ongaro, F. & Pugno, N. M. (2017) A J-integral-based arc-length solver for brittle and ductile crack propagation in finite deformation-finite strain hyperelastic solids with an application to graphene kirigami. *Computer Methods in Applied Mechanics and Engineering*, **315**, 713–743.

Ongaro, F., Pugno, N. M. & Barbieri, E. (2017) Mechanics of mutable hierarchical composite cellular materials. *Mechanics of materials*, under peer review.

Ongaro, F., Pugno, N. M. & Barbieri, E. (2017) The ancient Japanese art of kirigami inspires a novel class of cellular materials: the *kirigami honeycomb*.
In preparation.